Mechanical Behavior of a Bulk Metallic Glass and its Composite over a Wide Range of Strain Rates and Temperatures

Thesis by

Jun Lu

In Partial Fulfillment of the Requirements
for the Degree of
Doctor of Philosophy

California Institute of Technology
Pasadena, California

2002
(Submitted March 20, 2002)

Acknowledgements

I have been extremely fortunate to be accompanied by so many creative people during the years of my study at Caltech. No matter how independent I like to think myself, I could not have completed this thesis without their help.

It is extremely difficult to overstate my deep gratitude to my advisor, Prof. Guruswami Ravichandran. My graduate life at Caltech changed dramatically since I joined his group, which is full of fun and friendship. Without his continuous enthusiasm and inspiration on science and life, I would have been totally lost. I am indebted to him for offering the freedom to pursue scientific research and introducing me to the wonderful world of experimental mechanics. He is a mentor who always shared my happiness during my good times and gave sincere trust and encouragement during my bad times. This made my days at Caltech especially enjoyable and memorable. I am grateful to many of his bright ideas that definitely helped me to advance to where I am standing today. If I had to do it again, I don't think there would be anyone else for whom I would rather work.

I would like to deeply appreciate the support from my second advisor, Prof. William L. Johnson, who continuously leads me through the fantastic field of amorphous metals. I am grateful for the numerous discussions with him. As an applied physicist, his insights and passion for science substantially enhanced my knowledge in materials research. I was truly inspired by his ideas and benefited from all the resources in his group. Without the support from these advisors, none of this interdisciplinary research would have been possible.

I would like to express my thanks to the other thesis committee members, Prof. Wolfgang Knauss, Prof. Kaushik Bhattacharya and Prof Ersan Ustundag, for taking time to read the thesis and for offering many valuable suggestions and criticisms. Prof. Ustundag deserves a special thanks for his generosity in letting me use his equipment at Keck Labs, which helped me to improve the quality of results in the first part of this thesis. I am also grateful to Prof. Ares Rosakis, for allowing me to use his lab facilities; to Prof. Brent Faultz, who offered an excellent materials lab course to me; to Prof. Subra Suresh for the fruitful discussions on indentation of bulk metallic glass; to Prof. John Hall, who brought me to Caltech, arranged financial support for the first two years and helped me a lot in gaining my teaching experience.

Special thanks goes to Dr. C. Hays, who for the first time taught me to fabricate Vitreloy samples. Many thanks to Dr. Paul Kim, who helped me and provided some of the pure metallic glass samples during the early stages of my research. I appreciate the help from Dr. Chi Ma for the excellent training he provided me on the SEM. Thanks to Dr. Eric Andrews for the discussions on dynamic indentation. I also would like to thank Dr. Dale Conner who introduced me the Keck materials lab at the very beginning of my research.

I am indebted to many friends for their help in providing a stimulating and fun environment in which to learn and grow. I am especially grateful to Dr. Shiming Zhuang, who not only collaborated with me on the last chapter of this thesis, but also offered tremendous amount of ideas and help to me. I would like to express my deep appreciation to Dr. Eric Burcsu for many countless suggestions and help. Many thanks also go to Dr. Wei Zhang, Dr. Murat Vural, Dr. Tamim Carin, Dr. Benjamin Chow, Dr. Rena Yu, Dr. David Anderson, Dr. Pradeep Guduru, Dr. Weidong Zhu, Dr. Sangwook Lee, Dr. Kenji Oguni, Dr. Daniel Rittel, Dr. David Owen, Dr. Hansuk Lee, Mr. Petros Arakelian, Ms. Denise Thobe, Ms. Pam Albertson, Ms. Rongjing Zhang and Ms. Cynthia Torres for their outstanding help. I would like to express my gratitude to Dr. Yun Hsu for always being a source of help for problem solving and technical writing.

If there were anybody who deserves a special award, it would have to be my lovely wife Shufang. Thanks to her for hanging in there and loving me through all this, and, for always believing in me.

The research presented in this thesis was supported at various stages by the MRSEC Program of the National Science Foundation (NSF) under award #DMR-0080065, by the Defense

Advanced Research Projects Agency (DARPA) under grant #DAAD19-01-1-0525 and by the Army Research Office. I would like to gratefully acknowledge their support.

Abstract

The development of *bulk* metallic glasses (BMG), which have exceptional mechanical properties such as high strength, high hardness and corrosion resistance, as well as good glass forming and shaping abilities, using relatively inexpensive materials and processing techniques, offers great opportunities to use this class of solids as structural amorphous materials (SAM). In this thesis, the mechanical behavior of a bulk metallic glass $Zr_{41.2}Ti_{13.8}Cu_{12.5}Ni_{10}Be_{22.5}$ (Vitreloy 1) and its composite (β-phase Vitreloy 1 composite, i.e., $Zr_{56.2}Ti_{13.8}Nb_{5.0}Cu_{6.9}Ni_{5.6}Be_{12.5}$) is investigated.

The stress-strain relations for Vitreloy 1 over a broad range of temperatures (from room temperature up to the crystallization temperature) and strain rates (10^{-4} to $2\text{x}10^{3}$ s^{-1}) were established in uniaxial compression using both quasi-static and dynamic Kolsky pressure bar loading systems. The effect of strain rate and temperature on steady state flow stress, viscosity and peak stress, as well as the effect of jump-in-strain-rate on the stress-strain behavior, were investigated. Based on the experimental results, boundaries between three main deformation modes are proposed, namely, Newtonian flow and nonlinear flow resulting in homogeneous deformation and shear-localized failure constituting inhomogeneous deformation. To characterize the constitutive behavior of the bulk metallic glass, a free volume based model as well as a fictive stress model are utilized to analyze the stress-strain behavior and a mechanism for shear band formation.

A unique deformation characteristic of a bulk metallic glass is the shear localization of the material in response to external mechanical loading, which may lead to catastrophic shear failure immediately after yielding under uniaixal loading and at low temperatures. A dynamic indentation experimental setup was developed to evaluate the high-strain-rate inelastic post yield deformation behavior of Viteloy 1 and its β-phase composite. Time-resolved depth and load responses during the process of indentation on the materials were obtained. Both materials are found to be strain rate insensitive up to 2,000 s^{-1}. Numerical simulations of the indentation experiments, using both pressure insensitive (J_2 von Mises) and pressure dependent (Drucker-Prager) flow models, reveal that both materials are pressure (or normal stress) dependent. Intense multiple shear bands are observed in the indentation craters and are responsible for the observed overall inelastic deformation.

To further examine the inelastic deformation and as well as whether a pressure sensitive or normal stress is more appropriate for Vitreloy 1, multiaxial compression experiments using a confining sleeve technique were performed. In contrast to the catastrophic shear failure behavior in uniaxial compression, Vitreloy 1 exhibits large inelastic deformation of more than 10 percent under confinement, indicating the nature of ductile deformation under constrained conditions. It is found that the metallic glass follows a pressure dependent Tresca criterion, $\tau = \tau_0 + \beta p$, and the coefficient of the pressure dependence, β, is 0.17. Multiple parallel shear bands are observed on the outer surfaces of the deformed specimens.

Motivated by potential use of Vitreloy 1 in impact related applications, the shock compression characteristics of both Vitreloy 1 and β-Vitreloy composite were studied using planar impact loading. A surprisingly low amplitude elastic precursor bulk wave, corresponding to the elastic response of the 'frozen structure' of the intact metallic glasses, was observed to precede the rate-dependent large deformation shock wave. A concave downward curvature after the initial increase of the U_s-U_p shock Hugoniots suggests that a phase-change-like transition occurred during shock compression. In addition, compression damage occurred due to the shear localization. The spalling inside Vitreloy 1 was induced by shear localization, while in β-Vitreloy 1, it was due to debonding of the β-phase boundary from the matrix. The spall strengths at strain rate of 2×10^6 s^{-1} were 2.35 GPa and 2.11 GPa for Vitreloy 1 and β-Vitreloy 1, respectively.

Contents

Chapter 1 **Introduction**

1 Motivation and objectives

Amorphous materials are not new to the scientific community and engineering world at all. What is relatively new, however, is the development of bulk amorphous alloys (i.e., bulk metallic glasses) having fairly large dimensions, say, a few centimeters, obtained using conventional quenching or casting processing techniques. This class of bulk metallic glasses is also known as structural amorphous metals (SAM) for engineering applications (Johnson, 1999).

For example, one type of amorphous materials is an amorphous polymer (e.g., Haward and Young, 1997), which has low level of structural symmetry and can be easily made by cooling its melt, which leads to rapid increase in viscosity and the rate of the intermolecular rearrangement is too small to cause any reconfiguration of the system, such that the formation of crystalline structure is difficult. Metallic glass, on the other hand, is extremely difficult to be formed in most alloy systems. There does not exist a universal rule for predicting the glass forming ability of any given metallic system. The discovery of the first metallic glass at Caltech by Duwez and coworkers was somewhat of an unexpected result during their study of solid solubility in a binary noble metallic system (Klement *et al.*, 1960). Structural applications of metallic glasses were not feasible until the development of *bulk* metallic glasses in the 1990s using relatively inexpensive materials and simple processing techniques pioneered primarily by the research groups of Inoue at the Tohoku University in Japan and Johnson at the California Institute of Technology in the U.S. (e.g., Inoue, 1998; Johnson *et al.*, 1998).

The physical and mechanical properties of metallic glasses are closely related to their unique amorphous structure. Metallic glasses exhibit very high yield strengths, high hardness, large elastic limits, excellent wear and corrosion resistance as well as good forming and shaping ability. An interesting yet limiting factor for SAM to find widespread application is the deformation mechanism associated with the amorphous structure of the materials. In crystalline materials, macroscopic plastic deformation is achieved by the movement and interaction of numerous dislocations that have definite slip systems or by other mechanisms such as twinning. Moreover, dislocations also interact with inclusions and grain boundaries in polycrystalline materials, which give rise to work hardening behavior. However, metallic glasses have long-range disordered atomic configuration and dislocation mechanisms can not be used to explain the observed inelastic deformation in such systems (e.g., Leamy *et al.*, 1972).

Before bulk metallic glasses were developed, mechanical deformation experiments on their thin ribbons of about tens of microns proved to be very difficult. Most of these experiments were conducted subject to uniaxial tensile loading conditions. The scatter in geometric properties such as ribbon thickness made accurate measurement of mechanical properties extremely difficult and less reliable. The studies of mechanical properties of metallic glasses in ribbon form, which were not considered structural materials, were merely driven by scientific curiosity. The availability of bulk metallic glasses not only offers greater opportunities to study the thermodynamic characteristics and kinetics of their corresponding supercooled liquids (e.g., Busch *et al.*, 1995), but also various mechanical properties including constitutive behaviors, flow criteria, fracture and fatigue. Although there have been a number of investigations exploring the mechanical behaviors of bulk metallic glasses since 1990s, complete characterization of the mechanical behaviors and deformation mechanisms of bulk metallic glasses is a challenging task. Constitutive relations and flow criteria appear to be important factors in describing part of the unique mechanical behaviors of metallic glasses and their composites. One interesting deformation phenomenon associated with bulk metallic glasses is the shear band formation at room temperature and low strain rate, which also limits their ductility. The objectives of this thesis are to systematically explore the deformation and flow characteristics of a Zr-based bulk metallic glass, Vitreloy 1 (Peker and Johnson, 1993), and its β-phase composite (Hays *et al.*, 2000) over a broad range of strain rates, stress states and temperatures, and, to identify appropriate constitutive relations and flow criteria to describe their mechanical behaviors. Also, the role of shear band formation on the material behaviors at room temperature is explored over a wide range of stress states and strain rates.

2 Metallic glass and glass formation

Generally speaking, a glass is an amorphous solid or a vitrified liquid, lacking any long-range order, formed by quenching a liquid at a certain cooling rate to reach a viscosity higher than, say, 10^{13} poise, a commonly quoted value for this purpose. Metallic glass or amorphous metal is a sub-class of glasses that has primary metallic bonding and consists mostly, but not necessarily exclusively, of metallic elements and exhibits many characteristic properties associated with metals in their electrical, optical and magnetic behavior (e.g., Elliott, 1984; Peker, 1994). Many metallic glasses have a fairly good electrical conductivity and thermal conductivity. Typical polished metallic glass has a reflecting mirror-like surface. Fe-based metallic glass has shown remarkable magnetic properties and has been widely used in many magnetic applications (e.g., Warlimont, 2001). What is more remarkable is the superior strength of as-cast metallic glass which does not need any thermomechanical treatment as in the case of crystalline alloys to obtain high strength. The amorphous structure of metallic glass is typically examined and verified by X-ray diffraction and transmission electron microscopy (TEM) techniques.

Three possibilities exist when a liquid above its melting temperature is cooled to solidify, (i) crystallization occurs and the liquid becomes a crystalline solid; (ii) the undercooled liquid undergoes configurational freezing, resulting in a fully amorphous solid, i.e., metallic glass; (iii) there results a coexistence of an amorphous solid interdispersed with crystalline particles or clusters of varying size and shape. The last possibility is of particular interest, usually when one considers processing *in-situ* ductile, particle-reinforced amorphous matrix composites (Hays *et al.*, 2000; Kim, 2001). The ease of forming an amorphous solid primarily depends on the nature of the atomic or molecular units that constitute the liquid. It is relatively difficult for complex and covalently bonded units of polymer or oxide melts to form nuclei, due to prolonged relaxation behavior and high viscosity of such strong liquids, in which case crystallization can not take place in the laboratory time scale. For metallic glass, the nucleation units are relatively small in size, probably only a few times the size of individual constituent atoms, and atoms diffuse more easily as supported by evidence that even the best metallic glass former has lower viscosity at normalized undercooled temperatures with respect to its glass transition temperature, which is in contrast to its glassy polymer or oxide counterparts (Busch *et al.*, 1995).

The difference between crystal and glass can be manifested by looking at the change in volume with temperature when undercooling a liquid (e.g., Elliott, 1984). Crystallization is accompanied by an abrupt decrease in volume at the melting temperature, whereas a glass transition is characterized by a continuous decrease in volume. So the glass transition occurs in a temperature range, rather than at a well-defined temperature. Alternatively, glass transition also occurs in a glass during continuous heating. The volume and thermodynamic variables such as entropy and enthalpy are continuous through the glass transition. However, many experiments have shown that their temperature derivatives have a rather rapid change in value around the glass transition. Thus, the second-order thermodynamic variables such as thermal expansion and heat capacity do not vary in a smooth manner, but change rather rapidly over a narrow temperature range, defined as the glass transition temperature interval. Although strictly speaking, this narrow temperature range can not be shrunk to a specific temperature; nevertheless, the so called glass transition temperature for a material, T_g, is conventionally defined as the starting temperature of its glass transition temperature interval, or more specifically, the point of inflection of the rising heat capacity or thermal expansion coefficient, and the latter definition will be adopted throughout the thesis.

A glass is a metastable phase whose evolution towards the equilibrium phase is suppressed by a kinetic barrier (Johnson, 1994). Glass transition sounds like a second order thermodynamic phase transition, but it is not, since kinetics plays a central role in the glass forming process. The glass transition temperature of a glass is not a fixed temperature – it is a function of thermal history of the glass, for instance, a function of the heating rate. Studies have shown that the glass transition temperature of the Vitreloy 1 metallic glass are 602, 625 and 645 K at cooling rates of 0.2, 20 and 100 K/min, respectively (Hiki and Takahashi, 2000).

The maximum size of a metallic glass specimen that can be achieved without crystallization is mainly dependent on the critical cooling rate of the glass. No metallic glass has ever been made in laboratory using a pure metallic element like Ni whose critical cooling rate is estimated to be as high as 10^{10} K/s (e.g., Chen, 1976). As mentioned earlier, the first metallic glass ($Au_{75}Si_{25}$ binary system, see Klement *et al.*, 1960) was formed at Caltech by rapid gun quenching technique that provides a quenching rate of 10^7 K/s. This 10 μm thick Au-Si metallic glass thus obtained was unstable even at room temperature. Cohen and Turnbull's theory (Cohen and Turnbull, 1961; Turnbull, 1969) provided a roadmap for the development of other new metallic glasses. They pointed out that strong metallic glass formers favor deep-eutectic compositions and high reduced glass transition temperature, $T_{rg}=T_g/T_m$, where T_m is the melting temperature of the glass.

Early searches for metallic glass formers were focused primarily on binary late transition metal-metalloid type, binary transition metal type deep eutectic systems until Chen and Turnbull (Chen and Turnbull, 1969; Chen, 1974, 1976) discovered "thick" metallic glass (1 to 3 mm) in Pd-M-Si and Pd-T-P systems (where M=Rh, Au, Ag and Cu and T=Ni, Co and Fe) using water quenching technique which had a cooling rate of around 10^2 to 10^3 K/s. Drehman *et al.*, (1982) demonstrated the making of an amorphous $Pd_{40}Ni_{40}P_{20}$ rod of 5.3 mm in diameter at a cooling rate of 1.4 K/s, using surface etching and thermal cycling technique. Kui *et al.*, (1984), by using a flux treatment (molten surface flux of dehydrated boron oxide) and thermal cycling to suppress heterogeneous peculations, increased the maximum thickness of $Pd_{40}Ni_{40}P_{20}$ to 10 mm at an approximate cooling rate of 4 K/s. This appears to be the largest metallic glass ever made before 1990s. However, this tedious fabrication technique is much more suitable for laboratory synthesis rather than for industrial production. In addition, the thermal stability of $Pd_{40}Ni_{40}P_{20}$ was not improved at all and further search for better glass formers was necessary.

The development of bulk metallic glasses, which are strong glass formers that can be easily formed in centimeter scale, started in the late 1980s and early 1990s in two research groups at Tohoku University and Caltech. Inoue and coworkers (see Inoue, 2001) systematically investigated a variety of systems including ternary, quaternary and quinary systems such as Mg-based Mg-TM-Ln, Ln-based Ln-Al-TM, Zr-based Zr-Al-TM (TM = transition metal), whose critical cooling rates ranged from 10^1 to 10^2 K/s, making it possible to cast such alloys with a thickness of up to 1 cm.

Peker and Johnson at Caltech discovered a family of bulk metallic glasses based on the Zr-Ti-Cu-Ni-Be system (Vitreloy family). One extensively studied example of this glass family is Vitreloy 1 $(Zr_3Ti)_{0.55}(Cu_5Ni_4)_{0.225}Be_{0.225}$, i.e., $Zr_{41.2}Ti_{13.8}Cu_{12.5}Ni_{10}Be_{22.5}$ (see Peker and Johnson, 1993). Direct experimental study has shown that this glass has a critical cooling rate of 1 K/s and it can be cast in rods with a diameter of up to 5 cm (Johnson, 1996). This alloy is one of the strongest glass forming alloys to date without a noble metallic element. Johnson (1996) summarized that nearly all the discovered bulk metallic glasses can be described as pseudo ternary alloys of the form $ETM_{1-x-y}LTM_xSM_y$, where ETM refers to early transition metal or Lanthanide group metal such as Zr, Ti, Nb and La, LTM refers to late transition metal such as Fe, Co, Ni and Cu, and SM refers to simple metal such as Al, Be, Mg. Almost all the bulk metallic glasses have compositions which favor deep eutectic behavior in their phase diagram. Besides the reduced glass transition temperature (T_g/T_m) of around 2/3 or better, most bulk metallic glasses have large supercooled liquid region of more than 80 K upon heating. They also have significant difference in atomic sizes among the main constituent elements. For example, the atomic size difference between Zr and Be in $Zr_{41.2}Ti_{13.8}Cu_{12.5}Ni_{10}Be_{22.5}$ is 30%.

As mentioned earlier, an important limiting factor in using metallic glasses for structural applications at room temperature is their high susceptibility to shear localization. One way of preventing catastrophic failure due to shear localization in the bulk metallic glasses at room temperature is to use them under multiaxial loading conditions, which is not attainable in all structural applications. As an alternative, reinforcement in various forms, such as particles, short fibers, long fibers, etc., can be also used to enhance mechanical performance (e.g., Clyne and Withers, 1993). Before bulk metallic glasses were discovered, Cytron (1982) used Ni-Nb glass ribbons to reinforce an aluminum alloy, and Vaidya and Subramanian (1990, 1991) employed metallic glass ribbon in a ceramic matrix to enhance the overall toughness of the composites. Considerable efforts have been recently made in Johnson's group at Caltech for developing bulk metallic glass composites to enhance ductility and fracture toughness of such materials. *Ex-situ* bulk metallic glass composites were made by adding SiC, TiC, WC, W, Ta and Re particles, W or Fe fibers, due to the thermal stability of the glass, which exhibits high resistance to crystallization (e.g., Choi-Yim *et al.*, 1997; Conner *et al.*, 1998). *In-situ* chemical partitioning was also utilized (Hays *et al.*, 2000; Kim, 2001) to produce a stable two-phase composite (β-Vitreloy 1 composite) having ductile bcc crystals in a Vitreloy 1-like glass matrix. The strong glass forming ability of bulk metallic glasses (e.g., Vitreloy 1) suppresses the heterogeneous nucleation and growth of crystalline phases in the glass matrix. Most of the bulk composites developed either by melt infiltration or chemical partitioning have demonstrated the ability to attain large inealstic strains when compared with that of pure metallic glasses (e.g., Conner *et al.*, 1998; Kim, 2001).

Vitreloy 1 and its β-phase composite will serve as the model materials for bulk metallic glasses investigated in this thesis. One reason for studying these materials is because extensive research has been performed on the metallic glass, Vitreloy 1, and many of its physical, thermodynamic and mechanical properties are readily available in literature to assist in further understanding its mechanical behavior. The details of the physical and mechanical properties of Vitreloy 1 and its composite (β-Vitreloy 1) are available from tables in Chapters 2-5. Some of the relevant properties of Vitreloy 1 are listed in Table 1.

Table 1. Selected properties of Vireloy 1 metallic glass

Critical cooling rate (K s^{-1})	1.0[a]
T_g (K) at heating rate 20 K/min	625[a]
Reduced glass transition temperature	0.63[a]
Density (g/cm^3)	6.0
Young's modulus (GPa)	96
Poisson's ratio	0.36
Elastic strain limit	0.02
Tensile yield strength (GPa)	1.90

Source: [a] Peker and Johnson (1993)

3 Thesis outline

The thermodynamic and mechanical properties of $Zr_{41.2}Ti_{13.8}Cu_{12.5}$ $Ni_{10}Be_{22.5}$ bulk metallic glass (Vitreloy 1) and its composites could lead to their many potential applications as structural materials. The constitutive behavior of $Zr_{41.2}Ti_{13.8}Cu_{12.5}Ni_{10}Be_{22.5}$ bulk metallic glass over a broad range of strain rate, temperature and stress state is the main subject of investigation in this thesis and its outline is given below.

The role of thermomechanical loading on uniaxial deformation behavior of Vitreloy 1 is investigated in Chapter 2. One of the goals is to experimentally obtain the stress-strain relationship over a broad range of temperatures (295 to 683 K) and strain rates (10^{-5} to $10^{3}s^{-1}$) using both quasi-static and dynamic loading systems. The effect of strain rate and temperature on steady state flow stress, viscosity and peak stress are investigated. The effect of jump-in-strain-rate on the stress-strain behavior is also explored. Deformation modes are characterized as a function of strain rate and temperature. As a first step to characterize the constitutive behavior of the bulk metallic glass, a free volume based model as well as a fictive stress model are utilized to analyze the stress-strain behavior as well as a mechanism for shear band formation.

A dynamic indentation technique is developed and employed to characterize the dynamic behavior of Vitreloy 1 and its β-phase composite in Chapter 3. This study is used to establish the appropriate flow criterion under dynamic loading conditions. The dynamic indentation apparatus is capable of measuring time-resolved depth and load during indentation. Intense shear bands are found in the indentation crater and are responsible for the overall inelastic deformation. The process of dynamic indentation is simulated using explicit finite element codes. Pressure independent material models such as the J_2 von Mises flow model are found to be incapable of predicting the experimental load-depth indentation curves. It is found that the Drucker-Prager flow model which incorporates pressure-dependence of the yield surface is able to adequately model the mechanical response of Vitreloy 1 and β-Vitreloy 1 in the dynamic indentation experiments. A methodology for estimating the strain rate sensitivity of flow stress using the dynamic indentation technique is also presented. No strain rate sensitivity for flow stress is discernible for both Vitreloy 1 and β-Vitreloy 1.

One important question that arises based on the dynamic indentation experiments and simulations is whether a pressure dependent or a normal stress dependent flow criterion is more appropriate in describing the mechanical behavior of metallic glasses. Having confirmed by the previous studies that Vitreloy 1 is strain rate independent at temperature much lower than the glass transition temperature, Chapter 4 is intended to experimentally study the inelastic deformation of Vitreloy 1 under multiaxial compression using the sleeve-confinement technique at quasi-static strain rates. Shear band orientation observed in the experiments indicates that the maximum shear stress is independent of the normal stress, implying that a pressure dependent flow model of the form $\tau = \tau_0 + \beta p$ is appropriate, rather than the normal stress based Mohr-Coulomb criterion. The metallic glass under confinement exhibits large inelastic deformation because of the ability to form multiple shear bands and subsequently arresting them.

Chapter 5 presents the first ever investigation of a bulk metallic glass subjected to shock compression. The motivation for this study is based on recent findings, which revealed that Vitreloy 1 composites have excellent performance in impact related applications (Conner *et al.*, 2000). The shock particle velocity profiles and shock U_s-U_p Hugoniots obtained experimentally, and, as well as the scanning electron microscopy (SEM) examination of recovered specimen samples, indicate a complex deformation process during shock compression. The unusual shock Hugoniots suggest that failure occurs during shock compression and is due to shear localization.

References

Busch, R., Kim, Y. J. and Johnson, W. L., Thermodynamics and kinetics of the undercooled liquid and the glass-transaction of the $Zr_{41.2}Ti_{13.8}Cu_{12.5}Ni_{10}Be_{22.5}$ alloy, J. Appl. Phys., **77** (8) 4039-4043 (1995).

Chen, H. S. and Turnbull, D., Formation, stability and structure of palladium-silicon based alloy glasses, Acta Metall., **17**, 1021-1031 (1969).

Chen, H. S., Metallic glass, Mater. Sci. Eng., **25**, 59-69 (1976).

Chen, H. S., Thermodynamic considerations on the formation and stability of metallic glasses, Acta Metall., **22**, 1505-1511 (1974).

Choi-Yim, H. and Johnson, W. L., Bulk metallic glass matrix composites, Appl. Phys. Lett. **71** (26), 3808-3810 (1997).

Clyne, T. W. and Withers, P. J., An introduction to metal matrix composites, Cambridge University Press, Cambridge (1993).

Cohen, M. H. and Turnbull, D., Composition requirements for glass formation in metallic and ionic system, Nature, **189**, 131-132 (1961).

Conner, R. D., Dandliker, R. B. and Johnson, W. L., Mechanical properties of tungsten and steel fiber reinforced $Zr_{41.25}Ti_{13.75}Cu_{12.5}Ni_{10}Be_{22.5}$ metallic glass matrix composites, Acta Mater., **46** (17), 6089-6102 (1998).

Conner, R. D., Dandliker, R. B., Scruggs, V. and Johnson, W. L., Dynamic deformation behavior of tungsten-fiber/metallic-glass matrix composites, Int. J. Impact. Eng., **24** (5) 435-444 (2000).

Cytron, S. J., A. Metallic glass-metal matrix composite, J Mater. Sci. Lett., **1** (5), 211-213 (1982).

Drehman, A. L., Greer, A. L. and Turnbull, D., Bulk formation of a metallic glass: $Pd_{40}Ni_{40}P_{20}$, Appl. Phys. Lett., **41** (8), 716-717 (1982).

Elliott, S. R., Physics of amorphous materials, Longman, New York, 1984.

Haward, R. N. and Young, R. J., Eds., The physics of glassy polymers, 2nd edition, Chapman & Hall, 1997.

Hays, C. C., Kim, C. P. and Johnson, W. L., Microstructure controlled shear band pattern formation and enhanced plasticity of bulk metallic glasses containing in situ formed ductile phase dendrite dispersions, Phys. Rev. Lett., **84** (13), 2901-2904 (2000).

Hiki, Y. and Takahashi, H., Study on thermal relaxation in metallic glasses, in *the Fourteenth Symposium on Thermophysical Properties*, Boulder, Colorado, 2000.

Inoue A., Bulk amorphous alloys, in *Amorphous and nano-crystalline materials: preparation, properties and applications*, Eds. Inoue, A. and Hashimoto, K., Springer, 2001.

Inoue, A., Bulk amorphous alloys: preparation and fundamental characteristics, Trans Tech Publications, Switzerland (1998).

Johnson, W. L., Bulk glass-forming metallic alloys: science and technology, MRS Bull., **24** (10), 42-56 (1999).

Johnson, W. L., Fundamental aspect of bulk metallic glass formation in multicomponent alloys, Mater. Sci. Forum, **225-227**, 35-50 (1996).

Johnson, W. L., Inoue, A. and Liu, C. T., Eds., Bulk metallic glasses, Mater. Res. Soc. Symp. Proc., Vol. **554**, Massachusetts (1998).

Johnson, W. L., Metastable phase, in *Intermetallic Compounds*, Vol. 1, Principles, Eds. Westbrook, J. H. and Fleischer, R. L., John Wiley & Sons (1994).

Kim, C. P., Ductile phase reinforced bulk metallic glass composites formed by chemical partitioning, Ph.D. Thesis, California Institute of Technology (2001).

Klement, W. J., Willens, R. H. and Duwez, P., Non-crystalline structure in solidified gold-silicon alloys, Nature, **187**, 869-870 (1960).

Kui, H. W., Greer, A. L. and Turnbull, D., Formation of bulk metallic-glass by fluxing, Appl. Phys. Lett., **45** (6), 615-616 (1984).

Leamy, H. J., Chen, H. S. and Wang, T. T., Plastic flow and fracture of metallic glass, Metallurgical Transaction, **3**, 699-708 (1972).

Peker, A. and Johnson, W. L., A highly processable metallic glass: $Zr_{41.2}Ti_{13.8}Cu_{12.5}Ni_{10.0}Be_{22.5}$, Appl. Phys. Lett., **63**, 2342-2344 (1993).

Peker, A., Formation and characterization of bulk metallic glasses, Ph.D. thesis, Caltech (1994).

Turnbull, D., Contemp. Phys., **10**, 473 (1969).

Vaidya, R. U. and Subramanian, K. N., Discontinuous metallic-glass ribbon reinforced glass ceramic matrix composites, J. Mater. Sci., **26** (23), 6453-6457 (1991).

Vaidya, R. U. and Subramanian, K. N., Metallic-glass ribbon-reinforced glass-ceramic matrix composites, J. Mater. Sci., **25** (7), 3291-3296 (1990).

Warlimont, H., Amorphous metals driving materials and process innovations, Mater. Sci. Eng., **A304-306**, 61-67 (2001).

Chapter 2 **Deformation Behavior of Vitreloy 1 at Various Strain Rates and Temperatures**

Abstract

The thermodynamic and mechanical properties of $Zr_{41.2}Ti_{13.8}Cu_{12.5}Ni_{10}Be_{22.5}$ bulk metallic glass (Vitreloy1 or Vit 1) makes it a suitable structural material in many potential applications. The stress-strain relations for the material over a broad range of temperatures (room temperature to its supercooled liquid region) and strain rates (10^{-4} to 2×10^{3} s^{-1}) were established in uniaxial compression using both quasi-static and dynamic Kolsky (split Hopkinson) pressure bar loading systems. Relaxation and jump in strain rate experiments were conducted to further understand the time dependent behavior of Vitreloy 1. The material exhibited superplastic flow above its glass transition temperature (623 K) and strain rates of up to 1 s^{-1}. Based on the experimental results, boundaries between three main deformation modes are proposed, namely, Newtonian flow and nonlinear flow resulting in homogeneous deformation and shear-localized failure constituting inhomogeneous deformation. The viscosity in the homogeneous deformation regime was found to decrease dramatically with increasing strain rate. The limitations of the applicability of existing free volume model are discussed and a phenomenological fictive stress model was used to describe the basic deformation features of Vitreloy 1 under constant strain-rate loading as well as multiple strain-rate loading at high temperatures.

Keywords: Bulk metallic glasses; Glass transition; Supercooled liquid; Viscosity; Homogeneous and inhomogeneous flow; Shear bands; High strain rate

1 Introduction

Progress made in the last few decades has shown that metastable glassy metals can be formed in binary, ternary and multi-component alloy systems (e.g., Johnson, 1994; Inoue, 1998). Different types of atoms can be kinetically constrained or frozen by rapid quenching techniques such that no long-range order exists in the as processed alloy systems. Following the discovery of a binary Au-Si amorphous alloy at Caltech in form of thin ribbon using very high cooling rate of 10^5-10^6 K/sec (Klement *et al.*, 1960), the early search for bulk glass forming alloys dated back to the 70s, when several ternary metallic glass formers were found such as Pd-Ni-P (Chen, 1976) and Pd-Cu-Si (Chen, 1978), with dimensions in the millimeter scale. The late 80s and early 90s witnessed a revolution in the development of bulk metallic glasses with lower cooling rates resulting in larger sizes and thus making them attractive candidates for many structural applications (Inoue, 1988; Peker and Johnson, 1993; Johnson 1996a, 1996b).

Among these new bulk glass forming metallic alloys, a Zr-based material, $Zr_{41.2}Ti_{13.8}Cu_{12.5}Ni_{10}Be_{22.5}$ (Vitreloy 1), exhibits high resistance with respect to crystallization in its wide supercooled liquid region. It has a low cooling rate of around 1 K/s (Peker and Johnson, 1993) and can be cast up in sizes of up to 2 to 4 centimeters in thickness. The high yield stress (Bruck *et al.*, 1994, 1996) and the high strength to density ratio of this bulk metallic glass makes the material an excellent candidate for structural applications. Research on its viscosity, relaxation, kinetics and crystallization (Kim *et al.*, 1994; Busch *et al.*, 1995a; Masuhr *et al.*, 1999a, 1999b) has shown that thermo-mechanical characterization up to its crystallization temperature is possible by the increased thermal stability of the glassy alloy with respect to crystallization.

Generally speaking, the deformation of metallic glasses can be classified into two modes, namely, homogeneous and inhomogeneous deformation. In spite of their metallic bonding, all the metallic glasses discovered so far exhibit shear localization at room temperature, leading to catastrophic shear failure immediately following yield. As the temperature increases, they can be deformed homogeneously, exhibiting considerable amount of inelastic deformation. Recently, homogeneous deformation of several metallic glasses around their glass transition temperature were investigated, including the tensile deformation of 20 μm thick $Zr_{65}Al_{10}Ni_{10}Cu_{15}$ ribbons (Kawamura *et al.*, 1996, 1999a, 2001) and 40 μm thick $La_{55}Al_{25}Ni_{20}$ ribbons (Kawamura *et al.*, 1999b, 2001). The use of ribbons instead of their bulk forms in millimeter scale was probably due to limitations in the availability of materials and the experimental setup. In these investigations, necking appears during most tensile tests, making the observation of variation of the steady state stress difficult. Experiments on bulk $Zr_{55}AL_{10}Ni_5Cu_{30}$ specimens of 3 mm in diameter (Kato *et al.*, 2000) and bulk $Pd_{40}Ni_{10}Cu_{30}P_{20}$ specimens of 2 mm in diameter (Kato *et al.*, 1998) have been performed in their homogeneous deformation regime. The strain rate was limited to the quasi-static range and the temperature in the vicinity of the corresponding glass transition temperature.

There exist a number of theories to describe the deformation behavior of metallic glasses. Argon developed a model based on the idealization of two deformation modes, namely the diffuse shear transformation and the dislocation loop formation, to analyze the boundary between homogeneous and inhomogeneous flow of Pd-Si metallic glass (Argon, 1979, 1983; Megusar and Argon, 1979). Speapen proposed a theory based on the free volume created by external stress and its annihilation by diffusion (Speapen, 1977; Spaepen and Turnbull, 1982). This was further modified by Steif to analyze mechanical deformation problems by including additional free volume change due to pressure (Steif and Spaepen, 1982). Khonik suggested a directional structural relaxation model, which states that each rearrangement event can be interpreted as a thermally activated shear due to local atomic structures and subsequently nearly athermal viscous flow by external stress (Khonik, 2000). Among these models, Speapen's free volume based model seems to be the most widely cited to interpret the deformation behavior of metallic glasses.

Duine used the free volume based viscosity assumption by Speapen and defect evolution assumption to analyze the kinetic process of defects and their steady state concentration (Duine *et al.*, 1992). de Hey *et al.* applied the same idea to temperature induced structural evolution of some metallic glasses, leading to the conclusion that additional free volume is created as compared with thermal equilibrium due to plastic deformation (de Hey *et al.* 1997, 1998; van Aken *et al.*, 2000). Recently, Kato adopted a simple model based on the concept of fictive stress to simulate stress-strain behavior of metallic glasses (Kato *et al.*, 2000; Chen *et al.*, 2000) and it will be discussed in detail later.

Deformation of bulk metallic glass differs from that of a crystalline metallic material due to the absence of long-range order, i.e., amorphous in nature. Relatively little is known regarding the effect of rate and temperature on the deformation behavior of bulk metallic glasses, particularly in the supercooled liquid region. The objective of this study is to systematically explore the thermo-mechanical behavior of the $Zr_{41.2}Ti_{13.8}Cu_{12.5}Ni_{10}Be_{22.5}$ (Vitreloy 1) bulk metallic glass under uniaxial compression subject to a wide range of strain rates and temperatures. Compression loading was chosen in the present study because tensile loading typically induces necking at relatively small strains while compression can result in uniform deformation up to large strains provided care is used in conducting the experiments. The experimental results can aid in the development of appropriate constitutive models and delineate possible deformation modes for bulk metallic glasses over such a wide range of temperatures and strain rates. Such constitutive models are expected to provide design rules for processing and structural applications of bulk metallic glasses. In addition, they may be also employed in the design of a new generation of high pressure casting facilities and net-shape forming thermomechanical processes.

2 Experimental

2.1 Material

The bulk metallic glass used in this investigation is $Zr_{41.25}Ti_{13.75}Cu_{12.5}Ni_{10}Be_{22.5}$ with the commercial name, Vitreloy 1 (or commonly referred to as Vit 1). Vitreloy 1 is the trademark (^{TM}) name owned by Amorphous Technologies, Inc., Laguna Niguel, CA, for the bulk metallic glass $Zr_{41.25}Ti_{13.75}Cu_{12.5}Ni_{10}Be_{22.5}$ originally developed at the California Institute of Technology. The processing and physical properties of this material are well documented in the literature (see for example, Peker and Johnson, 1993; Bruck *et al.*, 1994, 1996; Kim *et al.*, 1994; Busch *et al.*, 1995a, 1995b; Masuhr *et al.*, 1999b). Relevant themophysical and mechanical properties of Vitreloy 1 are given in Tables 1 and 2. The material was obtained in the form of a 4 mm cast sheet with in-plane dimensions of about 200 mm x 100 mm, manufactured by Howmet Corporation, Greenwich, CT. The as-received plate was carefully lapped and polished to a surface finish of 5 microns. The plate was then electrical discharge machined (EDM) into smaller rectangular plates with a size of nominally 50 mm x 100 mm (2 in. x 4 in.), which were subsequently cut with a low speed diamond saw into compression specimens having a rectangular cross-section of 3.7 mm x 3.7 mm and a nominal length of 7.4 mm such that the length-to-width aspect ratio is close to 2:1. The long cut faces of each specimen were also polished using 600 grit polishing paper. Subsequently, the end faces of each specimen, clamped with a specially designed mounting block, were polished down to 6-micron surface finish. The main purpose of the mounting block was to keep the polished surface flat while ensuring the two end surfaces of each specimen were made parallel to each other within a tolerance of 10 μm gap. During the experiments, a high temperature lubricant, molydisulfide powder was applied on both surfaces to minimize the effect of friction. In addition, to further reduce friction, circular shallow grooves machined or ground on the end loading surfaces of the specimen were used to contain the lubrication medium. The as-received samples were examined using X-ray diffraction. The typical presence of broad diffuse peaks and lack of discrete peaks revealed that the as-received Vit 1 material is amorphous. Differential scanning calorimetry (DSC) study of the as-received material revealed that the temperatures at the onset of the glass transition and at the onset of the crystallization are 623 K and 710 K, respectively.

2.2 Experimental conditions

For the experiments conducted in the present study, the ambient temperature was varied from room temperature (293 K) up to the crystallization temperature (710 K), well beyond the glass transition temperature (623 K) for Vitreloy 1. The strain rate was varied over a wide range, from quasi-static, 10^{-5} s^{-1}, to dynamic, 10^{3} s^{-1}. All the experiments were conducted under uniaxial compressive stress condition. The experimental setup for both quasi-static and dynamic experiments will be described in the following sections.

2.2.1 Quasi-static setup

The quasi-static experiments were carried out using a screw-driven Instron (model# 4024) system with a 50 kN load cell and a servo-hydraulic Materials Testing System (MTS with a 319 series axial/torsional load frame and 358 series load units) having a 25 kN load cartridge and a 5.95 mm displacement cartridge. The strain rate achieved using these systems for the size of the specimens employed ranges from 10^{-5} to 10^{0} s^{-1}.

Figure 1 shows the compression fixture used in the quasi-static experiments. The fixture was specially designed such that the two push rods for loading were perfectly aligned with each other. Any unwanted shear force on the specimen was minimized by employing precision linear bearings. The specimen was sandwiched between two micro-polished tungsten carbide inserts, each of which was placed in a centered cylindrical slot of the push rods. The inserts were tightly fitted in the slots to prevent any undesired sliding during compressive loading. The push rods were made of Inconel 718 alloy, a precipitation-hardened nickel-chromium alloy containing significant amounts of iron, niobium, and molybdenum along with lesser amounts of aluminum and titanium. The Inconel alloy has excellent creep-rupture strength of around 1 GPa at a temperature of 920 K, low thermal conductivity of 11.4 W/m-K and coefficient of thermal expansion of $1.3\times10^{-5}\ \mathrm{K}^{-1}$, thus providing excellent thermal stability, strength and temperature control.

The strain measurement was carried out by recording the relative displacement of the end surfaces of the two push rods using a Linear Variable Differential Transformer (LVDT), which is an electromechanical transducer that produces an electrical voltage output proportional to the displacement of its movable core. The technique of removing the machine compliance from the data was not adopted due to the variations of the compliance during the high temperature compression process, which could lead to erroneous values for the displacement and strain measurement. The main body of the LVDT consists of a set of three cylindrical coils (a primary coil and two secondary coils) with a cylindrical concentric cavity in the center for the free-movement of the rod-shaped magnetic core. The LVDT used in the experiments is a Schaevitz model # 050-MHR with a output sensitivity of around 2 to 3 mV/micron displacement with adjustable resolution using a Schaevitz ATA 2001 signal conditioner, which consists of a power supply, a carrier exciter, a demodulator and a pre-amplifier for a AC based LVDT. The output signal is subsequently filtered using an ITHACO (model# 4213) 20 Hz low pass analog filter to remove the noise generated by the carrier exciter of the signal conditioner.

Since most compression experiments were performed at an elevated temperature ranging from 373 to 683 K, the LVDT which has an operational temperature range of 218 to 423 K was placed outside the high temperature zone. To accomplish the displacement measurement, an extension-rod mini-apparatus was designed. Two pieces of Inconel 718 disks were attached tightly to the loading surfaces of the two push rods. Each disk (called upper or lower disk, hereafter) has a hole to allow a micro-polished tungsten disk to directly contact the end surface of each loading rod. Three pieces of Inconel 718 extension rods were rigidly linked to the upper disk to transfer the displacement of the upper push rod outside the high temperature zone. Likewise, three pieces of extension rods were connected to the lower disk to pass the displacement of the lower push rod outside the high temperature zone. Three clearance holes were made in the lower disk to allow the upper extension rods to pass through it. A light aluminum disk, rigidly connected to each set of extension rods, was placed underneath the furnace where the temperature is substantially lower. The main body of the LVDT was mounted on to the lower aluminum disk while the LVDT core was fixed to the upper aluminum disk. Thus, the relative movement of the push rods at the two loading surfaces can be obtained by the relative movement of the two tungsten carbide inserts.

To study the mechanical behavior of the Vitreloy 1 at various ambient temperatures, a feedback control heating system was designed. The system consists of, (1) two pieces of half-cylindrical electrical furnace (model# 5010-1057-00A, Lindberg, WI) that is 75 mm (3 inches) in diameter and 150 mm (6 inches) long, or two pieces of half-cylindrical ceramic fiber furnace (VS102A06S, Watlow, St. Louis, MO) that is 150 mm (6 inches) in diameter and 200 mm (8 inches) long; (2) a PID temperature controller (series CN77000, Omega Engineering); (3) two pieces of solid state relay (series SSR240DC25, Omega Engineering); (4) a K type thermocouple. The K-type thermocouple, placed next to the specimen located at the center of the furnace ensuring high heating efficiency and uniform temperature distribution, is wired to the PID controller. The proper placement of the sensing thermocouple with respect to the heating setup is of utmost importance for proper control. Due to thermal lag between the furnace and the sensor, overshoot and undershoot in general is unavoidable, especially at the moment when a desired set-point temperature is reached. However, by adapting proportional, integral and derivative (PID) control scheme, the temperature fluctuations could be reduced. The auto-tune function of the controller was found to be inappropriate for tuning the heating apparatus with a small thermal mass. Alternatively, through trial and error, it was found that the proportional band should be adjusted to be in the range 2 to 10 K; the parameter for the integral function works best in the range of 200 to 500 seconds; the parameter for the derivative function falls in the range of 2 to 10 seconds. Accordingly, a heating rate of 20 K/s was employed until the desired set-point temperature is reached. The ramp heating function works well under the current tuning parameters, except near the value of the set point. To avoid overheating, manual tuning was adopted at a temperature which is few degrees lower than that of the desired set point. Once the temperature begins to drop after it reaches the set point, PID auto control takes over for the rest of the duration of the experiment. The temperature variation during the compression loading was controlled to within $\pm 0.5\,\mathrm{K}$. Prior to loading, the specimen was held at the desired set point temperature for 180 to 300 seconds to establish thermal equilibrium and was immediately followed by mechanical compression. The controller directed its control signal in the form of DC voltage to two solid state relays (SSR) which are capable of switching on and off as fast as a few milliseconds, which proved to be sufficient for the requisite temperature control of the heating apparatus.

2.2.2 Dynamic setup

The Kolsky (split Hopkinson) pressure bar apparatus shown in Fig. 2, consisting of a striker bar, an incident bar and a transmission bar, has been extensively employed in the high-strain-rate testing of engineering materials such as metals, polymers and ceramics (e.g., Kolsky, 1949; Gray, 2000; Subhash and Ravichandran, 2000). Upon the impact of the striker bar, an elastic compressive stress wave, referred to as the incident wave, is generated and propagates along the incident bar towards the specimen that is sandwiched between the incident bar and the transmission bar. When the incident wave reaches the specimen, part of it is reflected back into the incident bar, while the remaining is transmitted through the specimen into the transmission bar. A few wave reflections within the specimen are essential before mechanical equilibrium is established. Strain gages mounted on the surfaces of the bars provide time-resolved measures of stress waves by which the nominal strain rate $\dot{\varepsilon}(t)$ can be calculated using $\dot{\varepsilon}(t) = -2c_o\varepsilon_r(t)/l$

and the nominal axial stress σ in the specimen is determined using $\sigma(t) = EA_o / A_s \varepsilon_t(t)$, where l is the undeformed length of the specimen, $\varepsilon_r(t)$ is the reflected strain signal in the incident bar, c_0 is the longitudinal bar wave speed in the bar material, A_s is the cross-sectional area of the specimen, and $\varepsilon_t(t)$ is the time-resolved strain in the transmission bar of area A_0.

Certain modifications are essential in using the Kolsky pressure bar for the investigation of high strength and quasi-brittle materials such as bulk metallic glasses at room temperature (e.g., Chen and Ravichandran, 1997). The modified Kolsky (split Hopkinson) bar is also shown in Fig. 2. A copper bead of 2 to 3 mm in diameter and 1 to 1.5 mm thick was utilized as a pulse shaper in this investigation. The pulse shaper was placed at the impact side of the incident bar which results in a bell-shaped pulse and prevents high-strength "brittle" materials from reaching failure before nominal equilibrium is achieved in the specimen. The choice of dimensions and material for the pulse shaper are dictated by the shape and duration of the pulse desired in the investigation of dynamic material behavior. Due to the presence of the phase shaper, force equilibrium can be established before the maximum compressive force causing failure is reached. Thus, the peak (failure/yield) stress can be obtained in a reliable manner, although the initial slope of stress-strain curve is not generally regarded as an accurate measurement of dynamic Young's Modulus. However, experimental results show that for Vitreloy 1 metallic glass, the slope is around 100 GPa at room temperature, which is in close agreement with its nominal quasi-static value (95 GPa) indicating that the dynamic measurement may be used in the estimation of Young's Modulus.

In addition to pulse shaping, reliable small strain data at room temperature can be obtained by mounting strain gages on the specimen surface. However, strain gage technique may not be applicable at elevated temperatures such as in the supercooled liquid region of Vitreloy 1. It can also be seen from Fig. 2 that the transmission bar is made shorter than the incident bar to prevent multiple loading of the specimen. The former acts as a momentum trap moving the transmission bar away from the specimen before a second compressive pulse due to reflected tensile pulse in the incident bar, thus preventing reloading of the sample (Chen and Ravichandran, 1997). This feature facilitates the characterization of the recovered samples after having been subjected to a single pulse loading. The two faces of the specimen were lubricated by applying a thin film of high temperature molydisulfide lubricant powder between the two specimen-bar interfaces to minimize the frictional effect, which may violate the 1-D loading assumption of the Kolsky bar technique.

A tubular furnace controlled by a temperature controller similar to that used for the quasi-static experiments described in section 1.3 was used to heat the specimens in the Kolsky bar. A small fixture was designed to support both the furnace and the cylindrical specimen with aspect ratio of nominally 1:1. Typically the specimen was held by a very fine copper wire connected to the surrounding fixtures. Subsequently, the specimen was aligned between the incident bar and the transmission bar before the experiment. The transmission and incident bars were brought in contact with the specimen just before the impact of the striker bar. The temperature measurement and control are similar to those of the quasi-static experimental setup and the details can be found in the previous section. The advantage of a tubular furnace over other heating elements such as an infrared heating lamp is that it can provide much more uniform temperature distribution in the central area of the tubular furnace thus assuring homogeneity of temperature in the specimen.

3 Results

The Vitreloy 1 specimens used in this investigation had a typical length-to-width aspect ratio of 2:1 and 1:1 in the quasi-static and the dynamic experiments, respectively. Careful alignment of the specimens with respect to the loading fixture as described in the previous section was performed to ensure least possible bending moment on the specimens. Quasi-static compression experiments were conducted at strain rates ranging from 10^{-5} to 10^{0} s^{-1} and dynamic compression experiments were carried out at strain rates in the range of 10^{2} to 10^{3} s^{-1}. The temperature at which the experiments were performed ranged from room temperature to the supercooled liquid region of Vitreloy 1. Differential scanning calorimetry (DSC) experiments on Vitreloy 1 indicated that the glass exhibits its onset of glass transformation at 625 K when subject to a heating rate of 20 K/min. The corresponding crystallization onset temperature was found to be around 710 K. It is not surprising that a slight change in the glass transition temperature T_g with respect to heating rate was observed, indicating that the T_g is not a unique physical property of the glass, but rather a thermal-history dependent kinetic quantity. In order to diminish the influence due to the variation of heating rate on the thermal history of the specimens during mechanical loading, a specific heating profile was designed as illustrated in Fig. 3. The specimen was constantly heated at a fixed heating rate of 20 K/min until a desired temperature was reached. Subsequently, the specimen was held at the desired temperature for 180 to 600 seconds (3 to 10 minutes) prior to loading. The temperature then remained unchanged during the course of compression. Since the present study attempts to investigate the effects of temperature on flow in detail, the following set of temperatures was selected: 293 K (room temperature), 373 K, 423 K, 473 K, 523 K, 573 K, 593 K, 603 K, 613 K, 623 K (the glass transition temperature of Vitreloy 1), 643 K, 663 K and 683 K. The TTT (time-temperature transformation) diagram for Vitreloy 1 (Masuhr *et al.*, 1999b) reproduced in Fig. 4 demonstrates a nose-shaped temperature-time crystallization behavior. The presence of phase separation and primary crystallization event occurs at approximately 1,000 seconds at 683 K and at more than 10,000 seconds at 600 K, providing a sufficient operational time windows for conducting the compression experiments. Compression experiments at even higher temperatures were also attempted. However, the relatively low viscosity and possible rapid crystallization at these temperature levels, 703 K and above, made the experiments uncontrollable and unreliable (also, there was a negligible, yet persistent initial permanent stress due to the measurement method). Therefore, all the experiments presented in this study will be confined to the temperature range of 295 to 683 K.

The stresses and strains presented here are "true" stresses and "true" (logarithmic) strains. One problem of making a definitive statement as to whether the concept of true strain and stress is valid for metallic glasses rely to most extent on the volumetric deformation of the amorphous system, which consists of both atoms and associated unoccupied free volume (Spaepen, 1977). The latter plays an important role from a statistical point of view in assisting in atomic arrangements driven by external forces and/or thermal energy: even a tiny change of the free volume could induce dramatic variation of the flow behavior (e.g., Steif and Spaepen, 1982). The study by Masuhr *et al.,* (1999a) provides a value for the normalized free volume in Vit 1 to be approximately 3% around the glass transition temperature and the supercooled liquid region. However, no data on free volume variation, if Vit 1 is subjected to large mechanical deformation, is readily available in the literature. However, the result for $Pd_{40}Ni_{40}P_{20}$ metallic glass (de Hey et al., 1998) elucidates that the normalized free volume only altered from 3.1% to 3.4% after a uniaxial deformation to a strain of 0.11 at 556 K and a strain rate of $1.7\times10^{-4}\ s^{-1}$. Inasmuch as free volume has negligible influence on volume change, the adaptation of true measures of strain and stress in the present study appear reasonable. Further study of the compressibility of metallic glasses under thermomechanical loading is needed.

3.1 Effect of temperature on stress-strain behavior

Figure 5 shows the stress-strain curves for Vitreloy 1 at four different strain rates, namely, $1.0\times10^{-5}\ s^{-1}$, $3.2\times10^{-5}\ s^{-1}$, $1.0\times10^{-4}\ s^{-1}$ and $3.2\times10^{-4}\ s^{-1}$ for different ambient temperatures. The axial strains were determined from the high sensitivity LVDT output and the stress was computed from the load cell output.

The stress-strain curves at $1.0\times10^{-5}\ s^{-1}$ are shown in Fig. 5(a) for two values of temperature (T), with the upper and the lower curves corresponding to 593 K and 613 K respectively. At T=613 K, the stress increased monotonically as the strain increased until it reached a steady state value and subsequently leveled off as the strain increased further. The temperature sensitivity is much larger compared with traditional crystalline metallic alloys since the steady state stress decreased by over 50% as the temperature increased by 20 K over 593 K. Imposed strain rates lower than 1.0×10^{-5} s^{-1} were not pursued further due to possible phase separation and crystallization at elevated temperatures during compression. Also, as mentioned earlier, according to the TTT diagram (Fig. 4), compression at higher temperature, for example, such as 663 K and at 1.0×10^{-5} s^{-1} will also introduce phase separation and crystallization. Therefore, no experiments were conducted at higher temperatures. The pronounced *zigzag* shape of the stress-strain curve at 593 K could be due to some artifact of the experimental method and will not be regarded as real material behavior at this particular temperature and strain rate (such phenomenon was not observed during other experiments).

The use of the TTT diagram was based on the assumption that the stress-driven material phase change is negligible compared with annealing. Although stress-driven free volume creation has been reported by other researchers (de Hey *et al.*, 1998), to the author's knowledge, no observation on the stress-driven phase separation has been reported in the literature, but this remains an interesting topic for further study.

The stress-strain curves at a strain rate of 3.2×10^{-5} s^{-1} and temperatures ranging from 573 K to 623 K are shown in Fig. 5(b). In this temperature range, deformation remained homogeneous up to the strain value demonstrated on each curve. The term "homogeneous deformation" as used here means uniform deformation of the specimen at a macroscopic scale, i.e., shape and size of the cross-sections of the deforming specimen change simultaneously everywhere along the loading axis, remaining self similar, and no macroscopic shear localization is observed. The counterpart of the homogeneous deformation is the catastrophic shear failure triggered by a major shear band propagation, which is referred to as "inhomogeneous deformation" later. The maximum strain value of each curve in presenting homogeneous deformation data was merely chosen for convenience in each experiment since there were no indications of any possible catastrophic failure. Stress overshoot, the difference between peak stress and steady stress, began to emerge at some temperatures. The cause of the stress overshoot was due to the free volume induced structural relaxation (Spaepen, 1977), which will be discussed in detail in the following section. The stress-strain curves featured an increase of the initial slope as the temperature decreased, which indicates that the initial Young's Modulus (or shear modulus) is inversely dependent on temperature, analogous to similar effect in crystalline metallic alloys.

The influence of temperature on failure modes is one of the key features of deformation of materials and their characterization, i.e., brittle to ductile transition. Stress-strain curves corresponding to shear dominated failure as well as homogeneous deformation are shown in Fig. 5(c) for a strain rate of 1.0×10^{-4} s^{-1}. To clearly distinguish each stress-strain curve while presenting all of them in the same plot, some of the curves were shifted along the strain axis by a strain value in the range of 0 to 0.02. The transition from catastrophic shear failure to homogeneous deformation occurred at a temperature between 523 K and 573 K. Vitreloy 1 exhibited a high failure stress of 1,908 MPa at room temperature and failed by the formation of a single shear band and subsequently shearing it. As the temperature was increased to 373 K, the maximum stress decreased slightly to 1,820 MPa. This general trend of the decrease in the maximum stress continued until the temperature was increased to 573 K, where the deformation mode switched from being inhomogeneous (shear failure) to being homogeneous. It is not surprising that the peak stress (the term "peak stress" is used instead of "maximum stress" in the homogeneous deformation regime) decreased with subsequent increase in temperature. Large stress overshoots were present at temperatures of 573 K, 593 K and 603 K.

The shear dominant failure occurred at a higher temperature for a strain rate of 3.2×10^{-4} s^{-1} as illustrated in Fig. 5(d). Deformations at higher strain rates in the range of 1.0×10^{-3} s^{-1} to 1.0×10^{-0} s^{-1} are plotted in Fig. 5 (e)-(l). No zigzag phenomenon was observed for any of the curves in the homogeneous deformation region. At a strain rate of 1.0×10^{-3} s^{-1}(Fig. 5(e)), experiments at 10 different temperatures were conducted in the range of 295 K to 663 K. The transition from homogeneous to non-homogeneous deformation occurred at a temperature between 593 K and 613 K. It is noticed that after a stress overshoot and before the stress-strain curve reached its steady state value, a stress undershoot appeared as a result of relaxation process at T=613 K. At a strain rate of 3.2×10^{-3} s^{-1}, as shown in Fig. 5(f), homogeneous-to-inhomogeneous deformation transition occurred at a temperature between 613 and 623 K. As the strain rate increased further, the minimum temperature at which Vit 1 can be deformed homogeneously also increased (see Figs. 5 (g)-(l)).

Strain rates higher than 1 s^{-1} and lower than 100 s^{-1} are also of considerable interest. However, for the current specimen configuration, achieving such intermediate strain rates seem to be not feasible using the available screw-driven or servo-hydraulic static testing facilities or the Kolsky (split Hopkinson) pressure bar. However, the newly developed shear compression specimen (SCS) configuration by Rittel *et al.*, (2002) may be useful in investigating material behavior in this strain rate range. The stress-strain curves at higher strain rates, typically in the range of 10^3 s^{-1}, are not shown in Fig. 5 and will be discussed in the next section.

3.2 Effect of strain rate on stress-strain behavior

In addition to the strong temperature dependence of the deformation of Vitreloy 1, the strain rate dependence of the stress-strain curves was also investigated. Note that all the stress-strain curves at high strain rates were obtained based on the experiments using the Kolsky (split Hopkinson) pressure bar. Two typical dynamic strain rates, 2.5×10^2 s^{-1} and 1.0×10^3 s^{-1}, were chosen for the Kolsky bar experiments to investigate the material behavior in the same temperature range as in the quasi-static experiments.

Figures 6(a)-(e) illustrate the stress-strain curves at temperatures of 295 K, 373 K, 423 K, 473 K and 523 K respectively for strain rate in the range of 1.0×10^{-4} s^{-1} to 1.0×10^3 s^{-1}. Some curves have been shifted to the right to avoid overlapping curves of similar shapes and sizes. The strain rate value in the first line of the legend window of each plot corresponds to the first stress-strain curve counting from the right; the second strain rate value corresponds to the second curve from the right and so on. It was found that shear localized failure characterized the deformation mode in this temperature range regardless of strain rate. Comparing to what happened at quasi-static strain rates, the stress-strain curves in this strain rate range have a linear slope until failure and no inelastic post-yielding was evident. After reaching the maximum stress, the stress dropped to its zero value immediately, typical of "brittle" failure. The failed surface exhibited a "vein-like" melting pattern on each of the recovered specimens due to shear band propagation. Yet, the general tendency is that the maximum stress decreased slightly with increasing strain rates at 373 K, 423 K and 473 K with the only exception at room temperature (293 K), the change in the maximum stress is negligible in comparison with the pronounced decrease in peak stress at higher temperature after the glass transition.

From the stress-strain curves shown in Figs. 6 (f)-(m), it is clear that increase in strain rate led to the transition from homogeneous flow to inhomogeneous deformation. Therefore, the effect on the stress-strain curves due to decrease in strain rate is similar to that due to increase in ambient temperature, as depicted in Fig. 5. It can be deduced from Fig. 6(m) that no shear failure (localization) occurred for deformation at 683 K and strain rate in the range of 1.0×10^{-2} s^{-1} to 1.0×10^{0} s^{-1}. Recalling that strain rates higher than this range were not feasible at 683 K due to the limitations of the quasi-static experimental setup, localized shear failure at 683 K could occur at a higher strain rate since the deformation modes at 683 K are not expected to be different from those at 663 K (both are in the supercooled liquid region).

3.3 Peak stress and overshoot stress

The peak stress, one of the principal parameters that characterizes the strength of the bulk metallic glass, is plotted as a function of strain rate and temperature in Figs. 7 and 8, respectively. In the homogeneous deformation region, the tendency of peak stress variation is quite similar to that of steady state stress that will be discussed later. Both these stress quantities have pronounced dependence on strain rate and temperature. On the other hand, the variation of the peak stress in the inhomogeneous region is quite small compared to its variation in the homogeneous region. The average peak stress reduced from around 1,850 MPa at room temperature to about 1,570 MPa at about 573K. However, a remarkable drop in peak stress occurred at higher temperatures. For instance, the peak stress dropped from 1,680 MPa at 573 K to about 50 MPa at 653 K, by a factor of 33 for a change in temperature of only 80 K. These features are further illustrated by the three-dimensional (3D) view and contour plot for the peak stress presented in Figs. 9(a) and 9(b). These results suggest that Vitreloy 1 should not be used in applications where ambient temperature is substantially higher than 573 K, which can be regarded the threshold temperature beyond which this metallic glass cannot be employed as a structural material, but could be viewed as the temperature above which it can be processed or cast into net shape easily.

Stress overshoot with respect to strain rate and temperature is shown in Fig. 10. The overshoot stress increased monotonically as the strain rate increased, and increased with decreasing temperature. This clearly illustrates the opposing roles played by strain rate and temperature on the deformation and failure modes of Vitreloy 1.

3.4 Relaxation

Preliminary experiments on the relaxation behavior of Vitreloy 1 were conducted at ambient temperatures of 593 K, 613 K, 623 K and 643 K. A specimen was uniaxially compressed to a certain strain level at a prescribed strain rate selected for each temperature and held fixed at that strain level. The strain levels are chosen such that the corresponding initial stress (σ_0) is lower than its steady state flow stress. The stress relaxation is then recorded as a function of time using the load cell data. The normalized stress, σ / σ_0, where σ is the stress during the relaxation and σ_0 is the stress at the beginning of the relaxation, are shown in Figs. 11(a), (b) and (c) as a function of time in different scales. Note that the vertical axis (stress) is plotted in the logarithmic scale. A log-log plot is also presented in Fig. 11(a) to facilitate clear visualization of the rate of relaxation. If the relaxation time is denoted by the time when $\sigma / \sigma_0 = 1/e$ (0.368), then the relaxation time at temperatures of 593 K, 613 K, 623 K and 643 K are 21.5, 327, 1,530 and 5,920 seconds respectively (see Fig. 11(d)).

4 Discussion

4.1 Effects of strain rate and temperature on viscosity

At sufficiently low temperatures, metallic glass behaves like a typical hard solid material. To process such a material, it is necessary to heat it to a temperature at which it either softens or melts to undergo a shape change operation. Thus, the ability to measure and characterize the viscosity of a metallic glass is important for optimizing its processing conditions. Among all fluids, Newtonian fluid is the simplest one to describe its constitutive behavior, where the rate of deformation is directly proportional to the stress applied to the fluid regardless the shearing rate. However, some fluids exhibit a non-linear (i.e., non-Newtonian) response to shearing stress, where viscosity is a shear rate dependent quantity. Polymeric fluids, such as melts and solutions, often do not follow the simple Newtonian fluid in their flow behavior, demonstrating shear-rate dependent viscosities (e.g., Matsuoka, 1992). The physical similarity between the amorphous structure of metallic glasses and glassy polymers suggests that metallic glasses at higher temperature exhibit behavior similar to that of polymers. For Vit 1 metallic glass at high temperatures, the characterization of its flow behavior has been limited to the Newtonian range (Masuhr *et al.*, 1999). In this section, the variation of viscosity (i.e., shearing viscosity) with strain rate will be studied, where the shearing viscosity is deduced from the experimental data as one-third of the ratio of the steady state stress to the corresponding uniaxial strain (loading) rate (e.g., Scherer, 1992; Gupta, 2000).

The values of steady-state flow stress are plotted in Fig. 12 with respect to strain rate at various temperatures. The steady state stress for a given temperature increased linearly at lower strain rates. As the strain rate increased further before the specimens failed due to shear localization, a non-linear effect appeared, featuring a bending-over of the stress-strain rate curves, or in another words, the rate of the increase in steady state stress slowed down as the strain rate increased. This effect is manifested by the strain rate and temperature dependence of the viscosity shown in Fig. 13, where the viscosity of Vitreloy 1 is plotted as a function of strain rate at various temperatures. At strain rates lower than some specific value for each temperature, the viscosity remained essentially unchanged or changed very little, within the experimental error. Although it was not easy to observe this phenomena at relatively low temperatures, say, 573 K to 713 K, using the current compression setup and loading system, steady state viscosities at lower strain rates and temperatures of 573 K, 593 K, 603 K and 613 K can be obtained using the three point beam bending apparatus (Masuhr *et al.*, 1999b). Higher strain rates, however, led to a remarkable decrease in the viscosity for temperatures in the range of 573 K to 683 K, indicating that the flow is transitioning from Newtonian to non-Newtonian in character. The experimental results clearly show that stress overshoot accompanies all the stress-strain curves in the non-Newtonian homogeneous deformation regime. In the linear Newtonian regime, relaxation of the material is fast enough to keep up with the external loading rate, resulting in no stress overshoot but resulting in a monotonically increasing stress-strain curve. Nevertheless, both the stress-strain curves with overshoot and the ones without overshoot (i.e., monotonically increasing behavior) were present in the Newtonian deformation regime.

As demonstrated in Fig. 14(a), a master curve (relation) can be constructed for the steady-state flow stress of Vitreloy 1 with respect to normalized strain rate $\dot{\varepsilon}\eta_N$, which is the product of Newtonian viscosity η_N and imposed strain rate $\dot{\varepsilon}$. Likewise, a master curve (relation) in terms of viscosity ratio η/η_N and the normalized strain rate can also be generated, as shown in Fig.

14(b). The master curve describing the viscosity can be expressed in the form (e.g., Matsuoka, 1992),

$$\eta / \eta_N = 1 - \exp\left(-\left(\frac{\alpha}{\dot{\varepsilon}\, \eta_N} \right)^{\beta} \right) \tag{1}$$

where α and β are fitting parameters for the experimental data. For Vitreloy 1, the values of α and β are 172 MPa and 0.85 respectively and were obtained by fitting the current experimental data. η_N is the Newtonian viscosity which can be described by a free volume model (Masuhr *et al.*, 1999),

$$\eta_N = \eta_0 \exp\left(b\, v_m / v_f \right) \tag{2}$$

where v_f is the temperature dependent average free volume per atom according to the Cohen and Grest model (Grest and Cohen, 1981), bv_m is the critical volume for the glass flow and η_0 is a fitting parameter having the units of viscosity. The values of bv_m and η_0 were given by Masuhr *et al.* (1999) for Vit 1. The Newtonian viscosity, i.e., the equilibrium viscosity, is also shown in Fig. 15.

The above two equations, (1) and (2) can be used to fully determine the viscosity within the homogeneous region, however, they cannot predict the onset of shear localization, or, in other words, the boundary between the homogeneous and inhomogeneous deformation.

4.2 Homogeneous and inhomogeneous deformation

As described in the previous sections, the deformation of Vitreloy 1 can be categorized into two major regions on a deformation map of strain rate versus temperature, one with homogeneous deformation and the other associated with inhomogeous deformation, the former featuring either Newtonian or non-Newtonian flow while the latter is characterized by linear elastic behavior followed by catastrophic shear failure. Based on the experimental data from the current investigation, Fig. 16 proposes the boundaries for Vitreloy 1 among the three distinct modes of deformation on the flow map. Two boundaries are shown in the figures, one for the transition from homogeneous deformation to inhomogeneous deformation, and the other for the transition from Newtonian to non-Newtonian flow. It has been realized from all the stress-strain curves that if shear failure occurs in Vitreloy 1, the corresponding failure strain will always be less than 5%. The experiments have also confirmed that under uniaxial compressive loading condition, if failure does not occur at peak stress, Vitreloy 1 will exhibit *superplasticity*, implying that the material has the capacity for substantial flow at the corresponding strain rate. Although the peak stress for the onset of shear localization varied with temperature, it fell in the range of 1,100 to 1,700 MPa.

4.3 Effects of jump in strain rate

The viscous nature of flow and high rate sensitivity of the flow stress of Viterloy 1 during homogeneous deformation suggests detailed investigation of the kinetics of flow and associated strength. By varying the strain rate during a uniaxial compression experiment, not only the influence of the preloading history on the steady state can be investigated, but also the effect of the relaxation at the first strain rate on the stress overshoot at the second strain rate can be examined, which provides additional information to further validate flow models for metallic glasses. Therefore, jump-in-strain-rate experiments provide an additional means to probe the relaxation response of materials that are deformed. A set of jump-in-strain-rate experiments were performed where strain rates were abruptly changed from one value to another, while holding the ambient temperature constant. Figure 17(a) shows the stress-strain curve where the strain rate was changed from 3.2×10^{-3} s^{-1} to 3.2×10^{-2} s^{-1} (by one order of magnitude) at a strain of around 0.13 at 643 K. The stress-strain curves at 643 K and constant strain rates of 5.0×10^{-3} s^{-1} and 3.2×10^{-2} s^{-1} are also plotted for reference. After the strain rate was changed, the stress-strain curve exhibited a second peak stress which is smaller than the one obtained under constant strain rate loading at the corresponding temperature. This is probably due to the preloading effect that relaxed the glass and/or increased free volume due to inelastic deformation. However, it is obvious that the steady state flow stress was not affected, within the experimental error. In other words, for the experimental conditions considered here, the steady state flow stress is independent of the material deformation history while the overshoot stress does depend on the loading history.

In continuing with the jump-in-strain-rate experiments, the two strain rates used before remained unchanged except the sequence in which they were applied. Figure 17(b) shows the stress-strain curve where the strain rate was changed abruptly from a higher value of $3.2\times10^{-2}\ \mathrm{s}^{-1}$ to a lower value of $3.2\times10^{-3}\ \mathrm{s}^{-1}$ at a strain of around 0.15 while keeping the same ambient temperature of 643 K. The stress-stain curve began to deviate from its path at the constant strain rate of $3.2\times10^{-2}\ \mathrm{s}^{-1}$ right after the jump in strain rate, followed by a stress undershoot and leveling-off before it approached steady state flow corresponding to the current strain rate.

Either the first strain rate or the second one or both used in the previous experiment were altered to further examine the strain rate history effect on deformation behavior of the metallic glass Vit 1. Figure 17(c) shows a stress-strain curve at 643 K under similar conditions similar to the experiment shown in Fig. 17(a), but the second strain rate ($1.0\times10^{-2}\ \mathrm{s}^{-1}$) is different. The resulting response further confirmed that the second peak stress was lower in comparison with the peak stress when the material was not subject to any preloading. Figure 17(d) shows the result at 643 K from another experiment where only the first strain rate was changed ($1.0\times10^{-3}\ \mathrm{s}^{-1}$) compared with Fig. 17(a). The previous conclusions remain valid within the experimental error.

To further investigate the material response of Vitreloy 1 at 643 K after the jump in strain rate, the second strain rate, $1\times10^{-2}\mathrm{s}^{-1}$, was restored back to its original value, $5\times10^{-3}\mathrm{s}^{-1}$, as depicted in Fig. 17(e). An initial strain rate of $3.2\times10^{-2}\ \mathrm{s}^{-1}$ was applied to the specimen, followed by a higher strain rate of 1.0×10^{-2} s^{-1}. At a strain of around 0.4, the strain rate was reset to its original value, 3.2×10^{-2} s^{-1}. As can be observed, the final steady state flow stress reached a value close to the steady state flow stress corresponding to constant strain rate deformation at 3.2×10^{-2} s^{-1}, as if there was no higher strain rate deformation exerted on the specimen at all. An appropriate conclusion can be made based on the above experiments: the steady state flow stress is independent of all the previous loading history while the transient response is highly path dependent. Other experiments at different temperatures were also performed and they exhibited similar behavior as the ones described here. Illustrative results from these experiments are shown in Figs. 18 (T=623 K) and 19 (T=613 K) and the corresponding experimental conditions are given in the figure captions.

5 Modeling

5.1 Concept of free volume

A hypothesis on the existence of free volume in glassy materials was first proposed by Cohen and Turnbull (1959) and was subsequently adapted for metallic glasses by Spaepen (1977). Metallic glasses are formed by rapidly quenching metallic melts (liquids) at certain rates to restrict their atomic movements and suppress crystallization. The total volume of such a metallic liquid is divided into the part occupied by atoms of various sizes and the part consisting of "holes" or "voids" of various sizes in to which atoms may jump. The concept of "free volume" is associated with the latter part, i.e., "holes" or "voids," which is the key to the diffusive arrangement of atoms. The possibility of an atom jumping into its adjacent hole (free volume) is dependent on the relative size of the atom and the hole. Free volume is generally a decreasing function of temperature. Upon quenching below a critical temperature, i.e., the glass transition temperature, the free volume is mostly frozen in place and the redistribution of the trapped free volume becomes substantially more difficult compared with that at higher temperatures. Free volume is considered to be pressure dependent in metallic glasses (e.g., Ruitenberg *et al.*, 1997). In general, the average free volume per atom subject to hydrostatic pressure may be described by (Cohen and Turnbull, 1959),

$$v_f = \alpha v_m (T - T_0) - \beta v_p \Delta P \tag{3}$$

where T_0 is the temperature at which the free volume disappears, α is the coefficient of thermal expansion at zero pressure, v_m is the mean atomic volume at zero pressure, β is the mean compressibility, and v_p is the mean atomic volume for the pressure increment ΔP. Studies have shown that the free volume of Vitreloy1 is much smaller compared to the average atomic volume (Masuhr *et al.*, 1999), so we can approximate Eq. (3) by

$$v_f = v_m \left(\alpha (T - T_0) - \beta \Delta P \right). \tag{4}$$

Free volume may be associated with one atom, which may jump from one site to another with a coincident collapse of the original cage of the neighboring atoms. Alternatively, free volume may be associated with more than one atom, and the motions of the atoms together will contribute to shear flow (Elliott, 1984). In a multicomponent amorphous alloy system, for example, Vitreloy 1, the shear flow could be of the second type. In a simple model described in the next section, free volume variation due to external shear stress will be addressed. Shear component of the deformation plays a key role in the general deformation of the glass including shear localization and failure. The concept of free volume has been used to model nonlinear theormechanical response of other amorphous solids such as polymers; see for example, Knauss and Emri (1981) and Losi and Knauss (1992).

5.2 Spaepan's free volume model

Spaepen developed a flow model (e.g., Spaepen, 1977; Steif *et al.*, 1981) based on the concept of free volume originally proposed by Cohen and Turnbull (Cohen and Turnbull 1959;

Turnbull and Cohen 1961, 1970). According to Cohen and Turnbull, the probability p of finding an atom with a free volume between v and v+dv is,

$$p(v)\mathrm{d}v = \frac{\alpha}{v_f}\exp\left(-\frac{\alpha v^*}{v_f}\right)\mathrm{d}v \tag{5}$$

where α is a geometrical factor on the order of 1, v_f is the average free volume per atom and v^* is the critical volume. The shear flow rate is the result of competition between the thermal activation barrier and the shear stress driven potential,

$$\dot{\gamma} = 2\nu\exp\left(-\frac{\alpha v^*}{v_f}\right)\sinh\left(\frac{\tau\Omega}{2kT} - \frac{\Delta G^m}{kT}\right), \tag{6}$$

where Ω is the atomic volume, k is Boltzmann constant, T is the temperature, ΔG^m is the activation energy, ν is the Debye frequency, and τ is the applied shear stress. The net rate of free volume change $\dot{v}_f$ is due to the competition between the creation by external shear stress that squeezes an atom into a hole smaller than itself, and the annihilation by diffusion jumps of atoms towards its metastable equilibrium, plus the effect due to the hydrostatic pressure and temperature variation,

$$\dot{v}_f = \nu v^* \exp\left(-\frac{\alpha v^*}{v_f}\right)\exp\left(-\frac{\Delta G^m}{kT}\right)\left\{\frac{2\alpha kT}{v_f S}\left[\cosh\left(\frac{\tau\Omega}{2kT}\right)-1\right]-\frac{1}{n_D}\right\}+v_m\alpha\dot{T}-\beta v_m\dot{P}, \tag{7}$$

where S is a function of the shear modulus and n_D is the average jump number to annihilate a free volume equal to v^*. The equations (6) and (7) are fundamental in understanding flow of a metallic glass using the statistical free volume concept. In order to fully describe the mechanical behavior of a metallic glass, the values of v^*, Ω, ΔG^m, ν, S, n_D and initial v_f are needed to solve the coupled differential equations.

The value of initial free volume, v_f, as mentioned earlier, has been obtained by Masuhr (Masuhr *et al.*, 1999). Ω is in the range of $16\times10^{-30}m^3$ for Vitreloy 1. v^* can be approximated (or replaced) by Ω. $\Delta G^m, v$ and S are all temperature dependent. Typical values of ΔG^m and v are in the range of 2 eV and 10^{13} s^{-1}, respectively, which can exert dramatic changes upon the thermo-mechanical response of the material, if varied. The parameter S, derived under the assumption of Eshelby's inclusion model, is approximated using the shear modulus and Poisson's ratio. Attempts were made to find the undetermined parameters based on experimental data. Steady state flow can be obtained by setting $\dot{\gamma}=0$ and $\dot{v}_f=0$ in Eqs. (6) and (7),

$$\ln\left(\frac{2v\exp\left(-\Delta G^m/(kT)\right)\sinh\tau}{\dot{\gamma}}\right)\left(\frac{\cosh(\tau\Omega/2kT)-1}{G\beta}\right)n_D=1, \tag{8}$$

where β is a function of Poisson's ratio and atomic volume (Speapen, 1977). To the author's knowledge, the free volume model has not been applied to a metallic glass to describe its flow behavior. Even under the simple assumption of steady state flow, v, ΔG^m and n_D have to be solved together. However, it was found, for instance, at a temperature of 643 K, that even using a wide range for the fitted values for v, ΔG^m and n_D (3 to 20), the model is not able to provide a reasonable description of the flow behavior for Vit 1.

Nevertheless, the free volume model (Spaepen, 1977) is valuable in demonstrating the physics of deformation in metallic glasses and shear localization such as the conceptual example shown in Fig. 20, which illustrates the shear deformation of a block of a model metallic glass whose material parameters and loading conditions are as follows: normalized shear modulus $\bar{G}=G\Omega/2kT=10$, normalized free volume $\bar{v}_f=v_f/\alpha v^*=0.0633$, normalized shear strain rate $\dot{\gamma}/v\exp(-\Delta G^m/kT)=5\times10^{-7}$, $n_D=10$ and $\alpha=\beta=1$ (see Steif *et al.*, 1982). In addition, a material imperfection in terms of free volume is assumed for a thin layer of glass, δL, with a slightly higher normalized free volume $\bar{v}_f=v_f/\alpha v^*=0.0643$ and a thickness ratio $\delta L/L=0.001$, where L is the total thickness of the glass, is included in the middle of the block of glass. Figure 20 indicates that the consequence of increasing the free volume in the thin layer by only 1.5% induces 700% more strain in the thin layer in comparison to the main body of the glass, noting that no temperature effect has been considered. Therefore this thin layer becomes a shear band. It is generally believed that small variations in free volume locally lead to strain localization during deformation. Experimental studies have shown that metallic glasses are the most susceptible among all materials to shear band formation at room temperature (e.g., Bai and Dodd, 1992).

Recently, a group of researchers (de Hey *et al.*, 1998) studied the free volume evolution based on the assumption that the heat release rate of an amorphous material is proportional to the rate of free volume. The rate of evolution of the defect concentration is the sum of an annihilation term $-k_r c_f (c_f - c_{f,eq})$ and a creation term $a_x \dot{\varepsilon} c_f \ln^2 c_f$, where $c_f = \exp\left(-\gamma v^* / v_f\right)$ and k_r is a thermal material parameter. In conjunction with Eq. (6), they modeled the flow behavior leading to the conclusion that the free volume increases with strain rate and increases with strain until steady state flow occurs.

5.3 Fictive stress model

In this section, a phenomenological model is employed to describe the flow behavior of Vitreloy 1 in the homogeneous regime. Recently, a model was proposed using the concept of fictive stress (Kato *et al.*, 1999) in which the uniaxial stress rate is described using a simple Maxwell model,

$$\frac{\mathrm{d}\sigma}{\mathrm{d}t} = E\frac{\mathrm{d}\varepsilon}{\mathrm{d}t} - \frac{\sigma}{\lambda}, \tag{9}$$

where E is Young's Modulus which is a function of temperature, ε is the strain, σ is the uniaxial stress and λ is the relaxation time. If the relaxation time λ is only a function of temperature, then for a given temperature and strain rate, the general solution for stress is a monotonically increasing function reaching a steady state after a strain of approximately $\varepsilon = \dot{\varepsilon}\lambda$. However, the actual response of metallic glasses does not always exhibit such a tendency. In the steady state regime, one can reasonably assume that the relaxation time scales according to the viscosity, i.e., $\eta/\eta_N = \lambda/\lambda_N$. If λ/λ_N(or η/η_N) is plotted as a function of σ_{flow}/σ^* as shown in Fig. 21, where σ^* is a "maximum" stress used to normalize the flow stress σ_{flow}, the flow stress can then be described using a function, $\sigma_{flow}/\sigma^* = f(\lambda/\lambda_N)$. Instead of using the free volume concept, one can then use the structural relaxation time λ_{relax} to represent the change in the microstructure of the material. Once a steady state flow stress is given, a corresponding λ_{relax} can be obtained by simply assuming $\lambda_{relax} \approx \lambda$. This concept can be further extended to the transient response of the material subjected to loading. A fictive stress σ_{fic} (Kato *et al.*, 1999) and a transient relaxation time λ_{tra} are introduced satisfying the same relation as for the flow stress, $\sigma_{fic}/\sigma^* = f(\lambda_{tra}/\lambda_N)$. The fictive stress is assumed to be dependent on both actual stress and the transient relaxation time λ_{tra} through the following kinetic relation,

$$\frac{\mathrm{d}\sigma_{fic}}{\mathrm{d}t} = \frac{\sigma - \sigma_{fic}}{\lambda_{tra}}. \tag{10}$$

It is easy to see from Eq. (10) that at steady state $\dot{\sigma}_{fic}$ =0, and the fictive stress is equal to the actual flow stress, consistent with the previous assumption. In light of the experimental data, an empirical relation for the transient relaxation time is assumed as follows:

$$\frac{\lambda_{tra}}{\lambda_N} = \left(1 - \frac{\sigma_{fic}}{\sigma^*}\right) \Bigg/ \left(1 + \frac{\sigma_{fic}}{\sigma^*}\right). \tag{11}$$

Consequently,

$$\frac{\mathrm{d}\lambda_{tra}}{\mathrm{d}t} = \frac{-2}{(1 + \lambda_f/\lambda_N)^2} \frac{\lambda_N}{\sigma^*} \frac{\mathrm{d}\sigma_f}{\mathrm{d}t}. \tag{12}$$

This simple model can now be used to describe the deformation behavior of a metallic glass in its homogeneous regime. Figures 22 to 34 show the comparison of model predictions with experimental data at various temperatures and strain rates. Young's modulus was chosen as a function of temperature and rate of deformation in accordance with the experimental results. The initial relaxation time λ_N and the reference stress σ^* are also based on the experimental results and the values used in the model are shown in the figure captions. For the initial relaxation time λ_N in the model, the relaxation time determined from the experiments as depicted in Fig. 11 was used and the resulting predictions were not in agreement with the experimentally obtained stress-strain curves. It was found that the experimental results were best modeled by scaling the relaxation time in Fig. 11 by a factor of 1/3 to 1/5 while keeping the relaxation time as a function of temperature, which is in accordance with the scaling suggested by Kato et al. (1999).

At a temperature of 643 K, five typical stress-strain curves corresponding to strain rates of $1\times10^{-4}\ \mathrm{s}^{-1}$, $2\times10^{-4}\ \mathrm{s}^{-1}$, $1\times10^{-3}\ \mathrm{s}^{-1}$, $5\times10^{-3}\ \mathrm{s}^{-1}$ and $1\times10^{-2}\ \mathrm{s}^{-1}$ are shown in Fig. 22. The predicted stress-strain curves agree reasonably well with the experimental results, as shown in the upper plot of Fig. 22. The stress peaks and the slopes at the early stage of the deformation also match reasonably well with the experimental data. At higher strain rates, the slopes of the descending part after the peaks seem to be steeper than what was observed in the experiments, and higher levels of steady state flow stress are predicted. The transition from Newtonian to non-Newtonian flow appears at a strain rate higher than $1\times10^{-3}\ \mathrm{s}^{-1}$, which is close to the value observed in the experiments (Fig. 16). The transition can be demonstrated again by looking at the relaxation time-strain relationship as shown in the lower left-hand side plot in Fig. 22. Clearly, at the two smallest strain rates, the corresponding transient relaxation time remains almost a constant, with very limited drops before the corresponding steady state stress levels off. At the strain rate of $1\times10^{-3}\ \mathrm{s}^{-1}$, a small stress overshoot emerges, accompanied by a pronounced decrease in the relaxation time of more than 10 percent. As the strain rate increases, the decrease in the relaxation time becomes so significant that oscillations are observed in the stress-strain curve. The fictive stress, on the other hand, serves as a bridge to link the transient relaxation time and the deformation. The plot on the lower left-hand side illustrates the variations of the fictive stress with respect to strain. Recalling the conceptual stress-strain and free volume-strain curves illustrated in Fig. 20, it is interesting that the variation of the free volume has a similar tendency compared with that of the fictive stress: both lag behind the actual stress of the material, which suggests that there might exist a correlation between the two variables. Consequently, in the context of the present phenomenological model, one can think of fictive stress as another empirical function of the free volume.

Shown in Figs. 23 to 26 are the comparison between model predictions and experiments for the stress-strain curves at other temperatures (613 K, 623 K, 663 K, and 683 K). The variations of fictive stress and transient relaxation time are also shown. The model generally captures the deformation features of the material at different temperatures and strain rates. However, at 623 K, in contrast to the experiment, as depicted in Fig. 24, the slope of the stress-strain curve at early stages of deformation is steeper and the oscillation period around the peak stress is shorter. It is also worth noting that stress undershoot is predicted by the model. As shown in Figs. 25 and 26, at 663 K and 683 K, in spite of good agreement between the predicted and experimental stress-strain curves at low strain rates, the steady state stresses at higher strain rates predicted by the model are larger than those observed in the experiments and the cause for this is unclear at present.

As shown earlier, jump in strain rate has a pronounced effect on the stress-strain response of Vitreloy 1. Such high strain rate sensitivity in the low strain rate regime is not generally observed in crystalline metallic materials. This effect can also be reproduced by the fictive stress model. Figure 27 shows both the predicted and experimental stress-strain curves where the strain rate is changed abruptly from 3.2×10^{-3} s^{-1} to 1.0×10^{-2} s^{-1} at a strain of about 0.08. For reference, the stress-strain curves at constant strain rates of 5.0×10^{-3} s^{-1} and 1.0×10^{-2} s^{-1} are also plotted. The stress jump observed in the experiment is reproducible by the model. The variations of the fictive stress and the transient relaxation time are shown in the lower plots of the figure. The variation of the fictive stress lags behind the actual stress, same as for the case where the material is loaded at a constant strain rate (see, for example, Fig. 22). Also, the change of fictive stress at the strain where the strain rate jumps is quite slow and smooth compared with that of the actual stress. The relaxation time begins to decrease at a higher rate after the jump in strain rate, and stress undershoot is clearly observed in the plot.

Simulations were also carried out for other strain rate combinations as shown in Figs. 28 to 32, at the same ambient temperature, 643 K, and in Fig. 33, for an ambient temperature of 623 K. The agreement between the model and the experiment is generally good except that the model predicts more gradual initial slope and smaller oscillation period for the stress-strain curves, particularly at high strain rates.

To further demonstrate the applicability of the model for studying the response of the material subjected to complex loading history, after the first jump in strain rate, the second strain rate is reset to its original value, i.e., the initial strain rate. At 643 K, as depicted in Fig. 34, an initial strain rate of $3.2\times10^{-2}\ s^{-1}$ is applied, then followed by deformation at a higher strain rate, $1.0\times10^{-2}\ s^{-1}$. At a strain of around 0.4, the strain rate is changed to its initial value, $3.2\times10^{-2}\ s^{-1}$. The model predictions show that the final steady state flow stress reaches a value close to the steady state flow stress at the initial strain rate of $3.2\times10^{-2}\ s^{-1}$, indicating that the intermediate deformation history has no significant effect. These features are in accordance with the experimental results shown earlier in Fig. 24.

6 Conclusions

The uniaxial stress-strain behavior of a bulk metallic glass, namely Vitreloy 1 ($Zr_{41.2}Ti_{13.8}Cu_{12.5}Ni_{10}Be_{22.5}$), was investigated experimentally over a wide range of strain rates as well as temperatures. The following conclusions can be drawn from this investigation:

1. The deformation of Vitreloy 1 bulk metallic glass is very sensitive to loading rate and temperature near and above its glass transition, 623 K, i.e., in the supercooled liquid region. Quasi-static experiments revealed that Vitreloy 1 exhibits high-strain-rate sensitivity over the temperature range of 573 K to 683 K, especially in the supercooled liquid region. However, under dynamic loading conditions, 10^2 s^{-1} to 10^3 s^{-1}, the strain rate effect is not significant when compared with the quasi-static range. At temperatures below 573 K, the material has high strength, exhibiting less strain rate sensitivity compared with the high temperature regime. At room temperature, Vitreloy 1 is virtually rate insensitive over a broad range of strain rates, up to 10^3 s^{-1}, which is consistent with the earlier observation (Bruck *et al.*, 1996).
2. The deformation of bulk metallic glasses can be divided into three modes, namely, Newtonian flow, non-Newtonian flow, and shear localization. It is found that homogeneous deformation in Vitreloy 1 can be achieved at a strain rate nominally higher than 1 s^{-1} in the high temperature side of its supercooled liquid region. The non-Newtonian viscosity of Vitreloy 1 is substantially smaller than its corresponding Newtonian viscosity in this range of temperatures. Such a trend can be well expressed using a master curve which describes normalized viscosity as a function of normalized strain rate. The studies of stress overshoot and relaxation also revealed that the flow of Vitreloy 1 is very sensitive in the supercooled liquid region and quasi-static strain rates.
3. A free volume based model by Spaepen (1977) was found incapable of describing the flow behavior of Vitreloy 1 quantitatively, though the model has been successful in demonstrating the general flow characteristics of metallic glass as well as shear localization as a result of material imperfection. Instead, a simple modified Maxwell viscoelastic model, originally proposed by Kato *et al.*, (2000), was employed. The relaxation time correlated well with a "fictive" stress which is the conceptual extension of the steady state flow stress in the transient deformation regime and was no longer assumed constant but varied during deformation. This model is able to capture the basic characteristics of the stress-strain

curves, as well as the jump-in-strain rate effects of Vitreloy 1 reasonably well. It also suggests that the variation of the "fictive" stress likely represents the trend of the free volume variation with inelastic deformation.

4. Due to its extreme high strength and light weight, Vitreloy 1 has been produced in large quantities for structural applications using high pressure injection casting. In order to obtain high quality material, attention needs to be focused on avoiding inhomogeneous shear localization, phase separation and crystallization. Since Vitreloy 1 is highly metastable with a large supercooled liquid region to suppress crystal formation, preventing inhomogeneous shear localization is of major concern in deformation processing and casting. An important issue is the choice of processing conditions for bulk metallic glasses to avoid shear localization and yet achieve a high rate of productivity. From the current investigation, it is evident that the processing speed (or pressure) must be set such that the corresponding effective strain rate is smaller than the critical effective strain rate of inhomogeneous deformation predetermined at the mold temperature. In this respect, the data for Vitreloy 1 in Fig. 16 provides the necessary design data for optimal processing conditions. Casting process should be controlled within the homogeneous deformation region away from the boundary of shear localization in order to produce high quality material.

References

Argon, A. S. and Shi, L. T., Development of visco-plastic deformation in metallic glasses, Acta Metall., **31**, 499-507 (1983).

Argon, A. S., Plastic deformation in metallic glasses, Acta Metall., **27**, 47-58 (1979).

Bai, Y. and Dodd, B., Adiabatic shear localization: occurrence, theories and applications, Pergamon, Oxford, 1992.

Bruck, H. A., Rosakis, A. J. and Johnson, W. L., The dynamic compressive behavior of beryllium bearing bulk metallic glasses, J. Mater. Res., **11**, 503-511 (1996).

Bruck, H. A., Christman, T., Rosakis, A. J. and Johnson, W. L., Quasi-static constitutive behavior of $Zr_{41.2}Ti_{13.8}Cu_{12.5}Ni_{10}Be_{22.5}$ bulk amorphous alloys, Scripta Metall., **30**, 429-434 (1994).

Busch, R., Kim, Y. J. and Johnson, W. L., Thermodynamics and kinetics of the undercooled liquid and the glass-transaction of the $Zr_{41.2}Ti_{13.8}Cu_{12.5}sNi_{10}Be_{22.5}$ alloy, J. Appl. Phys., **77** (8) 4039-4043, (1995a).

Busch, R., Kim, Y. J., Johnson, W. L., Rulison, A. J., Rhim, W. K. and Isheim, D., Hemispherical total emissivity and specific-heat capacity of deeply undercooled $Zr_{41.2}Ti_{13.8}Cu_{12.5}Ni_{10.0}Be_{22.5}$ melts, Appl. Phys. Lett., **66** (23), 3111-3113 (1995b).

Chen, H. S., Metallic glass, Mater. Sci. Eng., 25, 59-69 (1976).

Chen, H. S., The influence of structural relaxation on the density and Young's Modulus of metallic glass, J. Appl. Phys. **49**, 3289-3291 (1978).

Chen, H. S., Kato, H. and Inoue, A., A fictive stress model calculation of stress-overshoot: A nonlinear viscoelastic behavior in metallic glass, Jap. J. Appl. Phys. Part 1, **39** (4A) 1808-1811 (2000).

Chen, W. and Ravichandran, G., Dynamic compressive failure of a glass ceramic under lateral confinement, Journal of the Mechanics and Physics of Solid, **45**, 1303-1328 (1997).

Cohen, M. H. and Turnbull, D., Molecular transport in liquids and glasses, J. Chem. Phys., **31** 1164-1169 (1959).

Conner, D. R., Mechanical behavior of bulk metallic glass matrix composites, Ph.D. Thesis, California Institute of Technology, 1998.

de Hey, P., Sietsma, J. and van den Beukel, A., Creation of free volume in amorphous $Pd_{40}Ni_{40}P_{20}$ during high temperature deformation, Mat. Sci. Eng. **A226-228**, 336-340 (1997).

de Hey, P., Sietsma, J. and Van den Beukel, A., Structural disordering in amorphous $Pd_{40}Ni_{40}P_{20}$ induced by high temperature deformation, Acta Meter., **46** (16), 5873-5882 (1998).

Duine, P. A., Sietsma, J. and van den Beukel, A., Defect production and annihilation near equilibrium in amorphous $Pd_{40}Ni_{40}P_{20}$ investigated from viscosity data, Acta Metall., **40**(4), 743-751 (1992).

Elliott, S. R., Physics of amorphous materials, Longman, New York, 1984.

Fecht, H. J., Thermodynamic properties of amorphous solids - glass-formation and glass-transition, Mater. Trans., JIM, **36** (7), 777-793 (1995).

Gray, G. T. III., Classic split-Hopkinson pressure bar testing, in ASM Handbook, Vol. 8, ASM International, Metals Park, OH, 462-476 (2000).

Grest, G. S. and Cohen, M. H., Adv. Chem. Phys., **48**, 455 (1981).

Gupta, R. K, Polymer and composite rheology, Marcel Dekker, 2000.

Inoue, A., Bulk amorphous alloys: Preparation and functional characteristics, Trans Tech Publication Ltd. Switzerland, 1998.

Inoue, A., Ohtera, K., Kita, K. and Masumoto, T., New amorphous Mg-Ce-Ni alloys with high-strength and good ductility, Jpn. J Appl. Phys., **27** (12), L2248-L2251 (1988).

Ishihara S. and Inoue A., Superplastic deformation of supercooled liquid in Zr-based bulk glassy alloys containing nano-quasicrystalline particles, Mater. Trans. JIM, **42** (8), 1517-1522 (2001).

Johnson, W. L., Fundamental aspect of bulk metallic glass formation in multicomponent alloys, Mater. Sci. Forum, **225-227**, 35-50, (1996a).

Johnson, W. L., Bulk metallic glass-a new engineering material, Solid State & Mater. Sci., **1,** 383-386, (1996b).

Johnson, W. L., Metastable phases in intermetallic compounds: vol. 1, Principles. (Ed. J. H. Westbrook and R. L. Fleischer), John Wiley & Sons, (1994).

Kato, H., Kawamura, Y., Chen, H. S. and Inoue, A., A fictive stress model calculation of nonlinear viscoelastic behaviors in a Zr-based glassy alloy: Stress growth and relaxation, Jap J. Appl. Phys., **39** (9A), 5184-5187 (2000).

Kato, H., Kawamura, Y., Inoue, A. and Chen, H. S., Newtonian to non-Newtonian master flow curves of a bulk glass alloy $Pd_{40}Ni_{10}Cu_{30}P_{20}$, Appl. Phys. Lett., **73** (25), 3665-3667, (1998).

Kato, H., Kawamura, Y., Inoue, A. and Chen, H. S., Transition from linear to nonlinear viscoelasticity during deformation in a Zr-based glassy alloy, Mater. Trans. JIM, **41** (9), 1202-1207 (2000).

Kawamura, Y., Nakamura, T., Inoue, A. and Masumoto, T., High-strain-rate superplasticity due to Newtonian viscous flow in $La_{55}Al_{25}Ni_{20}$ metallic glass, Mater. Trans. JIM **40** (8), 794-803 (1999b).

Kawamura, Y., Nakamura, T., Kato, H., Mano, H. and Inoue, A., Newtonian and non-Newtonian viscosity of supercooled liquid in metallic glasses, Mat. Sci. Eng. **A304**, 674-678 (2001).

Kawamura, Y., Shibata, T., Inoue, A. and Masumoto, T., Deformation behavior of $Zr_{65}Al_{10}Ni_{10}Cu_{15}$ glassy alloy with wide supercooled liquid region, Appl. Phys. Lett., **69** (9), 1208-1210 (1996).

Kawamura, Y., Shibata, T., Inoue, A. and Masumoto, T., Stress overshoot in stress-strain curves of $Zr_{65}Al_{10}Ni_{10}Cu_{15}$ metallic glass, Mater. Trans. JIM, **40** (4), 335-342 (1999a).

Khonik, V. A., The kinetics of irreversible structural relaxation and homogeneous plastic flow of metallic glasses, Phys. Status. Solidi. **A177** (1), 173-189 (2000).

Kim, Y. J., Busch, R., Johnson, W. L., Rulison, A. J. and Rhim, W. K., Experimental determination of a time-temperature-transformation diagram of the undercooled

$Zr_{41.2}Ti_{13.8}Cu_{12.5}Ni_{10.0}Be_{22.5}$ alloy using the containerless electrostatic levitation processing technique, Appl. Phys. Lett., **68** (8), 1057-1059 (1996).

Kim, Y. J., Busch, R., Johnson, W. L., Rulison, A. J. and Rhim, W. K., Metallic-glass formation in highly undercooled $Zr_{41.2}Ti_{13.8}Cu_{12.5}Ni_{10.0}Be_{22.5}$ during containerless electrostatic levitation processing, Appl. Phys. Lett., **65** (17), 2136-2138 (1994).

Knauss, W. G. and Emri, I. J., Non-linear viscoelasticity based on free-volume consideration, Comp. Struct., **13**(1-3), 123-128 (1981).

Kolsky, H., An investigation of the mechanical properties of materials at very high rates of loading, Proc. R. Soc., London, **B62**, 676-700, (1949).

Losi G. U. and Knauss W. G., Free-volume theory and nonlinear thermoviscoelasticity, Polym. Eng. Sci., **32**(8), 542-557 (1992).

Masuhr, A., Busch, R. and Johnson, W. L., Thermodynamics and kinetics of the $Zr_{41.2}Ti_{13.8}$ $Cu_{12.5}Ni_{10.0}Be_{22.5}$ bulk metallic glass forming liquid: glass formation from a strong liquid, J. Non-Cryst. Solids, **252**, 566-571, Part 2, (1999a).

Masuhr, A., Waniuk, T. A., Busch, R. and Johnson, W. L., Time scales for viscous flow, atomic transport, and crystallization in the liquid and supercooled liquid states of $Zr_{41.2}Ti_{13.8}Cu_{12.5}sNi_{10}Be_{22.5}$, Phys. Rev. Lett., **82** (11), 2290-2293 (1999b).

Matsuka, S., Relaxation pehnonmena in polymers, Oxford University press (1992).

Matsuoka, S., Relaxation phenomenon in polymers, Oxford University press, New York, (1992).

Megusar, J., Argon, A. S. and Grant, N. J., Plastic flow and fracture in $Pd_{80}Si_{20}$ near T_g, Mater. Sci. Eng., **38**, 63-72 (1979).

Ohsaka, K., Chung, S. K., Rhim, W. K., Peker, A., Scruggs, D. and Johnson, W. L., Specific volumes of the Zr41.2Ti13.8Cu12.5Ni10.0Be22.5 alloy in the liquid, glass, and crystalline states, Appl. Phys. Lett., 70 (6), 726-728 (1997).

Owen, D. M., Rosakis, A. J. and Johnson, W. L., SM Report 98-22, Caltech (1998).

Peker, A. and Johnson, W. L., A highly processable metallic glass: $Zr_{41.2}Ti_{13.8}Cu_{12.5}Ni_{10.0}Be_{22.5}$, Appl. Phys. Lett., **63**, 2342-2344, (1993).

Ravichandran G. and Subhash, G., Critical appraisal of limiting strain rates for compression testing of ceramics in a split Hopkinson pressure bar, J. Am. Ceram. Soc., **77**(1), 263-267 (1994).

Rittel, D., Ravichandran, G. and Lee, S., Large strain constitutive behavior of OFHC copper over a wide range of strain-rates using the shear compression specimen, to appear in Mechanics of Metarials (2002).

Ruitenberg, G., de Hey, P., Sommer, F. and Sietsma, J., Pressure-induced structural relaxation in amorphous $Pd_{40}Ni_{40}P_{20}$: the formation volume for the diffusion defects, Phys. Rev. Lett, **79**(24), 4830-4832 (1997).

Scherer, G. W., Relaxation in glass and composites, Krieger Publishing, 1992.

Spaepen, F. and Turnbull, D., A mechanism for the flow and fracture of metallic glasses, Scripta. Metall., **8**, 563-568 (1974).

Spaepen, F., A microscopic mechanism for steady state inhomogeneous flow in metallic glasses, Acta. Metall., 25, 407-415 (1977).

Steif, P. S., Ductile versus brittle behavior of amorphous metals, J. Mech. Phys. Solids, **31**, 359-388 (1983).

Steif, P. S., Spaepen, F. and Hutchinson, J. W., Strain Localization in amorphous metals, Acta Metall., **30**, 447-455. (1982).

Subhash, G. and Ravichandran, G., Split Hopkisnon bar testing of ceramics, ASM handbook on mechanical testing and evaluation, Vol. **8**, 497-504, ASM International (2000).

Taub, A. I., Stress-strain rate dependence of homogeneous flow in metallic glass, Acta Metall., **28**, 633-637 (1980).

Turnbull, D. and Cohen, M. H., Free-volume model of the amorphous phase: glass transition, J. Chem. Phys., **34**, 120-125 (1961).

Turnbull, D. and Cohen, M. H., On the free-volume model of the liquid-glass transition, J. Chem. Phys., **52**, 3028-3041 (1970).

van Aken, B., de Hey, P. and Sietsma, J., Structural relaxation and plastic flow in amorphous $La_{50}Al_{25}Ni_{25}$, Mat. Sci. Eng. **A278** (1-2), 247-254 (2000).

Table 1. Thermodynamic and kinetic properties of Vitreloy 1

Critical cooling rate (K s^{-1})	1[a]
Onset glass transition temperature (K) at heating rate 20 K/min	625[b]
The onset of first crystallization temperature (K) at heating rate 20 K/min	705[b]
Supercooled liquid region (K) at heating rate 20 K/min	80[b]
The onset of second crystallization temperature (K) at heating rate 20 K/min	735[b]
Liquidus temperature (K)	993[b]
Viscosity at melting temperature (Pa s)	2-5[a]
Specific heat capacity (J/g-atom K) at room temperature	23[c]
Specific heat capacity (J/g-atom K) in the supercooled liquid region (J/g-atom K)	~30-50[c,d]
Linear thermal expansion coefficient (K^{-1}) (at 373 K-648 K)	10.1x10^{-6}[e]
Average volume thermal expansion coefficient (at 700 K-1300 K)	5.32x10^{-5}[f]
Average volume thermal expansion coefficient (at 400 K-550 K)	3.39x10^{-5}[f]
Average volume thermal expansion coefficient (at 400 K-850 K)	3.83x10^{-5}[f]
Emissivity (at 500 K-1100 K)	0.14-0.26[f]

[a]Busch *et al.*, 1995a; [b]Peker and Johnson, 1993; [c]Fecht *et al.*, 1995; [d]Busch *et al.*, 1995b; [e]Peker (unpublished); [f]Ohsaka *et al.*, 1997.

Table 2. Mechanical properties of Vitreloy 1 at room temperature

Density (g/cm^3)	6.0
Young's modulus (GPa)	96
Shear modulus (GPa)	34
Poisson's ratio	0.36
Elastic strain limit	0.02
Tensile yield strength (GPa)	1.90
Vikers hardness (kg/mm^2)	534[a]
Plane strain fracture toughness (MPa m$^{1/2}$) at loading rate of 10^{-2} MPa m$^{1/2}$s^{-1}	~55[a]
Dynamic fracture toughness (MPa m$^{1/2}$) at loading rate of 10^4 MPa m$^{1/2}$s^{-1}	~50-70[b]
Dynamic fracture toughness (MPa m$^{1/2}$) at loading rate of 10^7 MPa m$^{1/2}$s^{-1}	~150-300[b]

[a]Conner, 1998; [b]Owen *et al.*, 1998.

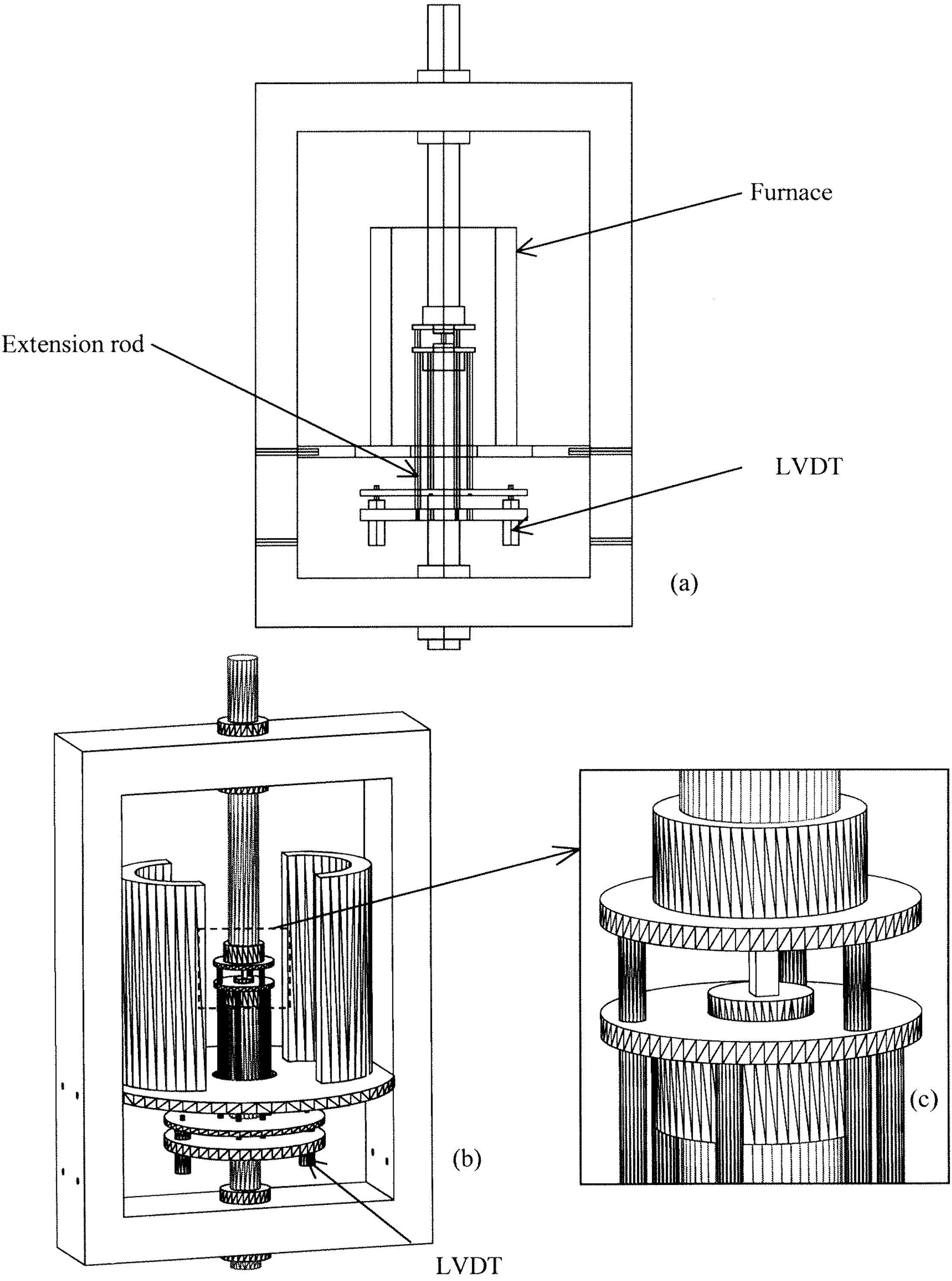

Figure 1. High precision quasi-static uniaxial compression fixture: (a) section view, (b) 3-D view, (c) enlarged view of the specimen loading section, and (d) the overall layout of the quasi-static testing system.

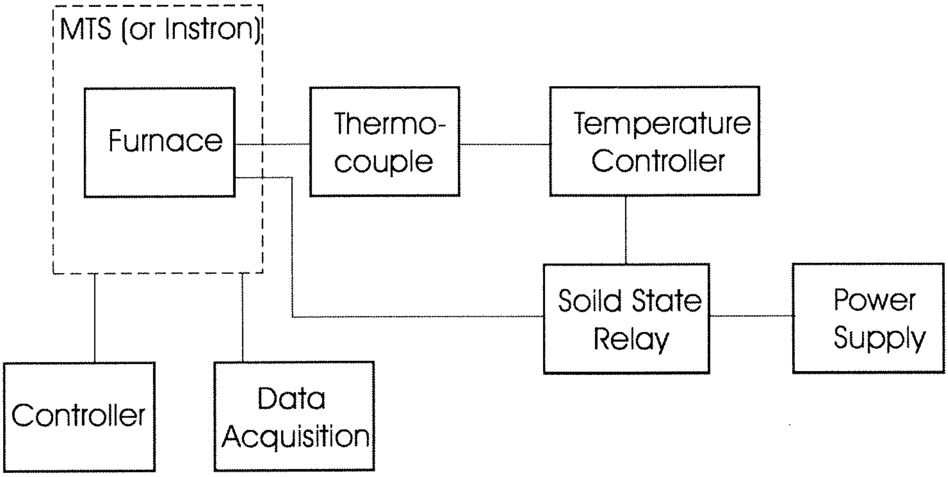

Figure 1. (d) (continued)

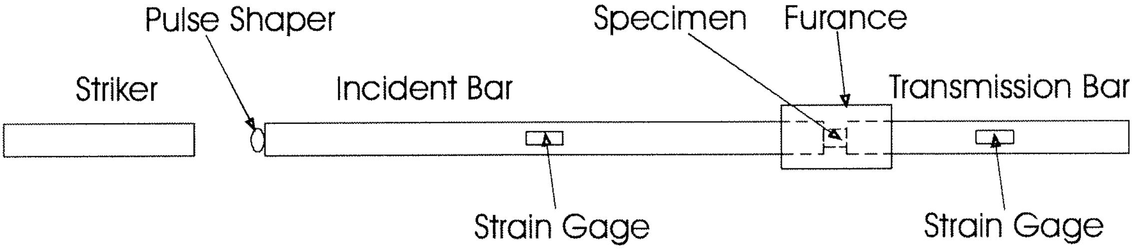

Figure 2. Schematic of a modified Kolsky (split Hokinson) pressure bar.

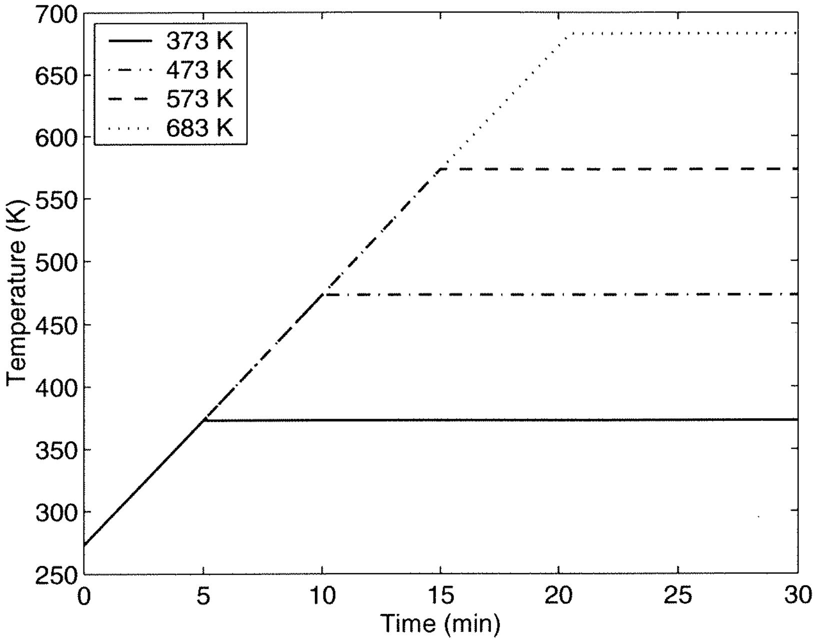

Figure 3. Specimen heating profile. Specimens were heated at a fixed heating rate of 20 K/min until a desired temperature was reached. The temperature remained unchanged during the course of compression loading.

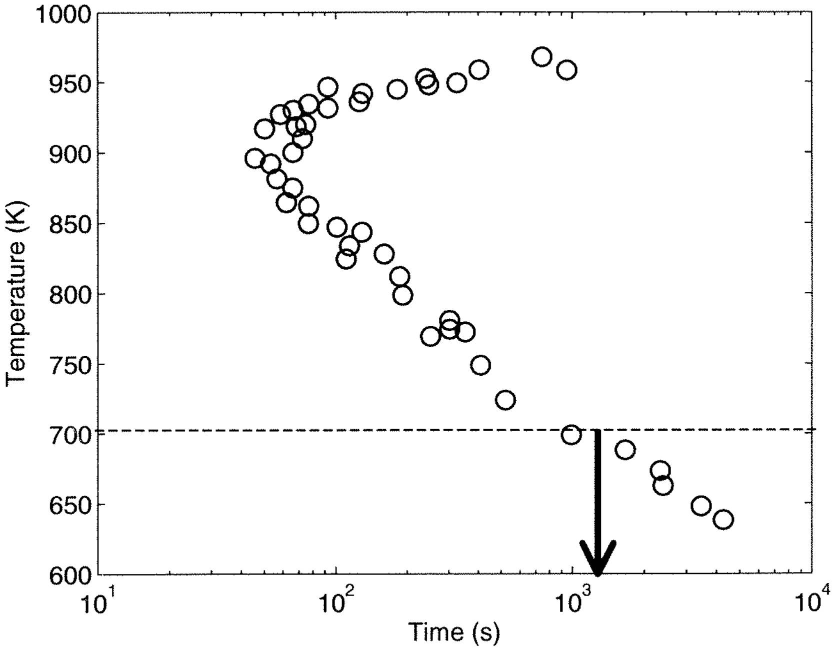

Figure 4. Time-temperature-transformation (TTT) diagram for the primary crystallization of Vitreloy 1. Reproduced from data by Kim *et al.* (1994). There exists a large time window at relatively low temperature (<700 K) for deformation without recrystallization.

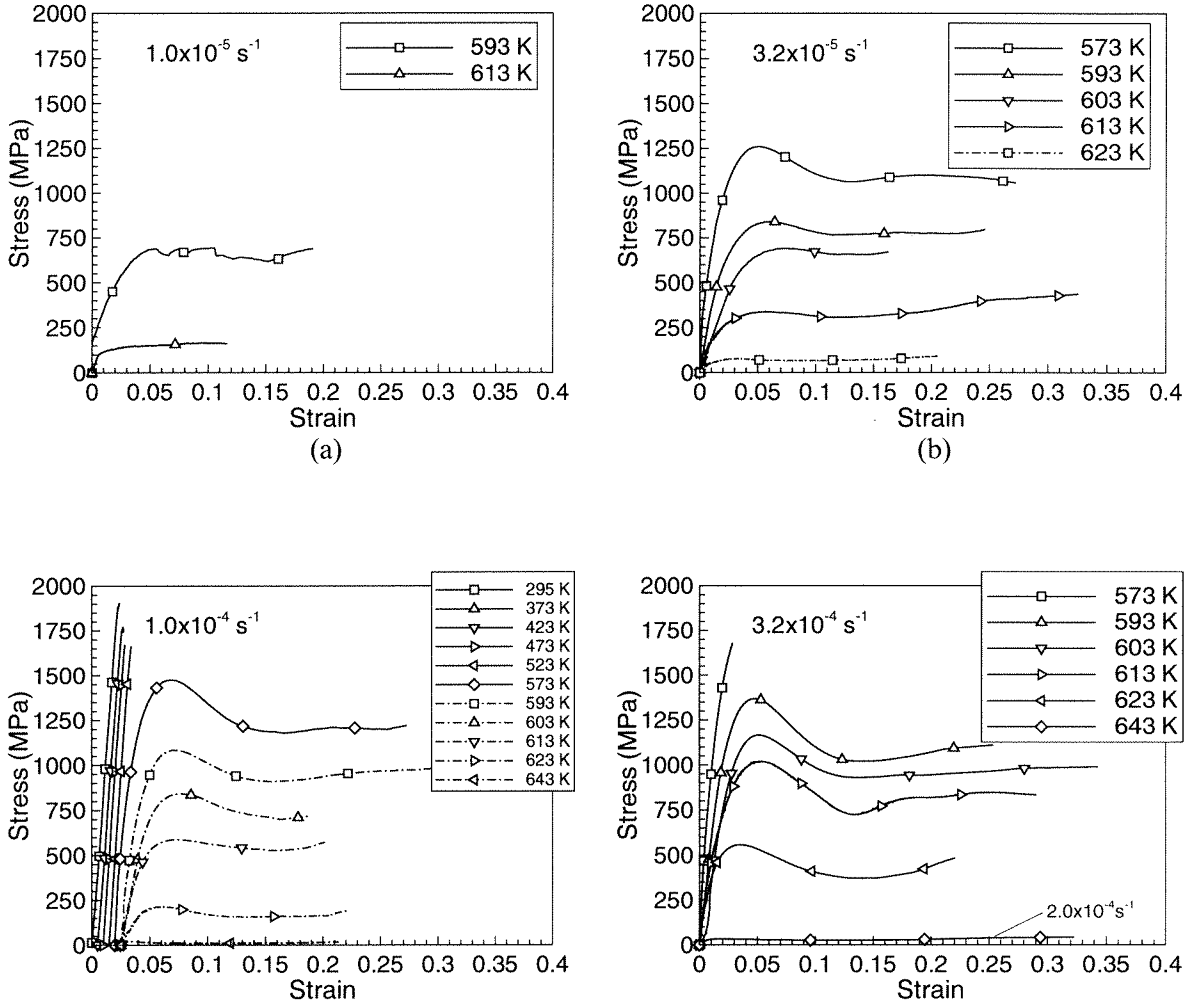

(a) (b)

(c) (d)

Figure 5. Uniaxial stress-strain curves for Vitreloy 1 at various temperatures and strain rates: (a) temperature, T=593 K and 613 K at strain rate $\dot{\varepsilon} = 1.0\times10^{-5}$ s^{-1}; (b) temperature, T=573 K, 593 K, 603 K, 613 K and 623 K at strain rate $\dot{\varepsilon} = 3.2\times10^{-5}$ s^{-1}; (c) temperature, T=295 K, 373 K, 423 K, 473 K, 523 K, 573 K, 593 K, 603 K, 613 K, 623 K and 643 K at strain rate $\dot{\varepsilon} = 1.0\times10^{-4}$ s^{-1}; (d) temperature, T=573 K, 593 K, 603 K, 613 K, 623 K and 643 K at strain rate $\dot{\varepsilon} = 3.2\times10^{-4}$ s^{-1}.

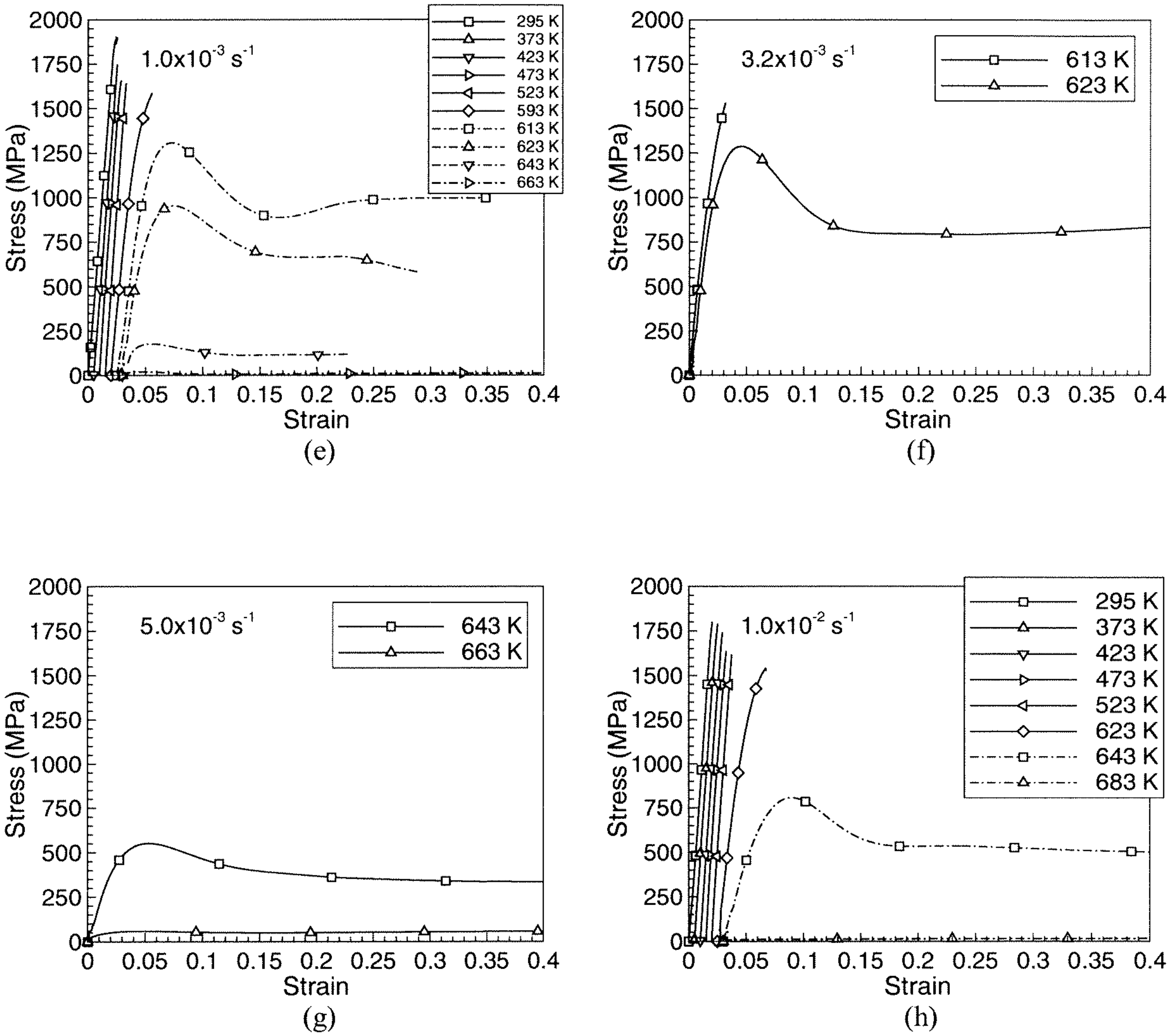

(e) (f)

(g) (h)

Figure 5 (continued). (e) temperature, T=295 K, 373 K, 423 K, 473 K, 523 K, 593 K, 613 K, 623 K, 643 K and 663 K at strain rate $\dot{\varepsilon} = 1.0\times10^{-3}\ \mathrm{s}^{-1}$; (f) temperature, T=613 K and 623 K at strain rate $\dot{\varepsilon} = 3.2\times10^{-3}\ \mathrm{s}^{-1}$; (g) temperature, T=643 K and 663 K at strain rate $\dot{\varepsilon} = 5.0\times10^{-3}\ \mathrm{s}^{-1}$; (h) temperature, T=295 K, 373 K, 423 K, 473 K, 523 K, 623 K, 643 K and 683 K at strain rate $\dot{\varepsilon} = 1.0\times10^{-2}\ \mathrm{s}^{-1}$.

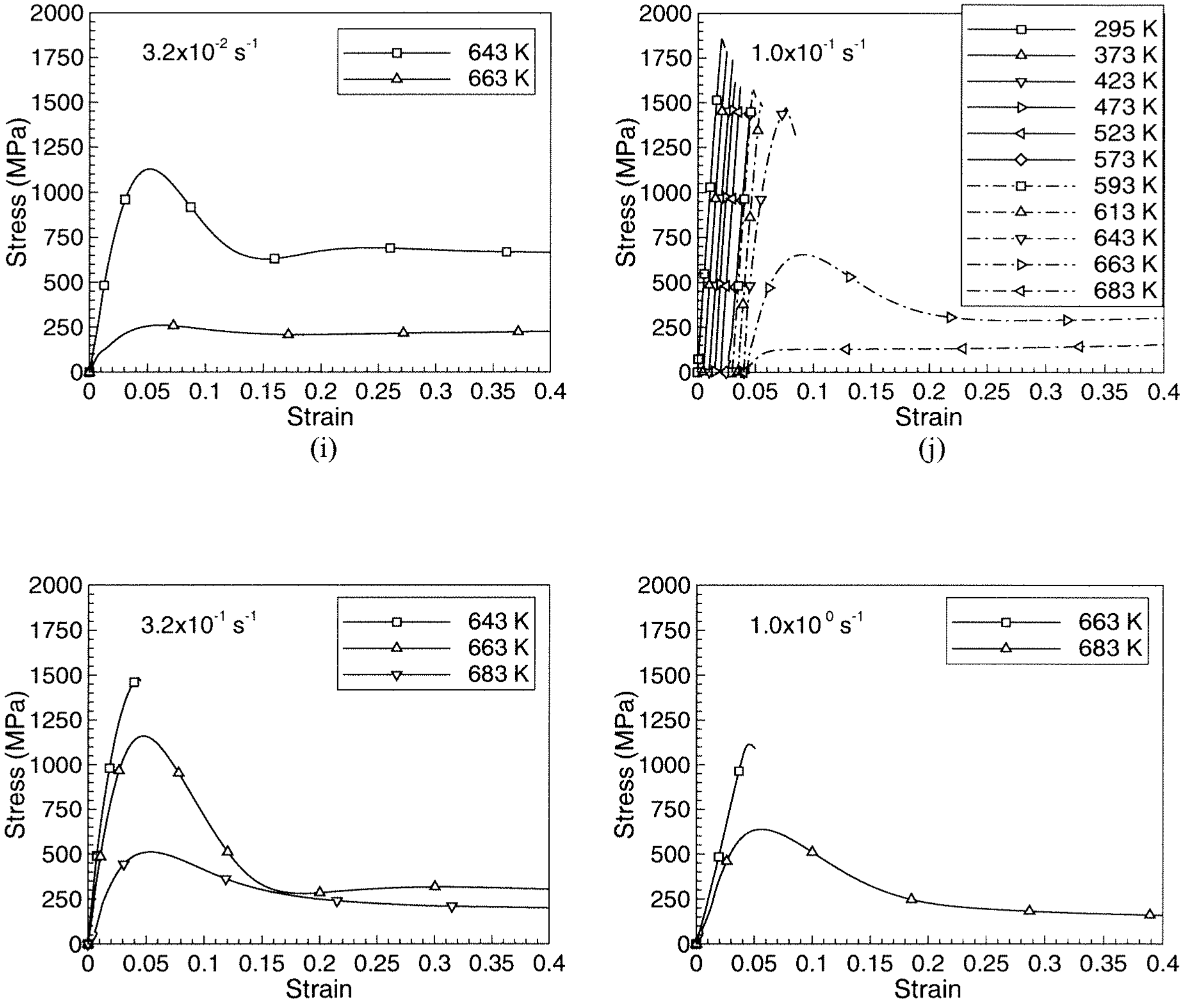

(i) (j) (k) (l)

Figure 5 (continued). (i) temperature, T=643 K and 663 K at strain rate $\dot{\varepsilon} = 3.2\times10^{-2}$ s^{-1}; (j) temperature, T=295 K, 373 K, 423K, 473 K, 523 K, 573 K, 593 K, 613 K, 643 K, 663 K and 683 K at strain rate $\dot{\varepsilon} = 1.0\times10^{-1}$ s^{-1}; (k) temperature, T=643 K, 663 K and 683 K at strain rate $\dot{\varepsilon} = 3.2\times10^{-1}$ s^{-1}; (l) temperature, T=663 K and 683 K at strain rate $\dot{\varepsilon} = 1.0\times10^{-0}$ s^{-1}.

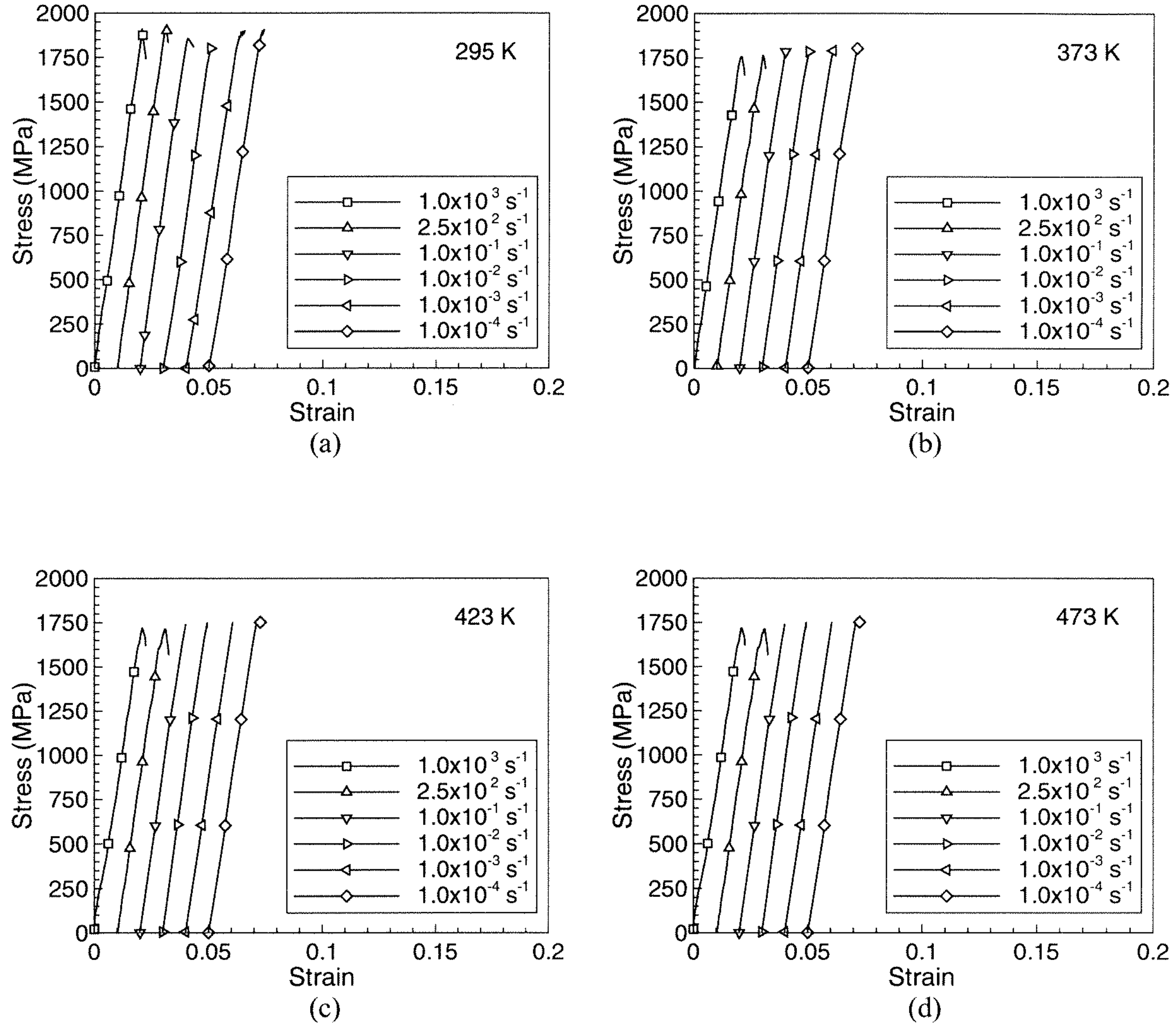

(a) (b)

(c) (d)

Figure 6. Effect of strain rate on the unixial stress-strain behavior of Vitreloy 1, at (a) temperature, T= 295 K; (b) temperature, T=373K; (c) temperature, T= 423 K; (d) temperature, T=473 K. Data for six different strain rates are included for all the cases ($\dot{\varepsilon} = 1.0\times10^{-4}$ s^{-1}, 1.0×10^{-3} s^{-1}, 1.0×10^{-2} s^{-1}, 1.0×10^{-1} s^{-1}, 2.5×10^{2} s^{-1} and 1.0×10^{3} s^{-1}).

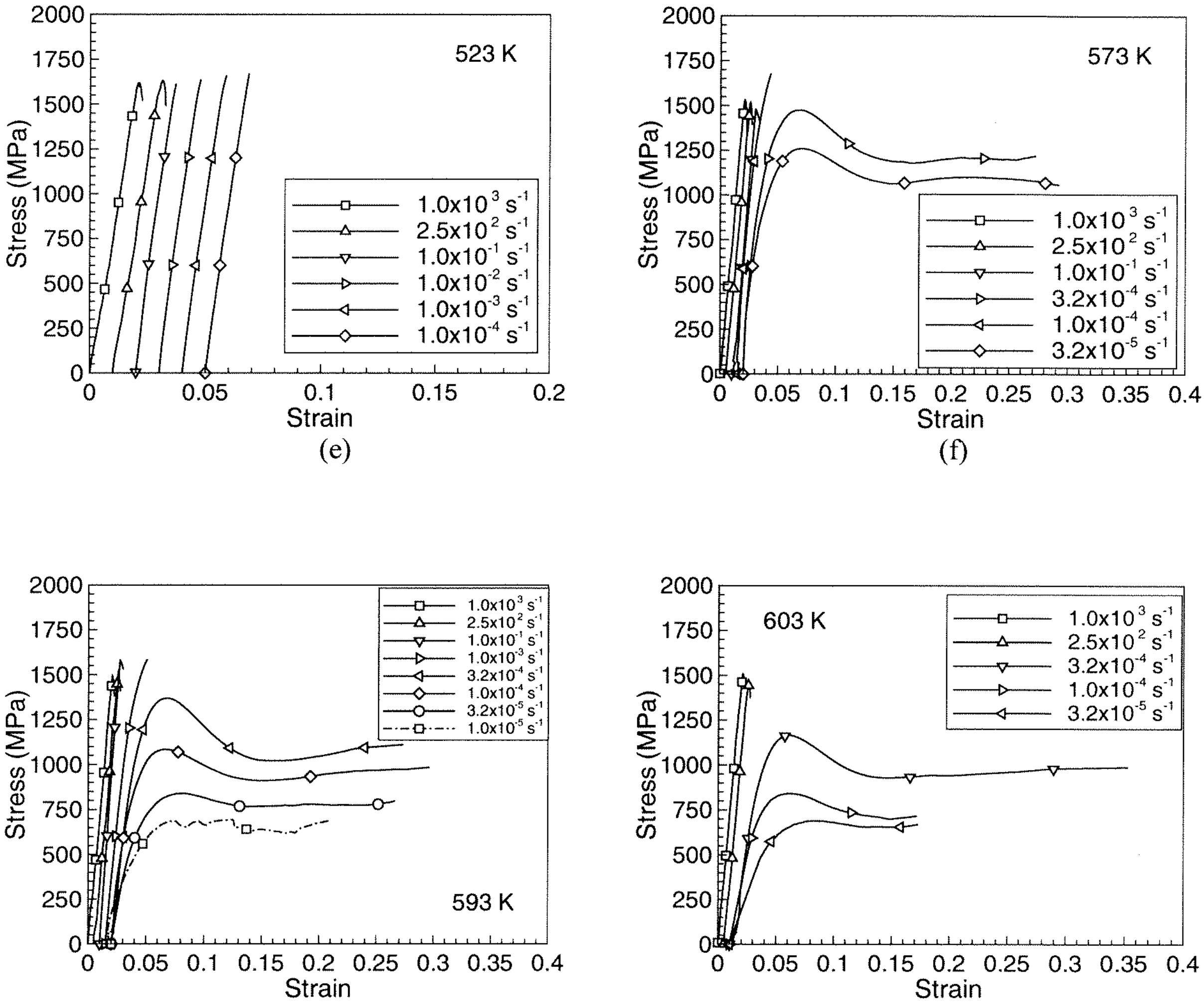

(e) (f)

(g) (h)

Figure 6 (continued). (e) temperature, T= 523 K; (f) temperature, T= 573 K; (g) temperature, T=593 K; (h) temperature, T=603 K.

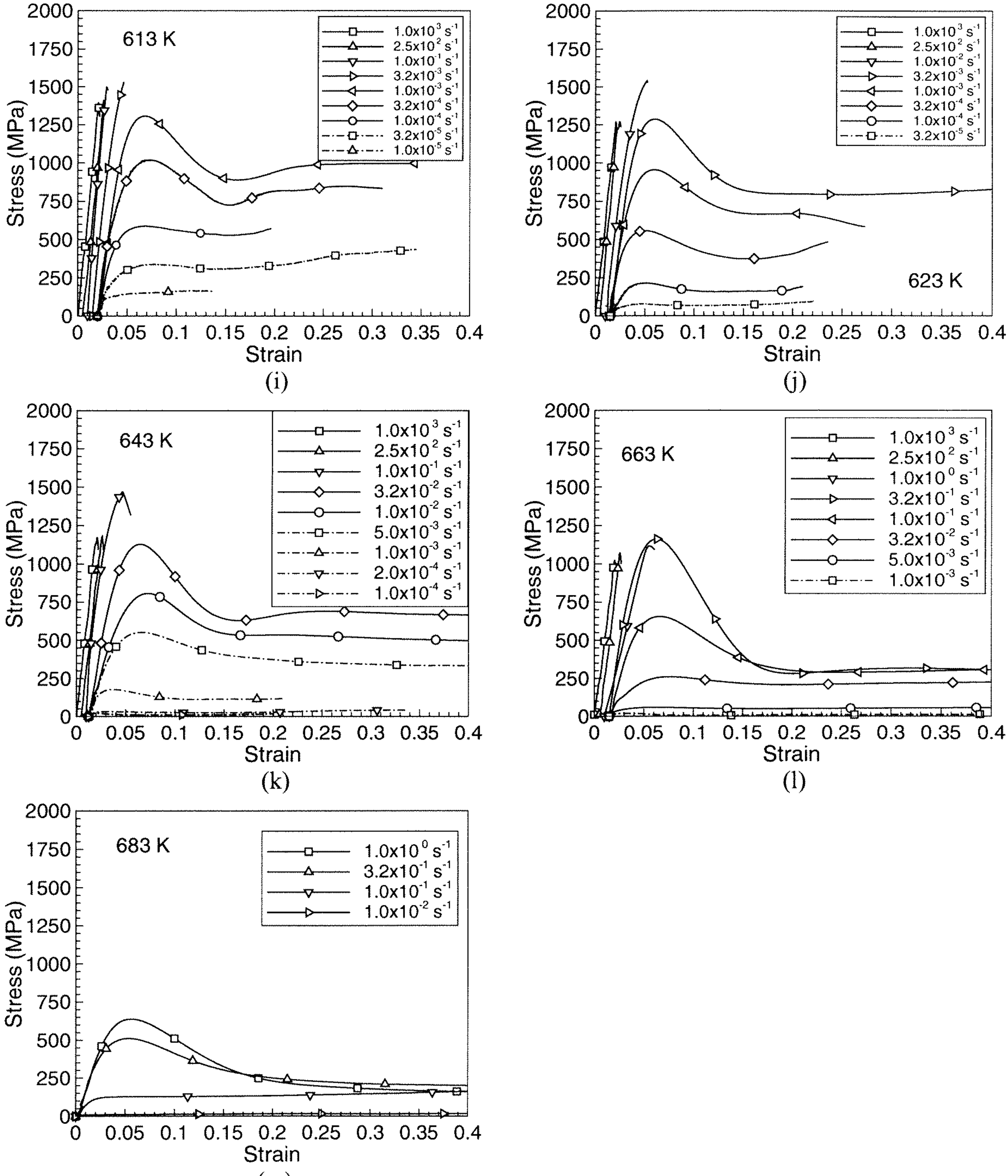

(i) (j) (k) (l) (m)

Figure 6 (continued). (i) temperature, T= 613 K; (j) temperature, T= 623K; (k) temperature, T= 643 K; (h) temperature, T= 663 K.

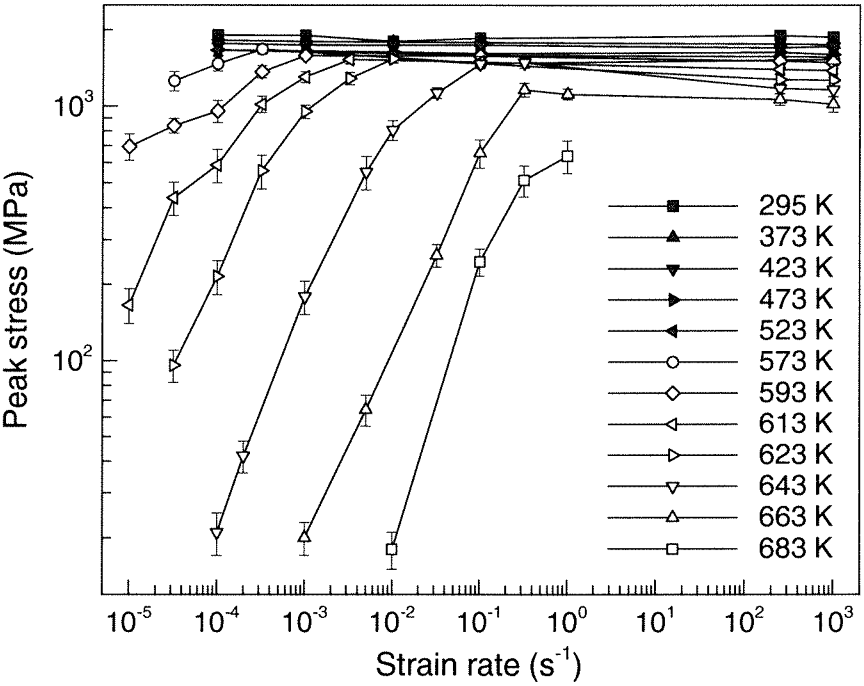

Figure 7. Plot of the peak stress as a function of strain rate at various temperatures.

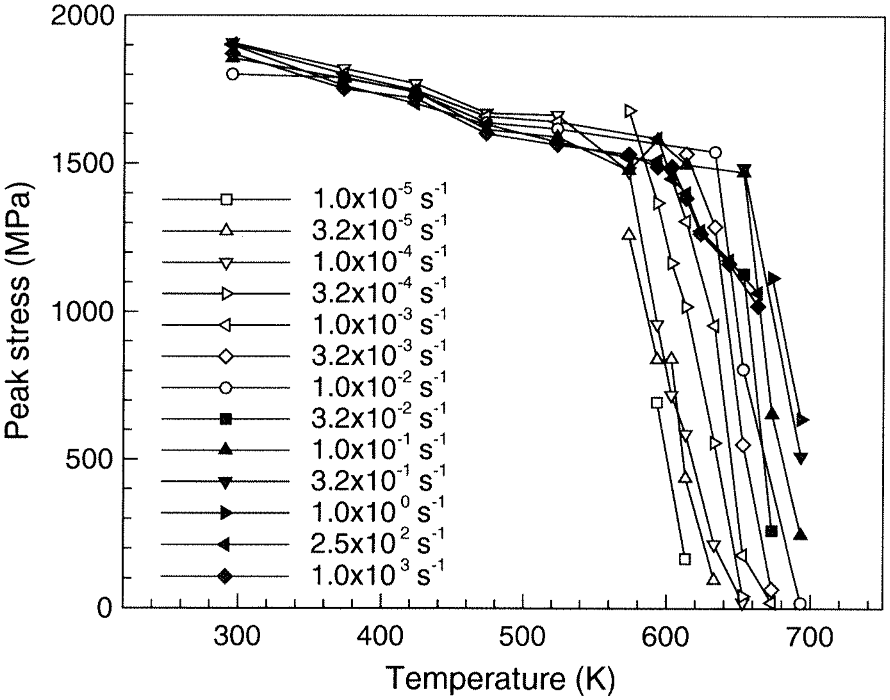

Figure 8. Plot of the peak stress as a function of temperature at various strain rates.

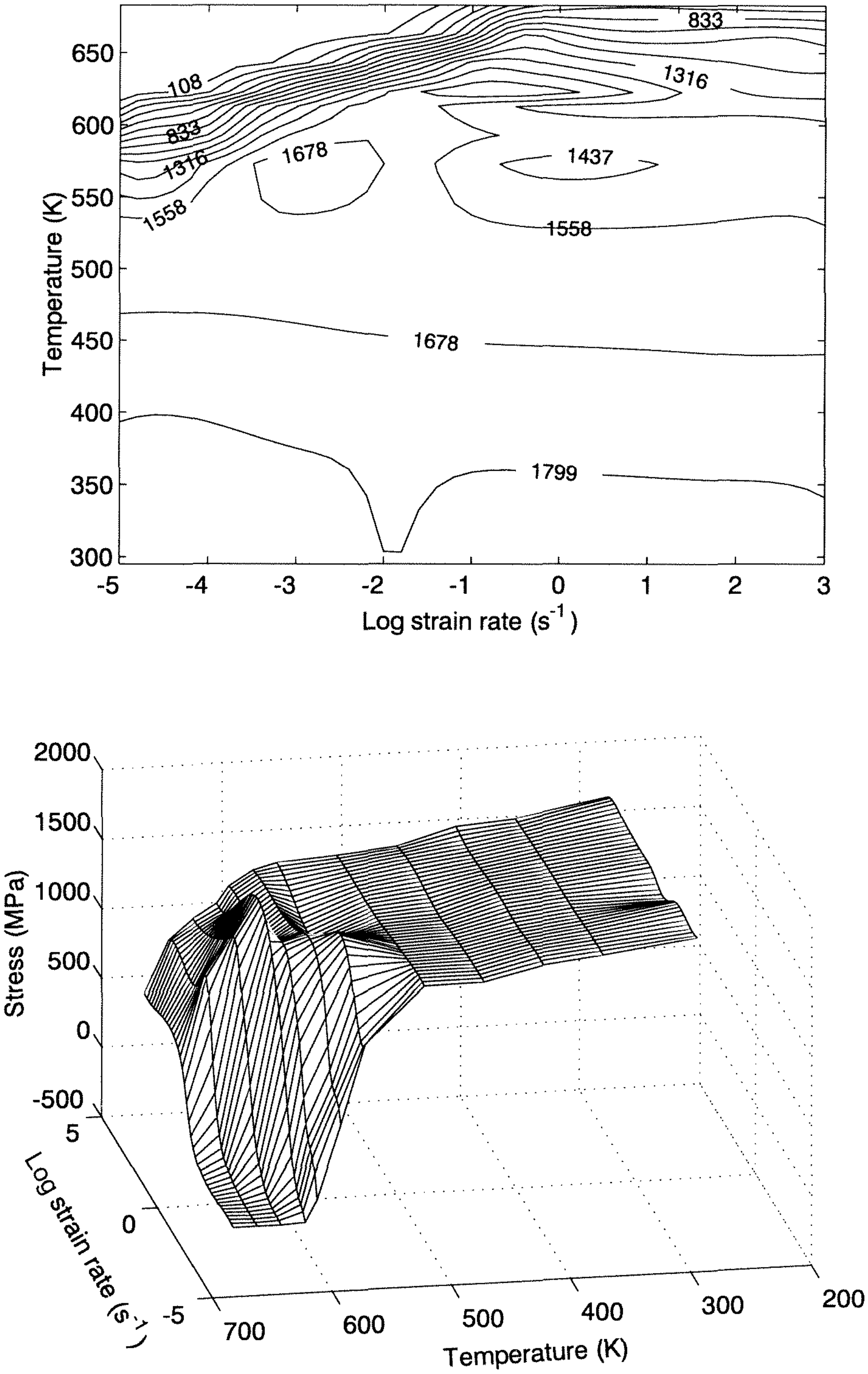

Figure 9. Plot of the contours and 3-D view of the peak stress as a function of strain rate and temperature. Value of the contours are in MPa.

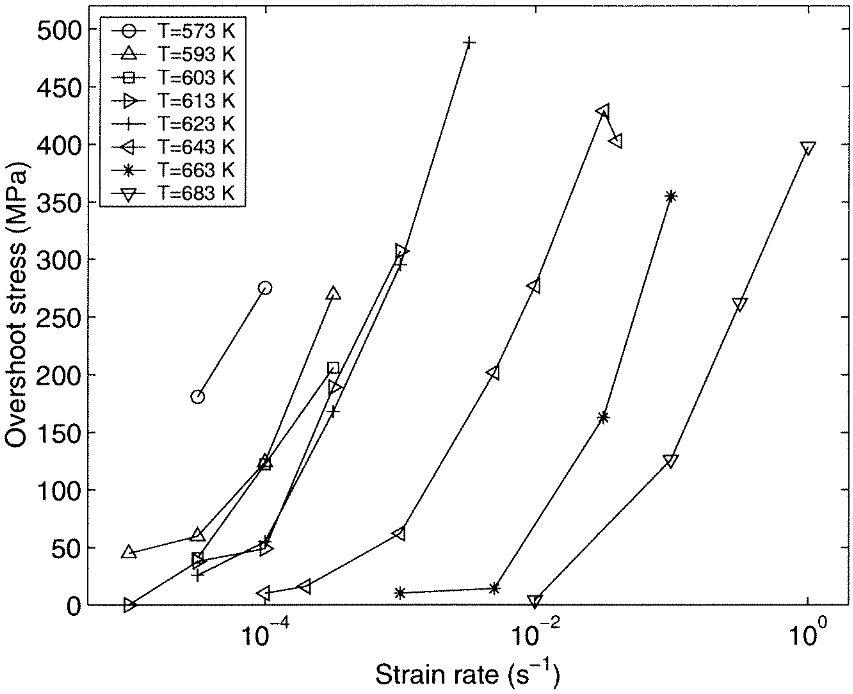

Figure 10. Overshoot stress as a function of strain rate at various ambient temperatures.

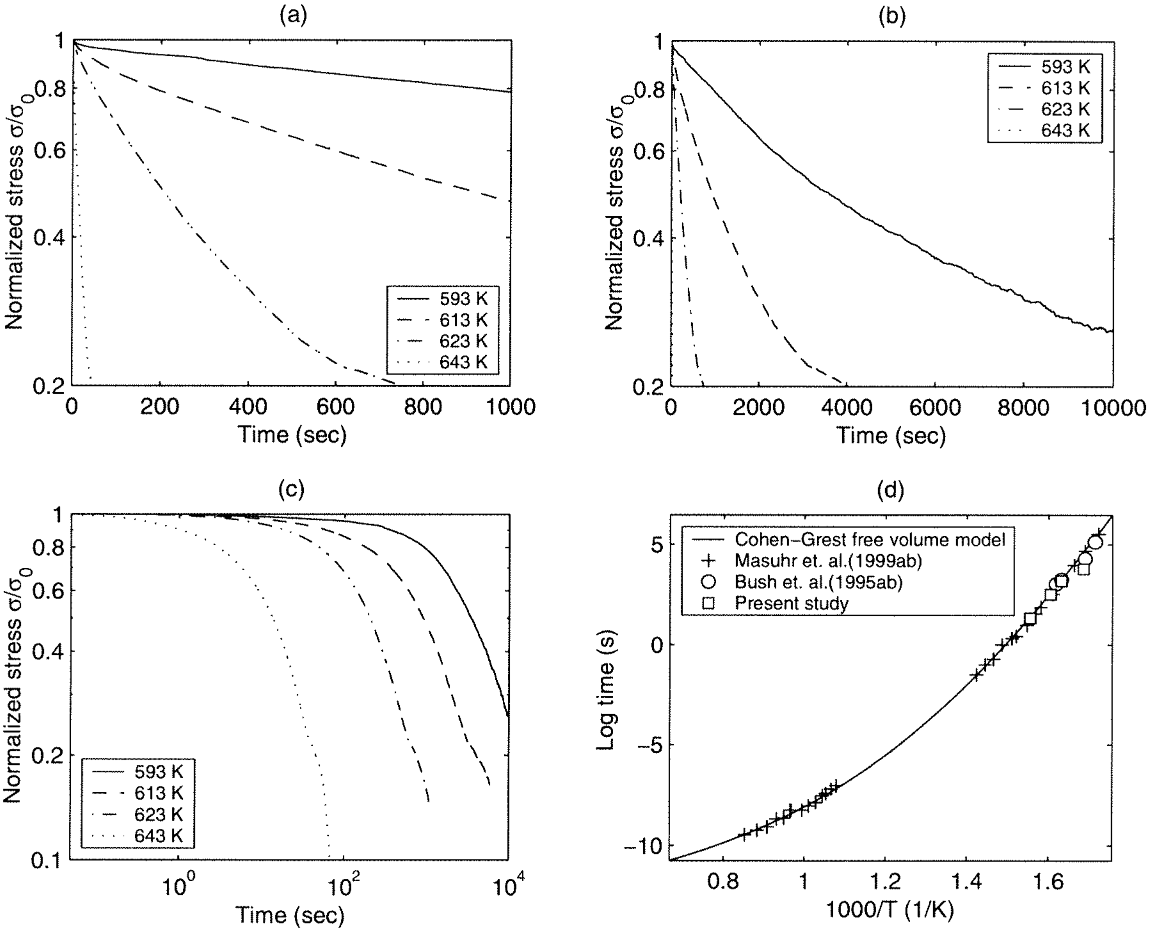

Figure 11. (a,b,c) Plot of the normalized stress as a function of time at various ambient temperatures; (d) plot of relaxation time as a function of reciprocal temperature.

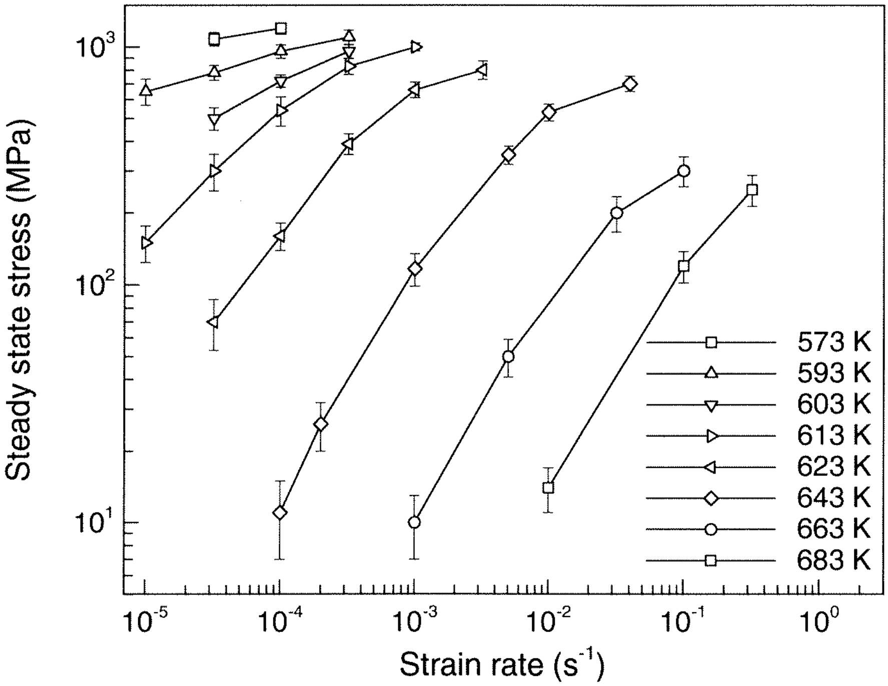

Figure 12. Steady state stress as a function of strain rate at temperatures T=573 K, 593 K, 603 K, 613 K, 623 K, 643 K, 663 K and 683 K.

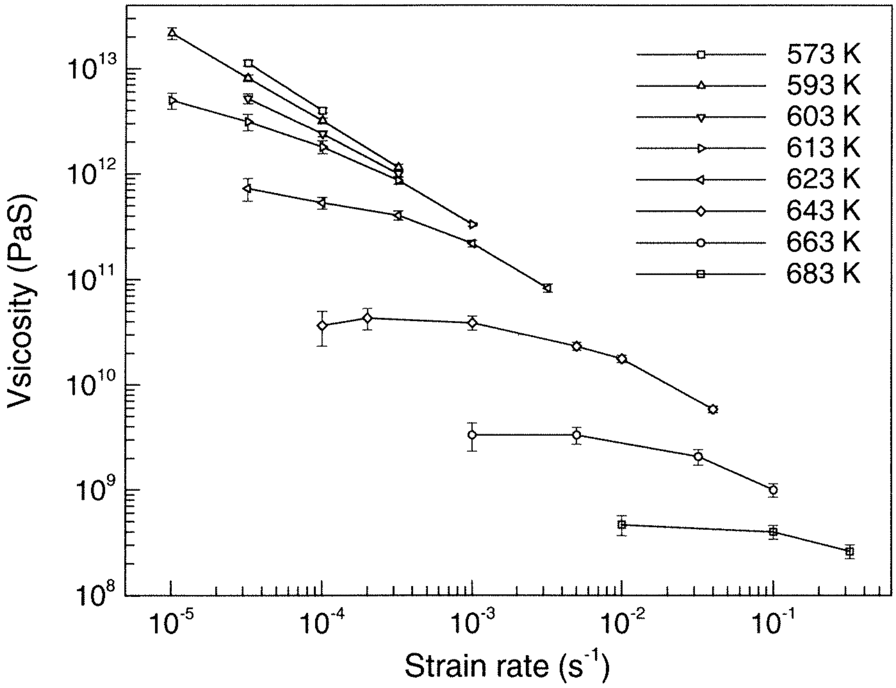

Figure 13. Viscosity as a function of strain rate at temperatures T= 573 K, 593 K, 603 K, 613 K, 623 K, 643 K, 663 K and 683 K.

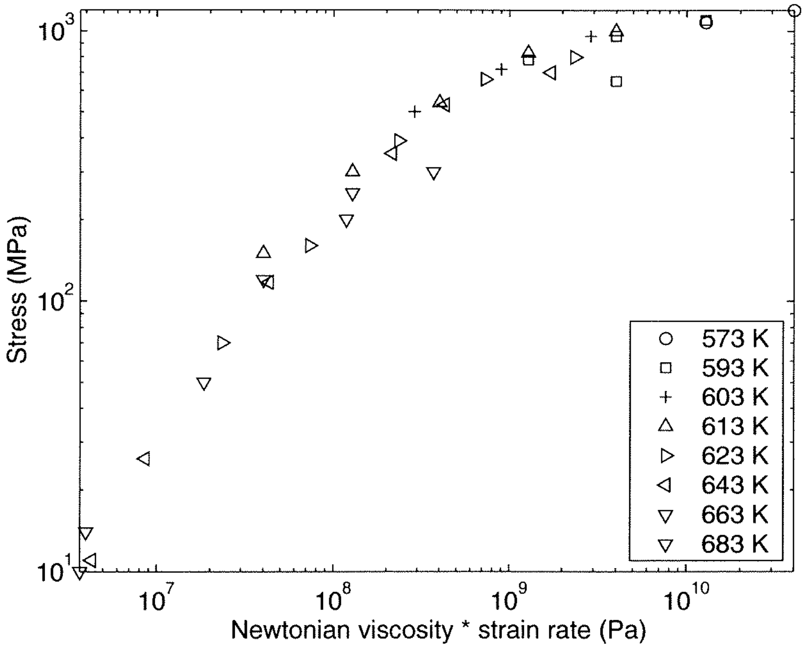

Figure 14(a). Normalized steady state stress as a function of strain rate at temperatures T= 573 K, 593 K, 603 K, 613 K, 623 K, 643 K, 663 K and 683 K.

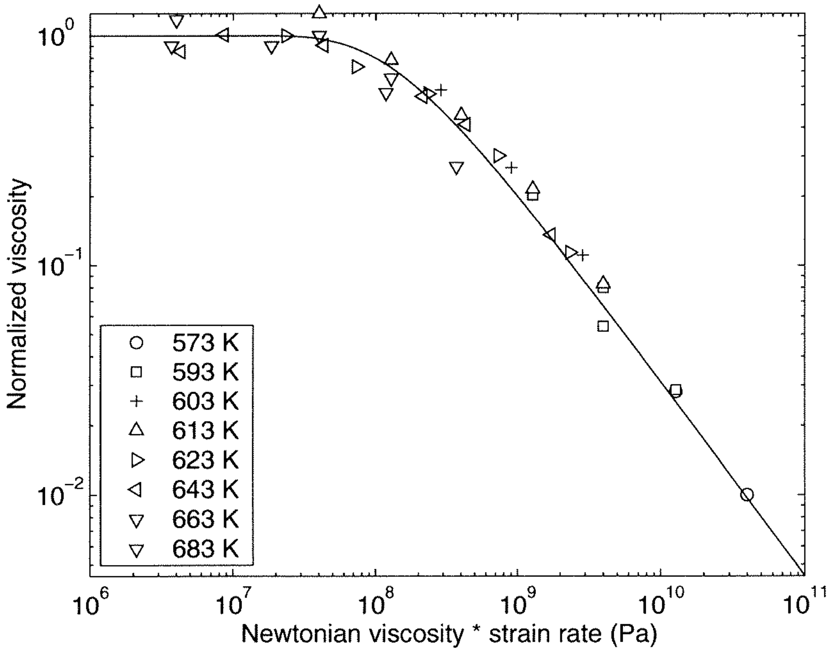

Figure 14(b). Normalized viscosity as a function of strain rate at temperatures T= 573 K, 593 K, 603 K, 613 K, 623 K, 643 K, 663 K and 683 K.

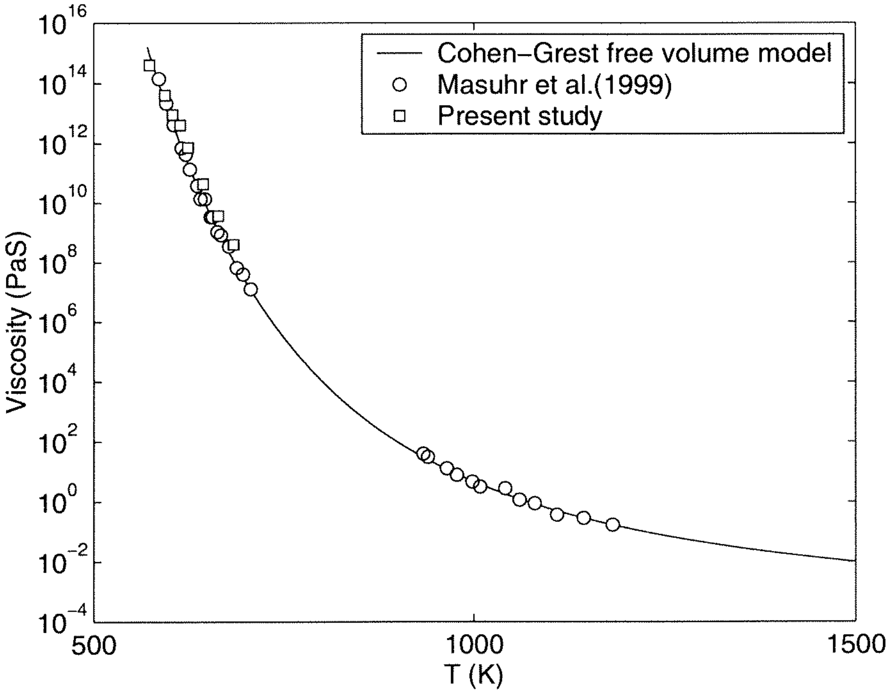

Figure 15. Equilibrium (Newtonian) viscosity as a function of temperature.

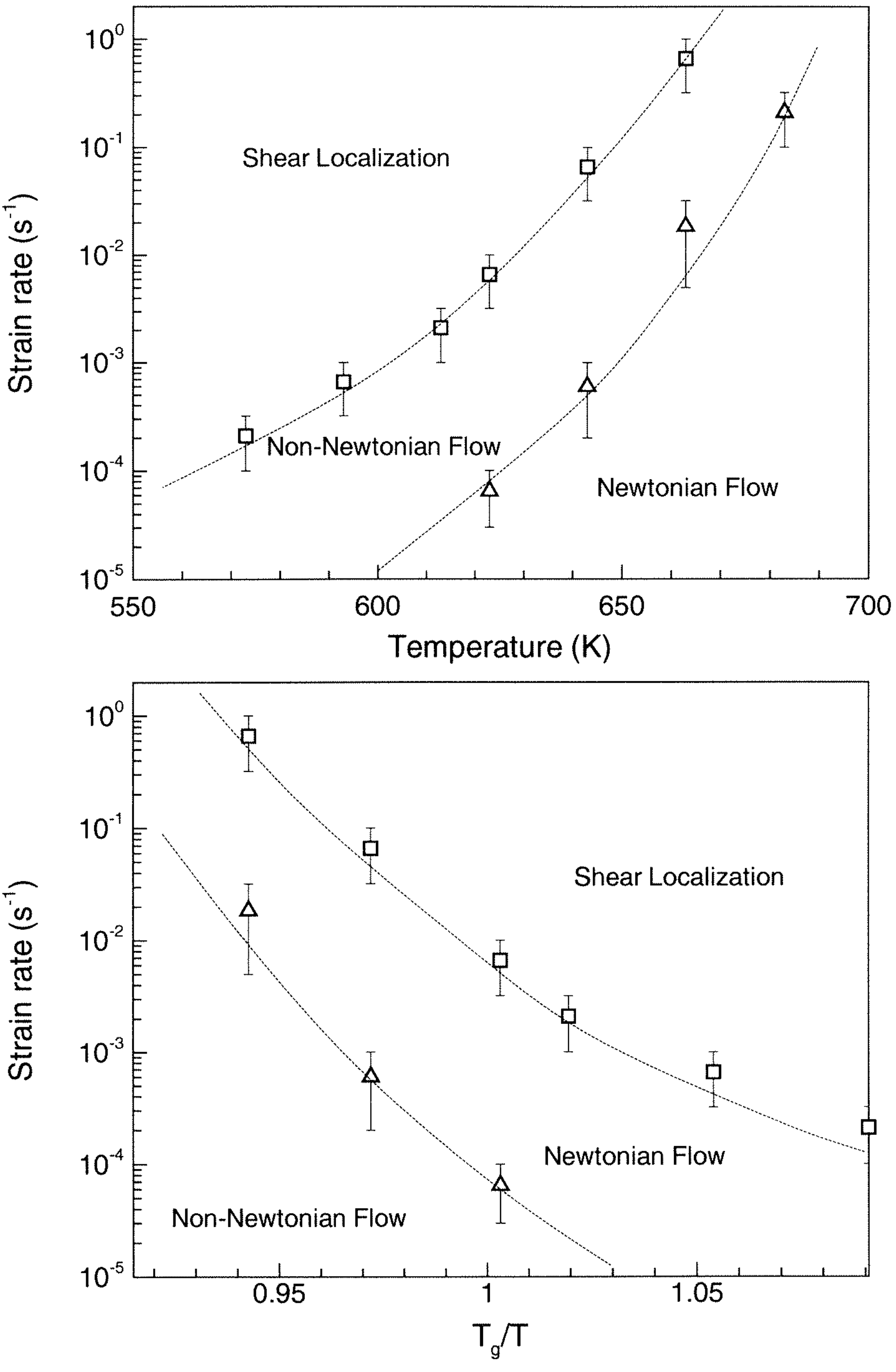

Figure 16. The boundaries between the three distinct modes of deformation for Vitreloy 1 as determined by the current investigation. Two boundaries are shown in each figure, one for transition from homogeneous deformation to inhomogeneous deformation, the other for transition from Newtonian to non-Newtonian flow. T and T_g are the ambient and glass transition temperature, respectively.

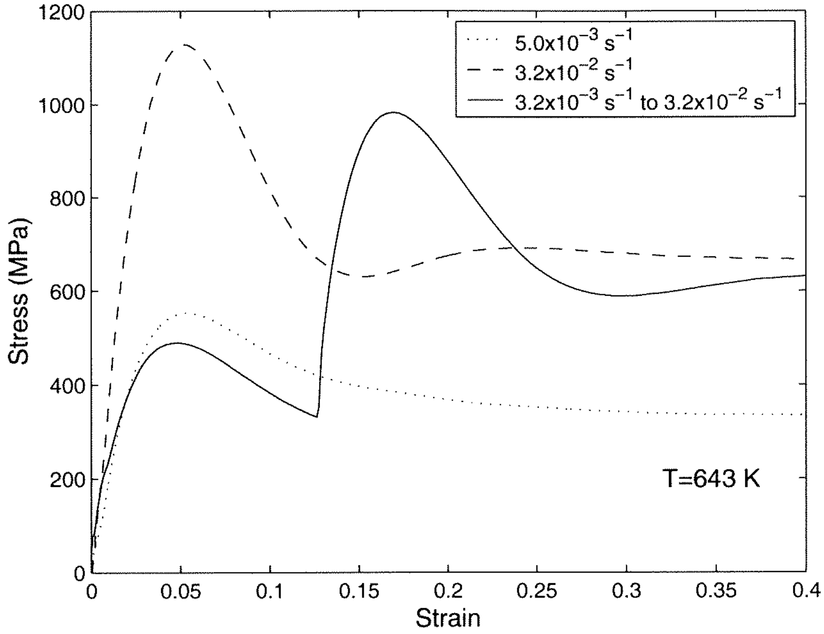

Figure 17(a). Effect of jump-in-strain-rate at 643 K from 3.2×10^{-3} s^{-1} to 3.2×10^{-2} s^{-1}. The strain at which the jump took place is 0.126.

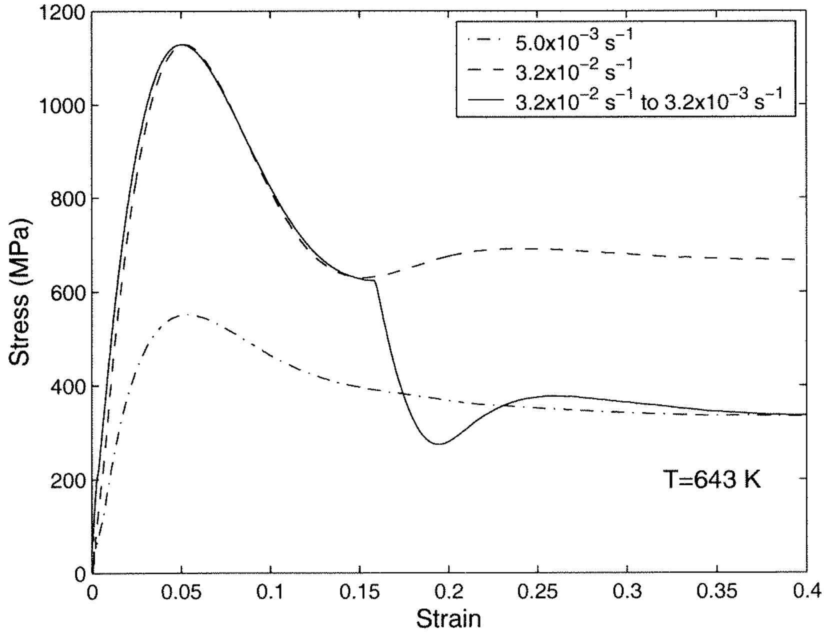

Figure 17(b). Effect of jump-in-strain-rate at 643 K from 3.2×10^{-2} s^{-1} to 3.2×10^{-3} s^{-1}. The strain at which the jump took place is 0.159.

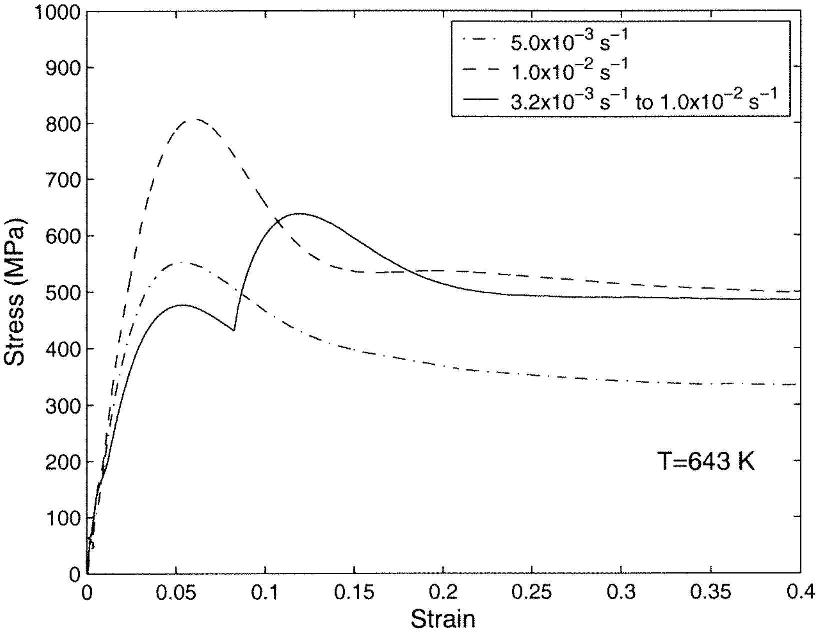

Figure 17(c). Effect of jump-in-strain-rate at 643 K from 3.2×10^{-3} s^{-1} to 1.0×10^{-2} s^{-1}. The strain at which the jump took place is 0.083.

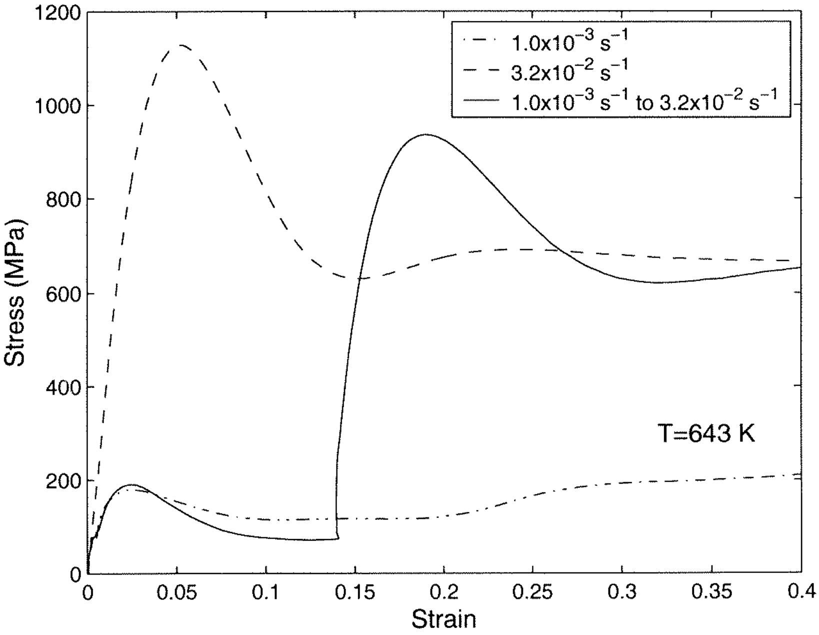

Figure 17(d). Effect of jump-in-strain-rate at 643 K from 1.0×10^{-3} s^{-1} to 3.2×10^{-2} s^{-1}. The strain at which the jump took place is 0.140.

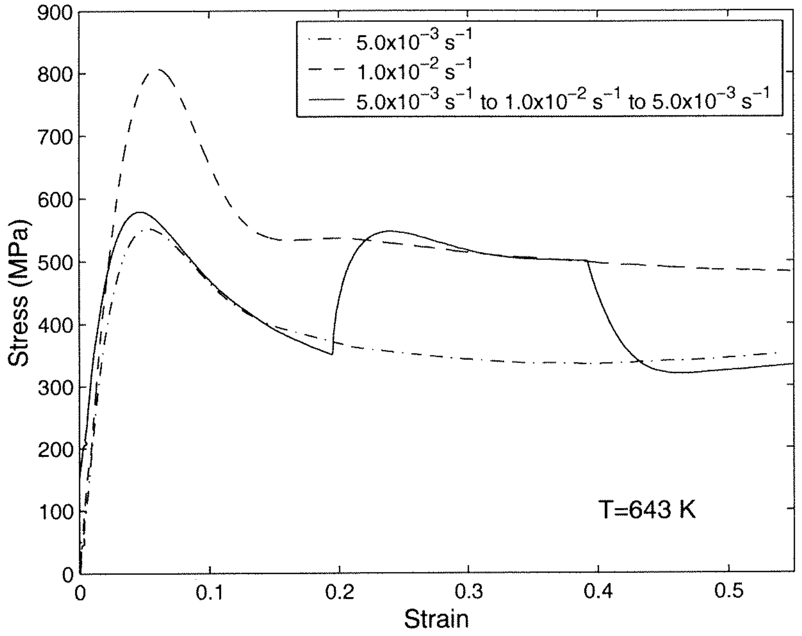

Figure 17(e). Effect of jump-in-strain-rate at 643 K from 5.0×10^{-3} s^{-1} to 1.0×10^{-2} s^{-1} and back to 5.0×10^{-3} s^{-1}. The strains at which the jumps took place are 0.194 and 0.392.

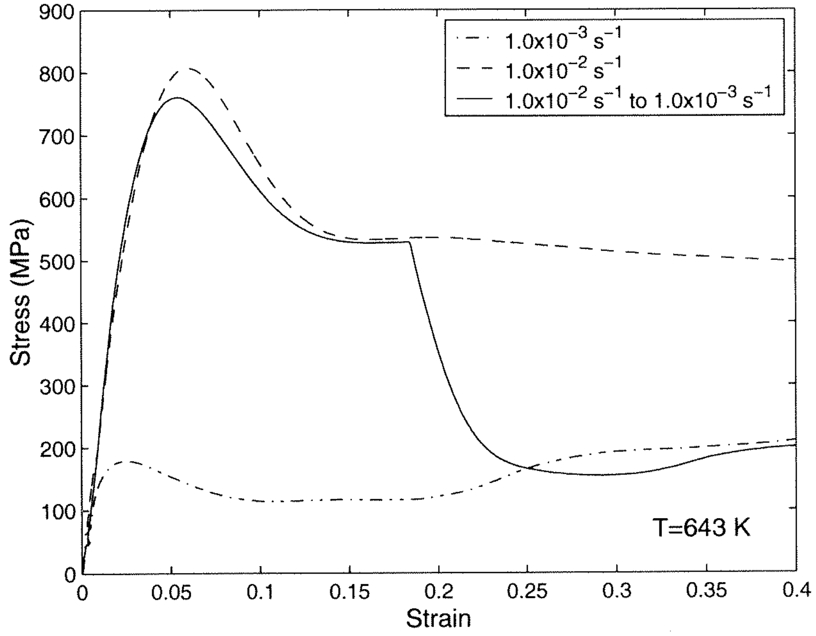

Figure 17(f). Effect of jump-in-strain-rate at 643 K from 1.0×10^{-2} s^{-1} to 1.0×10^{-3} s^{-1}. The strain at which the jump took place is 0.184.

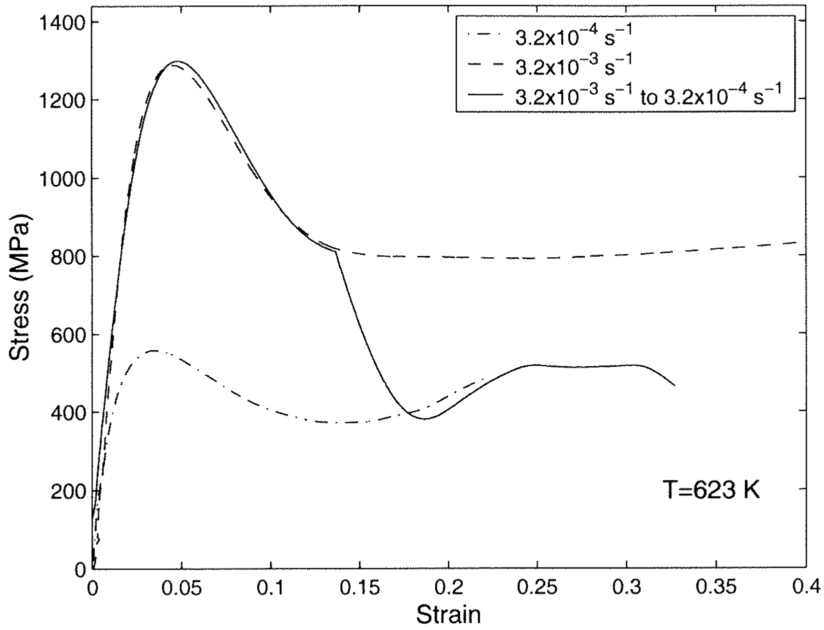

Figure 18. Effect of jump-in-strain-rate at 623 K from 3.2×10^{-3} s^{-1} to 3.2×10^{-4} s^{-1}. The strain at which the jump took place is 0.135.

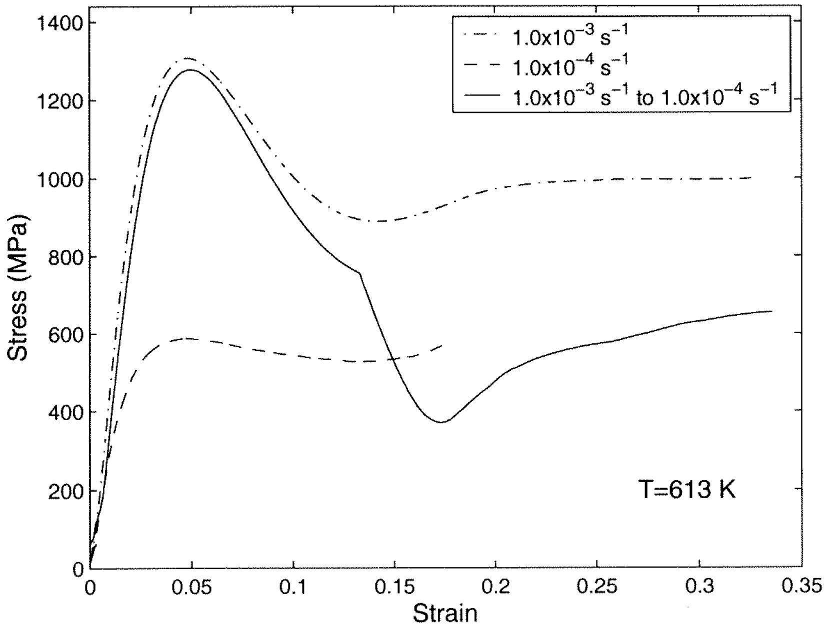

Figure 19. Effect of jump-in-strain-rate at 613 K from 1.0×10^{-3} s^{-1} to 1.0×10^{-4} s^{-1}. The strain at which the jump took place is 0.133.

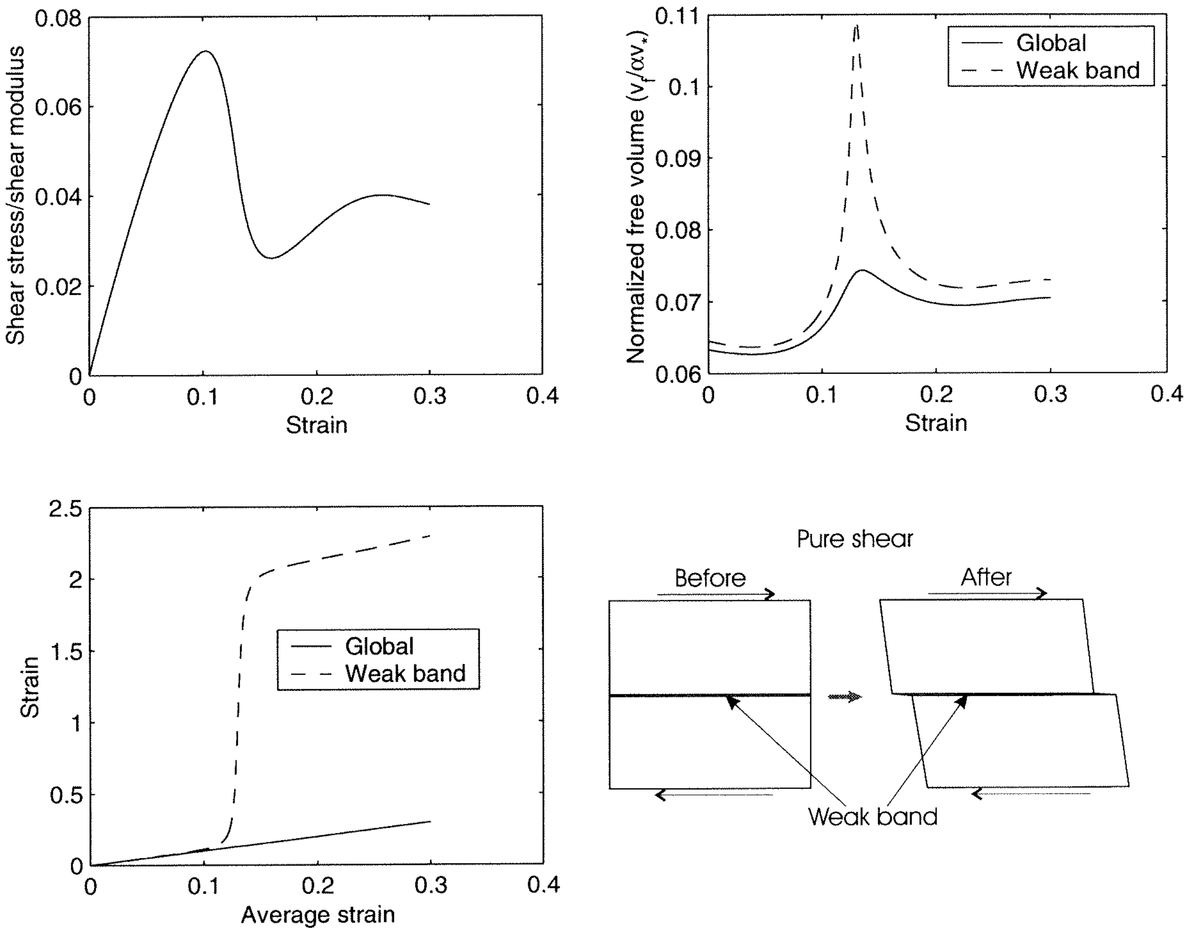

Figure 20. Conceptual example of shear band localization due to a perturbation of free volume by 1.5% inside the band. The thickness of the band is assumed to be 0.1% of the specimen thickness.

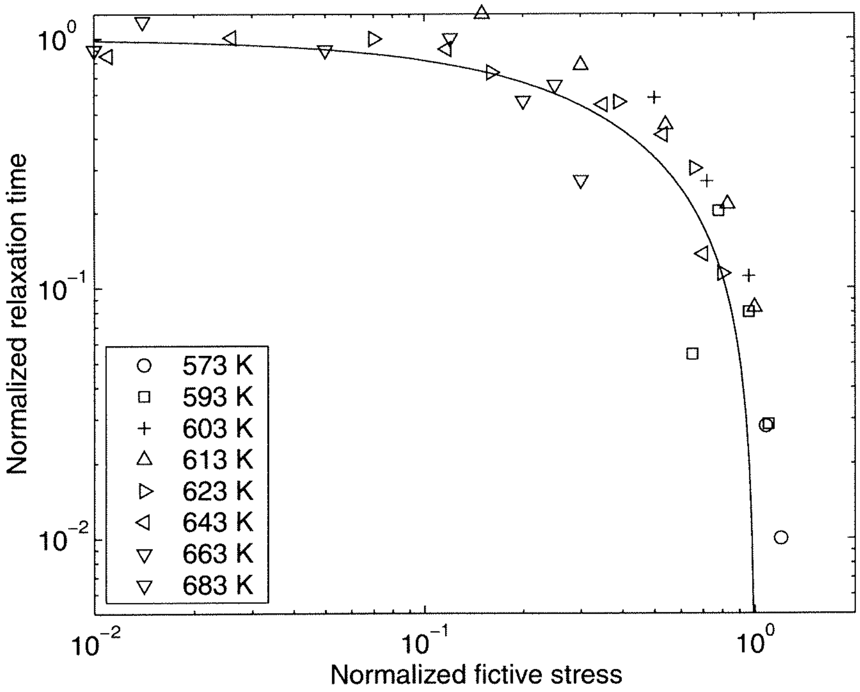

Figure 21. Normalized relaxation time λ / λ_N (or η / η_N) as a function of normalized fictive stress σ_{flow} / σ^*.

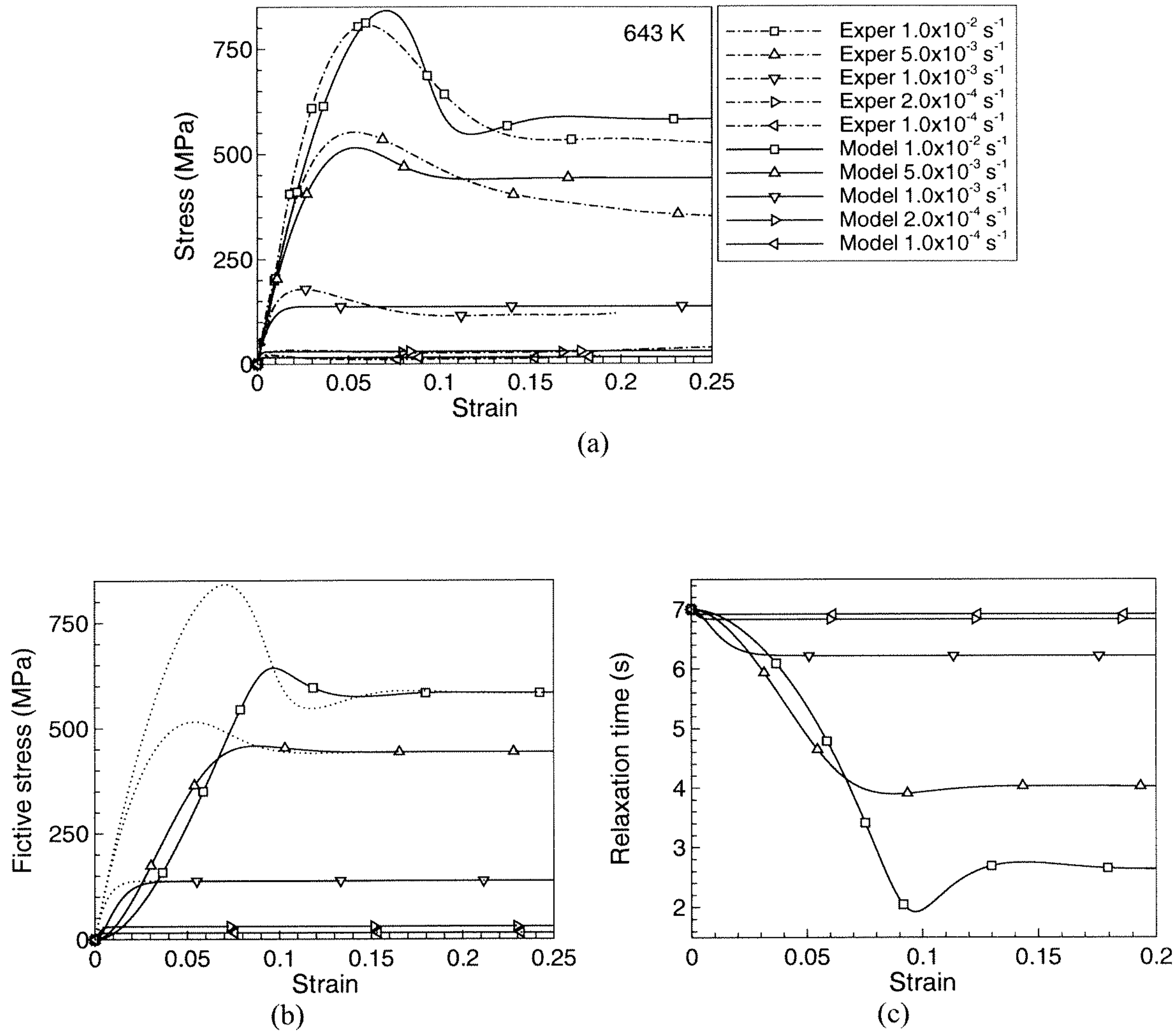

(a)

(b)

(c)

Figure 22. Model predictions at T=643 K based on the fictive stress model, E=22 GPa, σ^*=650 MPa, λ_N=7 s: (a) stress-strain curves with dashed lines correspond to the experimental data and the ones with solid lines correspond to the model prediction; (b) fictive stress (solid line) and stress (dotted line) as a function of strain; and (c) relaxation time as a function of strain.

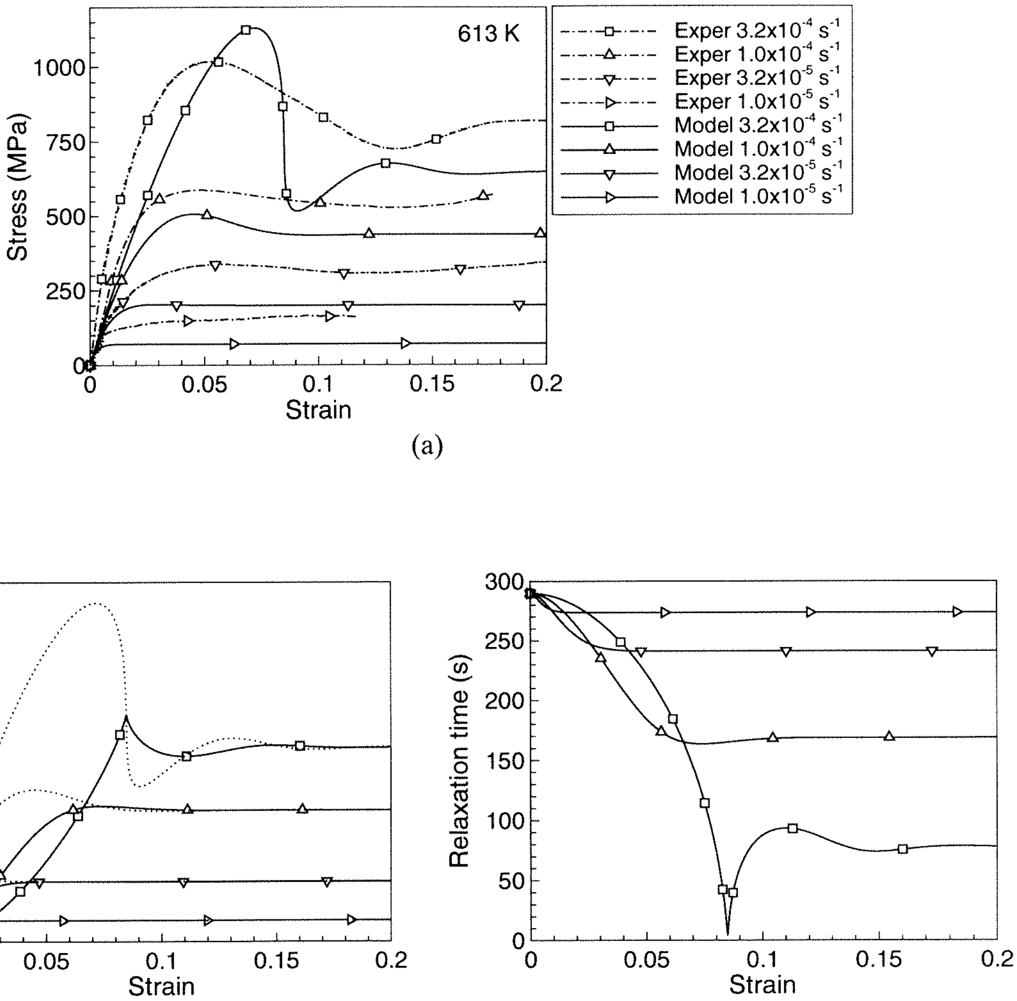

(a)

(b)

(c)

Figure 23. Model predictions at T=613 K based on the fictive stress model. E=26 GPa, σ^*=650 MPa, λ_N=290 s: (a) stress-strain curves with dashed lines correspond to the experimental data and the ones with solid lines correspond to the model prediction; (b) fictive stress (solid line) and stress (dotted line) as a function of strain; and (c) relaxation time as a function of strain.

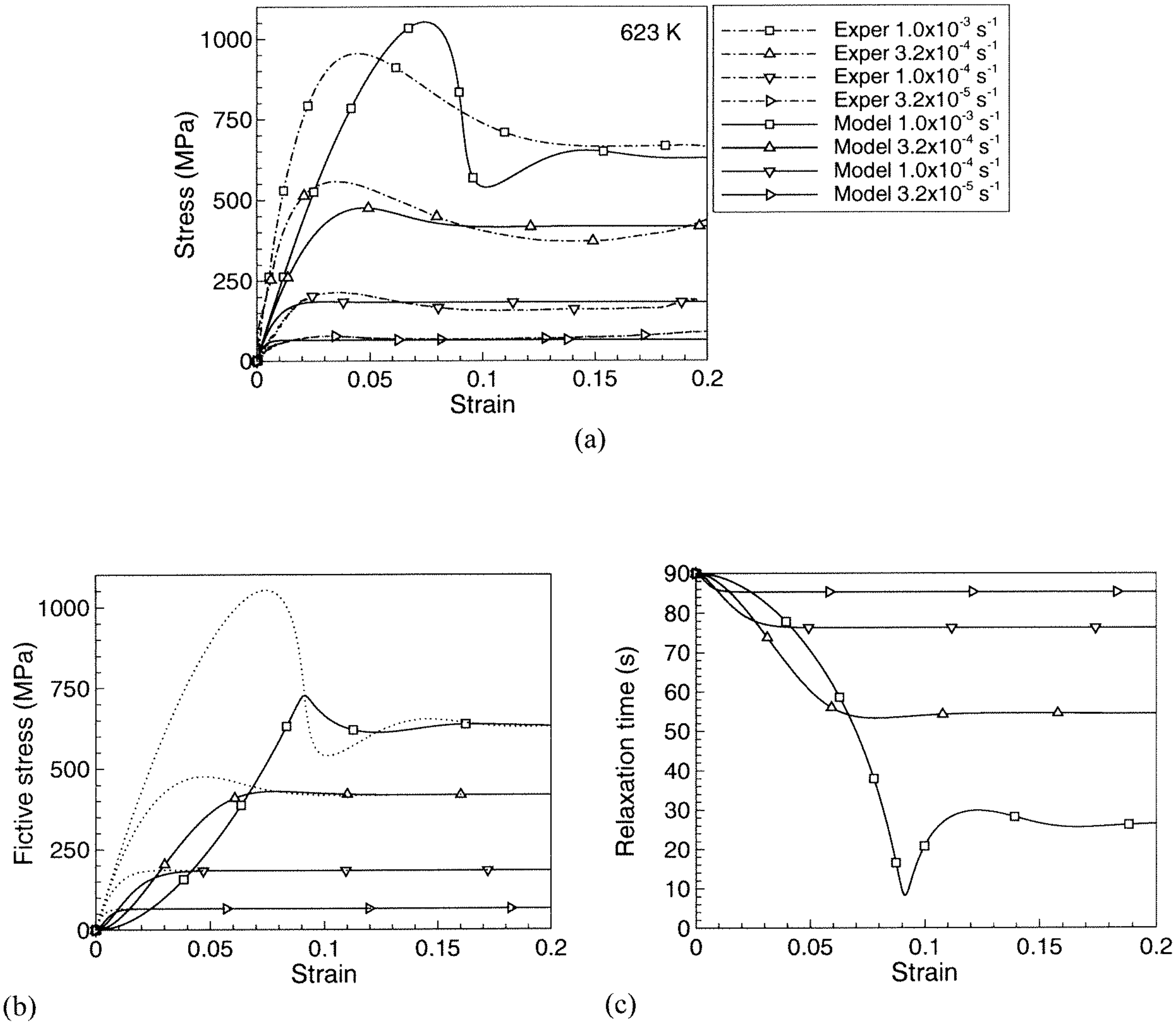

(a)

(b)

(c)

Figure 24. Model predictions at T=623 K based on the fictive stress model. E=24 GPa, σ^*=650 MPa, λ_N=90 s: (a) stress-strain curves with dashed lines correspond to the experimental data and the ones with solid lines correspond to the model prediction; (b) fictive stress (solid line) and stress (dotted line) as a function of strain; and (c) relaxation time as a function of strain.

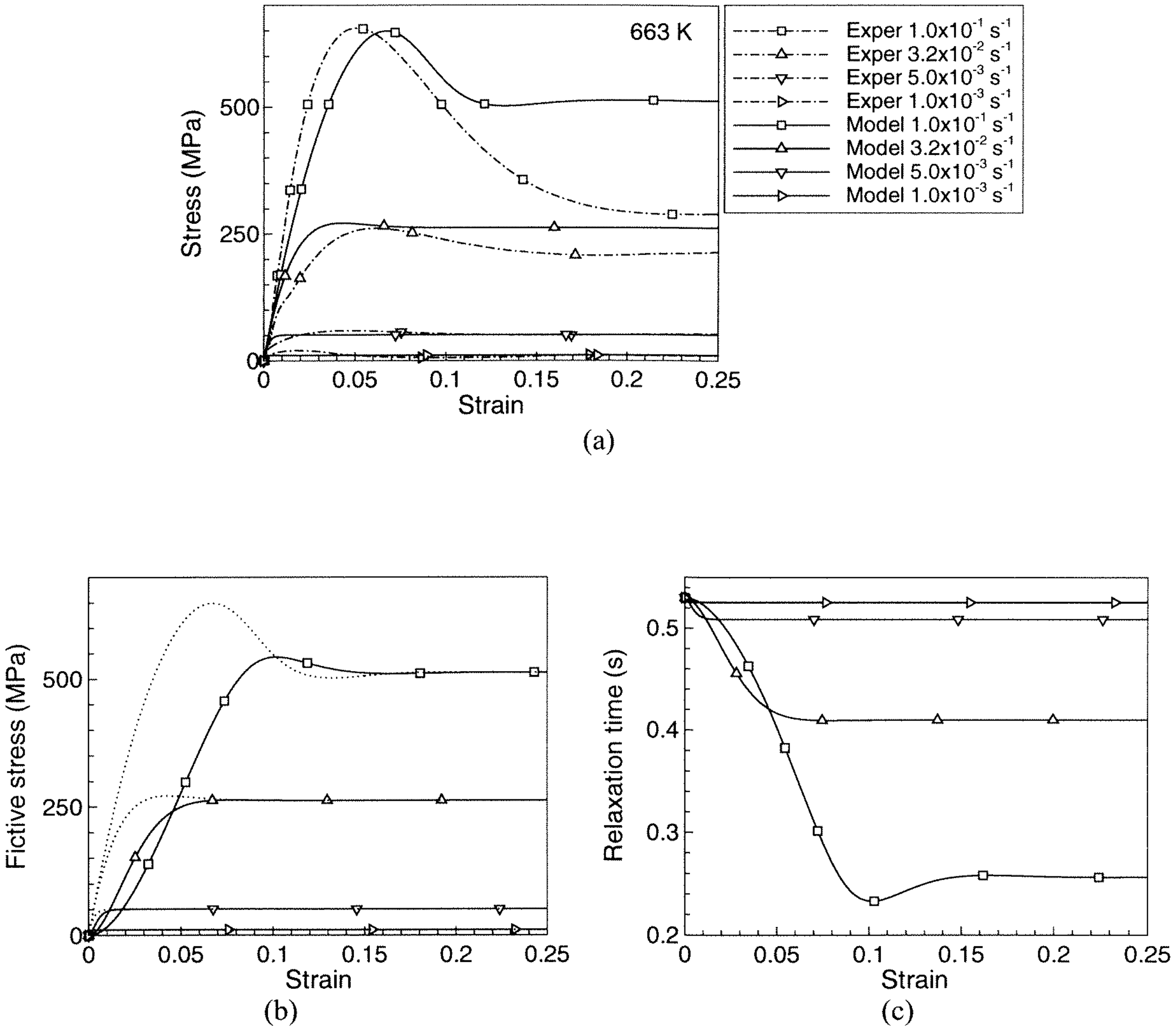

(a)

(b)

(c)

Figure 25. Model predictions at T=663 K based on the fictive stress model. E=20 GPa, σ^*=650 MPa, λ_N=0.53 s: (a) stress-strain curves with dashed lines correspond to the experimental data and the ones with solid lines correspond to the model prediction; (b) fictive stress (solid line) and stress (dotted line) as a function of strain; and (c) relaxation time as a function of strain.

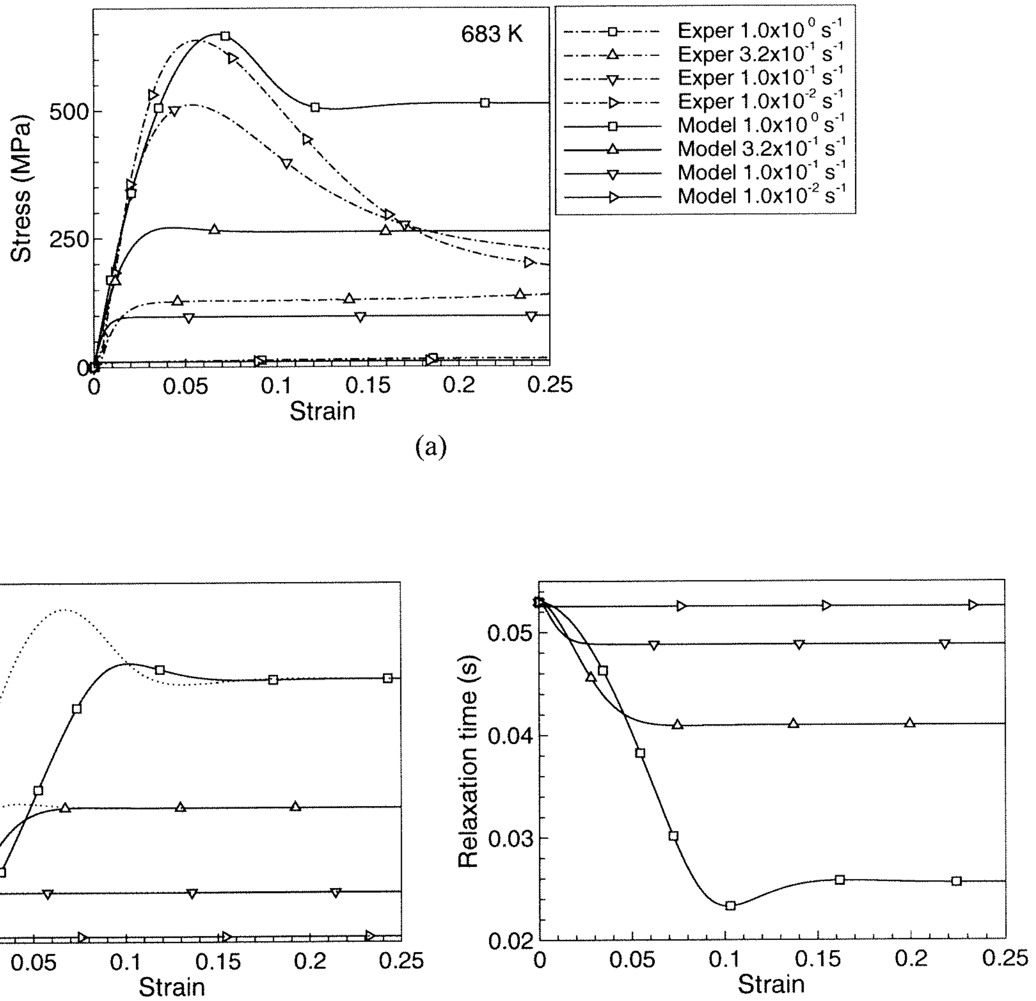

(a)

(b)

(c)

Figure 26. Model predictions at T=683 K based on the fictive stress model. E=20 GPa, σ^*=650 MPa, λ_N=0.053 s: (a) stress-strain curves with dashed lines correspond to the experimental data and the ones with solid lines correspond to the model prediction; (b) fictive stress (solid line) and stress (dotted line) as a function of strain; and (c) relaxation time as a function of strain.

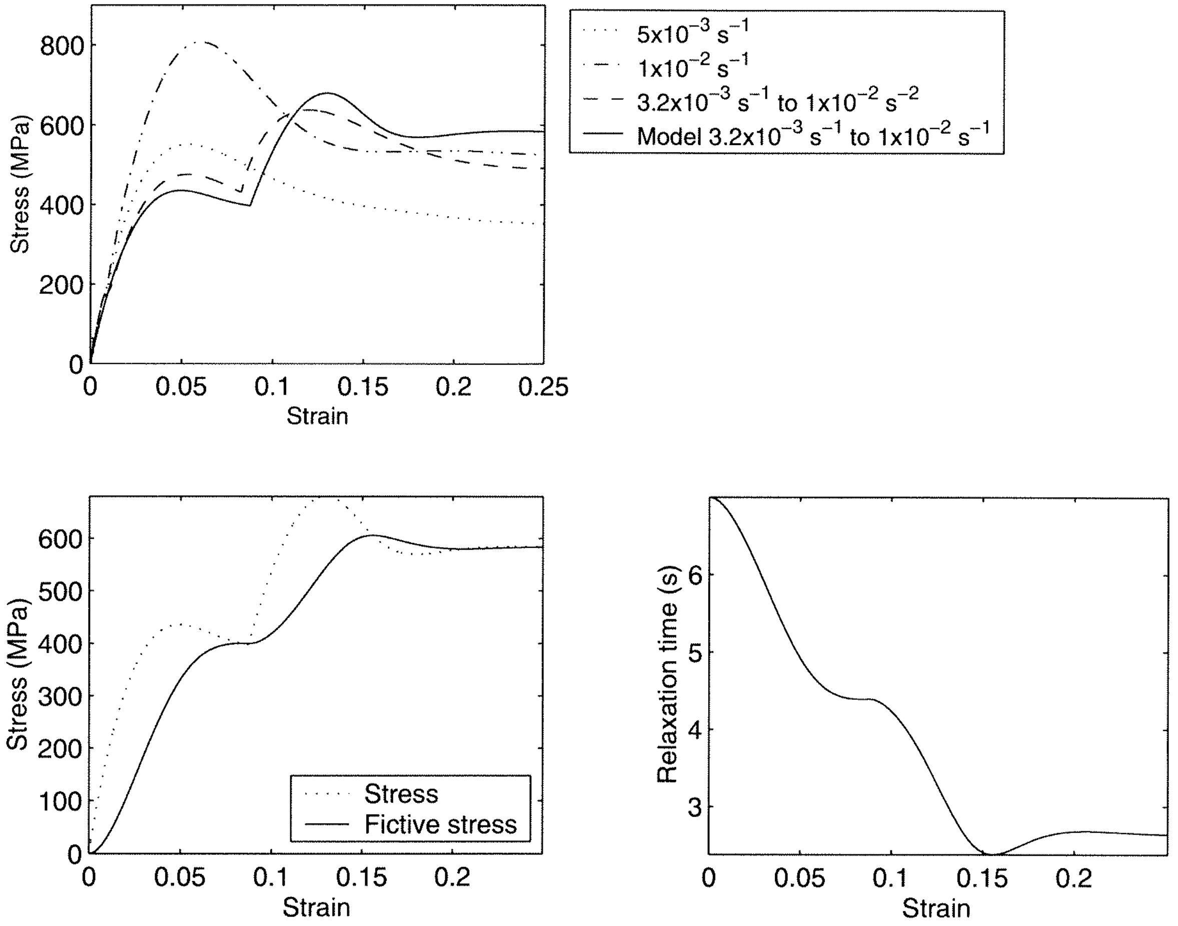

Figure 27. Model predictions of the effect of jump in strain rate at T=643 K based on the fictive stress model. The strain rate jumped from 3.2×10^{-3} s^{-1} to 1.0×10^{-2} s^{-1}: (a) stress-strain curves with dashed lines correspond to the experimental data and the ones with solid lines correspond to the model prediction; (b) fictive stress (solid line) and stress (dotted line) as a function of strain; and (c) relaxation time as a function of strain.

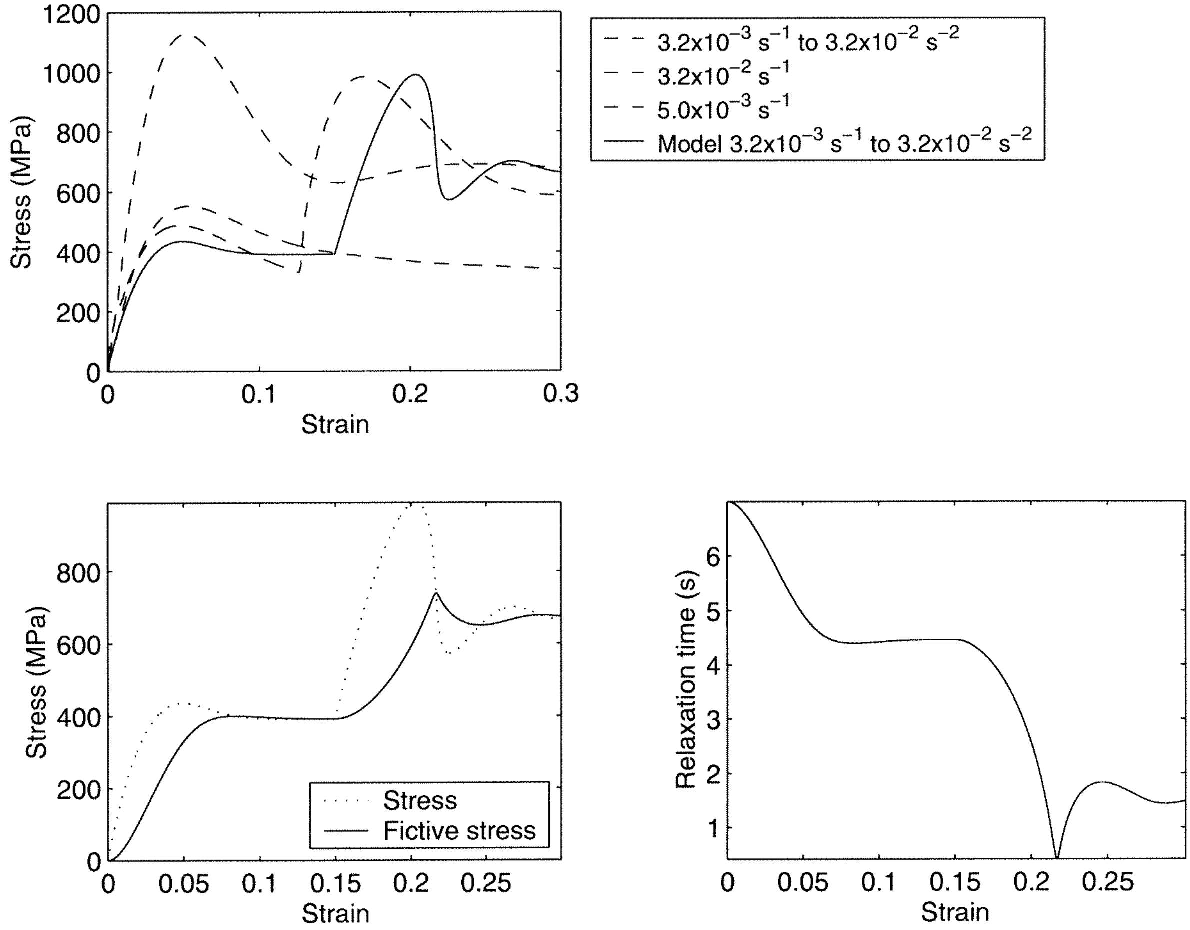

Figure 28. Model predictions of the effect of jump in strain rate at T=643 K based on the fictive stress model. The strain rate jumped from 3.2×10^{-3} s^{-1} to 3.2×10^{-2} s^{-1}: (a) stress-strain curves with dashed lines correspond to the experimental data and the ones with solid lines correspond to the model prediction; (b) fictive stress (solid line) and stress (dotted line) as a function of strain; and (c) relaxation time as a function of strain.

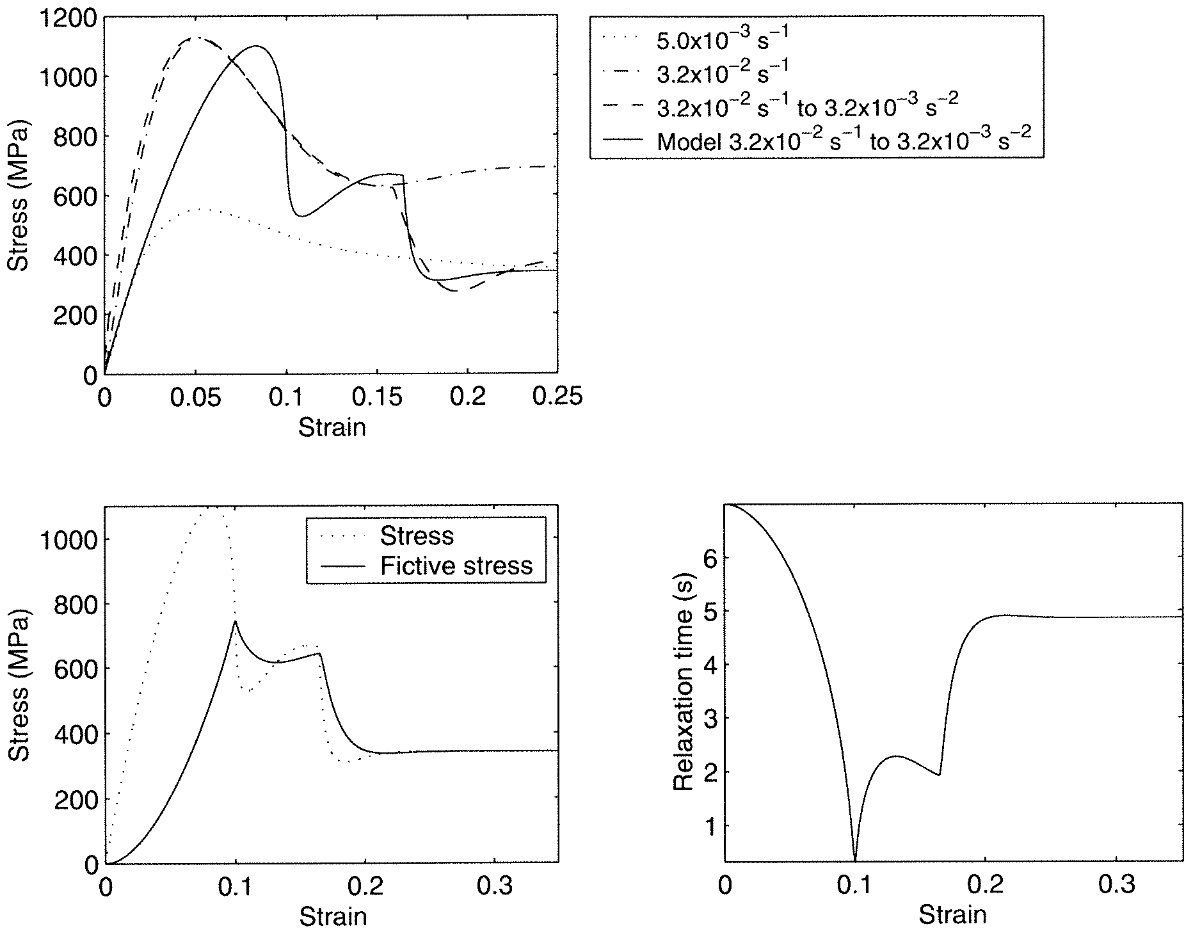

Figure 29. Model predictions of the effect of jump in strain rate at T=643 K based on a semi-empirical fictive stress model. The strain rate jumped from 3.2×10^{-2} s^{-1} to 3.2×10^{-3} s^{-1}: (a) stress-strain curves with dashed lines correspond to the experimental data and the ones with solid lines correspond to the model prediction; (b) fictive stress (solid line) and stress (dotted line) as a function of strain; and (c) relaxation time as a function of strain.

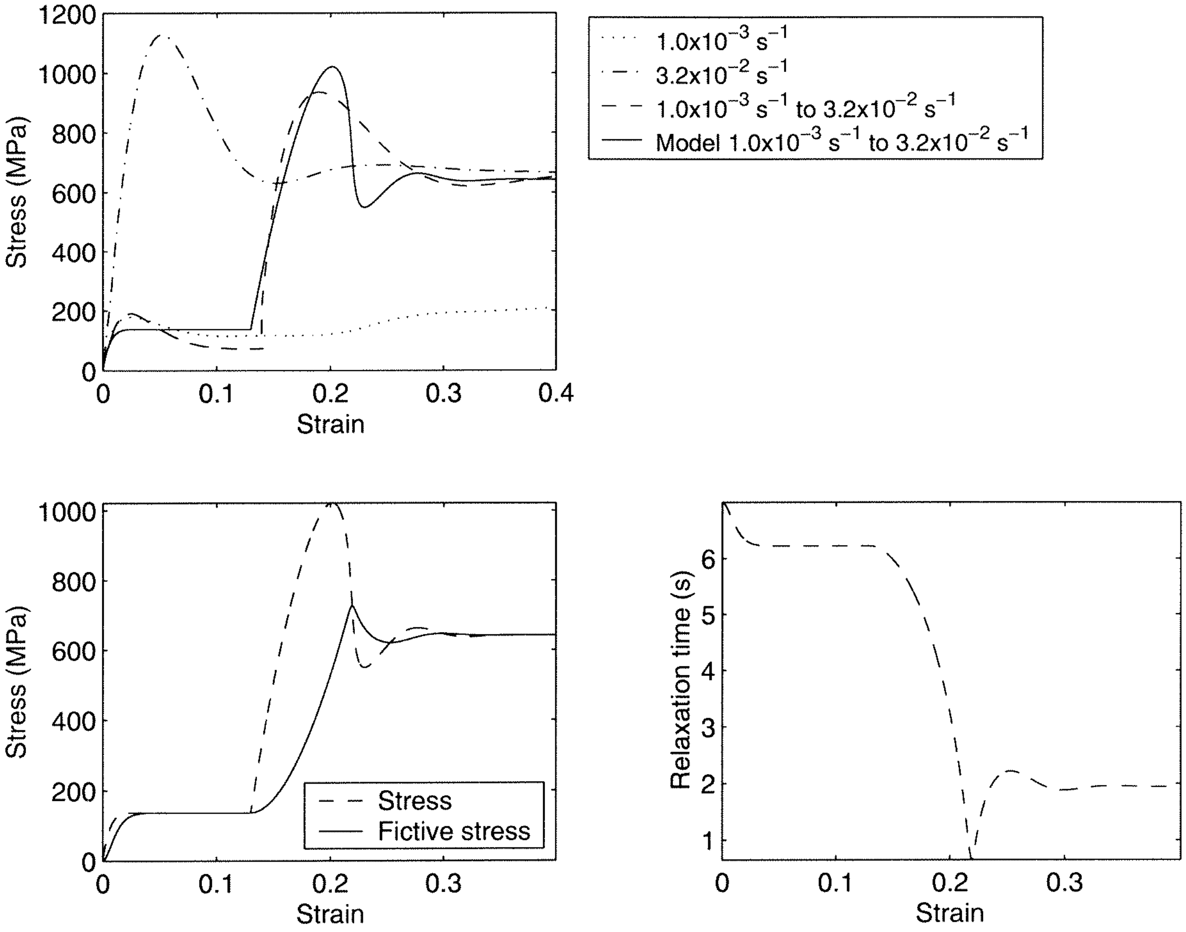

Figure 30. Model predictions of the effect of jump in strain rate at T=643 K based on the fictive stress model. The strain rate jumped from 1.0×10^{-3} s^{-1} to 3.2×10^{-2} s^{-1}: (a) stress-strain curves with dashed lines correspond to the experimental data and the ones with solid lines correspond to the model prediction; (b) fictive stress (solid line) and stress (dotted line) as a function of strain; and (c) relaxation time as a function of strain.

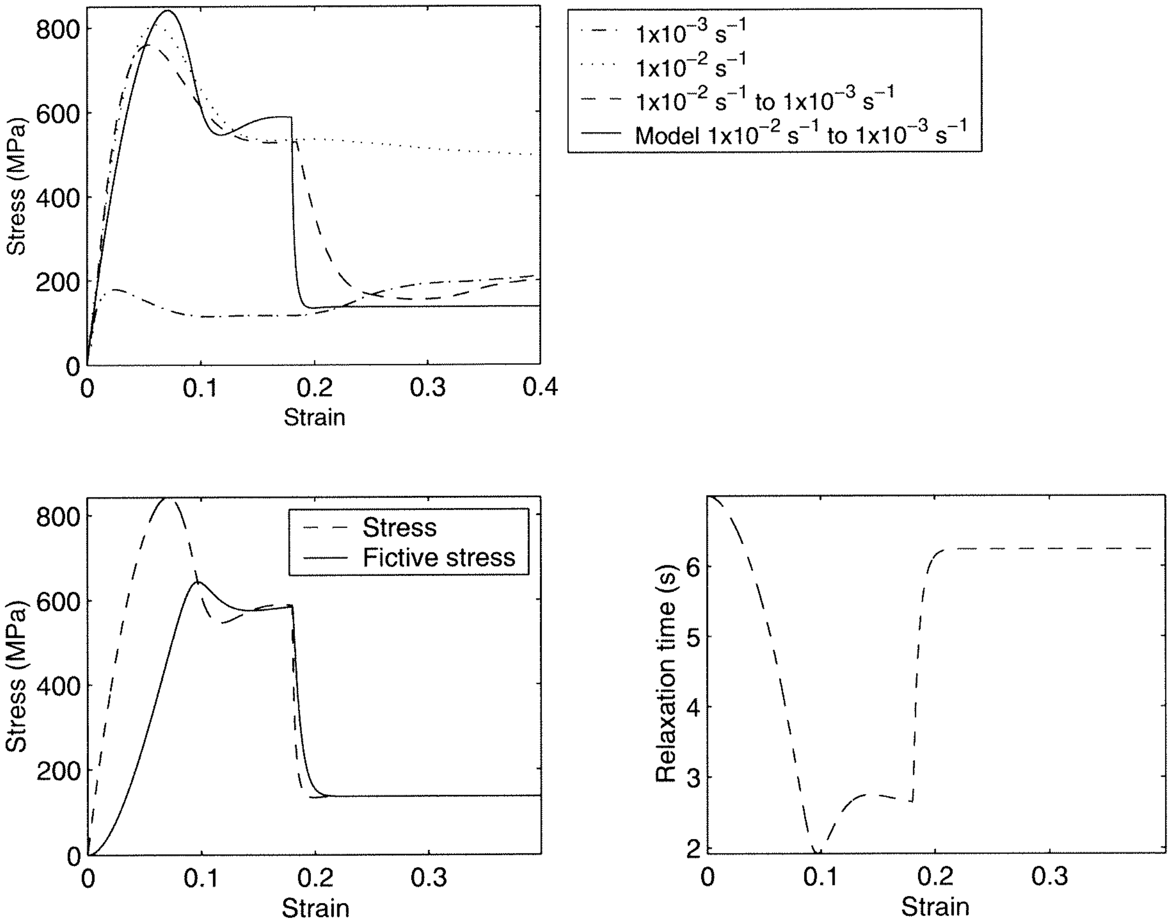

Figure 31. Model predictions of the effect of jump in strain rate at T=643 K based on the fictive stress model. The strain rate jumped from 1.0×10^{-2} s^{-1} to 1.0×10^{-3} s^{-1}: (a) stress-strain curves with dashed lines correspond to the experimental data and the ones with solid lines correspond to the model prediction; (b) fictive stress (solid line) and stress (dotted line) as a function of strain; and (c) relaxation time as a function of strain.

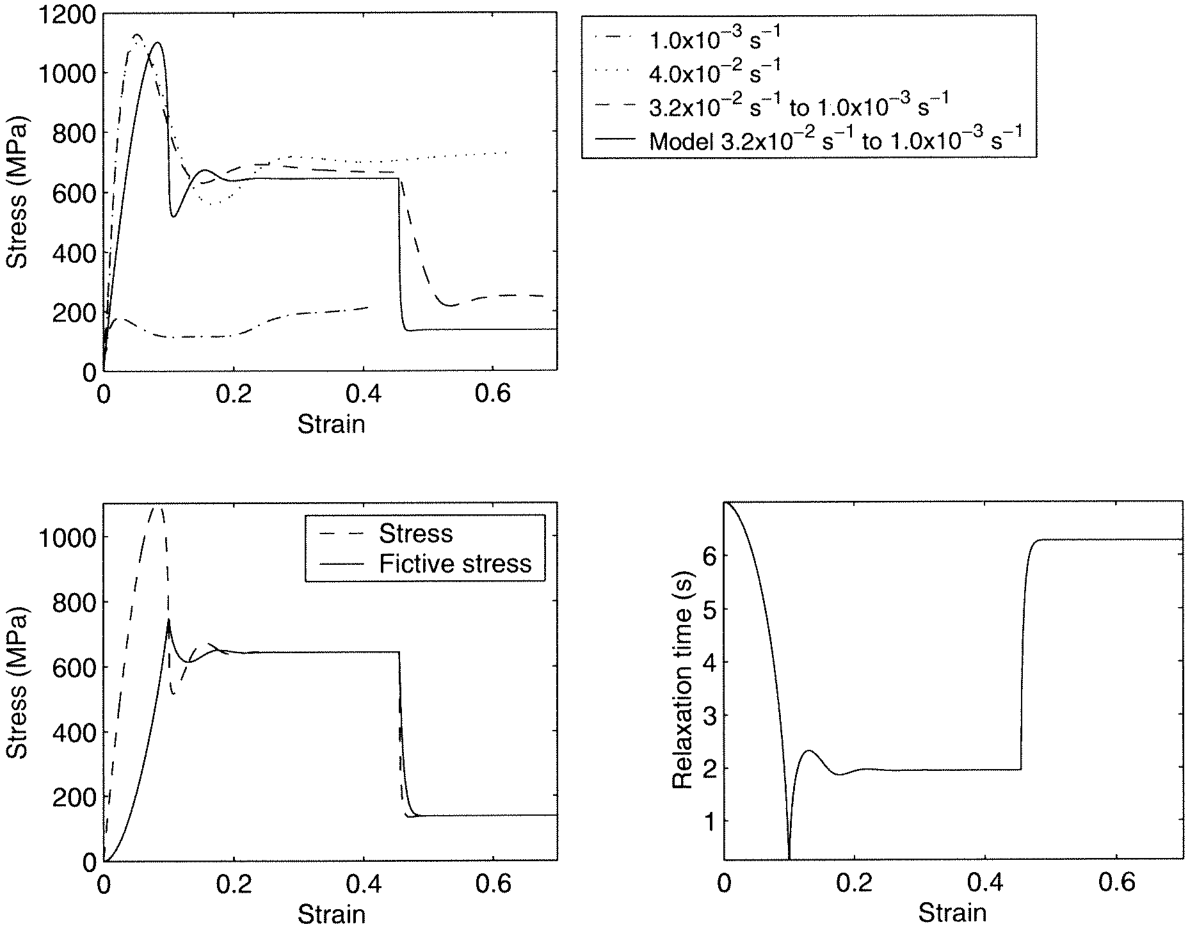

Figure 32. Model predictions of the effect of jump in strain rate at T=643 K based on the fictive stress model. The strain rate jumped from 3.2×10^{-2} s^{-1} to 1.0×10^{-3} s^{-1}: (a) stress-strain curves with dashed lines correspond to the experimental data and the ones with solid lines correspond to the model prediction; (b) fictive stress (solid line) and stress (dotted line) as a function of strain; and (c) relaxation time as a function of strain.

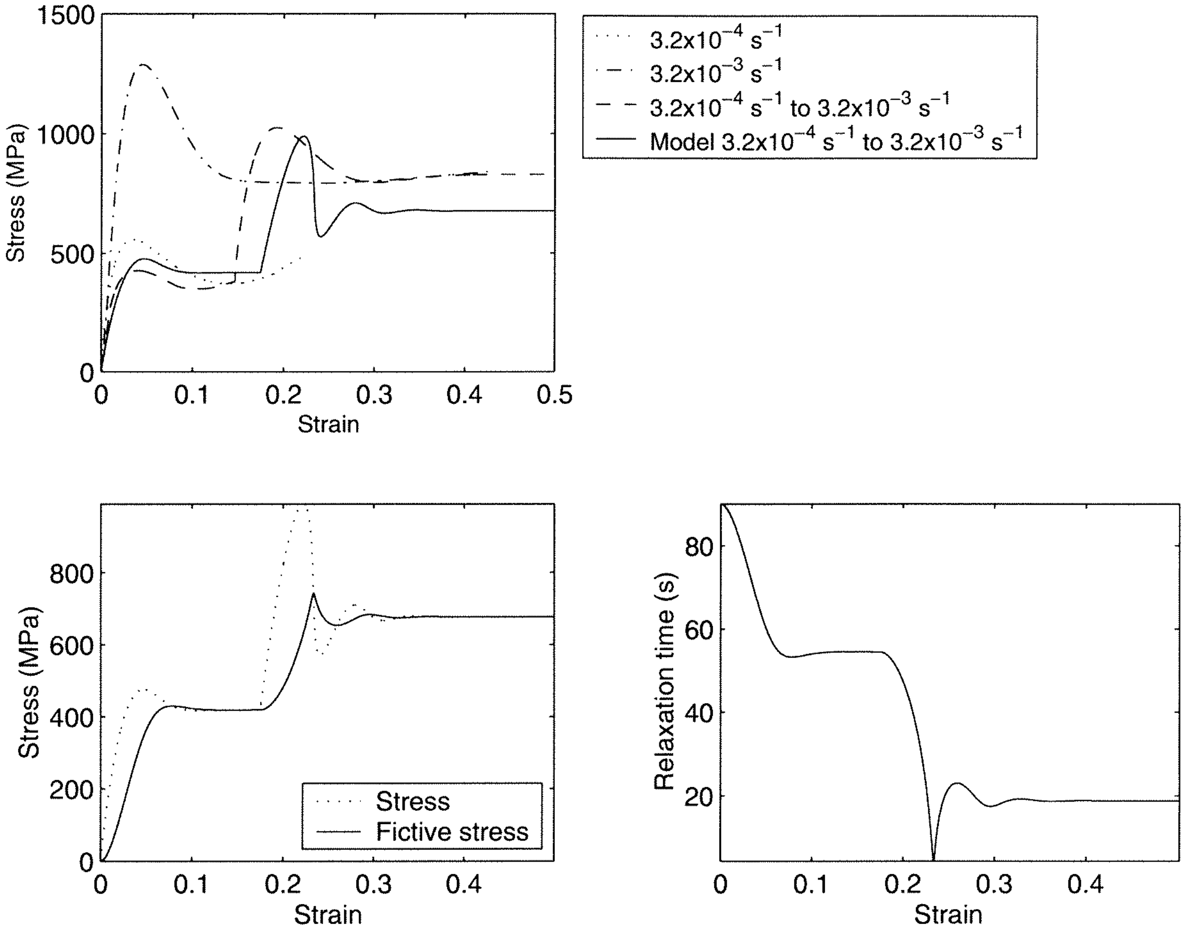

Figure 33. Model predictions of the effect of jump in strain rate at T=623 K based on a semi-empirical fictive stress model. The strain rate was switched from 3.2×10^{-4} s^{-1} to 3.2×10^{-3} s^{-1} and then back to 5.0×10^{-3} s^{-1}: (a) stress-strain curves with dashed lines correspond to the experimental data and the ones with solid lines correspond to the model prediction; (b) fictive stress (solid line) and stress (dotted line) as a function of strain; and (c) relaxation time as a function of strain.

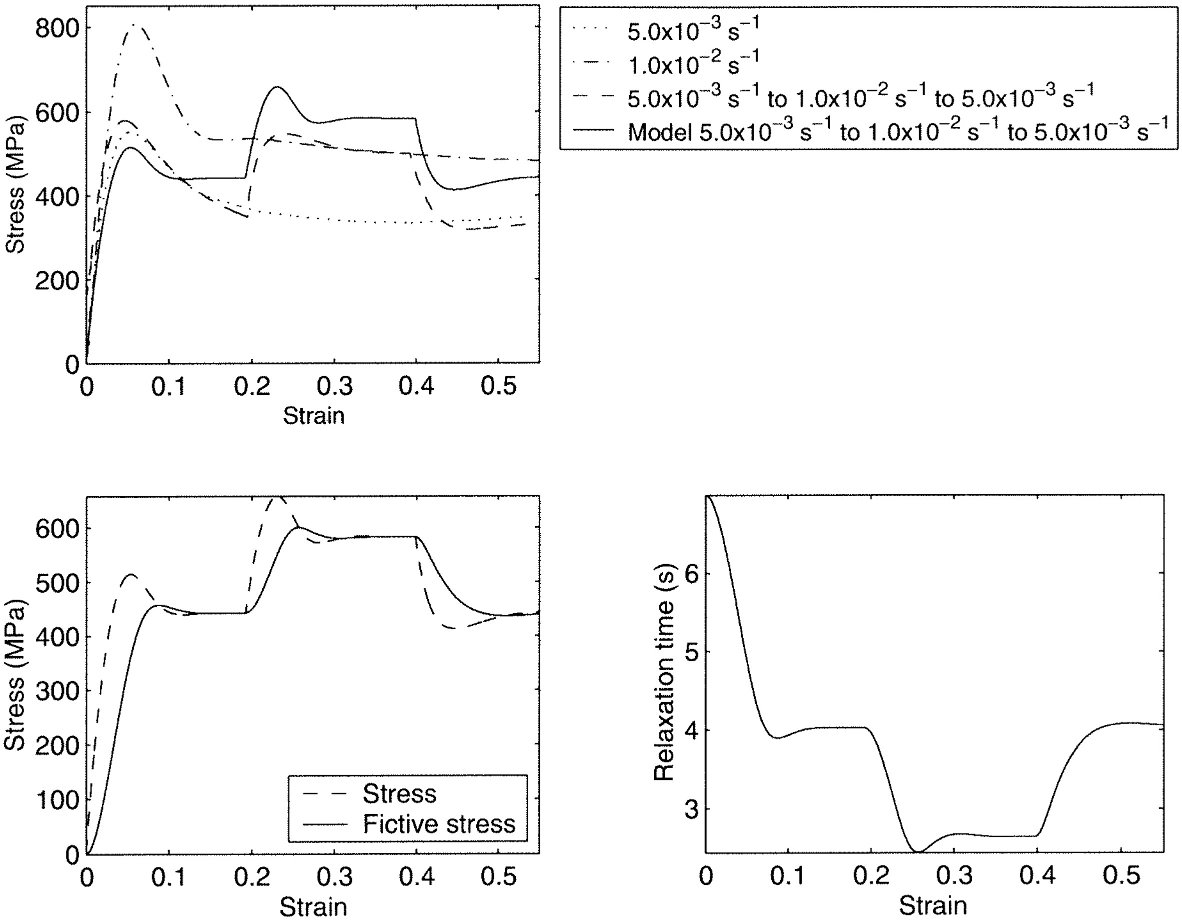

Figure 34. Model predictions of the effect of jump in strain rate at T=643 K based on the fictive stress model. The strain rate jumped from $5.0\times10^{-3}\ \text{s}^{-1}$ to $1.0\times10^{-2}\ \text{s}^{-1}$ and then back to $5.0\times10^{-3}\ \text{s}^{-1}$: (a) stress-strain curves with dashed lines correspond to the experimental data and the ones with solid lines correspond to the model prediction; (b) fictive stress (solid line) and stress (dotted line) as a function of strain; and (c) relaxation time as a function of strain.

Chapter 3 Dynamic Indentation of Vitreloy 1 and its β-phase Composite

Abstract

Indentation has long been established as a fundamental technique for materials characterization. Contrary to the well-studied static indentation, relatively little work has been done on dynamic indentation of materials. The objective of this work is to develop a dynamic indentation setup to measure time-resolved depth and load responses during the process of indentation, and to utilize the technique to assess the dynamic rate sensitivity and pressure dependence for bulk metallic glass Vitreloy 1 and its β-phase composite. A moiré interferometry based displacement measurement technique is utilized to measure the depth of indentation. The indentation responses of Vitreloy 1 and β-Vitreloy 1 were investigated and were modeled numerically using both pressure insensitive (J_2 von Mises) and pressure dependent (Drucker-Prager) flow models. Both the materials were found to be strain rate insensitive and pressure (or normal stress) dependent for strain rates up to 2,000 s^{-1}. Intense shear bands were observed in the indentation craters and are responsible for the overall inelastic deformation.

Keywords: Dynamic indentation; Moiré interferometry; High strain rate; Pressure dependence

1 Introduction

Bulk metallic glasses can be formed by slowly cooling their melts below their glass transition temperatures, resulting in frozen liquidlike amorphous structure, which is fundamentally distinct with their crystalline form of metallic alloys. The breakthrough in searching for centimeter-scale bulk metallic glasses did not occur until the early 1990s when the groups of Inoue (e.g., 1998) and Johnson (e.g., 1999) showed that many families of multi-component alloys can be easily formed with amorphous structure, lacking of any detectable crystalline structure. Some bulk metallic glasses have considerable potential as structural materials due to their exceptional physical and mechanical properties. One such bulk metallic glass is Zr-based Vitreloy 1 ($Zr_{41.2}Ti_{13.8}Cu_{10.0}Ni_{12.5}Be_{22.5}$), which has a critical cooling rate of 1 K/s (Peker and Johnson, 1993) and can be cast up to a size of 5 cm in thickness. High yield stress (Bruck *et al.*, 1994) and high strength-to-density ratio of the bulk metallic glass Vitreloy 1 makes it an excellent candidate for structural applications.

At elevated temperatures near or above its glass transition temperature, Vitreloy 1 exhibits viscoelastic behavior and its deformation behavior can be well characterized (see Chapter 1). However, at low temperatures, say, room temperature, without heat treatment, the high strength glass deforms elastically and fails in a brittle manner, although it is expected to be ductile in nature because of its metallic bonding. One cannot achieve large strains (Bruck *et al.*, 1994; also, see Chapter 1) in a bulk metallic glass under uniaxial loading condition, particularly at room temperature. Room temperature ductility is limited because of the catastrophic failure caused by shear localization, which is the primary and dominant inelastic deformation mechanism for metallic glasses. Therefore, it is *not* trivial to establish inelastic constitutive laws and to validate hypotheses that are often conflicting to examine if a metallic glass is pressure and/or rate sensitive. Indentation provides a means of constraining shear band propagation by surrounding elastic material that is not severely deformed. In addition, high pressures can be generated in the region underneath the indentation contact zone. Another way of arresting shear band is by using confining sleeves or high-pressure vessels, which will be the subject of study in the next chapter. Since the interest here is to understand both pressure and strain rate effects on the flow behavior of metallic glasses, a dynamic indentation technique appears as a reasonable and appropriate tool for such an investigation. Recently, Vaidyanathan *et al.* (2001) performed static micro-indentation on Vitreloy 1 and suggested that the yield stress of Vitreloy 1 exhibits normal stress dependence, in contrast to the behavior of crystalline metallic materials. In this chapter, the objective is to investigate such behavior in the dynamic range with typical strain rate of 1,000 s^{-1}. In the rest of this section, all major existing static and dynamic indentation methods and material characterization approaches will be briefly reviewed, followed by an introduction of a new macro- and dynamic indentation method developed in this study to eliminate the effect of material property variation observed in micro-indentation (Vaidyanathan *et al.*, 2001) and to fully take advantage of the bulk metallic glass samples which were not available even a few years ago.

Static indentation has been widely developed and extended as an indirect method to characterize many fundamental mechanical properties of materials including Young's modulus and yield stress, based on the experimentally determined loading and/or unloading curves, using sharp (or obtuse) indenters, such as Vickers (e.g., Doerner and Nix, 1986), Berkovich (e.g., Oliver and Pharr, 1992; Giannakopoulos and Suresh, 1999) or spherical indenters (e.g., Tirupataiah and Sundararajan, 1987; Alcala *et al.*, 1998). An important outcome of many of these indentation techniques is the "hardness" of the material, which is a useful engineering measure in ranking materials for design. Hardness, as a material "characteristic" from an engineering point of view, is the mutual manifestation of many mechanical properties. Due to the complicated nature of indentation-induced deformation, numerical methods played an important role to further evaluate various experimental methods and to propose new material characterization procedures (e.g., Hardy *et al.*, 1971; Bhattacharya and Nix, 1988, 1991; Giannakopoulos *et al.*, 1994, 1997; Biwa and Storakers, 1995; Larsson, *et al.*, 1996).

A typical indentation test involves pushing an indenter made of an extremely hard material into the flat surface of a target material made of relatively soft material whose mechanical properties are to be extracted. Although the experimentally measured plastic strain distribution underneath an indentation crater revealed that a much more complicated 2D/3D deformation pattern than the one encountered with uniaxial testing methods (Samuels and Mulhearn, 1957; Mulhearn, 1959; Lee *et al.*, 1972; Chaudhri, 1996, 1998;), significant effort has been devoted to extracting fundamental mechanical properties of materials using the indentation method due to its simplicity. Early comprehensive analysis of indentation dates back to 1950s when Tabor and coworkers suggested that for a spherical indenter, the ratio between the chord and the indenter diameters is an index of the representative strain in the plastic zone, and that a linear relation can be established between hardness and flow stress (Tabor, 1948, 1951, 1996), which is widely used for metals, especially in engineering practice. It was found that for a sharp indenter the ratio between hardness and flow stress is a function of the cone angle, and that one could possibly estimate constitutive behavior of materials (Dugdale, 1954; Lockett, 1963; Atkins and Tabor, 1965).

Although the static indentation techniques are instrumental in determining material properties under quasi-static loading condition, question arises as to whether such techniques can be extended to evaluate material performance under dynamic loading conditions that are comparable to, say, techniques such as the well-established Kolsky (split Hopkinson) pressure bar technique (Kolsky, 1949) while maintaining simplicity. To the author's knowledge, relatively little work has been done on dynamic indentation compared with its static counterpart although simple techniques such as the Shore Scleroscope have been developed and utilized. Davis and Hunter (1960) employed a pendulum equipped with a conical indenter to study rate sensitivity in the range of indenter speed up to 30 cm/s. Mok and Duffy (1964,1965) increased the indentation speed of their spherical indenters up to 5 m/s, showing that the strain rate sensitivity deduced was roughly comparable to that evaluated using the Kolsky pressure bar technique. Nobre (1997) utilized a pendulum machine equipped with a piezoelectric transducer, which allowed measurement of impact impulses in order to analyze the dynamic hardness-strain data. Sundararajan *et al.* used high speed (up to 200 m/s) impact with a hard spherical ball as an indenter in their dynamic indentation experiments to study the relationship between average strain, average strain rate and flow stress or dynamic hardness; no time-resolved signals from indentation being recorded in the experiments (Sundararajan and Shewmon, 1983; Tirupataiah and Sundararajan, 1991). Recently, Subhash and coworkers developed a dynamic indentation technique utilizing one-dimensional elastic wave propagation principle widely used in the Kolsky (split Hopkinson) bar experiments (Subhash and Koeppel, 1999; Koeppel and Subhash, 1999; Anton and Subhash, 2000). A load transducer was used to capture the load-time response and a steel strip with a strain gage mounted onto its surface was used to monitor the indentation depth during the experiment. The displacement deduced from strain gage signal was based on simple static beam theory, which limits the displacement measurements to relatively low velocities where the wave propagation and dispersion effects are negligible. Recently, Andrews *et al.* (2002) proposed a "rigid body" dynamic indentation model for pressure and rate independent materials based on Newton's second law, which generally agrees well with their finite element simulations at impact speeds less than 100 m/s. This model confirmed that for rate independent materials a "quasi-static" condition is established during low speed impact process. A "quasi-static" condition refers to equilibrium that requires impact duration long enough to allow multiple wave reflections in the plastic region of the target and the indenter (see Tirupataiah and Sundararajan, 1991).

It is worth mentioning that the existing dynamic indentation techniques cannot be employed to capture the time-resolved indentation depth-time history, thus possibly losing vital information related to the effective strain and effective strain rate in the course of dynamic indentation. The purpose of this study is to develop an experimental method capable of measuring transient indentation depth enabling the study the dynamic behavior of bulk metallic glasses, including pressure dependence and strain rate sensitivity, based on the load-depth-time relations. In section 2, the experimental technique will be discussed in detail and its performance will be examined. The newly developed dynamic indentation apparatus is then employed to investigate the dynamic material behavior of bulk metallic glass Vitreloy1 and its β-phase particulate composite, which is described in section 3. Numerical simulations were performed to interpret the experimental results and conduct parametric studies, and their results are discussed in section 4. The limitations of the experimental method and the conclusions for the present study are presented in section 5.

2 Experimental

This section describes a simple and efficient dynamic indentation technique developed for the study, following a brief overview of various available techniques for measuring displacements during transient events or in dynamic experiments.

2.1 Techniques for dynamic displacement measurement

Barker and Hollenbach (1964) developed a technique that uses a slant thin metallic wire as part of a variable electrical resistor to measure free surface movement of metallic objects. The contact resistance, which was assumed to be only function of the contact length, actually depends on electrical properties of the moving surface and the pressure between the wire and the points of contact. In addition, the nonlinearly due to the heating of the wire makes the compensation circuit complicated. It is also difficult to attach such an apparatus to a dynamic indentation system. Capacitance based technique (Rice, 1961) is more flexible than a resistance transducer in the sense that there is no direct contact between the moving object and the target. However, the circuit construction and insulation is critical, and errors may result from noise, charge leakage, and stray capacitance in cable connections.

One of the most widely used displacement sensors is the linear variable differential transformer (LVDT), which is an electromechanical transducer that produces an electrical signal proportional to the displacement of a movable magnetic core. With high resolution and variable measurement ranges, LVDT has been widely used as quasi-static and vibration displacement sensors. However, two drawbacks of the LVDT limit its application in high-speed transient displacement measurement. First, the use of LVDT is restricted by the inertia of its moving core and the difficulty of installing the core under an impact environment. Second, a typical duration of a dynamic indentation experiment is around 50 microseconds, which corresponds to a frequency of 10 kHz and other high frequency components accompanying the signal in the indentation depth-time profile. The applied frequency to the LVDT should be at least 10 times the frequency to be measured, resulting in an excitation frequency of at least several hundred kilohertz, which is unattainable in currently available commercial LVDTs.

Optical interferometry is the most widely used technique in dynamic displacement measurement. For instance, Michelson interferometry is commonly used to measure surface displacement and Doppler effect (Barker and Hollenbach, 1972) is used to measure free surface or interface particle velocity in shock wave propagation experiments. Of all the manifestations of light interferometry effects, geometric moiré interferometry is one of the simplest. Whenever a line structure is overlaid/superimposed with its replica, a moiré pattern forms which has a very important characteristic: very large shift in moiré pattern is can be caused by small relative motion between two superposed line networks. Such a mechanism can be defined as a displacement magnifier, which could be used as a highly sensitive displacement sensor. Probably the first systematic study of the moiré pattern was carried out by Guild (1956, 1960). The moiré gratings could be made with very fine lines even in late 1960s (Holister and Luxmoore, 1968) and has been widely used in engineering measurements (e.g., Patorski, 1993; Cloud, 1998).

The distance between two adjacent geometric moiré fringes, can be expressed as (see Appendix),

$$d = \frac{a_1 a_2}{\sqrt{(a_1 - a_2)^2 + a_1^{\,2}\theta^2}} \tag{1}$$

assuming that the two gratings have pitches a_1 and a_2, respectively, and, assuming that the relative inclination angle θ between the two gratings is small. If the difference between the two pitches are small such that $|a_1 - a_2| \ll a_1$, then Eq. (1) can be simplified as

$$d = \frac{a_1}{\theta} \tag{2}$$

Equation (2) is the basic governing equation for the geometric moiré technique, and the possible diffraction effect associated with it will be further examined later in this section.

2.2.1 Motion sensing apparatus

Costin and Duffy (1976, 1979) successfully utilized the geometric moiré fringe technique to measure dynamic crack opening displacement (COD), which was used in determining the loading rate dependence of fracture toughness in structural steels. Their specimen was a solid round steel bar with a fatigued circumferential sharp crack at the tip of a notch. In their experiments, after a grating was produced by contact print of a glass grating plate onto a polished flat area on the upstream side of the notch of the specimen, the glass grating plate was cemented to the bar on the downstream side of the notch such that the plate spanned the notch and overlapped the grating on the specimen. Therefore, relative movement between the two gratings as a result of the crack opening produced a detectable shift of the moiré fringe formed by the two gratings.

Based on the technique of Costin and Duffy, the device employed in the present study uses two matched moiré grating films with identical rulings produced by contact printing using high-resolution films. The indentation depth-time profile was monitored by the relative movement of a grating film affixed to a moving indenter with respect to another identical grating film affixed to the window of a square tube that served as a gun barrel for guiding the indenter. The indenter has a square cross-section of length 25.4 mm (1 inch) and possesses a conical tip with a cone-angle of

140.6°, as shown in Fig. 1. The non-circular cross-section of the indenter was used to prevent the indenter from rotation during the indentation process. Before gluing the grating film onto the indenter, a flat area of the indenter was sanded down using 150, 300 and 600 grit sandpapers followed by polishing using 15, 6, 3μm diamond paste successively until a mirror-like surface was achieved. A five-minute epoxy was used to glue the grating film to the polished surface. Precaution was taken to remove any air gap between the film and the surface, and to distribute the epoxy uniformly into a thin film and reduce surface roughness down to a few microns. The ruling direction was in a direction perpendicular to the axis of the indenter, but absolute normality between the two is not essential since a mechanism to facilitate angular rotation was available for the other grating film attached to the window of the tube.

The internal shape of the gun barrel tube carrying the indenter is also shown in Fig. 1. The basic interior shape of the tube is a square with an additional slot on one side, providing room for the movement of the grating film during flight. Considering that rotation can impair the quality of the detection of sensitive moiré fringe pattern, the design of the cross-section is to facilitate non-contact optical measurements while keeping the indenter from rotation during impact. A 10 μm gap was provided between the indenter and the tube, allowing frictionless one-degree-of-freedom movement for the indenter. One way to reduce the influence of diffraction is to have an adjusting mechanism to minimize the gap between the two grating films. A grating film of the same kind, attached to a rigid plate with back support springs in the window slot (Fig. 1), was placed at a short distance in front of the target and at a small angle orthogonal to the axis of the tube. The horizontal position and the angle of the film can be adjusted relative to the indenter until a clear moiré fringe with desired fringe width was observed. The fringe pattern was checked once again under an optical microscope for finer tuning. The window slot was machined 0.25 mm (ten thousandth of an inch) deep into the tube to allow for the adjustment of the gap.

Grating films having 250 lines per inch or 40 lines per mm (1016 lines per inch) were successfully employed for obtaining the desired moiré fringe pattern at different indentation velocities. As shown in Fig. 2, two examples of typical moiré fringes patterns formed by *in-situ* superposition by grating films of 40 lines per mm and 250 lines per inch give clear demonstration of the patterns and their potential use as motion magnifiers, i.e., displacement transducers. In Fig. 2(a), the ruling pitch of the grating that was used is 51 μm. Figures 2(b) and (c) correspond to moiré fringe patterns for pitch value of 12.5 μm for two different rotation angles. Note that the widths of both the light and the dark fringes are equal which is an indication of the high fidelity of the present system. The use of high-resolution glass grating plates as proposed by Costin and Duffy (1976, 1979) is impractical in dynamic indentation due to the brittleness of glass. Although photo-resistive film transfer technique is an alternative to the gluing of grating films on the indenter surface, ultraviolet (UV) exposure of soft emulsion films are still rather vulnerable to scratches and may require redepositing gratings very often. In contrast, it was found that the high-resolution grating films were very reliable, and they were still functional after many indentation experiments.

An optical intensity recording subsystem for the recognition of the fringe pattern under a very short duration of time, say, 100 microseconds and less, is illustrated in Fig. 3. It consists of a laser source (10 mW He-Ne laser, wavelength, λ=0.633 μm) with frequency and intensity stabilizer, an optical fiber positioner, a 50 μm input optical fiber and a 300 μm output fiber, an optical fiber probe with two small lenses and a photodiode detector. The optical fiber probe is used to focus light from the input optical fiber onto the film surface, and to collect most of the reflected light back into the output optical fiber, which then directs the light to the photodiode. Two miniature lenses were assembled on two ends of a round fiber probe, one for focusing light from the input fiber onto the reflecting surface, and the other for focusing reflected light back to the output fiber. The output fiber has a large diameter, which increases light receiving efficiency and allows a large depth-of-field of 5 mm. The distance from the probe to the reflecting surface is nominally 30 mm. The focus spot size is nominally 100 to 500 μm in diameter, which is appropriate for the current application. The fiber probes are reusable several times, unlike a capacitance transducer or LVDT, which could be easily damaged during impact.

During the indentation, initial indenter velocity varied from a few meters per second up to 50 m/s. For a grating of n lines per mm and a typical initial indentation velocity V m/s, if we assume a bright-to-dark transition detected by the photodiode corresponds to a movement of either a dark or black ruling in the grating, then the time duration τ for the transition would be $\tau=(nV)^{-1}$ ms. For the case of 40 lines per mm and an indentation velocity of 10 m/s, this time duration will be $\tau=2.5$ μs. The photodiode (Model #13DSH005, Melles Griot) that was used has a typical rise time of a few nanoseconds (~2.5-3.5 ns), providing adequate frequency response. The photodiode signals were recorded using a 4 channel Nicolet digital oscilloscope at a 10 M points/s sampling rate.

One of the most important factors in the current displacement transducer is the moiré fringe width. As mentioned earlier (Fig. 2), the moiré fringe width can be changed by varying the relative angle between the gratings. A good fringe contrast can be achieved by making the fringe width slightly smaller than that of the diameter of the light beam from the input optical fiber. Obviously, a minimum requirement for the bright and dark contrast is that the size of the focused light spot is the same as the fringe width. If this is violated, *i.e.*, either the spot size is too large or the fringe width is too small, the contrast could be reduced or lost since more than one fringe is covered by the focused light beam. Because of practical difficulty in reducing the size of the laser beam from an optical fiber, the choice will be to enlarge the fringe width by retaining a small relative angle between the gratings. It is also worth mentioning that in principle the use of laser is not necessary and an alternative light source with strong beam intensity and narrow beam size can also be employed.

2.2.2 Fringe shape and error

Strictly speaking, moiré fringes are complicated optical phenomena due to diffraction effects (Guild, 1956). The system employed in the present study consists of a transparent grating and another transparent grating with a reflecting surface on its backside. Illumination from the front of the two gratings must pass through both transparent gratings twice before being reflected back to the intensity detecting device, i.e., the photodiode. Such a system is equivalent to having four gratings: the two transparent gratings and their virtual images due to the mirror surface. The first two are physically independent gratings, which generate fringes if there exists relative rotation and translation. The fourth virtual grating is capable of interacting with its original, the first grating, creating undesirable fringes if the original grating is slightly inclined to the mirror surface. Because of perfect bonding of the second grating film to the mirror surface, one will not see any fringes due to the second grating and its virtual image. The interaction between the third and the fourth grating is identical to that between the two real gratings since no additional information is introduced by the system. The intensity function and error estimation will be based on a system consisting of two transparent gratings. It is a good practice in any circumstance to make the two grating plates parallel, especially for gratings with relatively high line density.

The operational principle of a moiré fringe system consisting of two diffraction gratings is briefly described here. When a beam of monochromatic light is incident on the first grating, it will be diffracted into beams of various orders. The simplest case will be a sinusoidal diffraction grating, which generates zeroth and first order diffracted beams. Generally speaking, the maximum order of the diffracted beam by the first grating will be larger than one so there will be higher order beams designated by 2, 3, 4 and so on. The diffracted beams from the first grating will be incident on the second grating with the same pitch and diffraction character, and will be diffracted once again into different orders. The second grating redistributes the intensity and the brightness is the combined effect due to the two gratings. The intensity function of static fringes can be expressed in the following form (Guild, 1956, 1960):

$$B = 1 + B_1 \cos\left(\frac{2\pi(d-d_1)}{W}\right) + B_2 \cos\left(\frac{4\pi(d-d_2)}{W}\right) + \cdots + B_n \cos\left(\frac{2n\pi(d-d_n)}{W}\right) \qquad (3)$$

where W denotes the fringe width corresponding to perfect sinusoidal gratings. The third and higher terms are the higher order terms corresponding to shorter periods. B_i is the amplitude of the i^{th} group, and d_i (i = 1, 2, 3...) is the position where i^{th} maximum amplitude occurs. The actual fringe width in the experiments was adjusted to be between 1 and 1.5 mm, which is larger than that of the laser spot size. A typical intensity waveform recorded by the photodetector is shown in Fig. 4. The waveform behaves like a sinusoidal wave with very clear peaks and valleys. It was established experimentally that the higher order fringes were negligible and one peak-to-peak cycle corresponds to the relative movement of one pitch size if the indenter moves at a constant speed during that time,

$$B \cong 1 + B_1 \cos\left(\frac{2\pi(d-d_1)}{W}\right). \qquad (4)$$

Thus, the moiré fringe displacement constant is estimated to be at least 12.5 μm for a 40 lines-per-mm grating and at least 50 μm for a 250 lines/inch grating. It was also noticed that under identical conditions, the magnitude of the detector voltage decreased with increase in the indenter velocity.

The gratings used in the experiments were examined carefully under a light microscope, and it was found that they had good and even rulings. Non-parallelism of grating surfaces is one of the major sources of error in the geometric moiré technique. An estimation of the fringe movement δL (Guild, 1956, 1960) due to this effect can be expressed as

$$\delta L = \delta t(\cos\alpha - \cos\beta)w/\lambda \qquad (5)$$

where δt is the change in the gap thickness, α is the angle of incidence, and β is the angle of emergence of the second-order diffracted light such that

$$\sin\beta - \sin\alpha = \lambda / w \tag{6}$$

and hence Eq. (5) becomes

$$\delta L = \delta t \tan\frac{\alpha+\beta}{2}. \tag{7}$$

Assuming an incident angle $\alpha = 5^{\circ}$ for a sinusoidal grating with pitch of 25 μm and wavelength of laser light to be 0.633 μm, the first order diffraction angle is 6.5°. The corresponding error is $0.1\delta t$ which suggests that the movement of the fringe due to gap variation is roughly 10 μm if the gap variation is 0.1 mm. Thus, this error is relatively small and it will not accumulate with fringe number.

2.3 Loading apparatus: indenter

The square cross-section of the indenter has a side of 10.9 mm and a length of 25.4 mm (1 inch). Another slightly different cross-sectional shape was also utilized, but the cross-sectional area remained the same. No difference in the indentation profiles was observed because of this variation. A circular cross-section was avoided because such a shape could cause severe rotation of the indenter during impact, impairing the quality of the moiré fringes. The indenter has a ground and polished conical tip with a cone-angle of 140.6° (e.g., Jayaraman *et al.*, 1998; Andrews *et al.*, 2002). The objective of selecting such a conical tip is to simplify an otherwise fully three-dimensional indentation problem (i.e., Berkovich or Vickers Indentation) to an axisymmetric problem. This indenter can be regarded as an "equivalent" Berkovich indenter because the ratio of the projected contact area to the indentation depth is the same as that of the Berkovich indenter. An "equivalent" Vickers indenter was not employed due to its relatively larger equivalent cone angle (108.8°) that could enhance the frictional effect. The indenter (mass, 44.8 grams) is made of tungsten carbide (85% WC and 15% Co composition with high strength and fracture toughness), which has a hardness of 90 HRA, much larger than 76 HRA, the Rockwell A-scale hardness (converted from a Vickers hardness of 530 kg/mm^2) of the metallic glass, Vitreloy 1, as determined by static indentation (Conner *et al.*, 1998). The deformation of the indenter remains elastic and relatively small compared to that of the target material. As shown in Fig. 3, a striker propelled by a gas gun was used to launch the indenter. The striker would then lose contact with the indenter and is eventually stopped by a stopper.

2.4 Load measurement

The indentation load was recorded using a quartz load transducer (Fig. 3 (a)). Similar techniques were employed to measure transient load history (e.g., Subhash *et al.*, 1999) in earlier studies to study dynamic indentation of materials. The load sensor used in this study is a Kistler model #9011A or a #9021A quartz transducer (with load capacities of 15 kN and 35 kN, respectively). Quartz disks inside the transducers by virtue of their piezoelectric characteristic produce electrical charge that is proportional to the external transient load. Not suitable for measuring static loads, quartz transducers are ideal for dynamic load measurement due to the high natural frequency of quartz (>1 MHz). The transducers have a high sensitivity of 4.2 pC/N and excellent linearity up to their maximum specified load capacities. The material to be investigated was placed in tight contact with one side of the quartz transducer, which was held by a supporting block. A low noise cable (Kistler #1361A1 cable) was used to connect the transducer to a high-speed charge amplifier (Kistler model #5010B), equipped with a standard filter (Kistler model # 5311) that has a bandwidth of 180 kHz (at -3dB), best among the commercially available charge amplifiers. The output signal from the linear charge amplifier (with adjustable charge to voltage ratio) was recorded using a 4-channel Nicolet 440 digital oscilloscope (12 bit vertical resolution) at a sampling rate of 10 M points/s. Both the transducer and the charge amplifier have good linearity, making the load measurement relatively convenient. A typical example of a load signal recorded by the oscilloscope is shown in the lower part of Fig. 4, which composes of a rising segment, corresponding to loading part of an indentation, and a falling portion, referred to as the unloading part of the indentation. Sensitive quartz transducers have also been used in Kolsky pressure bar system to measure elastic waves of low amplitude (e.g., Wasley *et al.*, 1969; Chen *et al.*, 2000). In such cases, typical installation involves sandwiching a piece of quartz in between the two halves of a bar, in the place of a strain gage.

2.5 Data reduction

An optical probe and a high-speed photodiode were used to detect the light intensity due to the moiré fringes that contain the information regarding indenter displacement as described earlier in this section. The optical probe was held fixed and was focused on the mid point (focus point) of the grating window attached to the indentation barrel. After the striker impacts the indenter, the indenter moved at a constant velocity until it contacted the target. At about 1 ms before the indenter impacts the specimen (target), the grating film on the indenter overlaps the grating plate at the focusing point on the window, generating moiré fringes, which shift in a direction perpendicular to the axis of the indenter. The fringe shifting speed is directly proportional to the speed of the indenter. A complete movement of the center of a white fringe to the center of its adjacent black fringe, with respect to the focusing point, corresponds to the change of electrical output signal from a peak (local maximum) to a valley (local minimum). The time associated with this change is exactly the time by which the indenter traveled a distance corresponding to the pitch of the grating (see Eq. (2)).

An example of the indenter movement is illustrated in the upper part of Fig. 4, which also has the corresponding load-time history in the lower part. The moiré fringe profile has a very good "sinusoidal" shape, indicating a very smooth black-white-black moiré fringe transition. The time instances associated with each peak and valley were first determined from the moiré fringe profile in the upper part of the figure. The instance when the indenter changed its direction of movement, i.e., from loading to unloading, was determined by the instance when the maximum load occurred. Once this connection was established between the two curves/profiles, one needs to perform some simple interpolation next. Generally, the time at which the peak load is reached does not correspond to a peak or a valley in the moiré fringe, as can be seen in Fig. 4. Since the resolution of the indentation profile was limited by the pitch (12.5 μm for the example shown in Fig. 4) of the grating used in experiments, the indentation depth associated with the peak load was linearly interpolated with respect to its adjacent peak or valley. Then the indentation depth-time, load-time and load-depth history can be determined at all the times using the peaks and the valleys of the fringe profile. The starting point and the end points may also need to be interpolated. Since the load-time history is a continuous curve, the resolution of the indentation profile was limited by the pitch of the grating used. The velocity at any given instance was computed by differentiating the depth-time profile using a central difference scheme. In general, due to the interpolation used in data extraction, the error associated with the data processing is estimated to be less than half of the pitch, i.e., 6.25 μm. This value is negligible for the indentation at large indentation depth, as shown in Figs. 5 and 6.

3 Materials and specimens

3.1 Bulk metallic glass

The bulk metallic glass used in this investigation has a nominal composition, $Zr_{41.2}Ti_{13.8}Cu_{10.0}Ni_{12.5}Be_{22.5}$, which was originally developed at Caltech (Peker and Johnson, 1993). Vitreloy 1 (commonly referred to as Vit 1) is the trademark (^{TM}) name owned by Amorphous Technologies, Inc., Laguna Niguel, CA, and Howmet Corporation, Greenwich, CT, for the bulk metallic glass $Zr_{41.2}Ti_{13.8}Cu_{10.0}Ni_{12.5}Be_{22.5}$. The processing and physical properties of Vitreloy 1 are well described in the literature (e.g., Johnson, 1999) and the relevant mechanical properties are listed in Table 1. X-ray diffraction studies were conducted on the as-received samples of Vitreloy 1, and the presence of typical broad diffuse peaks and lack of discrete peaks revealed that the material is amorphous.

3.2 Bulk metallic glass composite

An *in-situ* two-phase metallic glass composite was developed at Caltech (Hays *et al.* 2000; Kim, 2001) to enhance the ductility of Vitreloy 1 based materials. The composite has a small amount of niobium in place of some of the titanium in Vitreloy 1. A ductile bcc crystalline dendrite phase (β-phase) nucleates and grows upon cooling the melt at a typical cooling rate of 1-100 K/s. The size, shape and proportion of the ductile bcc phase can be controlled by varying the temperature versus time cooling profile, as well as the atomic volume of the niobium in the composite, and keeping composition of the matrix in the good glass forming range of the Vitreloy family. A good example of the β-phase composites has a composition of $(Zr_{75}Ti_{18.34}Nb_{6.66})_{75}(Be_9Cu_5Ni_4)_{25}$, i.e., $Zr_{56.2}Ti_{13.8}Ni_{5.0}Cu_{6.9}Ni_{5.6}Be_{12.5}$ (Hays *et al.*, 2000; Kim, 2001). Such a composite made in the laboratory has an atomically sharp crystal-glass interface and a dendrite phase whose primary axis and radius are around 100 μm and 5 μm respectively.

The β-phase Vitreloy 1 composite (referred to as β-Vit 1 thereafter) used in this study was manufactured by Howmet Corporation with a nominal composition of $Zr_{56.2}Ti_{13.8}Ni_{5.0}Cu_{6.9}Ni_{5.6}Be_{12.5}$. The composite has a flake-like ductile bcc phase of a smaller characteristic size, instead of a dendrite phase present in the material prepared in a research laboratory. This was the effect of higher quenching rate achieved by Howmet (>100 K/s). The volume fraction of the β-phase in the composite is approximately 0.25. The relevant physical and mechanical properties of β-Vitreloy 1 composite (Kim, 2001) are listed in Table 1.

3.3 Specimen preparation

The as-received rectangular Vitreloy 1 plates and β-phase Virtreloy 1 plates had dimensions of 100 mm x 200 mm x 4 mm and 20 mm x 200 mm x 3.5 mm, respectively. One side of each plate was carefully lapped and polished to a surface finish of 5 microns. The plates were then electrical discharge machined (EDM) or cut by a low speed diamond saw into smaller rectangular plates with a nominal size of 12 x 12 mm (~0.5 x 0.5 inch). The cut edges of each specimen were also finished using 600 grit polishing paper. Before each indentation experiment, the specimen was ensured of good contact with the load transducer either by applying a thin layer of grease or super glue, and the contact surface was subsequently cleaned after each experiment.

4 Experimental results

Dynamic indentation on Vit 1 metallic glass and β-Vit 1 composite were performed at indentation velocities of up to 10 m/s. Macro static indentation experiments were also performed to compare with the dynamic indentation results. The dynamic indentation depth-time history, load-time history of dynamic indentation experiments were directly deduced from the moiré fringe and quartz load transducer signals.

4.1 Indentation profiles

The indentation profiles of Vit 1 and β-Vit 1 at various indentation velocities are shown in Figs. 5 and 6 respectively. The initial indentation velocity was varied from quasi-static up to around 10 m/s. Only typical experimental results are presented here. Indentation velocities of 4.5, 5.4, 6.1, 8.5 and 10 m/s were used in the experiments for Vit 1, while indentation velocities of 1.7, 2.8, 4.9, 5.1, 5.6, 7.1, 7.7, 9.1 and 9.9 m/s were employed for β-Vit 1. For each initial indenter velocity, in addition to the variations of load and depth with time, the variation of the indentation speed is also plotted as a function of time. Also, the indentation load in the loading as well as the unloading process is plotted as a function of the indentation depth. The indentation depth-time curve can be further understood by examining the corresponding velocity-time history. The variation of the indentation velocity with respect to time is not linear: the rate at which the indenter velocity reduces increases with time until the peak load was reached. The indenter velocity is zero when the indentation load (displacement) reaches its maximum value. Subsequently, the indenter rebounds and gains a constant velocity after it separates from the target. As illustrated by all the load-time curves, initially the increase in load was gradual during the early stages of the loading period, then increased approximately linearly with time except during the final stage of the loading when the load nearly leveled off and reached its maximum. The resulting load-depth (indentation) curves at different velocities are summarized in Fig. 7 for Vit 1 and in Fig. 8 for β-Vit 1.

4.2 Microscopic examination of flow

Metallic glass exhibits catastrophic shear failure at room temperature under uniaxial stress, making the measurement of post-yield response of the material quite difficult. By using indentation, due to the presence of self- confinement, the propagation of shear localization can be suppressed, allowing the occurrence of multiple shear bands, which are responsible for the macroscopically perceived inelastic deformation. This is in contrast to crystalline materials in which dislocations are responsible for plastic deformation.

In all the experiments, the indentation craters were well preserved and the specimens remained intact. The flow mechanisms in the metallic glass materials subjected to dynamic indentation were examined using scanning electron microscopy (SEM). A typical shear band pattern of Vit 1 on the surface of indentation crater is shown in Fig. 11 where the material had been subjected to impact at a velocity of 10 m/s. The total area of the shear bands is much smaller than that of the total area of the crater of the indent. The projection of the average shear band spacing and the shear band thickness onto the crater surface are less than 10 microns and less than 1 micron, respectively. Near the edge of the indentation crater (Figs. 11(a) and (b)), shear bands that were formed intersected with the crater surface along the radial direction on the surface. The orientations of the planes of shear bands could not be observed using SEM. At a location in between the edge and the center of the crater, as shown in Fig. 11(c), shear bands form predominantly in two directions, one along the radial direction, and the other along a direction at an angle of 40-50° with respect to the radial direction. At the center of the crater, as shown in Fig. 11 (d), the shear bands form a network in which there is no primary/dominant surface shear slip direction. Different stress states at different locations on the crater surface might account for the different shear band patterns. The hydrostatic pressure near the center of the indentation is somewhat higher than in regions away from the center, and this might also be responsible for the different shear band patterns observed here. The overall inelastic deformation is due to the accumulation of highly localized shear slip, which has been extensively studied by Donovan and Stobbs (1981) in a metallic glass, $Ni_{76}P_{24}$. The static micro-indentation investigation by Vaidyanathan *et al.* (2001) on Vitreloy 1 indicates that shear band "rings" formed outside and near the indentation crater. The presence of shear bands inside the crater was not reported in this study.

Originating from the study on polymer materials (e.g., Knauss and Emri, 1981; Losi and Knauss, 1992), evolution of free volume has been widely accepted as a key to the flow behavior of a metallic glass. The general nature of the pressure (or normal stress) dependence of metallic glass is "similar" to that of polymer in spite of its long molecular chains. Argon and Shi (1982) used a bubble model for metallic glass to elucidate the net volume increase due to shearing deformation. The sensitivity on pressure of an operating shear band is probably because the atoms inside the band are more dilated than the ones in the region outside where shear strain is small such that it is reversible (i.e., elastic). Metallic glass typically has a Poisson's ratio of 0.35 at room temperature while an incompressible material has a Poisson's ratio approaching 0.5, suggesting that metallic glasses are not "ideally" packed and there is room to compress the glasses into denser state. The inelastic flow and the viscous flow are closely related to each other, and the process involves stress-driven diffusional jumps of single atoms (Spaepen, 1977) and shear deformation of a small cluster of atoms (Argon, 1979). Homogeneous deformation occurs at high temperatures and low strain rates where stress induced structural disorder can be diffusively relaxed. On the other hand, inhomogeneous deformation at low temperatures and high strain rates is due to shear localization which introduces structural disorder in narrow shear bands that can cause catastrophic shear failure if deformed uniaxially, or macroscopic inelastic deformation due to the surrounding confinement if deformed multiaxially, as is the case for dynamic indentation.

Figure 12 (a) shows the microstructure of the β-Vit 1 with flake-like bcc crystals. The surface deformations beneath a dynamic indenter (impact velocity, 10 m/s) are illustrated in Figs. 12 (b) and (c) where shear steps in between crystalline β-phase particles are visible along the edge of the indentation crater. The shear band patterns in the indentation carter were not quite clear as a result of surface roughness. Nevertheless, since the composite exhibits considerable inelastic deformation under bending and uniaxial loading conditions, it is instrumental to review the function of ductile phase in the composite studied by previous researchers. Pekarskaya *et al.* (2001) clearly demonstrated using transmission electron microscopy (TEM) that shear bands of thickness as small as 10 nm exists in thin Vit 1 samples strained *in-situ*. Shear band branching was also observed as a mechanism of enhanced inelasticity. Changes in the microstructure of the shear band was also observed: less dense structure occurs in the shear band region when compared with region that is not localized. In some cases, when large amount of shear deformation occurred in the glass matrix, the shear deformation was transmitted to the ductile phase due to dislocation mobility in the ductile phase. Small shear deformation tends to delocalize the deformation in the ductile phase. An investigation by Hays *et al.* (2000) on the inelastic deformation of a bulk β-Vit 1 (Fig. 12 (d)) in bending indicated that the ductile phase in the composite arrests shear bands and enhances the overall inelasticity of the composite. The thickness of shear band is larger in this case (~500 nm), indicating the effect of the specimen thickness on localization phenomenon.

5 Analysis and modeling

As mentioned earlier, a major objective of performing dynamic indentation on Vit 1 and β-Vit 1 is to study the deformation behavior of these materials at strains beyond yield. The indentation profiles obtained from the experiments were regarded as "intermediate" results because further analysis is necessary to extract more useful information regarding the flow behavior as well as pressure/rate sensitivity of materials. Compared with uniaxial dynamic loading in a Kolsky bar experiment, dynamic indentation load-depth profile unavoidably possesses some drawbacks in studying the flow behavior as well as the pressure/rate effect of materials due to the complex three-dimensional nature of stress and strain distributions in the target. However, its unique role in studying the mechanical behavior of metallic glasses is because of the self-confinement that can suppress shear failure. This section begins with the analysis of the mechanical parameters that can be obtained from dynamic indentation. In the following part of this section, a simple method for estimating the strain rate sensitivity of materials using dynamic indentation is introduced and the strain rate sensitivity of Vit 1 and β-Vit 1 are examined. In the last part of the section, appropriate flow criterion for the bulk metallic glass and its composite were examined using numerical simulation of the experiments.

5.1 Parametric analysis

Fick's Law, $P = Ch^2$, has been widely used to describe sharp indentation in materials, where P and h are load and depth of indentation, respectively, and C is a material constant. Davis and Hunter (1960) and Andrews *et al.* (2002) employed rigid body dynamics and the Fick's law to model dynamic indentation process. For rate independent materials, they calculated the maximum load,

$$P_{\max} = C^{1/3}\left(\frac{3mV_{ini}^2}{2}\right)^{2/3} \propto V_{ini}^{4/3} \tag{8}$$

where m is the mass of the indenter and V_{ini} is its initial velocity. C is the material parameter in the widely used Fick's law. C is a function of the Young's modulus and the flow stress of the material, indenter geometry, etc. The functional relationship of P_{max} versus V_{ini} from the current experiments is plotted in Fig. 7(a) and it is described by the $P \propto V^{4/3}$ relation very well, in agreement with Eq. (8). Several researchers have proposed formulas to estimate the material parameter, C. For the Berkovich indenter, Suresh and coworkers suggested (Giannakopoulos and Suresh, 1999)

$$C = M_1 \sigma_{0.29} \left(1 + \frac{\sigma_y}{\sigma_{0.29}}\right)\left(M_2 + \ln\left(\frac{E^*}{\sigma_y}\right)\right) \tag{9}$$

where M_1=6.618, M_2= -0.875, σ_y is the yield stress, $\sigma_{0.29}$ is the flow stress at a characteristic plastic strain of 0.29, and $E^* = \left(\frac{1-\nu^2}{E} + \frac{1-\nu_{ind}^2}{E_{ind}}\right)^{-1}$, where E and ν are Young's modulus and Poisson's ratio of the material, respectively, and the subscript *ind* refers to indenter material. Johnson (1970) proposed a model,

$$C = \frac{2\pi\sigma_y}{3\tan^2\beta}\left(1 + \ln\left(\frac{E}{3\sigma_y}\tan\beta\right)\right), \tag{10}$$

where β =19.7 for the Berkovich indenter. Larsson *et al.* (1996) provided an empirical relation based on their simulations results for indentation by a Berkovich indenter on some alloys,

$$C = 1.273(\tan 24.7^\circ)^{-2}\sigma_y(1 + \sigma_r/\sigma_y)\left(1 + \ln\left(\frac{E\tan 24.7^\circ}{3\sigma_y}\right)\right) \tag{11}$$

where σ_r is the flow stress at a plastic strain of 0.3. The values of C based on the above formulas were compared with the value of C determined from the present experimental data, and the static micro indentation work of Vaidyanathan *et al.* (2001) are listed in Table 2. One observes differences among the experimentally obtained values and the predicted values using Eqs. (9)-(11): the predicted values are much smaller. The reason for this discrepancy may be due to the fact that the flow behavior of metallic glasses is not considered in these above stated models. Bulk metallic glasses do not exhibit strain hardening but have pressure/normal stress dependence of flow stress.

From the indentation data, Young's modulus (E^*) can be estimated using the following equation (Giannakopoulos and Suresh, 1999),

$$E^* = \left(\frac{1-\nu^2}{E} + \frac{1-\nu_{ind}^2}{E_{ind}} \right)^{-1} = \frac{1}{c^* \sqrt{A_{\max}}} \left(\frac{dP}{dh} \right) = \frac{1}{c^* \sqrt{\pi h_{\max}^2 / \tan^2 \beta}} \left(\frac{dP}{dh} \right), \tag{12}$$

where $\beta = 19.7^{\circ}$ and $c^* = 1.167$ for the Berkovich indenter, $A_{\max}$ is the maximum projected contact area and $\frac{dP}{dh}$ is the unloading slope of the load-depth curve. From the experimental load-depth curves, the computed $\frac{dP}{dh}$ values at V=10.5 m/s for Vit 1 and at V=9.11 m/s for β-Vit 1 are 2.66×10^8 N/m and 2.45×10^8 N/m, respectively. Thus, one can estimate the values of E^* for Vit 1 and β-Vit 1 to be 115 GPa and 100 GPa respectively assuming ν is known *a priori* (Table 1), and the following values for the indenter, E_{ind}=650GPa and ν_{ind}=0.20. The estimated Young's modulus for the two materials based on Eq. (12) is slightly larger (15%) than their corresponding well-established values shown in Table 1.

5.2 Strain rate sensitivity

The loading duration of a dynamic indentation experiment can be estimated using the following equation of motion in the absence of strain rate effect (see Davis and Hunter, 1960; Johnson, 1970; Giannakopoulos and Suresh, 1999; Andrews *et al.*, 2002),

$$\frac{d^2 h}{dt^2} + \frac{2\pi\sigma_y}{3m \tan^2 \beta} \left[1 + \ln\left(\frac{E}{3\sigma_y} \tan \beta\right) \right] h^2 = 0\,, \tag{13}$$

which immediately leads to the estimation of the loading time (unloading time is not included),

$$t_0 = 1.4\left(\frac{3m}{2V_0}\frac{3\tan^2\beta}{2\pi\sigma_y}\frac{1}{1+\ln(\frac{E}{3\sigma_y}\tan\beta)}\right)^{1/3} \tag{14}$$

where β is an angle associated with the included cone-angle, and $\beta = (180^\circ - 140.6^\circ)/2 = 19.7^\circ$ in the present study, m is the mass of the indenter, σ_y is the yield stress, E is the Young's modulus and V_0 is the initial indentation velocity.

In the experiments, the indentation velocity was varied from quasi-static up to around 10 m/s. For an initial velocity of 10 m/s, the estimated loading time t_0 for Vit 1 using Eq. (14) is 59.7 μs while the experimentally determined value was 59 μs; at a velocity of 4.5 m/s, the estimated loading time is 77.9 μs while the experimentally determined value was 78 μs. The loading time and the total indentation time are plotted in Fig. 7(b). It appears that this estimate of loading time (Eq. (14)) agrees with the experimentally measured values extremely well. The indentation loading time t_0 determined directly from the experiments were in the range of 58 to 76 μs for Vit 1 and 60 to 95 μs for β-Vit 1.

The average strain rate in a dynamic indentation experiment can be estimated by

$$\dot{\varepsilon} = \frac{\varepsilon_c}{t_0} \tag{15}$$

where ε_c is the average characteristic (e.g., effective) strain in the plastic zone beneath the indenter and t_0 is the loading time. According to Tabor (1965), such an average strain does exist in the material beneath the indenter: the value used for the indenter in this study (equivalent to a Berkovich indenter) is around 0.07 ~ 0.10. Hence, the average strain rate in the current investigation fell approximately in the range of 1,000 to 2,000 s^{-1} for both Vit 1 and β-Vit 1, according to Eq. (15).

For rate insensitive materials, many static indentation investigations as well as current experimental study and numerical simulations have confirmed the Fick's law, i.e., load-depth relationship of the form, $P = Ch^2$ (e.g., Giannakopoulos and Suresh, 1999), where C is a function of the indenter shape and the mechanical properties of target material. Considering two indentation experiments with two different peak loads P_1 and P_2 due to two different initial velocities, the work done by the indenter before the unloading are $W_1 = {}^{1}\!/_{3}\,Ch_1^3$ and $W_2 = {}^{1}\!/_{3}\,Ch_2^3$, respectively. The normalized ratio between the two naturally leads to $\frac{W_1 / h_1^3}{W_2 / h_2^3} = 1$. If the flow stress of the target material is rate sensitive, then a rate sensitivity parameter f for the flow stress at an effective dynamic strain rate with respect to a quasi-static strain rate can be defined and approximated by

$$f = \frac{\sigma_{flow}(\dot{\varepsilon}_{dynamic})}{\sigma_{flow}(\dot{\varepsilon}_{static})} = \frac{\frac{1}{h_1^3}\int_0^{h_1} P_1(h, \dot{\varepsilon}_{dynamic})\mathrm{d}h}{\frac{1}{h_2^3}\int_0^{h_2} P_2(h, \dot{\varepsilon}_{static})\mathrm{d}h} \tag{16}$$

where $\dot{\varepsilon}_{static}$ and $\dot{\varepsilon}_{dynamic}$ can be estimated using Eq. (15), $P_1(h, \dot{\varepsilon}_{dynamic})$ and $P_2(h, \dot{\varepsilon}_{static})$ are the static and dynamic load-depth curves at the estimated strain rates $\dot{\varepsilon}_{static}$ and $\dot{\varepsilon}_{dynamic}$, respectively. The above expression is based on the fact that the general shape of the load-depth curve is not seriously altered as a result of rate sensitivity (see Fig. 8 for a schematic illustration of the load-depth curves for rate dependent and rate independent materials), and that average pressure by indentation is proportional to the flow stress at a certain representative strain, which is in the range of 0.07 to 0.10 for the conical indenter employed in the present study.

Quasi-static indentation with average strain rate of around $5\times10^{-3}\,\mathrm{s}^{-1}$ was performed using the same conical indenter used in the dynamic experiments on both Vit 1 and β-Vit 1 and the corresponding load-depth curves are also plotted in Figs. 9 and 10, respectively, for comparison with the dynamic curves. No apparent difference exists between the static and dynamic indentation curves since they all overlap within the experimental error and scatter of the material properties. Comparison of the load-depth indentation curves at different initial velocities as well as the one from quasi-static loading leads to the observation that all the load-depth curves can be described by a unified master curve except that different maximum loads were reached, which can be attributed to the strain rate insensitivity of both materials according to Eq. (16). This is consistent with the results from Kolsky (split Hopkinson) bar experiments which showed that Vit 1 does not manifest any significant strain rate sensitivity for the yield stress for strain rates of up to 2,500 s^{-1} (Bruck *et al.*, 1996; Chapter 2). Preliminary investigation on rate sensitive materials such as oxygen free high purity copper (OFHC copper) has shown that Eqs. (15) and (16) can be used to quantitatively estimate strain rate effect in metals.

The reason why indentation at higher velocities was not pursued is two-fold. First, further increase in the indentation velocity will only increase the average strain rate at a very slow rate according to the estimate by Andrews *et al.* (2001),

$$\dot{\varepsilon}_{eff} \propto V^{1/3} m^{-1/3} . \tag{17}$$

Second, the extremely high yield strength of the materials that are being investigated may cause the indenter to slide along the contact surface at high impact speeds.

5.3 Numerical modeling

Due to the difficulties in directly analyzing and interpreting load-depth curves from dynamic indentation experiments, numerical simulations were employed to assist in the material characterization and in interpreting the experimental data. One of the numerical simulation tools employed in the present study is LS-DYNA (1999), originally developed by Lawrence Livermore National Laboratories and further developed by the Livermore Software Technology Corporation, Livermore, CA. It is an explicit finite element code for analyzing dynamic response of two- and three-dimensional structures. In addition, the ABAQUS/Explicit finite element software (HKS, Inc., Pawtucket, RI) was also employed to use some of its material models. Due to large deformation of the elements beneath the indenter tip, the adaptive mesh feature in ABAQUS/Explicit was invoked to remesh highly distorted elements during the indentation process.

5.3.1 Model geometry

The design of the conical indenter was mainly to utilize its geometrical axisymmetric characteristic and avoid the three-dimensional nature of deformation associated with a Berkovich indenter. To save computational effort, the rectangular specimen used in the experiment is treated as a disk specimen with equivalent area. This simplification is reasonable in the sense that the intense deformation beneath the indenter is confined to a small region in comparison to the in-plane dimensions of the specimen. Therefore, the indentation experiment was numerically modeled as an axisymmetric problem. Otherwise, a fully three-dimensional model needs to have finite elements 20-100 times as many as that used in an axisymmetric problem for the same mesh size. To obtain smooth and converged load-depth curves as well as to reduce the computation time further, finer mesh was employed near the contact zone and the mesh gradually becomes coarser in the region far away from the contact region. Typically, 6,500 four-node linear elements were used in LS-DYNA simulations and 10,880 four-node linear elements were used in ABAQUS/Explicit simulations for the specimen and the minimum element size was about 15 to 19 μm. The bottom of the specimen was held by a rigid surface that was fixed in space corresponding to the load transducer and the rigid block supporting it during the experiments. The conical indenter with a cone (apex) angle of 140.6° was modeled as a rigid body with total mass of 44.8 grams, which corresponds to the mass of the indenter used in experiments. An initial velocity of 5 to 10 m/s was applied to the indenter at the beginning of each simulation. The simulation time was sufficiently long for the indenter to separate from the target, a typical time interval being 100 μs. The time step was calculated automatically by the codes which depends on the minimum element size and the wave speed of the material and varied during the simulation accounting for the distortion of elements. A typical average time step is 1.5 ns and took about 3000 seconds of CPU time to simulate an indentation experiment on a Dell Dimension 4100 workstation equipped with a 800 MHz CPU and 256 MB memory.

5.3.2 Pressure independent J_2 von Mises flow model

In order to determine whether a pressure or normal stress dependency exists for the flow stress, a J_2 von Mises flow model was employed first using the known mechanical properties of Vit 1 and β-Vit 1 whose yield stress, Young's modulus, density and Poisson's ratio are listed in Table 1. The von Mises yield surface characterized by J_2 ($S_{ij}S_{ij}/2$), the second invariant of the deviatoric stress tensor **S**, and for elasto-plastic materials can be written as

$$\left(\frac{3}{2}S_{ij}S_{ij}\right)^{1/2} - \sigma_Y = 0 \tag{18}$$

where σ_Y is the yield stress. The deviatoric stress tensor **S** is defined in terms of the Cauchy stress tensor σ, $S_{ij} = \sigma_{ij} - (\sigma_{kk}/3)\delta_{ij}$, where δ is the Kronecker delta or the identity tensor. No strain hardening is included in the model, which is supported by both uniaxial stress-strain response (Bruck *et al.*, 1994; Kim, 2001; Chapter 2) and physics of deformation for the metallic glass (Donovan and Stobbs, 1981; Pekarskaya *et al.*, 2001).

The effect of specimen size on the load (P)-depth (h) responses of Vit 1 and β-Vit 1 were first examined as depicted in Figs. 13 and 14. Two different specimen dimensions were considered, one corresponding to the actual specimen size (approximated by a disk having a diameter of 12 mm and thickness 3.5 mm) and the other having a larger size of 25.4 mm (1.0 inch) in diameter and 12.7 mm (0.5 inch) thick. The results showed that the influence of the size on the loading part of the depth-load curves is negligible at least up to an indentation velocity of 10 m/s, although a slight deviation in the unloading response is noticeable. Since the unloading process is not of primary concern in the present investigation, which contains information regarding the elastic properties of the target material, the size of the specimen used in the study was found to be acceptable. Further simulations on the interface friction between the indenter and the target revealed that for the indentation cone-angle (140.6°) employed in the experiments, the influence of the friction coefficient ranging from 0 to 1 on the load-depth curve is negligible (less than 1 %). Since the friction coefficient between the indenter and the target materials is typically much smaller than 1.0, this insensitivity alleviates the necessity/difficulty of measuring/characterizing the dynamic friction coefficient. It is also worth mentioning that such insensitivity of the indentation curves to friction is not true for any arbitrary cone angle. For instance, numerical simulation has shown that a cone-angle of 100° may cause large error (more than 10%) if the friction coefficient is not known a priori and could lead to erroneous results.

As stated earlier, a measure for the average strain rate was introduced as a general indication of overall strain variation with time, see Eq. (15). Numerical simulation of a typical dynamic indentation experiment revealed that the strain rate is not a time invariant quantity, i.e., not a constant. For instance, in a region directly underneath the indenter, the effective strain increased at a higher rate during early stages of the indentation than at later stages. Moreover, such a variation is much more pronounced in the region in close proximity to the indenter tip. In essence, the effective strain rate is a function of both time and space. Nevertheless, the concept of average strain rate introduced here is a useful concept in describing the strain rate sensitivity of materials using the dynamic indentation technique.

The simulated load-depth curve at an indentation velocity of 10 m/s is plotted in Fig. 9 for Vit 1 and in Fig. 10 for β-Vit 1. Finite element calculations using the J_2 von Mises model clearly demonstrate the discrepancy between the simulated load-depth curves and the experimentally determined curves. This is similar to the observations by Vaidyanathan *et al.* (2001) in their investigation of Vit 1 using static microindentation. During the indentation experiment, the indenter induces inelastic deformation in the target, resulting in multiaxial and nonuniform strain distribution in a region near the contact area. This deformation is quite different from the stress and strain states achieved in uniaxial loading. The complicated deformation pattern in indentation experiments makes the determination of stress-strain response difficult, although reasonable estimates are still possible using spherical indentation (e.g., Alcala *et al.*, 1998). However, indentation is a suitable method to study the pressure-dependent deformation of bulk metallic glass due to its unique way of exerting local self-confinement induced high pressure. Metallic glass exhibits catastrophic shear failure under uniaxial condition, and, hence, the measurement of post-yield response of the material is quite difficult. Using indentation, the propagation of shear failure due to strain localization can be suppressed, allowing multiple shear bands to contribute to the overall inelastic deformation, similar to crystalline materials in which mobility of large number of dislocations are responsible for plastic deformation. Figures 9 and 10 indicate that the indentation loads from the experiments are larger than those predicted by von Mises models for Vit 1 and β-Vit 1 respectively, for the same indentation depth. This implies a pressure or normal stress dependent model of yield strength is needed. So the assumption of von Mises yield criterion is not appropriate for the bulk Vit 1 and its composite materials. Moreover, for example, the typical Mises stress contour and pressure contour predicted based on Mises model for Vit 1 are shown in Fig. 15, where the hydrostatic pressure underneath the indenter is around 4 GPa. Such high pressures can have dramatic effect on the flow stress of Vit 1 if it is a pressure dependent material. The contour plots will be used later to compare with predictions from a pressure dependent model in the next subsection.

5.3.3 Pressure dependent or normal stress dependent models

To study the effect of pressure dependence on yield stress, a Drucker-Prager model was used to describe the constitutive behavior of metallic glass. The Drucker-Prager model is a generalized von Mises model that considers pressure-dependence of the yield surface, and, for perfectly plastic materials, it can be written as

$$\left(\frac{3}{2}S_{ij}S_{ij}\right)^{1/2} - p\tan\beta - \sigma_Y = 0 \tag{19}$$

where β is the friction angle and p is the equivalent pressure defined as $p = -1/3\,\mathrm{trace}(\boldsymbol{\sigma})$. In the general-purpose finite element package ABAQUS/Explicit, an extended Drucker-Prager model is available, which degenerates to the original Drucker-Prager model when considering associated flow and assuming that the triaxial yield stress in tension is equal to the triaxial yield stress in compression (ABAQUS/Explicit User's Manual, 2001).

Equivalently, the Mohr-Coulomb model may be employed to take into account the pressure-dependence of yield stress in metallic glasses. Drucker-Prager model can be viewed as a smoothed version of the Mohr-Coulomb model. Furthermore, it is more convenient to use Drucker-Prager model in finite element analysis because the sharp corners of the yield surface in Mohr-Coulomb model cannot guarantee a unique plastic flow direction. Another main difference between these two models is that Drucker-Prager model considers the influence of the intermediate principal stress on the yield surface, while the Mohr-Coulomb model does not. The Mohr-Coulomb yield criterion is commonly written as

$$\tau = \tau_0 - \alpha\sigma_\mathrm{n} \tag{20}$$

where τ is the shear stress, τ_0 is the "cohesion" of the material, σ_n is the normal stress, and $\alpha = \tan\phi$ (ϕ is the friction angle in Mohr-Coulomb model) is a dimensionless parameter, commonly referred to as the frictional slope. In general, the Mohr-Coulomb model can be made to correspond to the Drucker-Prager model; for instance, in the case of plane strain deformation, the relationship between the friction angle ϕ in Mohr-Coulomb model and the friction angle β in Drucker-Prager model is (ABAQUS/Explicit User's Manual, 2001)

$$\sin\phi = \frac{\tan\beta}{\sqrt{3 - \frac{1}{3}\tan^2\beta}} \tag{21}$$

where β is the friction angle in the Drucker-Prager model. Simulations were carried out using the Drucker-Prager model in ABAQUS/Explicit for various values of friction angle, β ranging from 0 to 10 degrees. Friction angle of $\beta=0^{\circ}$ corresponds to pressure insensitive yielding model, i.e., von Mises J_2 flow model. The other required material parameters remained the same as before and are listed in Table 1.

In Fig. 16, the predicted indentation (*P-h*) curves for Vit 1 for different impact velocities are compared with experimental results. It reveals that rate-independent Drucker-Prager model is capable of capturing the material response of Vit 1 under dynamic indentation. The pressure-dependent term cannot be neglected in such situations when pressure can be very high due to the contact between the sharp indenter and the specimen. A friction angle of 7° in the model provides a best match between the experiments and the simulation results for Vit 1. This indicates that the J_2 flow model proposed in the previous subsection, which does not account for material pressure dependence, fails to explain the increased indentation load as a result of large hydrostatic pressure underneath the indenter, at a given velocity and indentation depth. The pressure dependent Drucker-Prager model is able to reproduce the load-depth profiles that agree with the experimental results.

Similar results have been obtained for simulations carried out for the composite material, β-Vit 1. The β-Vit 1 composite has a smaller Young's modulus and a smaller yield stress as shown in Table 1. The finite element model cannot take into account the microstructural changes in the material when Vit 1 is replaced by β-Vit 1, but by changing the macroscopic properties of the material, it appears that a smaller friction angle is more appropriate for β-Vit 1. Fig. 17 shows that a friction angle of 3° yields the best correlation between numerical simulation and experiment at impact velocity of about 9 m/s. However, it appears that a larger friction angle (e.g., $\beta=4^{\circ}$) is needed to fit the experimental results better for lower impact velocities. Therefore, a friction angle between 3 and 4° is deemed appropriate for β-Vit 1 in the Drucker-Prager model.

The smaller friction angle for β-Vit 1 in comparison to the corresponding value for Vit 1 (7°) can be attributed to the pressure-insensitive response of the crystalline β-phase particles. It is clearly seen that the prediction from Drucker-Prager model compares with the experimental result much better than the one from the von Mises model.

Figure 18(a) shows a typical Mises stress contour for an initial indenter velocity of 10.5 m/s, at the maximum load, for Vit 1 using Drucker-Prager model, where the mesh has been removed to provide a better view of the contour lines. The maximum Mises stress is above 2.4 GPa, which is much higher than the yield stress under uniaxial loading, 1.9 GPa. This is because the pressure-dependent term $p\tan\beta$ in Eq. (19) results in higher flow stress when the pressure increases. The distribution of Mises stress from the J_2 flow model (Fig. 15(a)) is somewhat similar to that from the Drucker-Prager model (Fig. 18(a)); however, higher flow stresses near the indentation crater occur when using the Drucker-Prager model. The contours of pressure for Vit 1 using Drucker-Prager model is shown in Fig. 18(b). It is seen that large pressure occurs directly beneath the indenter and the maximum pressure is more than twice the maximum Mises stress.

The friction angles β=7° for Vit 1 and β=3 to 4° for β-Vit 1 in the Drucker-Prager model correspond to friction angles ϕ=4.1° ($\alpha = 0.07$) and ϕ=1.7 to 2.3° ($\alpha = 0.03 - 0.04$), respectively, in the Mohr-Coulomb model. The stress state in indentation experiments is not equivalent to plane strain state, but Eq. (21) can be used as an approximate relationship of the friction angles between Drucker-Prager model and Mohr-Coulomb model, for comparison purposes.

Hardness from sharp indentations, such as conical indentation, is conveniently defined as a quantity that is proportional to the ratio of indentation load to contact area. By conducting static micro-indentation on Vit 1 samples, Vaidyanathan *et al.* (2001) found that there was a 20% increase in the hardness of Vit 1 compared with the hardness calculated from the J_2 von Mises model. The present investigation indicates that the hardness increase of Vit 1 compared with the prediction by von Mises model is around 15%, which is slightly less than that of the static indentation. Moreover, the pressure dependence of β-Vit 1 is characterized by around 10% hardness increase, which is weaker than that of Vit 1. Donovan (1989) and Davis and Kavesh (1975) also considered Mohr-Coulomb model to describe the flow criterion of metallic glasses. Vaidyanathan *et al.* (2001) concluded that if Mohr-Coulomb model is used to describe the behavior of Vit 1, the value of α is around 0.13, which is larger than that found in the present study. This is probably due to thermal softening at high strain rates during dynamic indentation. In addition, a hybrid pressure and normal stress dependent model was also suggested (e.g., Donovan, 1989),

$$\tau = \tau_0 + \alpha\sigma_n - \beta p \tag{22}$$

where p is the pressure, and α and β are material constants. However, the current dynamic indentation study cannot be used to distinguish whether a normal stress dependent or a pressure dependent model is a more appropriate description of the overall behavior of the metallic glass and its composite.

The amorphous matrix of the composite, β-Vit 1, is very similar to Vit 1 with slightly different composition $Zr_{47}Ti_{12.9}Nb_{2.8}Cu_{11}Ni_{9.6}Be_{16.7}$ and the ductile phase are bcc crystals with composition of $Zr_{71}Ti_{16.3}Nb_{10}Cu_{1.8}Ni_{0.9}$ (Hays *et al.*, 2000; Kim, 2001). This suggests that the decrease in the pressure dependence of β-Vit 1 compared with Vit 1 can be attributed to the reduced volumetric fraction of the bulk metallic glass (~75%). Examination of the indentation craters also revealed that the deformation of Vit 1 at the edge of the craters was much coarser compared with that of β -Vit 1. Indeed, β-Vit 1 exhibits considerable ductility in comparison with the catastrophic shear failure of Vit 1 under uniaxial loading condition (Hays *et al.*, 2000; Kim, 2001). Unlike the Vit 1 metallic glass, the macroscopic deformation of β-Vit 1 is not only due to the confinement of the surrounding elastic material and high pressure, but also the ability of ductile particles to deform, withstanding shear offset due to terminating shear bands and transferring otherwise highly unstable shear bands into the ductile particles, which act as barriers to abrupt failure (Pekarskaya *et al.*, 2001).

6 Conclusions

One of the unique deformation characteristics of a bulk metallic glass is the shear localization of the material in response to external mechanical loading. Since metallic glasses fail by catastrophic shear failure immediately after yielding under uniaixal loading, alternative techniques are needed for studying their post yield behavior and establishing constitutive laws. Indentation technique provides self confinement which enhances the macroscopic inelastic flow of metallic glasses through multiple shear band formation. This technique is also suitable for characterizing the pressure dependence of this class of materials. The following conclusions are based on a combined experimental and numerical investigation of *dynamic* indentation on a bulk metallic glass, Vitreloy 1 and its composite with ductile phase as reinforcement.

1. A new dynamic indentation technique was developed as a complementary tool to static indentation to investigate the flow behavior of a Zr-based bulk metallic glass and its β-phase metallic glass composite. A key feature of the indentation apparatus is the use of the moiré fringe as a non-contact dynamic displacement transducer superior to other motion sensors under dynamic loading conditions.
2. It was deduced from the indentation experiments that the flow behavior of both Vit 1 and β-Vit 1 are insensitive to strain rate in the range from quasi-static up to 2,000 s^{-1}. Localized shear bands were observed at the surface of the indentation craters, although no catastrophic shear failure occurred due to the self-confining effect of the elastic material surrounding the inelastic region. Introducing ductile particle barriers in β-Vit 1 composite made the shear failure less probable as compared with Vit 1, as revealed by microstructural examination.

3. Numerical simulations were performed to model the constitutive behavior of the metallic glass and its composite. Pressure independent material models such as the J_2 von Mises model were found incapable of capturing the experimentally measured load-depth curves. It was found that the Drucker-Prager model which considers pressure-dependence of the yield surface is able to simulate the mechanical response of Vit 1 and β-Vit 1 in dynamic indentation experiments. A friction angle of 7° was found to be appropriate for Vit 1 in the Drucker-Prager model. But a smaller angle, 3° to 4°, appears to be suitable to describe the behavior of the composite β-Vit 1, which should be attributed to the pressure-insensitivity of the crystalline β-phase particles. The parameters of Drucker-Prager model have also been converted to corresponding parameters in Mohr-Coulomb model. The corresponding parameters for the frictional slope are $\alpha = 0.07$ for Vit1 and $\alpha = 0.03 - 0.04$ for β-Vit1.
4. Whether a pressure or normal stress dependent material model is more appropriate is inconclusive based on the current investigation.

One of the original goals of this dynamic indentation study is to determine the dynamic stress (dynamic hardness)-strain relations since different representative strains and representative rates can be obtained by varying the cone angle of the indenter. This is possible using sharp indenters if the friction of between the indenter and the target can be neglected. However, numerical analyses show that as the cone angle decreases, friction has a dramatic effect on the load-depth curve, leading to unreliable stress-strain curves. Nevertheless, one might employ *spherical* indentation technique to estimate the stress-strain curve (see Sundararajan and Shewmon, 1983).

Appendix Governing equations for the geometric moiré technique

The derivation of the governing equations of the geometric moiré technique is briefly described here, following closely the treatment by Guild (1960). Assume that there are two grating patterns with equidistant straight lines of slightly different pitches a_1 and a_2. Suppose in a rectangular coordinate system x_1ox_2, grating with pitch a_1 is placed with its lines parallel to the x_2 axis while the other grating with pitch a_2 is placed in such a way that its lines are inclined at angle θ counterclockwise to the x_2 axis. The vertical grating can be described by $x_1 = n_1\, a_1$, where n_1 is an integer prescribing the order of a line in its family. The other grating pattern can be described by another set of equations given by $n_2a_2 = x_1 \cos\theta + x_2 \sin\theta$, where n_2 is an integer prescribing the order of a line in its family.

One defines the origin of the system to be the intersection of line $n_1 = 0$ and line $n_2 = 0$. The moiré fringe that passes through the origin is regarded as the zeroth order fringe. This leads to the observation that all the intersection points along the zeroth order fringe have the same property that, $n_2 - n_1 = 0$. Consequently, a generalized fringe order can be defined as $N = n_2 - n_1$. A general expression for a fringe of Nth order consists of locus of points for which the following equation is satisfied:

$$(a_1 \cos\theta - a_2)x_1 + \sin\theta a_1 x_2 = N a_1 a_2 . \tag{A1}$$

If the relative rotation between the gratings are very small such that θ<<1, (A1) can be simplified to a linear relation,

$$(a_1 - a_2)x_1 + a_1 x_2 \theta = N a_1 a_2 \qquad (\theta << 1). \tag{A2}$$

If the two gratings are identical, i.e., $a_1 = a_2 = a$, the orientation angle ϕ of the moiré fringes to the x_1 axis is

$$\phi = \tan^{-1}\left(\frac{a_2 - a_1}{a_1\theta}\right) = 0\,. \tag{A6}$$

In addition, the most important parameter, *i.e.*, the distance between the adjacent Moiré fringes, can be expressed as

$$d = \frac{a_1 a_2}{\sqrt{(a_1 - a_2)^2 + a_1^{\,2}\theta^2}} = \frac{a}{\theta} \qquad (\theta << 1). \tag{A7}$$

Equations (A6) and (A7) are the basic governing equations for the geometric moiré technique employed in the present study.

References

ABAQUS/Explicit User's Manual, Version 6.2, Hibbitt, Karlsson & Sorensen, Inc.(2001).

Alcala, J., Giannakopoulos, A. E. and Suresh, S., Continuous measurements of load-penetration curves with spherical microindenters and the estimation of mechanical properties, J. Mater. Res., **13** (5), 1390-1400 (1998).

Andrews, E. W., unpublished results (2001).

Andrews, E. W., Giannakopoulos, A. E., Plisson, E. and Suresh, S., Analysis of the impact of a sharp indenter, Int. J. Solids Struct., **39** (2), 281-295 (2002).

Anton, R. J. and Subhash, G., Dynamic Vickers indentation of brittle materials, Wear, **239**, 27-35 (2000).

Argon, A. S., Plastic deformation in metallic glasses, Acta Metall., **27**, 47-58 (1979).

Argon, A. S. and Shi, L. T., Analysis of plastic flow in an amorphous soap bubble raft by the use of an inter-bubble potential, Philos. Mag., **A46** (2), 275-294 (1982).

Atkins, A. G. and Tabor, D., Plastic indentation in metals with cones, J. Mech. Phys. Solids, **13**, 149-164 (1965).

Barker, L. M. and Hollenbach, R. E., Laser interferometer for measuring high velocities of any reflecting surface, J. Appl. Phys., **43** (11), 4669-4676 (1972).

Barker, L. M. and Hollenbach, R. E., System for measuring the dynamic properties of materials, Rev. Sci. Instrum., **35** (6), 742-746 (1964).

Bhattacharya, A. K. and Nix W. D., Finite-element analysis of indentation experiments, Int. J. Solids Struct., **24** (9), 881-891 (1988).

Bhattacharya, A. K. and Nix, W. D., Finite-element analysis of cone indentation, Int. J. Solids Struct. **27** (8), 1047-1058 (1991).

Biwa, S. and Storakers, B., An analysis of fully plastic Brinell indentation, J. Mech. Phys. Solids, **43** (8), 1303-1333 (1995).

Bruck, H. A., Christman, T., Rosakis, A. J. and Johnson, W. L., Quasi-static constitutive behavior of $Zr_{41.25}Ti_{13.75}Ni_{10}Cu_{12.5}Be_{22.5}$ Bulk amorphous-alloys, Scripta Metall., **30** (4), 429-434 (1994).

Bruck, H. A., Rosakis, A. J. and Johnson, W. L., The dynamic compressive behavior of beryllium bearing bulk metallic glasses, J. Mater. Res., **11** (2), 503-511 (1996).

Chaudhri, M. M., Subsurface plastic strain distribution around spherical indentation in metals, Phil. Mag. **A74** (5), 1213-1224 (1996).

Chaudhri, M. M., Subsurface strain distribution around Vickers hardness indentations in annealed polycrystalline copper, Acta Mater. **46** (9), 3047-3056 (1998).

Chen, W., Lu, F. and Zhou B., A Quartz-crystal-embedded split Hopkinson pressure bar for soft materials, Exp. Mech., **40** (1), 1-6 (2000).

Cloud, G., Optical methods of engineering analysis, Cambridge University Press (1998).

Costin, L. S. and Duffy, J., The effect of loading rate and temperature on the initiation of fracture in a mild rate sensitive steel, J. Eng. Mater. Tech., **101**, 258-264 (1979).

Costin, L. S., Duffy, J. and Freund, L. B., Fracture initiation in metals under stress wave loading conditions, p301-318, *Fast Fracture and Crack Arrest*, ASTM STP 627 (Hahn, G.T. and Canine, M.F. Eds.), American Society for Testing and Materials, Chicago (1976).

Davis, C. D. and Hunter, S. C., Assessment of the strain rate sensitivity of metals by indentation with conical indenters, J. Mech. Phys. Solids, **8,** 235-254 (1960).

Davis, L. A. and Kavesh, S., Deformation and fracture of an amorphous metallic alloy at high pressure, J. Mater. Sci**.,** **10**, 453-459 (1975).

Doerner, M. F. and Nix, W. D., A method for interpreting the data from depth-sensing indentation instruments, J. Mater. Res., **1** (4), 601-609 (1986).

Donovan, P. E., A yield criterion for $Pd_{40}Ni_{40}P_{20}$ metallic glass, Acta Metall., **37** (2), 445-456 (1989).

Donovan, P.E. and Stobbs, W. M., The structure of shear bands in metallic glasses, Acta. Metall., **29**, 1419-1436 (1981).

Dugdale, D. S., Cone Indentation experiments, J. Mech. Phys. Solids, **2,** 265-277 (1954).

Giannakopoulos, A. E. and Larsson, P.-L., Analysis of pyramid indentation of pressure-sensitive hard metals and ceramics, Mech. Mater., **25**, 1-35 (1997).

Giannakopoulos, A. E., Larsson, P.-L. and Vestergaard, R., Analysis of Vickers indentation, Int. J. Solids Struct., **31** (9), 2679-2708 (1994).

Giannakopoulos, A. E. and Suresh, S., Determination of elastoplastic properties by instrumented sharp indentation, Scripta Mater., **40** (10), 1191-1198 (1999).

Guild, J., Diffraction gratings as measuring scales: practical guide to the metrological use of moiré fringes, Oxford University Press, London (1960).

Guild, J., The interference systems of crossed diffraction gratings: theory of moiré fringes, Clarendon Press, Oxford (1956).

Hardy, C., Baronet, C. N. and Tordion, G. V., The elastic-plastic indentation of a half-space by a rigid sphere, Int. J. Num. Meth. Eng., **3**, 451-462 (1971).

Hays, C. C., Kim, C. P. and Johnson, W. L., Microstructure controlled shear band pattern formation and enhanced plasticity of bulk metallic glasses containing in situ formed ductile phase dendrite dispersions, Phys. Rev. Lett. **84** (13), 2901-2904 (2000).

Holister, G. S. and Luxmoore, A. R., The production of high-density Moiré grids, Exp. Mech., **8**, 210-216 (1968).

Inoue, A., Bulk amorphous alloys: preparation and fundamental characteristics, Trans Tech Publications, Switzerland, 1998.

Jayaraman, S., Hahn, G. T., Oliver, W. C. and Bastias, P. C., Determination of monotonic stress-strain curve of hard materials from ultra-low-load indentation tests, Int. J. Solids Struct., **35** (5-6), 365-381 (1998).

Johnson, K. L., The correlation of indentation experiments, J. Mech. Phys. Solids, **18,** 115-126 (1970).

Johnson, W. L., Bulk glass-forming metallic alloys: science and technology, MRS Bull., **24** (10), 42-56 (1999).

Kim, P., Ductile phase reinforced bulk metallic glass composites formed by chemical partitioning, Ph.D. thesis, California Institute of Technology (2001).

Knauss, W. G. and Emri, I. J., Non-linear viscoelasticity based on free-volume consideration, Comp. Struct., **13**(1-3), 123-128 (1981).

Koeppel, B.J. and Subhash, G., Characteristics of residual plastic zone under static and dynamic Vikers indentations. Wear, **224**, 56-67 (1999).

Kolsky, H., An investigation of the mechanical properties of materials at very high rates of loading, Proc. R. Soc., London, **B62**, 676-700 (1949).

Larsson, P.-L., Giannakopoulos A. E., Soderlund, E., Rowcliffe, D. J. and Vestergaard, R., Analysis of Berkovich indentation, Int. J. Solids Struct., **33** (2), 221-248 (1996).

Lee, C. H., Masaki, S. and Kobayashi S., Analysis of ball indentation, J. Mech. Phys. Solids, **14,** 417-426 (1972).

Lockett, F. J., Indentation of a rigid/plastic material by a conical indenter, J. Mech. Phys. Solids, **11,** 345-355 (1963).

Losi, G. U. and Knauss, W. G., Free volume theory and nonlinear thermoviscoelasticity, Polym. Eng. Sci., **32** (8), 542-557 (1992).

LS-DYNA keyword user's manual, Version 950, Livermore Software Technology Corporation, (1999).

Mok, C. H. and Duffy, J., The behavior of metals at elevated temperatures under impact with a bouncing ball, Int. J. Mech. Sci., **6**, 161-175 (1964).

Mok, C. H. and Duffy, J., The dynamic stress-strain relation of metals as determined from impact tests with a hard ball, J., Int. J. Mech. Sci., **7**, 355-371 (1965).

Mulhearn, T. O., The deformation of metals by Vickers-type pyramidal indenters, J. Mech. Phys. Solids, **7,** 85-96 (1959).

Nobre, J. P., Dias, A. M. and Gras, R., Resistance of a ductile steel surface to spherical normal impact indentation: use of a pendulum machine, Wear, **211** (2), 226-236 (1997).

Oliver, W. C. and Pharr, G. M., An improved technique for determining hardness and elastic-modulus using load and displacement sensing indentation experiments, J Mater. Res., **7** (6), 1564-1583 (1992).

Patorski, K., Handbook of the Moiré fringe technique, Elsevier (1993).

Pekarskaya, E., Kim, P. and Johnson W.L., *In-situ* transmission electron microscopy studies of shear bands in a bulk metallic glass based composites, J. Mater. Res., **16** (9), 2513-2518 (2001).

Peker, A. and Johnson, W. L., A highly processable metallic glass: $Zr_{41.2}Ti_{13.8}Cu_{12.5}Ni_{10.0}Be_{22.5}$, Appl. Phys. Lett., **63**, 2342-2344 (1993).

Rice, M. H., Capacitor technique for measuring the velocity of a plane conducting surface, The Review of Scientific Instruments, **32** (4), 449-451 (1961).

Samuels, L. E. and Mulhearn, T. O., An experimental investigation of the deformed zone associated with indentation hardness impressions, J. Mech. Phys. Solids, **5,** 125-134 (1957).

Spaepen, F., A microscopic mechanism for steady state inhomogeneous flow in metallic glasses, Acta. Metall., **25**, 407-415 (1977).

Subhash, G., Koeppel, B. J. and Chandra, A., Dynamic indentation hardness and rate sensitivity in metals, J. Eng. Mater. Tech., **121**, 257-263 (1999).

Sundararajan, G. and Shewmon, P. G., The use of dynamic impact experiments in the determination of the strain rate sensitivity of metals and alloys, Acta. Metall., **31**, 101-109 (1983).

Tabor, D., A simple theory of static and dynamic hardness, Proc. R. Soc., **A192**, 247 (1948).

Tabor, D., Indentation hardness: fifty years on - A personal review, Philos. Mag., **A74** (5), 1207-1212 (1996).

Tabor, D., The hardness of metals, Claredon Press, Oxford (1951).

Tirupataiah, Y. and Sundararajan, G., A comprehensive analysis of the static indentation process, Mater. Sci. Eng., **91**, 169-180 (1987).

Tirupataiah, Y. and Sundararajan, G., A Dynamic indentation technique for the characterization of the high-strain rate plastic-flow behavior of ductile metals and alloys, J Mech. Phys. Solids, **39** (2), 243-271 (1991).

Vaidyanathan, R., Dao, M., Ravichandran, G. and Suresh, S., Study of mechanical deformation in bulk metallic glass through instrumented indentation, Acta Mater. **49** (18), 3781-3789 (2001).

Wasley, R. J., Hoge, K. G. and Cast, J. C., Combined strain gauge-quartz crystal instrumented Hopkinson split bar, The Review of Scientific Instruments, **40** (7), 889-894 (1969).

Table 1. Physical and mechanical properties of Vit 1 and β-Vit 1 composite

Properties	Vit 1 1	β-Vit 1
Density (g/cm^3)	6.0	6.2
Young modulus (GPa)	96[a]	80[a]
Shear modulus (GPa)	34[a]	29[a]
Poisson's ratio	0.36[a]	0.37[a]
Elastic strain limit	0.02[b]	0.018[c]
Tensile yield strength (GPa)	1.90[b]	1.45[c]
Vickers hardness (kg/mm^2)	534[d]	–
Plane strain fracture toughness (MPam$^{1/2}$) at loading rate of 10^{-2} MPa m$^{1/2}$s^{-1}	~55[e]	–
Dynamic fracture toughness (MPam$^{1/2}$) at loading rate of 10^4 MPa m$^{1/2}$s^{-1}	~50-70[e]	–
Dynamic fracture toughness (MPa m$^{1/2}$) at loading rate of 10^7 MPa m$^{1/2}$s^{-1}	~150-300[e]	–
Charpy Impact resistance (J)	~8.0[c]	~24.0[c]

[a]deduced from ultrasonic measurements; [b]see Chapter 2; [c]Kim, 2001; [d]Conner, 1998; [e]Owen *et al.*, 1998.

Table 2. Coefficient C of the Fick's Law, $P=Ch^2$, for indentation (unit: GPa)

	Eq. (9)[a]	Eq. (10)[b]	Eq. (11)[c]	This study	Micro indentation [d]
Vit 1	80	86	69	117	121
β-Vit1	67	73	59	96	N/A

[a] Giannakopoulos and Suresh, 1999; [b] Johnson, 1970; [c] Larsson *et al.*, 1996; [d] Vaidyanathan *et al.*, 2001.

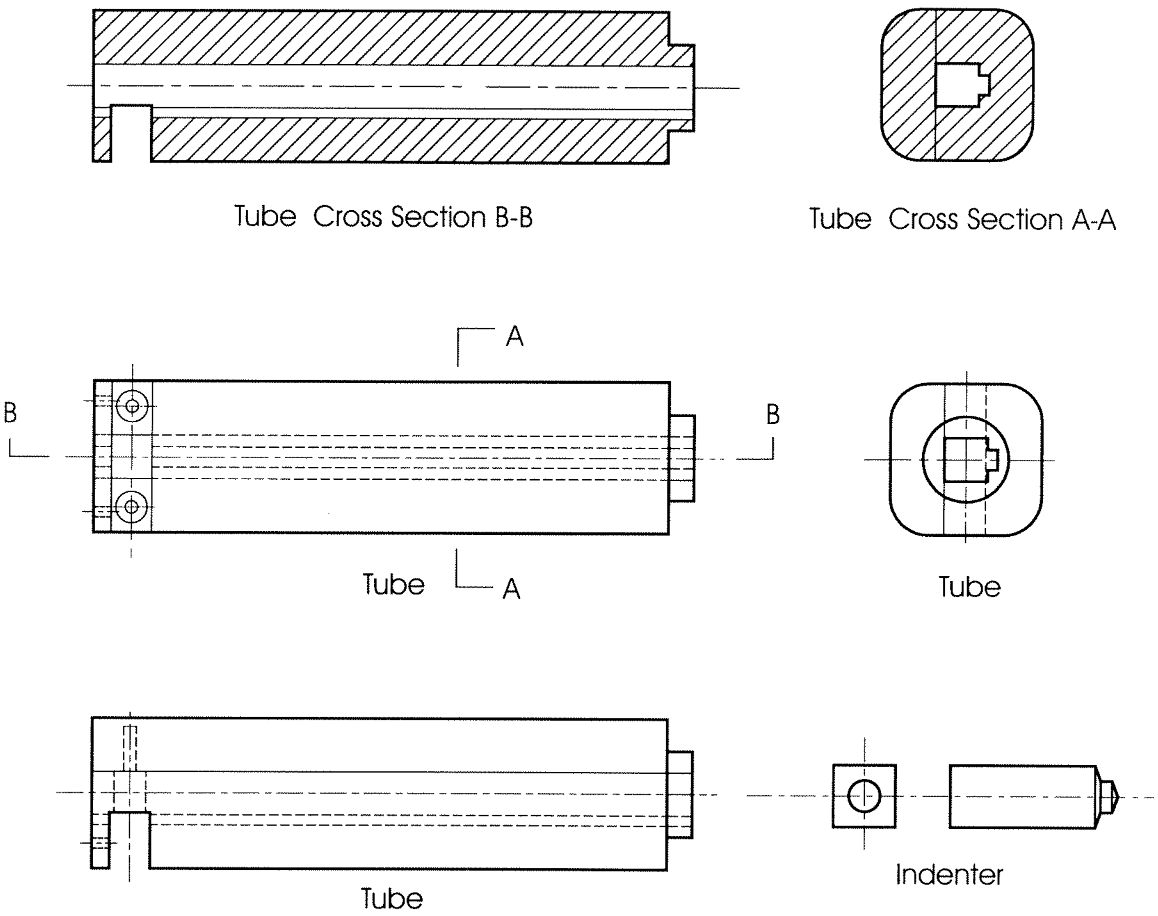

Figure 1. Geometry of the conical indenter and the barrel for launching the indenter.

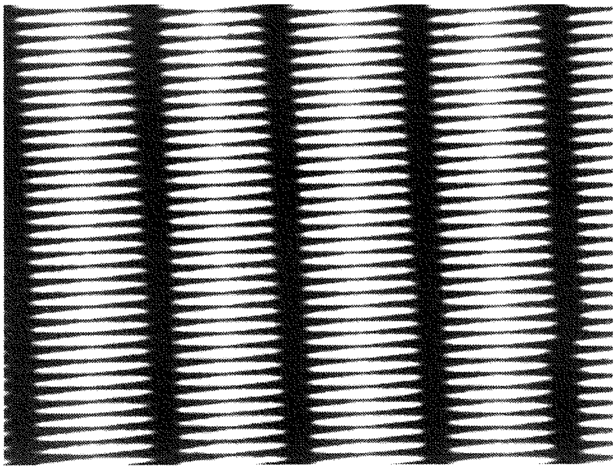

(a) 250 lines per inch

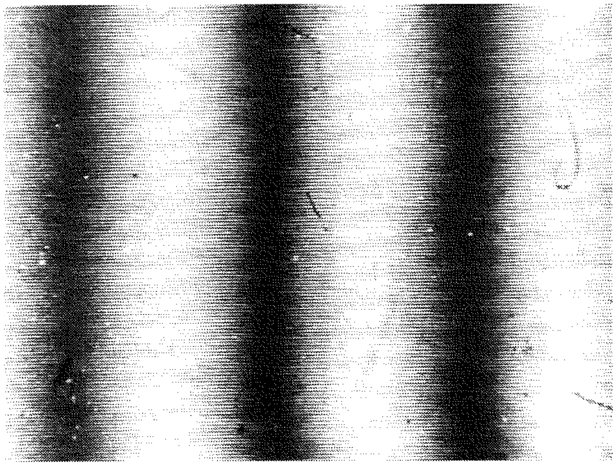

(b) 40 lines per mm (1016 lines per inch) grating with a small rotation angle (around 3^{o})

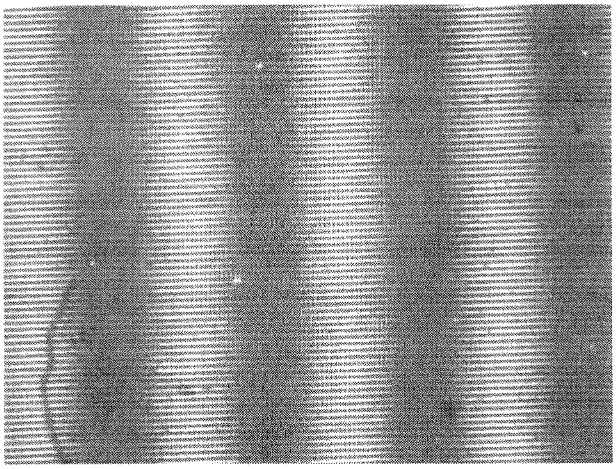

(c) 40 lines per mm (1016 lines per inch) with a large rotation angle (around 6^{o})

Figure 2. Geometric moiré fringe pattern for different line densities and rotation angles.

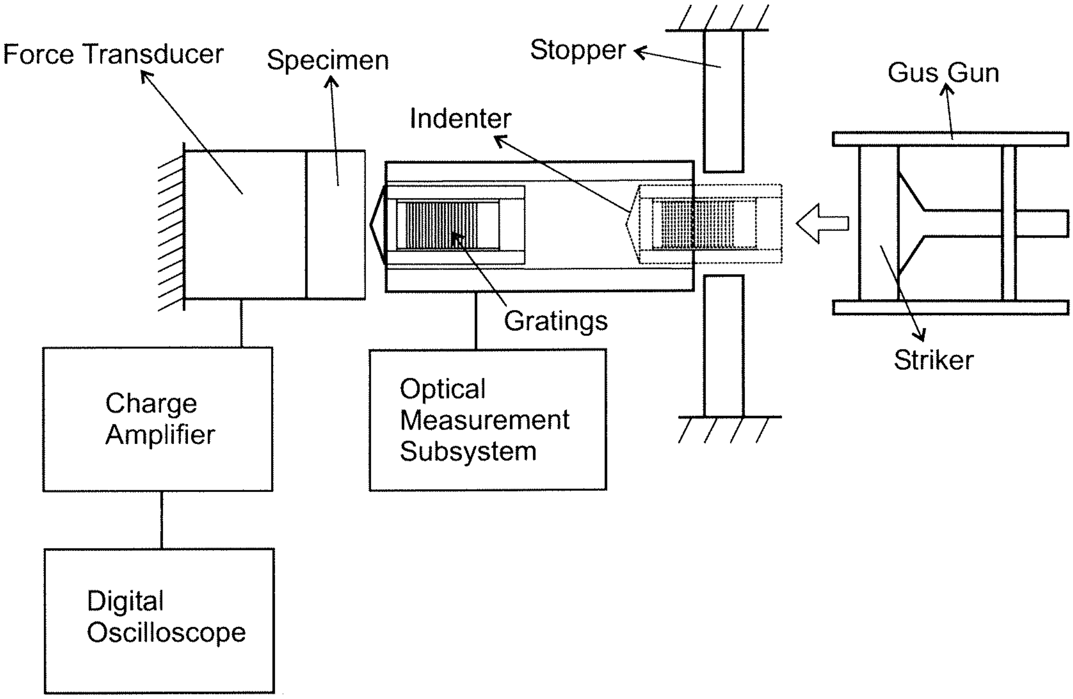

(a) Dynamic indentation system

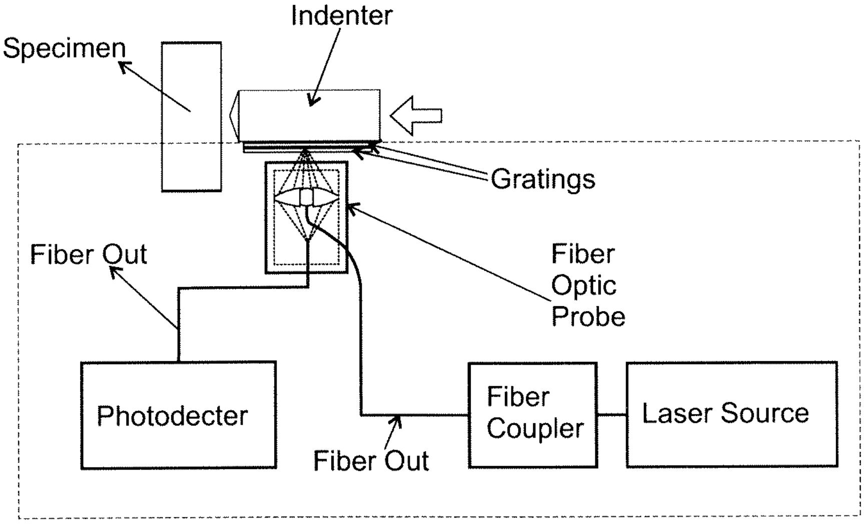

(b) Moiŕe interferometry recording subsystem

Figure 3. A schematic illustration of the experimental setup for dynamic indentation using geometric moiré interferometry.

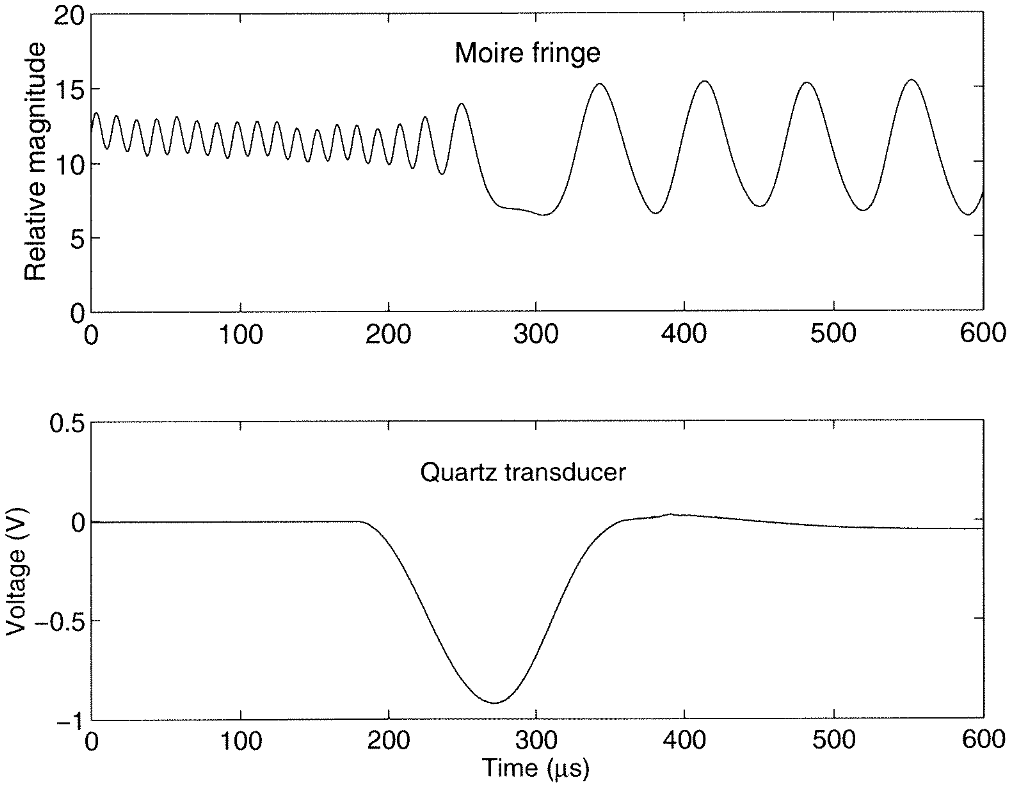

Figure 4. Typical examples of the moiré fringe signal and the force transducer signal.

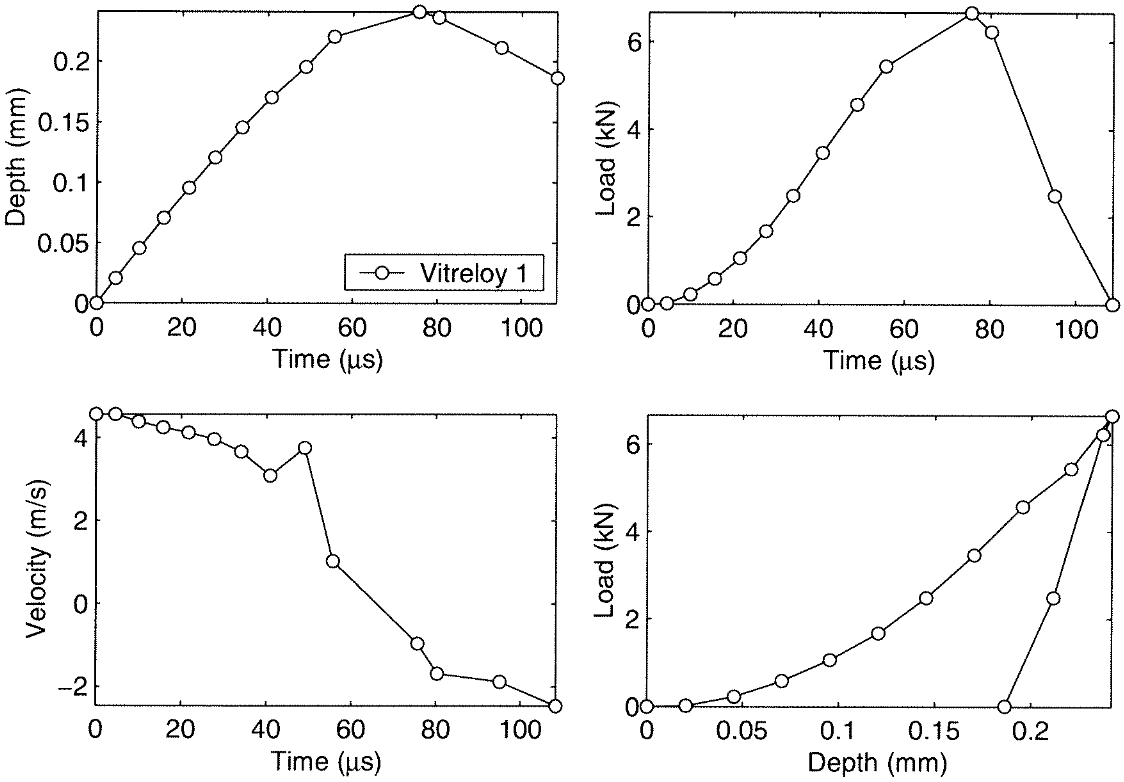

Figure 5. (a) Indentation profiles for Vit1 for an initial indenter velocity of 4.5m/s.

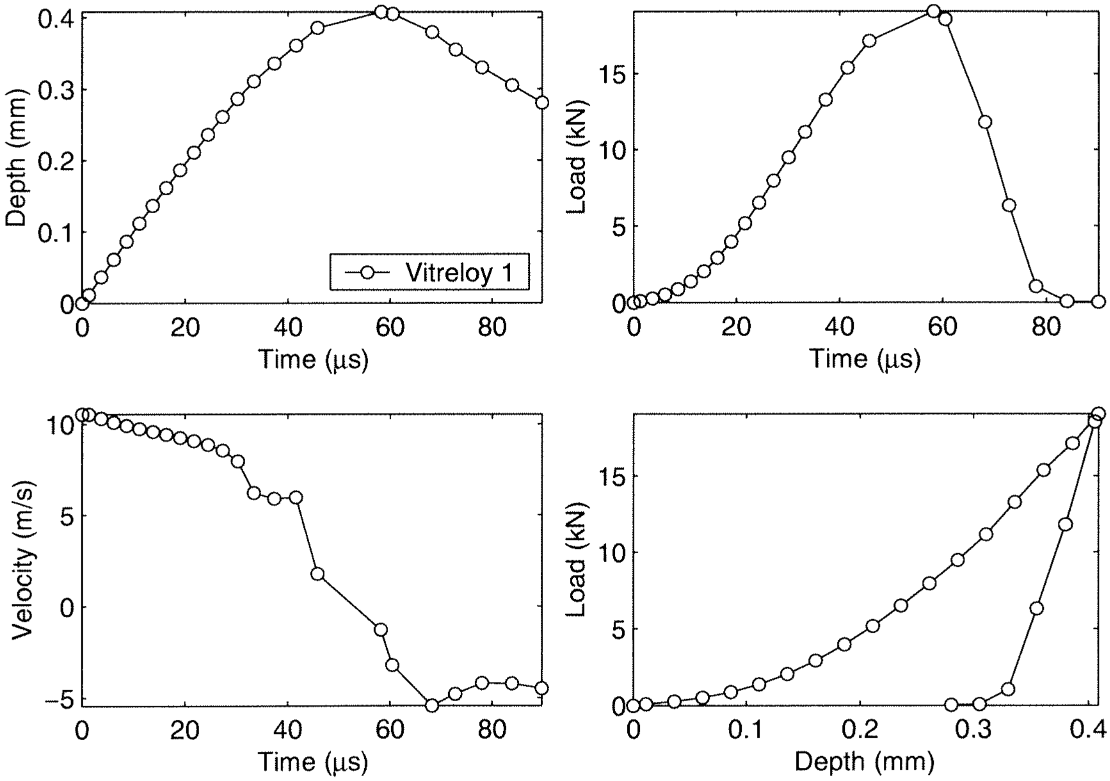

Figure 5. (b) Indentation profiles for Vit1 for an initial indenter velocity of 10.0m/s.

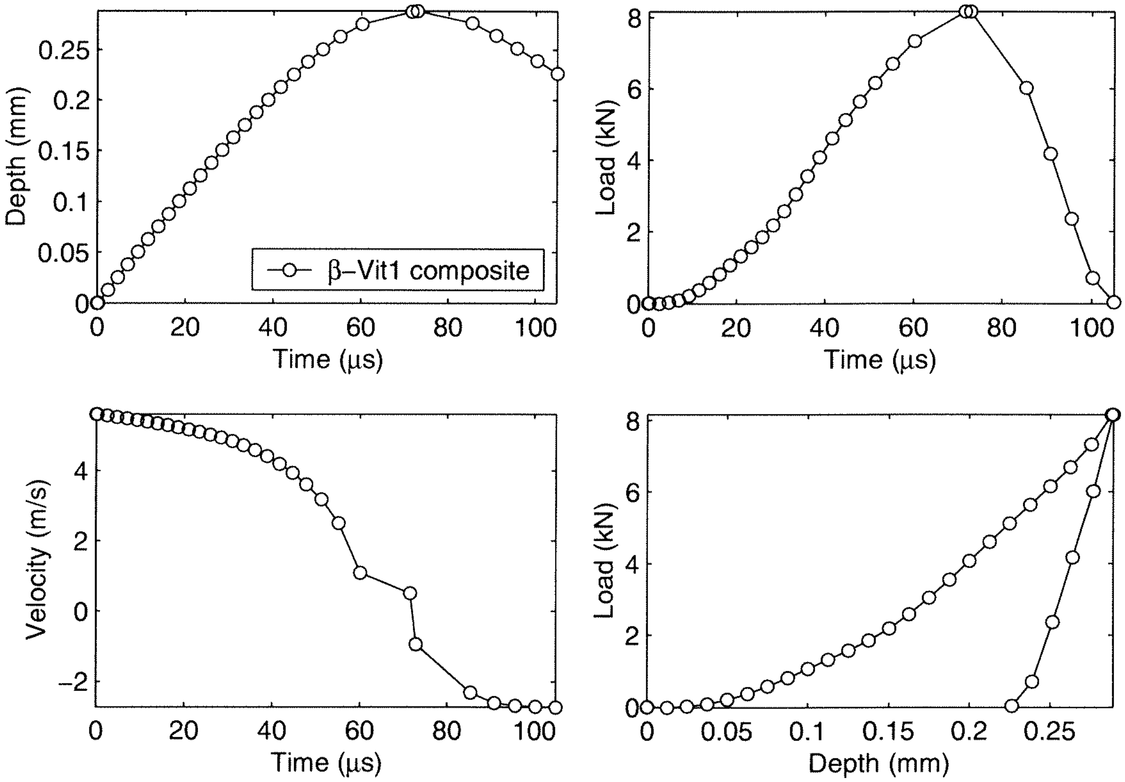

Figure 6. (a) Indentation profiles for β-Vit1 composite for an initial indenter velocity of 5.6m/s.

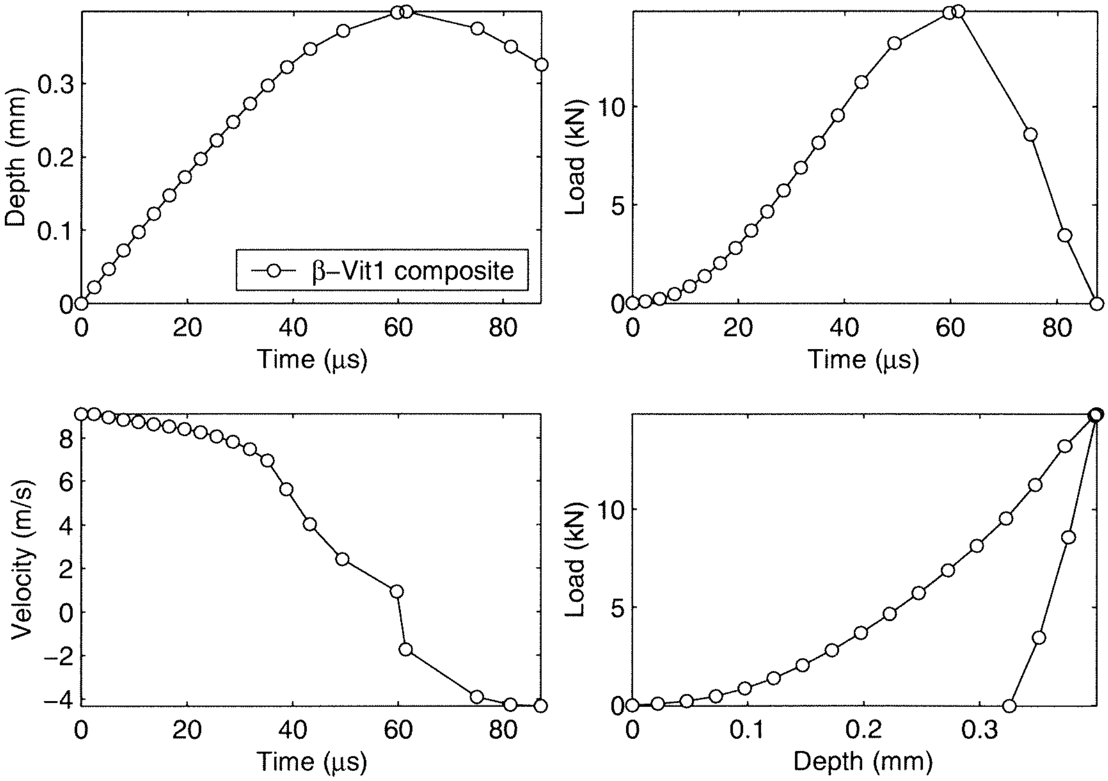

Figure 6. (b) Indentation profiles for β-Vit1 composite for an initial indenter velocity of 9.1m/s.

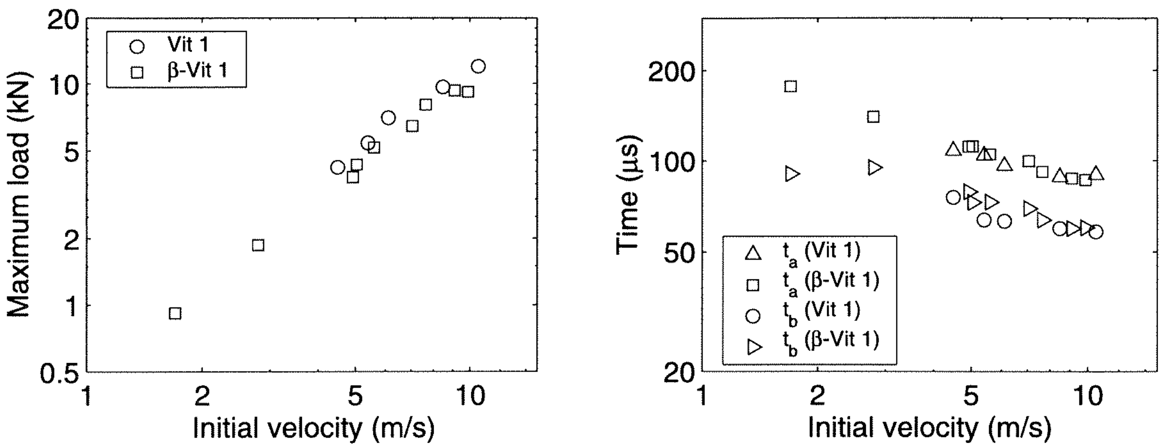

Figure 7. (a) Plot of the maximum load versus initial indentation velocity for Vit 1 and β-Vit 1. (b) Plot of loading duration versus initial indentation velocity for Vit 1 and β-Vit 1. Note that t_a refers to the loading duration (unloading duration is *not* included).

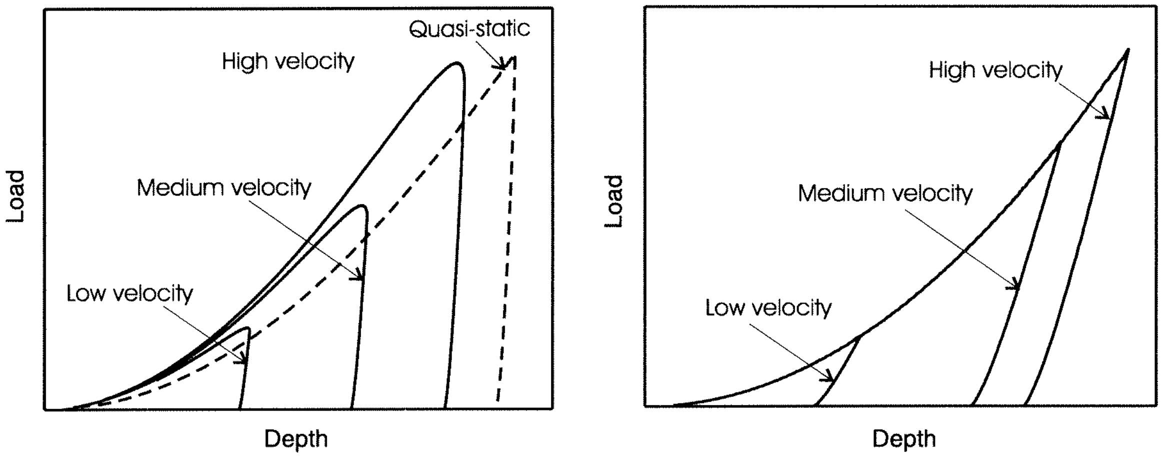

(a) (b)

Figure 8. Schematic load versus depth response for (a) rate dependent, and (b) rate independent material. The shape was based on the simulation results of model rate dependent and rate independent materials. For a rate independent material, the loading part of all the curves can be represented by a master relationship, $P=Ch^2$, where P is the load and h is the depth. However, for a rate dependent material, such master curve does not exist, but the $P=Ch^2$ approximation is still reasonable.

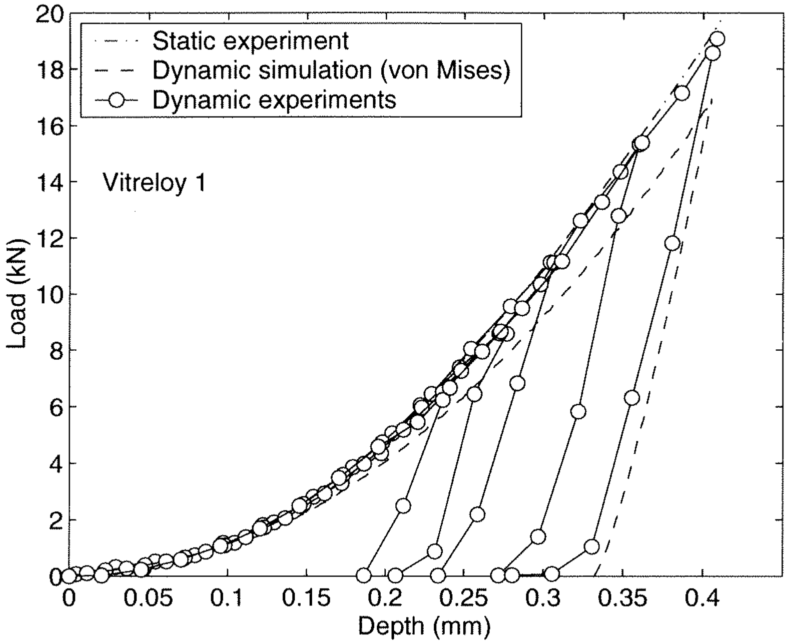

Figure 9. Indentation load-depth profiles for Vit 1. Initial indentation velocities of 4.5, 5.4, 6.1, 8.5 and 10 m/s were used in the experiments. Simulation (LS-DYNA) result for an initial indentation velocity of 9.1 m/s based on von Mises model is also shown. The discrepancy between the model and the experiment is apparent.

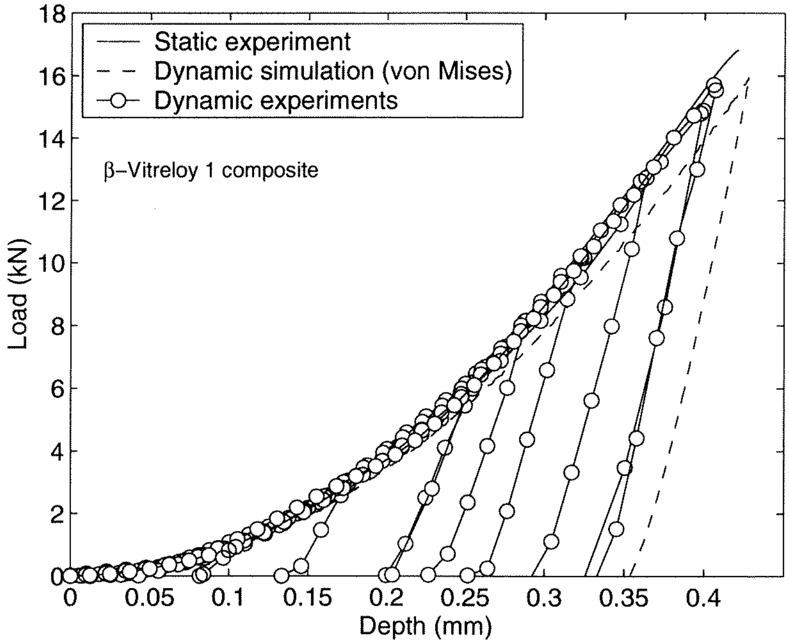

Figure 10. Indentation load-depth profiles for β-Vit1. Initial indentation velocities of 1.7, 2.8, 4.9, 5.1, 5.6, 7.1, 7.7, 9.1 and 9.9 m/s were used in the experiments. Simulation (LS-DYNA) result for an initial indentation velocity of 10 m/s based on von Mises model is also shown. The discrepancy between the model and the experiment is apparent.

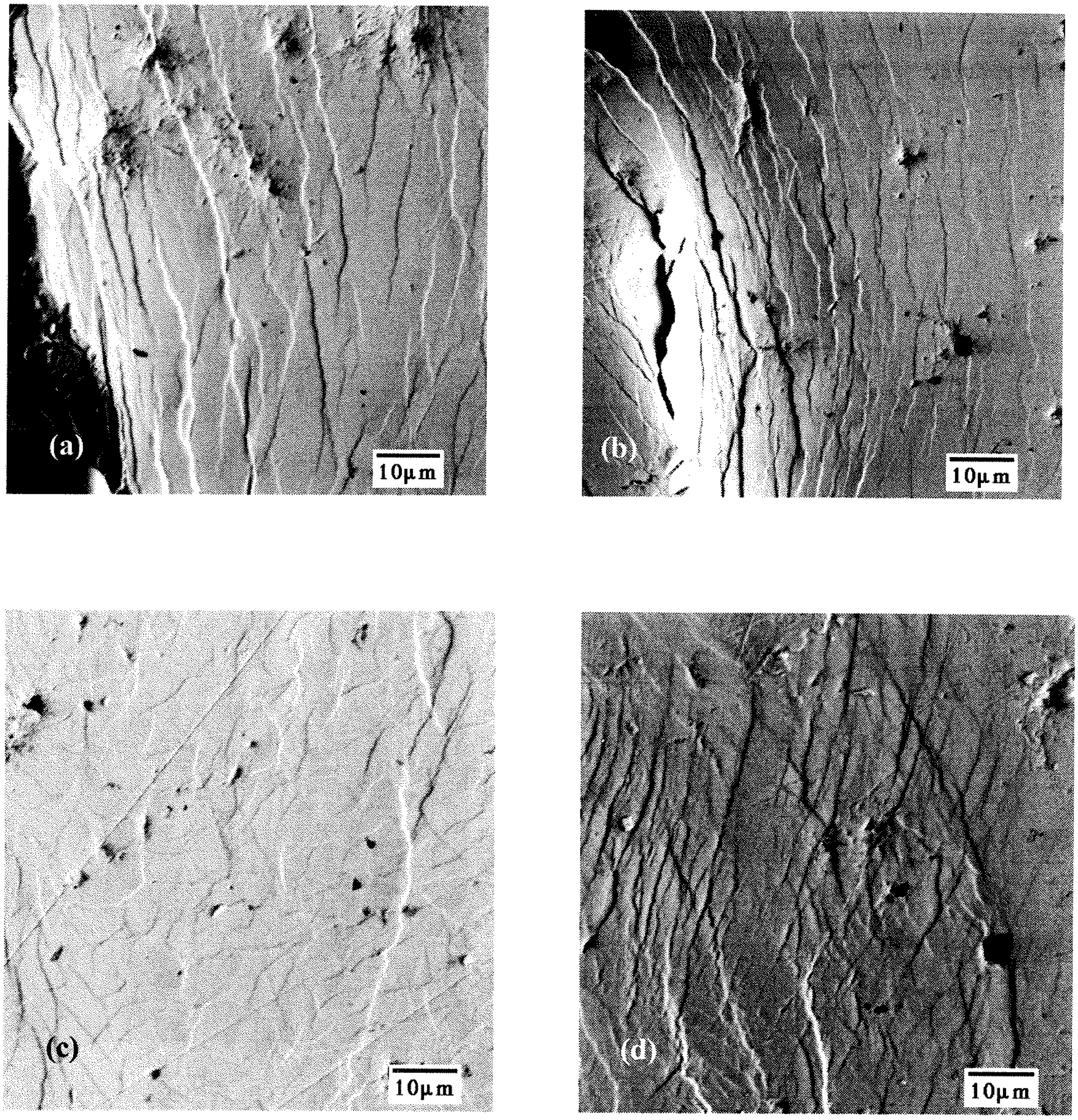

Figure 11. Intense shear bands on the surface of a crater formed by dynamic indentation of Vit 1: (a) (b) on the edges; (c) at the center; (d) at a location in between the center and the rim of the indentation crater.

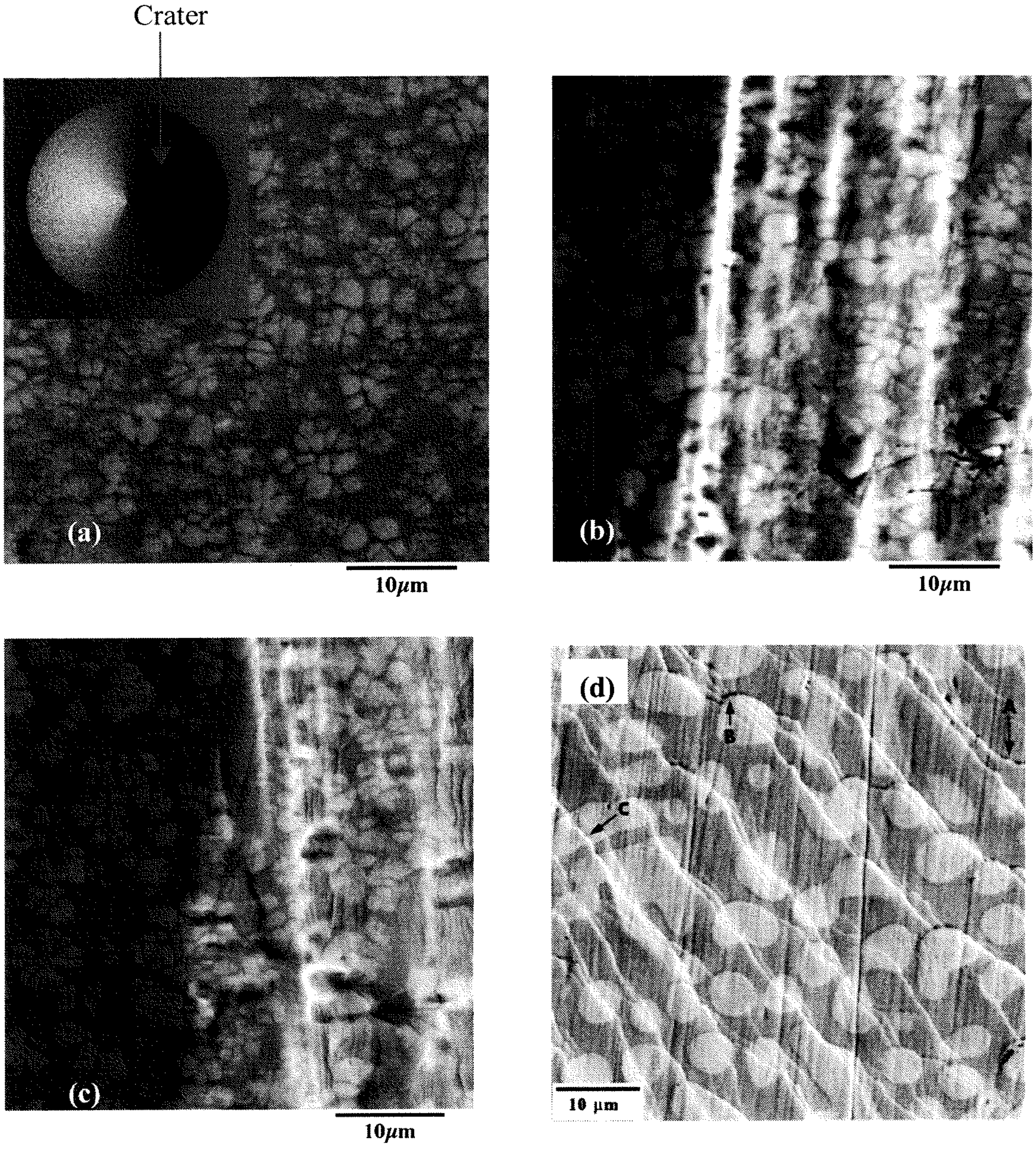

Figure 12. Intense shear bands on the surface of a crater formed by dynamic indentation of β-Vit1: (a) dendrite ductile bcc β-phase crystals embedded in Vit 1 matrix away from the indentation crater; (b) (c) examples of shear slip at the edge of the indenters. The shear slips on other parts of the craters are not clearly visible. (d) Another example of shear band pattern in the compression region of a bend test specimen (reproduced from Hays *et al.*, (2000)).

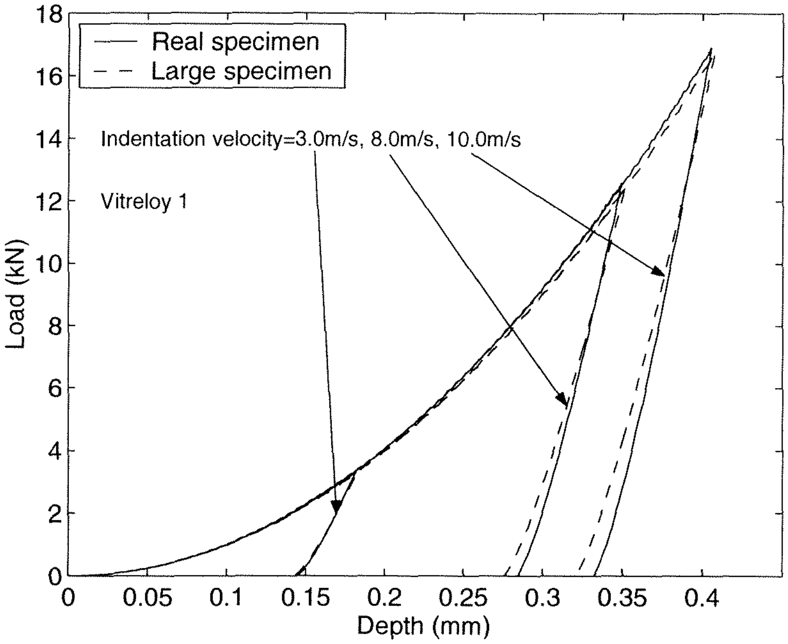

Figure 13. Effect of specimen size on the indentation load-depth profiles for Vit 1 (J_2 von Mises flow rule is assumed in the simulation using LS-DYNA).

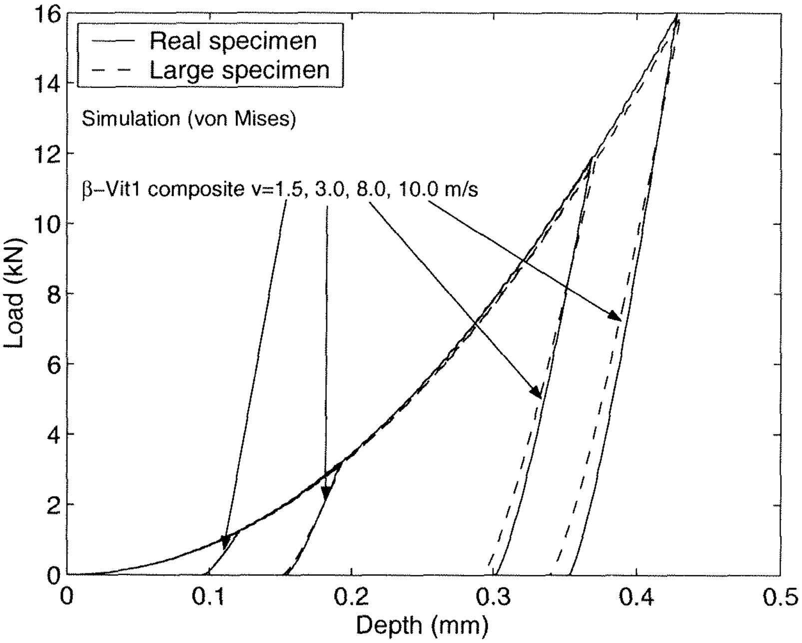

Figure 14. Effect of specimen size on the indentation load-depth profiles for β-Vit1 (J_2 von Mises flow rule is assumed in the simulation using LS-DYNA).

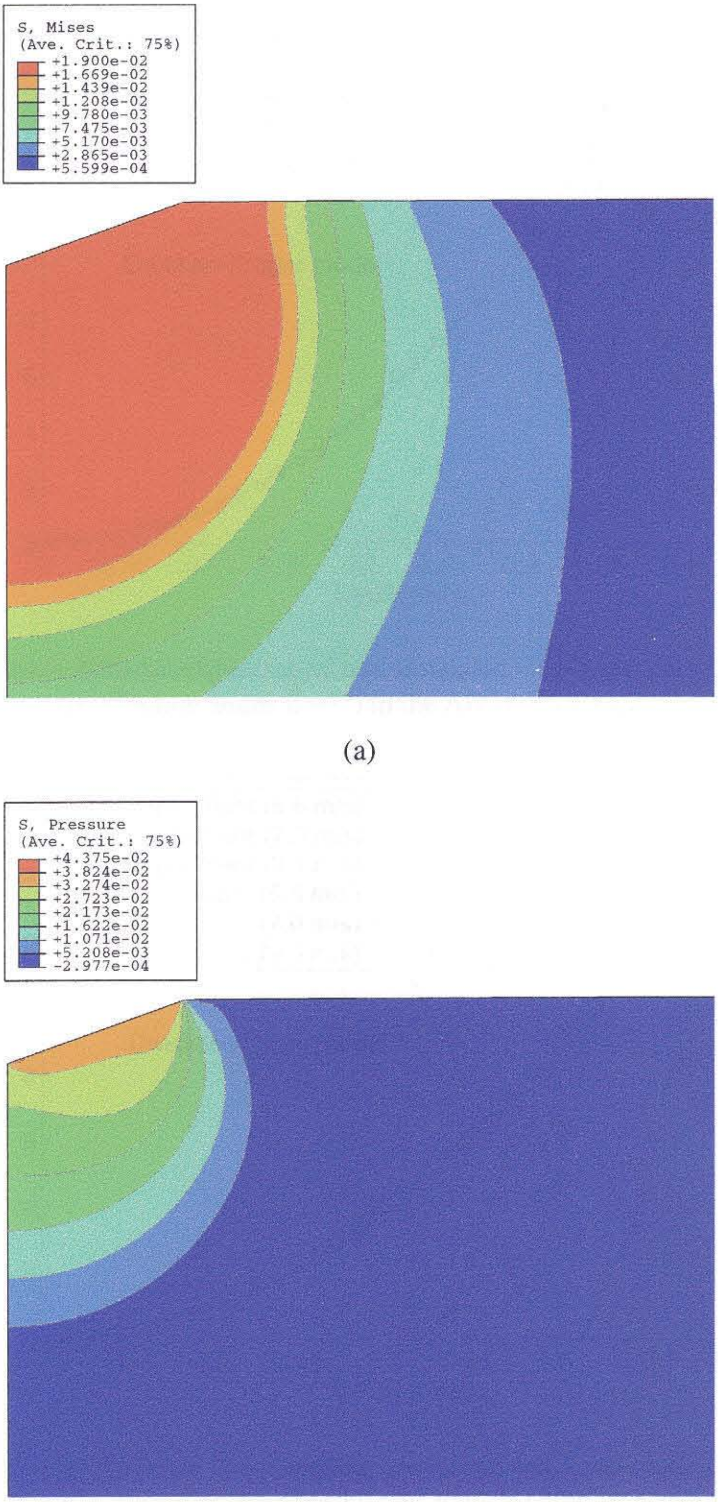

(a)

(b)

Figure 15. Results for Vit 1 using J_2 von Mises model by ABAQUS/Explicit code: (a) contours of Mises (equivalent) stress; (b) contours of pressure. Indentation velocity of 10.5 m/s was used.

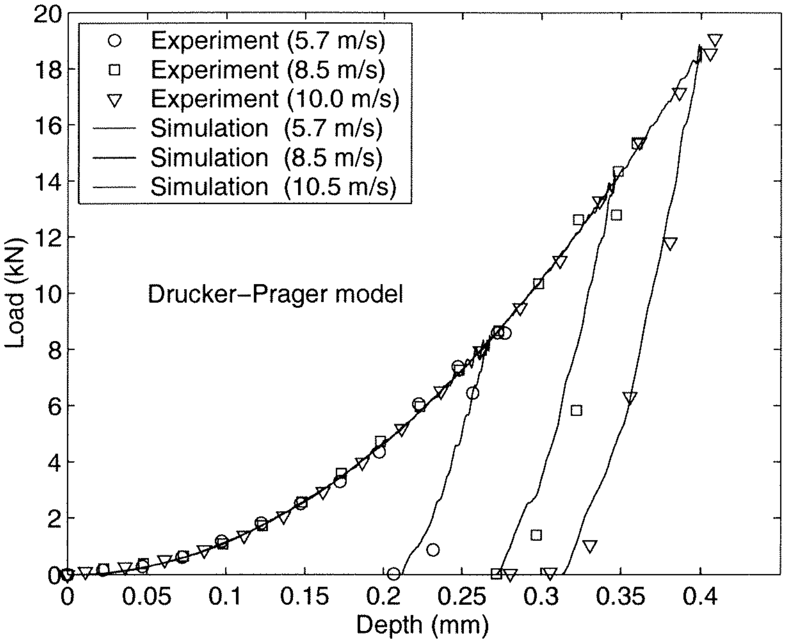

Figure 16. Comparison between experimental and simulated load-depth curves for Vit 1 using the Drucker-Prager model (friction angle, β =7°) in the ABAQUS/Explicit code.

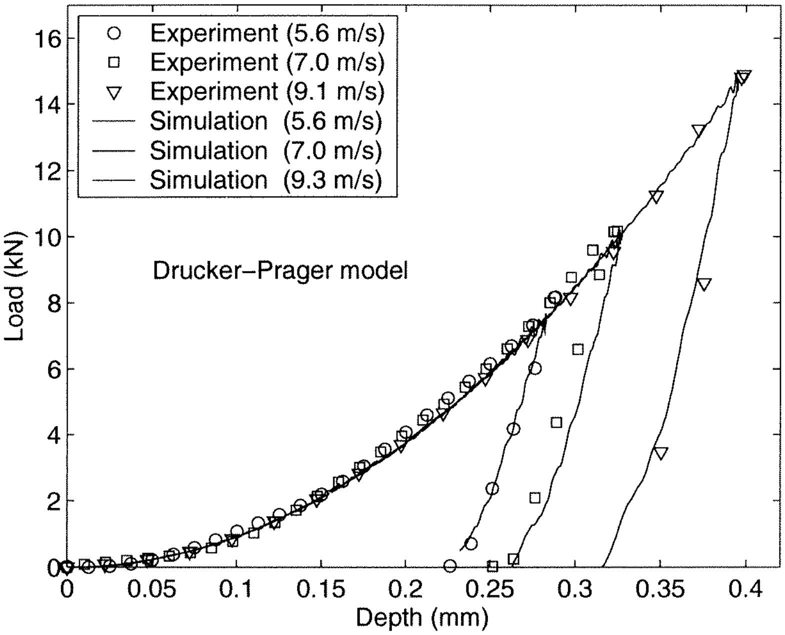

Figure 17. Comparison between experimental and simulated load-depth curves for β-Vit 1. Simulations carried out using the Drucker-Prager model (friction angle, β =3°-4°) in the ABAQUS/ Explicit code.

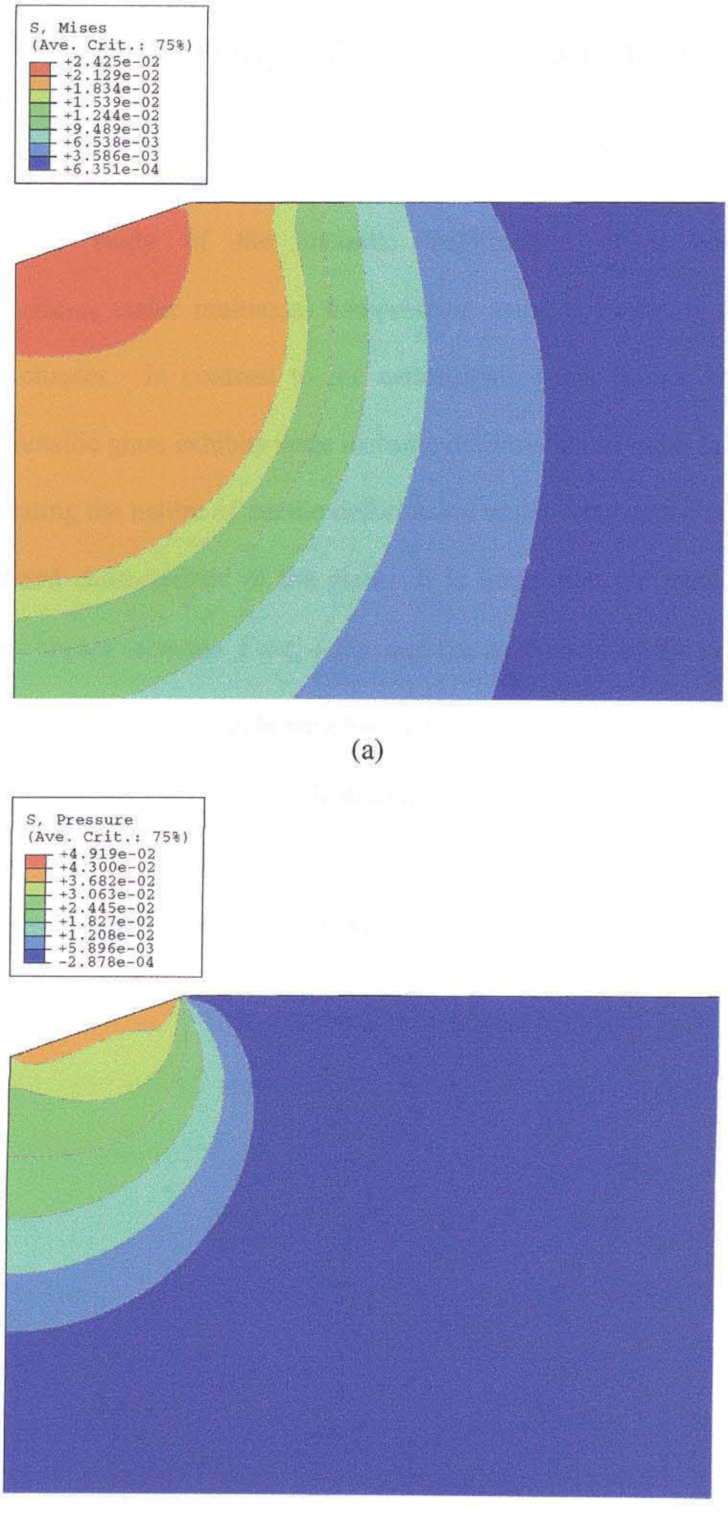

(a)

(b)

Figure 18. Simulation results for Vit 1 using the Drucker-Prager model (friction angle, β =7°) and the von Mises model in the ABAQUS/Explicit code (Indentation velocity =10.5 m/s): (a) contours of Mises (equivalent) stress; (b) contours of pressure.

Chapter 4 **Flow of Vitreloy 1 Subject to Confinement**

Abstract

An experimental study of the inelastic deformation of a bulk metallic glass $Zr_{41.2}Ti_{13.8}Cu_{12.5}Ni_{10}Be_{22.5}$ under multiaxial compression using a confining sleeve technique is presented in this chapter. In contrast to the catastrophic shear failure behavior in uniaxial compression, the metallic glass exhibits large inelastic deformation of more than 10 percent under confinement, indicating the nature of ductile deformation under constrained conditions in spite of long-range disordered characteristic of the glass. It is found that the metallic glass follows a pressure dependent Tresca criterion $\tau = \tau_0 + \beta p$ and the coefficient of the pressure dependence, β, is 0.17. Multiple parallel shear bands are observed on the surfaces of the deformed specimens, which are responsible for the overall inelastic deformation.

Keywords: Bulk metallic glass; Confinement; Pressure dependence; Inelastic deformation; Shear bands

1 Introduction

Since the discovery of a metallic glass at Caltech in the form of a thin ribbon by Klement *et al.* (1960), many metallic glasses in binary and ternary alloy systems have been developed prior to the 1980s. However, high critical quenching rate (10^3-10^7 K/s) required to form these metastable materials imposed a limit on the attainable sizes (typically smaller than a millimeter) for these metallic glass samples, mainly due to the factors such as thermal stability and thermal conductivity of these metallic glasses during the undercooling process. The scatter in geometric properties such as ribbon and wire thickness made the accurate measurement of mechanical properties extremely difficult and less reliable. Although some thick metallic glasses were developed (Chen and Turnbull, 1969), these glasses still had very limited thermal stability and sizes larger than 3 mm could not be achieved. The studies of mechanical properties of metallic glasses mostly in ribbon and wire form, which were not considered structural materials, were merely driven by scientific curiosity (e.g., Leamy *et al.*, 1972; Pampillo, 1975; Masumoto and Maddin, 1975; Gilman, 1975; Li, 1978, 1983). The application of metallic glasses as structural materials was impossible until the recent development of *bulk* metallic glasses in centimeter scale thickness using relatively inexpensive materials and simple processing techniques in the last decade (e.g., Inoue, 1998; Johnson *et al.*, 1998).

One of the most important bulk metallic glass families, named Vitreloy family, has been recognized as an intriguing class of potential structural amorphous material (SAM). Two typical examples of these alloys are $(Zr_{75}Ti_{25})_{55}(Cu_{55}Ni_{45})_{22.5}Be_{22.5}$ (Vitreloy 1) and $(Zr_{85}T_{15})_{55}(Cu_{43}Ni_{57})_{17.5}Be_{22.75}$ (Vitreloy 4). One of the most thoroughly studied bulk metallic glasses is Vitreloy 1 (Peker and Johnson, 1993), i.e., $Zr_{41.2}Ti_{13.8}Cu_{12.5}Ni_{10}Be_{22.5}$ (commonly referred to as Vit 1), which has many superior properties such as high specific strength and hardness, corrosion resistance and near net-shape casting ability (e.g., Gilbert, *et al.*, 1999; Wright *et al.*, 2001; Johnson, 1999, 2002) due to its lack of long-range order and absence of microstructure and extremely high thermal stability against crystallization (Johnson, 1999). It is finding applications as structural material in sporting equipment, coatings, defense applications and electronic packaging (Johnson, 2002).

At elevated temperatures near or above its glass transition temperature, Vitreloy 1 exhibits nonlinear viscoelastic behavior and its deformation behavior can be well characterized (see Chapters 1 and 2). However, at low temperature, say, room temperature, without heat treatment, the high strength metallic glass deforms elastically and fails in a brittle and catastrophic manner, although one may expect the material to be ductile because of its metallic bonding. While the study of high temperature homogeneous deformation behavior (Chapter 2) can assist in understanding the net-shape thermal casting process of Vitreloy 1, the deformation behavior of Vit 1 at low temperatures (lower than its glass transition temperature) is directly related to the structural applications of the material. One cannot achieve large inelastic strains at room temperature (Bruck *et al.*, 1994; also, see Chapter 2) in Vitreloy 1 under uniaxial loading condition. Room temperature ductility is impaired by the catastrophic shear failure caused by shear localization, which is the primary and dominant inelastic deformation mechanism for metallic glasses. The shear band formation in metallic glasses can be regarded as a "material instability" or "nucleation" of material imperfection. Therefore, it is not trivial to establish inelastic constitutive laws due to shear localization and to validate hypotheses in the literature that are often conflicting to examine if the flow stress of a metallic glass (e.g., Vitreloy 1) is a function of multiaxial stress states such as hydrostatic pressure and normal stress.

Classical dislocation mechanics has been successfully and extensively applied to explain a variety of plastic deformation mechanisms in crystalline materials and to establish the relation between the macroscopic inelastic deformation and the dislocation mechanisms at the microstructural level. Nevertheless, due to the amorphous nature of metallic glasses, such a theory does not have any physical basis to explain why the deformation of metallic glasses is very inhomogeneous at low temperatures, although attempts were made by some researchers along these lines using dislocation mechanics (e.g., Gilman, 1975). There is no complete theoretical and/or analytical framework in the literature that can be employed to model/predict the deformation behavior of metallic glass over a broad range of strain rates, temperatures and stress states. However, lack of detailed experimental work and paucity of data on deformation behavior of metallic glasses appears to be an obstacle in developing models for mechanical behavior of metallic glasses.

Probably the only theoretical framework for modeling the deformation of metallic glasses is the one based on the hypothesis of free volume in disordered metallic glasses (Spaepen, 1977). Recently, de Hey *et al.* studied the homogeneous structural evolution (global structural dilation) of $Pd_{40}Ni_{40}P_{20}$ and $La_{50}Al_{25}Ni_{25}$ metallic glasses at high temperatures (near and above their glass transition temperatures), leading to the conclusion that additional free volume is created, as compared to thermal equilibrium, due to inelastic deformation (de Hey *et al.*, 1997, 1998; van Aken *et al.*, 2000). Recently, using positron annihilation technique, Flores *et al.* (2001) indirectly observed a slight "free volume" increase in Vit 1 (local structural dilation) when it transforms from an undeformed state to an inelastically deformed state at room temperature (an inhomogeneously deformed state). In this study, the inhomogeneous deformed state was such that the amount of inhomogeneous deformation was small. Shear bands inevitably formed in Vit 1 although their distribution was not reported. The above experimental results at least support the existence and the importance of free volume in metallic glasses. Since the amount of free volume in amorphous materials is also related to hydrostatic pressure (Cohen and Turnbull, 1959) and as earlier studies on amorphous polymers showed the pressure and normal stress dependence of flow stress (e.g., Li and Wu, 1976), the existing of free volume in metallic glasses could lead to a similar conclusion that the yield stress of metallic glass may be dependent on hydrostatic pressure as well.

One may consider dislocations and free volumes to play major roles in deformation of crystalline alloys and amorphous metallic glasses, respectively. Dislocations are generally considered as structural defects in crystalline materials, and the study of dislocations both experimentally and theoretically has lead to vast improvements in understanding the macroscopic deformation behavior (e.g., plasticity) of crystalline materials. On the other hand, free volume, as the basic 'defect' in metallic glasses, probably is the key to understanding and characterizing the mechanical behavior of metallic glasses. Unfortunately, the highly disordered structure prevents the well established experimental techniques such as electron microscopy (e.g., high resolution transmission electron microscopy (HRTEM)) to directly study the positions, distributions of atoms and free volumes in multicomponent metallic glasses such as Vit 1 (Pekarskaya *et al.*, 2001). As a consequence, the mechanical behavior and their relation to free volume in metallic glasses mostly rely on experimental study at a macroscopic scale.

The unique mechanical properties of metallic glasses have attracted many researchers even long before metallic glasses found their structural applications in industry. Experiments on metallic glasses have suggested that their yield stress could be either normal stress dependent, or pressure dependent, or follow pressure independent von Mises flow criterion (e.g., Davis and Kavesh, 1975; Kimura and Masumoto, 1980; Donovan, 1988, 1989). Bruck *et al.* (1994) performed uniaxial tension and compression experiments, as well as pure torsion experiments on Vit 1, and concluded that the yield stress for the material is pressure independent and would obey the J_2 von Mises flow criterion. They were further reassured of their conclusion by the observation that the shear failure in specimens occurred at an angle of 45 degrees to the loading axis under uniaxial tension and compression. Vaidyanathan *et al.* (2001) used micro indentation to study the flow behavior of Vit 1 and concluded that the yield stress of the material follows the Mohr-Coulomb criterion. Lewandowski and Lowhaphandu (2002) investigated the flow criterion for Vit 1 subjected to a uniform axial *tensile* stress with lateral *compressive* stress. This investigation indicates that Vit 1 has a negligible pressure dependent behavior, and that the yield stress of Vit 1 may be characterized by a normal stress dependent flow criterion.

Indentation provides a means of constraining shear band propagation by surrounding elastic material that is not severely deformed. In addition, high pressures are present in the region directly underneath indentation contact zone. Uniaxial deformation and dynamic indentation experiments described in Chapters 2 and 3 indicate that the yield stress of Vit 1 is strain rate independent at temperatures lower than the glass transition temperature (625 K). Indeed, the deformation of Vit 1 may be approximated by the J_2 von Mises flow criterion under uniaxial loading conditions. However, the dynamic indentation study performed in Chapter 3 indicates that the yield stress of Vit1 is slightly dependent on either the normal stress or the pressure in both static and dynamic loading conditions, but it is not clear so far whether a pressure or normal stress dependent Mohr-Coulomb model is more suitable for metallic glasses (in particular for Vit 1) or not.

Another way of arresting shear band during deformation of metallic glasses is to use confining sleeves or high-pressure vessels. Complimentary to the experimental technique employed in the experiments by Lowhaphandu *et al.* (1999) and Lewandowski and Lowhaphandu (2002), a simple experimental technique is employed in this present study to further investigate the effect of stress state on the flow behavior of metallic glasses under multiaxial loading conditions. Specific attention is focused on the inelastic deformation of Vitreloy 1 under 'simple' multiaxial compression by sleeve-confinement technique at quasi-static strain rates. The term multiaxial stress state used here refers to axial compression of a cylindrical specimen with nominally proportional lateral compressive confinement. This stress state corresponds to a compressive stress state in all three principal directions, and the confining stress that can be applied is as high as 2 GPa (resulting in a hydrostatic pressure as high as 2.5 GPa), which is substantially higher than that achieved by Lowhaphandu *et al.* (1999, 2000). The stress states in this range have not been explored for bulk metallic glasses by previous studies (Lowhaphandu *et al.*, 1999). The experimental technique for imposing multiaxial compression is described in section 2. Under such a stress state, the resulting inelastic deformation is characterized and the resulting shear band patterns are examined in section 3. A pressure dependent flow criterion is formulated based on the experimental results in section 4. The strain rate independence of Vit 1 at room temperature (see Chapter 2) implies that the study of the quasi-static flow behavior of Vit 1 under lateral confinement could be used to interpret the behavior of Vit 1 in the dynamic loading regime as well. The conclusions for the present study are summarized in section 5.

2 Experimental

2.1 Material

The material used in this study is $Zr_{41.2}Ti_{13.8}Cu_{12.5}Ni_{10}Be_{22.5}$ (Vitreloy 1 or Vit 1), which is one of the best metallic glass formers ever developed (Peker and Johnson, 1993). It has excellent thermal stability against crystal nucleation, resulting quite easily in a glassy sample in centimeter scale, and making the confinement experiment that utilizes a confining sleeve possible. Ingots of alloys were made by a mixture of the metallic elements in a silver/copper boat or an arc-melter on a water-cooled copper plate, under a titanium gettered argon atmosphere (copper with purity of 99.999%, nickel with purity of 99.995%, titanium with purity of 99.995% were supplied by Cerac, Inc., zirconium with purity of 99.5% was supplied by Teledyne Wah-Chang, Inc., and beryllium with purity of 99.99% was supplied by Electronic Space Products International). To maintain the homogeneity of the ingot, copper, nickel and titanium were molten together in one batch and then the zirconium and beryllium were molten in a second batch. Finally, they were remelted together for a few minutes until a homogeneous sample was formed. Subsequently, the liquid was undercooled by stopping the heating to form a glassy ingot. As a last step of achieving a homogenous sample, the ingot was cut into smaller pieces, which were then remolten at a temperature of 1200 K, which is higher than the liquidus temperature (993 K) of Vitreloy 1 and much lower than the melting temperature of quartz, in a sealed quartz tube of 10 mm in diameter under high vacuum condition followed by slow quenching in water at a cooling rate higher than 1 K/s. The quenched rod of 8-10 mm long was ground to remove the attached quartz contaminant and a few millimeters of outer layer. The amorphous state of the ground Vit 1 thus processed was verified by X-ray diffraction. The processing and physical properties of this material are well documented in the literature (see, for example, Peker and Johnson, 1993; Bruck *et al.*, 1994; Kim *et al.*, 1994; Busch *et al.*, 1995a, 1995b; Masuhr *et al.*, 1999). The physical and mechanical properties of Vit 1 made using the approaches described above are listed in Table 1.

2.2 Specimen

The casting rods made using the quartz casting method were then centerless ground to the desired diameters of 3.81 mm (i.e., 0.15 inch, used for "A" size specimen), 5.08 mm (i.e., 0.20 inch, used for "B" size specimen) and 6.35 mm (i.e., 0.25 inch, used for "C" size specimen) with a surface finish of 6 μm. Subsequently, the rods were cut using a low speed precision diamond saw into compression specimens with 1 to 1.5:1 length-to-diameter ratio. Larger aspect ratio was not considered in this non-standard confinement experiment in order to reduce the effect of friction between the sleeves and the specimens. Subsequently, the end faces of each specimen, clamped with a specially designed mounting block, were polished down to 6-micron surface finish. The main purpose of the mounting block was to keep the polished surface flat while ensuring the two end surfaces of each specimen were made parallel to each other within a tolerance of 10 μm gap. A total of 14 specimens were fabricated following the procedures described above. The size of the specimens and other relevant experimental conditions are summarized in Table 2. Only the results from experiments A1, A2, B3, B4, C1 and C7 were reported in the next section since the experiments on other specimens failed because of the brittle failure of some of the tungsten carbide inserts at low stress, and the detachment of some of the strain gages during compression.

2.3 Compression fixture

A servo-hydraulic materials testing system (MTS with a 319 series axial/torsional load frame and 358 series load units) was used to apply axial compression on the confined specimens. The compression fixture used in the compression experiments is illustrated in Fig. 1. Confined specimens are sandwiched in between two finely polished tungsten carbide inserts of the same cross section as that of the specimens. The load acting on the inserts is transferred through two larger polished tungsten carbide disks onto the loading rods made of heat treated (900°F for 6 hours) C300 maraging steel (yield strength, 2.26 GPa), which are aligned with two precision linear ball bearings installed in a solid 2024 aluminum frame. High-pressure lubricant (extreme-pressure Moly-Graph™ multi-purpose grease, SAT-Lube, Inc., CA) was applied onto the contacting surfaces of the specimens, sleeves and the inserts to reduce friction among them.

2.4 Radial confinement

The lateral confinement to the material was realized by inserting the cylindrical specimen into the cavity of a hollow cylinder. The confining cylinder provides restraint against radial expansion, thus generating a uniform lateral stress on the specimen surface along the radial direction perpendicular to the loading axis. Ideally, it is assumed that the inner diameter of the sleeve is exactly the same as that of the specimen. The effect of the mismatch of these two diameters on the measurement of confining stress will be examined later in this section. It is also assumed that the deformation of the confining sleeve remains uniform during compression so that a strain gage placed on the outer surface of the sleeve along the hoop direction represents the uniform hoop strain everywhere on the outer surface of the sleeve. In addition, it is assumed that the friction in between the specimen and the sleeve is negligible in order for a simple analytical solution to be applied in deducing relevant quantities such as the confining stress. It is necessary to mention that the confining stress refers to the radial stress (or normal stress) exerted on the cylindrical specimen, and not the hydrostatic pressure in the specimen. Assuming that both the sleeve and the specimen deform elastically, one can estimate the radial confining stress,

$$\sigma_c = \frac{\sigma \nu / E}{\left(\frac{b^2 + a^2}{b^2 - a^2} + \nu_s \right) / E_s + (1 - \nu) / E}, \tag{1}$$

where E and E_s are the Young's modulus of the sleeve and the specimen materials, respectively; ν and ν_s are the Poisson's ratio of the specimen and the sleeve materials, respectively; a is the diameter of the specimen and the inner diameter of the sleeve and b is the outer diameter of the sleeve; σ is the loading stress in the axial direction. Assuming that the sleeve deforms elastically, after the specimen material yields, the confining stress becomes

$$\sigma_c = \frac{E_s}{2}\left(\frac{b^2}{a^2} - 1\right)\varepsilon_\theta^{\text{out}} \tag{2}$$

where $\varepsilon_\theta^{\text{out}}$ is the hoop strain at the outer surface of the sleeve. The stress state of the specimen can be thus determined based on the hoop strain as well as the axial deformation and stress.

Oguni *et al.* (2000) utilized this method of using elastically deforming sleeves made of aluminum to apply radial confinement in studying the multiaxial deformation and failure behavior of E-glass/vinylester composites. Ma and Ravi-Chandar (2000) employed 4340 steel sleeves to study multiaxial deformation behavior of a polymer, namely, polycarbonate. The materials used in these studies had relatively low strength such that the sleeves experienced only elastic deformation within the sleeves during the compression process. However, metallic glasses have high yield strength; for example, Vit 1 has a yield strength of about 1.9 GPa under uniaxial compression. Therefore, the assumption of the confining sleeve to remain elastic during deformation may not be realistic. Calculations have shown that only high strength materials like tungsten carbide (failure strength ~ 4 GPa) may possibly meet the requirement of having only elastic deformation in the confinement sleeve. However, besides the high cost of obtaining and grinding such a material, its high Young's modulus indicates that tungsten carbide is a very stiff material and is not quite suitable to allow radial inelastic expansion of the specimen resulting in high frictional stress.

Of the available high strength materials, maraging C300 steel is selected since it has high yield stress (2.26 GPa), relatively large strain (~8%) to failure and moderate value of Young's modulus (210 GPa). Compression experiments were performed on heat treated C300 samples, and it was found that C300 has a negligible strain hardening effect such that an elastic-rigid plastic model can be used to approximate its constitutive behavior. Before the sleeve yields, Eqs. (1) and (2) are valid for computing the confining stress. After the sleeve begins to yield, the boundary between the elastic and plastically deformed zones in the sleeve, i.e., the radial location ρ where the sleeve starts to yield (elastic-plastic boundary), can be expressed as

$$\rho = b\sqrt{\frac{\varepsilon_\theta^{\text{out}} E_s}{\sigma_s}} \tag{3}$$

where σ_s is the yield stress of the sleeve material. When this situation is reached, the corresponding confining stress σ_c becomes

$$\sigma_c = \sigma_s\left[\ln\frac{\rho}{a} + \frac{1}{2}\left(1 - \frac{\rho^2}{b^2}\right)\right]. \tag{4}$$

The maximum confining pressure that can be achieved according to Eq. (4) is

$$\sigma_c^{\max} = \sigma_s \ln\frac{b}{a}. \tag{5}$$

If the sleeve yields, Eqs. (3) and (4) and the axial stress in the loading direction fully describe the stress state in the material.

The hoop strain on the outer surface of the confining sleeve was measured using a strain gage (Micro-Measurements CEA-06-062UW(or AQ)-350) mounted on the outer surface. The strain gage was connected to a Wheatstone bridge with a 10 V DC power supply. All the signals including the load and displacement form the servo hydraulic materials testing system (MTS) were recorded using a 4-channel Nicolet 440 digital oscilloscope. The inner diameter of the confining sleeve is carefully ground or honed to provide minimum size misfit in between the sleeve and the specimen. The error caused by a size mismatch between the specimen and the sleeve will be discussed in the following section. The outer diameter (see Table 2) of the confining sleeve was chosen such that the diameter ratio (*b/a*) of 1.4, 2.0, 4.0 and 5.0 was realized in order to achieve various confining stress levels. For realistic dimensions of the specimen and the sleeve, the maximum possible confining stress that can be achieved is calculated to be around 400 to 1,000 MPa, if the sleeve deforms only elastically. Actually, for a specimen made of Vit 1 metallic glass, both the specimen and the sleeve will yield, leading to larger confining stress as can be seen in the experiments described in the next section. On the other hand, the maximum confinement stress is also limited by the strength of the tungsten carbide inserts whose nominal failure stress is around 4 GPa.

3 Results

Multiaxial compression experiments under lateral confining stress imposed by the sleeves were performed at a nominal axial quasi-static strain rate of $0.001\,\mathrm{s}^{-1}$ using the servo hydraulic materials testing system (MTS). The evolution of the hoop strain on the outer surface of sleeve, axial stress and axial displacement of the cylindrical Vit 1 specimen were recorded. The ratio between the outer diameter (b) and the inner diameter (a) of the sleeve was varied in the range of 1.25 to 5.0, which provided confining stress from 0 to about 2,000 MPa, as shown in Fig. 2. Further increase in the ratio, b/a, was not considered because it induces relatively little increase in the confining stress beyond the range mentioned above.

The hoop strain was obtained directly from the strain gage signal, and the axial stress and strain were calculated using the axial load and displacement as well as the compliance of the MTS loading frame. The relation between the confining stress and the hoop strain needs to be determined in each experiment for establishing the loading path experienced by the specimen. To do this, it is necessary to establish the confining stress, σ_c^{elas}, where the inner surface of the confining sleeve begins to yield. By resorting to Eqs. (2) and (4), the hoop strain ε_0 associated with σ_c^{elas} can be numerically solved using the following equation:

$$\frac{E_s}{2}\left(\frac{b^2}{a^2}-1\right)\varepsilon_0=\sigma_s\left[\ln\left(\frac{b}{a}\sqrt{\frac{\varepsilon_0 E_s}{\sigma_s}}\right)+\frac{1}{2}\left(1-\frac{\varepsilon_0 E_s}{\sigma_s}\right)\right]. \tag{6}$$

If $\varepsilon_\theta^{\text{out}} \le \varepsilon_0$, the confining sleeve is in the elastic range and Eq. (2) is used to calculate the confining stress. If $\varepsilon_\theta^{\text{out}} > \varepsilon_0$ and $\rho < b$, part of the confining sleeve yields and Eq. (4) is used to calculate the confining stress. But if $\varepsilon_\theta^{\text{out}}$ increases further, such that $\rho = b$ and the confining sleeve completely yields, the confining stress is the same as that when $\rho = b$ is initially reached.

3.1 Stress-strain response

A typical stress-strain curve for Vit 1 under uniaxial compression condition is linear up to a strain of about 0.02 (Young's modulus, *E*=95 GPa) followed by yielding due to shear band nucleation and propagation. Catastrophic shear failure occurs immediately following yield and a very limited amount of macroscopic inelastic strain that never exceeds 0.01. The maximum uniaxial compressive stress is in the range of 1.90 to 1.93 GPa; see Chapter 2 and also Bruck *et al.* (1994) and Kim (2001).

The relevant experimental conditions and associated parameters for the confinement experiments are listed in Table 2. Figure 2(a) shows the mechanical response of Vit 1 using a confinement sleeve with the ratio, *b/a*=1.25. The sleeve remained initially in the elastic range and the confining stress was proportional to the hoop strain before the hoop strain reaches 0.0069. As the hoop strain increased further, ρ, the radius of the elastic-plastic boundary inside the sleeve increased correspondingly until the sleeve completely yielded, indicating the maximum confining stress was reached. The yielding occurred after the confining stress reached 404 MPa, and after the sleeve was completely yielded, the increase in the axial stress was negligible. The measured hoop strain reached 0.016 before the sleeve was broken. The axial stress-strain curve and the confining stress-axial stress are also plotted in the figure. The irreversible axial inelastic strain in the specimen before the sleeve broke was 0.06, considerably lager than that observed in uniaxial compression (~0.01). Due to an imperfection in the MTS displacement recording system, the axial strain obtained using the crosshead displacement may contain some errors which makes an accurate determination of the initial yield stress difficult. Fortunately, the initial yield stress on the linear elastic stress-strain curve can be determined from the axial stress-hoop strain data based on the fact that the sleeve yielded only after the initial plastic deformation of the Vit 1 specimen. The elastic or the yield limit of Vit 1 at the current confining stress is around 2.11 GPa, which is slightly higher than that reported from the uniaxial compression experiments, namely, 1.9 GPa. The specimen failed by abrupt shear band propagation immediately after the confining sleeve failed in the hoop direction. Such a catastrophic shear failure was not expected to occur had the surrounding sleeve remained intact.

The maximum confining stress increased to 761 MPa when the *b/a* ratio was increased to 1.4, as depicted in Fig. 2(b), where an inelastic deformation of more than 0.09 was attained for the Vit 1 specimen prior to failure of the confining sleeve in the hoop direction. The same conclusion as before can be made that the sleeve yielded at a confining stress of 573 MPa, which is substantially larger than the confining stress at the elastic limit of Vit 1 specimen. The axial stress corresponding to the elastic limit in this case is 2.23 GPa.

As the ratio *b/a* increased to about 2.0, the confining sleeve began to yield after the confining stress was larger than about 805 MPa, which is once again larger than the confining stress at the elastic limit of the Vit 1 specimen; see Figs. 2(c) and (d). In contrast to the experiments at smaller *b/a* ratios, maximum axial stress of 3.81 to 4.15 GPa was achieved and was limited by the strength of the tungsten carbide inserts instead of by the plasticity/failure of the confining sleeve. The permanent inelastic deformation of Vit 1 that was measured can be as high as 0.1. It is interesting to note that some macroscopic shear slips occurred on the Vit 1 specimens as indicated in Fig. 2(d), which might be due to material imperfection that nucleated the slip steps. However, such shear slip propagation was further restricted and stabilized by the confining stress imposed by the confining sleeve. Indeed, this resulted in a lower value for the axial stress at same level of nominal confining stress as indicated by the data in Fig. 2(c), due to nonuniform distribution of the confining stress.

As shown in Figs. 2(e) and (f), confining stress as high as 1.7 to 1.88 GPa was reached for thicker confinement sleeves, as b/a was increased to a value of 5. Further increase in the *b*/*a* ratio results in insignificant increase in the confining stress. As clearly indicated in the figures, the sleeves did not fully yield for these thicker geometries and the maximum lateral stress of 1.05 GPa was achieved before the inner surfaces of the sleeves began to deform plastically. The permanent inelastic strain achieved in the specimens in these cases was in the range of 0.03 to 0.06 before the tungsten carbide inserts failed. Post-examination of recovered specimens reveal that a significant level of overall inelastic deformation observed in metallic glass under confinement is due to (a) considerable amount of multiple shear band formation and (b) the effect of multiaxial state of stress in stabilizing the otherwise catastrophic propagation of shear bands.

One critical factor in the measurement of the confining stress is the closeness of fit between the confining sleeves and the specimens. The measurements were based on the assumption that the sizes of the specimens were perfectly matched with their sleeves, i.e., there is no overlap or gap before the specimens were inserted to the sleeves. However, it is impossible to achieve such perfection, and to some degree, albeit small, dimensional mismatch is present. To reduce the uncertainty due to this dimensional mismatch, both the sleeves and the specimens were specially ground and honed such that the diameter of the specimen is equal or larger than inner diameter of the sleeves and the mismatch in the diameters is within 5 μm, which in turn results in a lateral pre-stress of around 0 to 75 MPa, estimated based on the linear elastic theory and the mechanical properties of both Vit 1 and C300 steel. Consequently, this confining stress is quite small compared to the confining stress of 450 MPa to 1,880 MPa at the onset of yield in Vit 1. The effect of the friction between the sleeve and the specimen has been minimized by applying high pressure lubricant, but the determination of the influence due to this friction is not straightforward. Although there exist these limitations of current experimental technique, the method of confining sleeve is still very instrumental as a first step in exploring and understanding the inelastic deformation behavior of metallic glasses subjected to high confining stresses.

The confining apparatus used in this investigation is probably the only one that can provide a lateral stress of as high as 2 GPa. Pressure vessels filled with pressurized liquid/gas usually provide pressures in the range of up to 700 MPa (e.g., Chalupnik and Ripperger, 1966; Lowhaphandu *et al.*, 1999). However, a drawback of the current apparatus is that it cannot provide a constant confining stress on the specimen, and, furthermore, the lateral stress is dependent on the interaction between the specimen and the sleeve. Nevertheless, the above experimental results have demonstrated the feasibility of the experimental setup in achieving high confining stresses.

3.2 Shear bands

All the confining sleeves with *b*/*a* ratio less than 1.4 broke in their hoop direction and the specimens confined by those sleeves were sheared off. For other experiments in which the sleeves remained undamaged, the specimens were recovered by carefully pressing them away from their confining sleeves. The axial stress applied to the specimens to remove them was not sufficient to create further inelastic deformation. The shear slips on the lateral surfaces due to the shear banding of the deformed specimens were then examined using scanning electron microscopy (SEM). Figure 3(a) illustrates a low magnification view of shear slip on the lateral surface of a specimen (C1) confined by a sleeve with *b*/*a*=1.25. The fracture surface seen at the upper-right hand corner of the figure was formed after the confining sleeve failed. In contrast to crystalline materials, particularly metals, whose plastic deformation is attributed to mobility of dislocations, the macroscopic inelastic deformation of metallic glasses takes place at much larger scales. Pekarskaya *et al.* (2001) have shown through in-situ straining in a transmission electron microscope (TEM) that shear localization of metallic glass (Vit 1) occurs at a length scale of tens of nanometers. The shear bands shown in Fig. 3(a) are distributed in a uniform manner and their typical width is about 1 to 2 microns. The direction of a typical shear slip, determined based on the grinding marks on the surface of the specimen, whose direction is perpendicular to the loading axis, forms an angle of 45 degrees with respect to the loading axis. A large shear induced local sliding is manifested in Fig. 3(b) in which a 20 μm relative shear offset is observed, which could have occurred after the sleeve was broken. The surface morphology of the major sheared surface following the damage of the confining sleeve is shown in Fig. 3(c), where the presence of a "vein" pattern clearly indicates that the local temperature increased substantially (beyond the glass transition temperature) during shear failure.

Further increase in the confining stress produced very similar shear slip patterns, as depicted in Figs. 3(d)-(g). It is important to note that all the slip lines are oriented at 45 degrees with respect to the loading axis as evidenced by the grinding marks on the surfaces of the specimens. It is worth mentioning that shear bands were created not only in one direction, but in multiple directions (Fig. 3(f)), forming families of conjugate slip, which might depend on the geometrical (surface) imperfections or the statistical distribution of the material properties, including the free volume.

4 Flow criterion

It has been well established that excess "free volume" plays an important role on the flow behavior of amorphous materials such as metallic glasses (e.g., Spaepen 1977; Argon 1979, 1983; Elliot, 1984). As mentioned in section 1, there exists experimental evidence supporting the hypothesis that free volume is a function of the inelastic deformation of metallic glasses. Early research (Kimura and Masumoto, 1980; Bruck *et al.*, 1994) suggested that metallic glasses obey von Mises flow criterion. However, it appears that no physical mechanism at the microscopic level supports such a flow criterion that is independent of pressure. The study of Davis and Kavesh (1975) was probably the first research report on the pressure dependency of flow stress in metallic glass, in which they used a liquid pressure system that can generate the confining stresses of up to 620 MPa. The pressure dependence of flow stress was found to be $\Delta\sigma / \Delta P \cong 0.077$ for stress states in compression and the ratio between the yield stress in uniaxial compression to that in uniaxial tension was found to be $\sigma_c / \sigma_t \cong 1.053$.

All principal stresses, including the intermediate stress, play important roles in determining the flow stress of polycrystalline materials due to the limited number of slip planes and the interactions of individual grains and irregular grain boundaries (e.g., Donovan, 1989). On the other hand, amorphous metallic glasses have an isotropic structure at the microstructural level, resulting in equal possibility of slipping in any direction, which in turn implies that the intermediate stress may not be critical in affecting the flow stress although it might contribute to the pressure dependent character of the flow. As a consequence, for Vit 1, one might employ a normal stress dependent Mohr-Coulomb criterion, which has been widely used in describing the mechanics of flow in soils and polymers (e.g., Means and Parcher, 1963; Bowden and Jukes, 1972),

$$\tau = \tau_0 + \alpha\sigma_n \tag{7}$$

where τ_0 is the cohesive shear stress, τ and σ_n are the shear stress and the normal stress components on the slip plane and in the directional normal to the slip plane, respectively, where the plastic flow occurs. α is a parameter related to the normal stress dependence. The dependence is strongly affected by the parameter α and the criterion will degenerate to Tresca flow criterion if α is zero.

Donovan (1989) performed compression, tension and shear experiments on a Pd-Ni-P metallic glass and concluded that a normal stress dependent Mohr-Coulomb is suitable to describe the yield behavior of the glass and the coefficient of the normal stress dependence α is 0.113. More recently, Lowhaphandu *et al.* (1999) performed a series of tensile experiments on Vit 1 with constant lateral confining stress of up to 700 MPa, which was generated by a pressure vessel. Their experimental results suggest that the influence of hydrostatic pressure on the flow behavior of Vit 1 is relatively small. However, the average angle between the fractured plane and the loading axis in the specimens was found to be 39.4°~42.2°, which appears to be more consistent with a normal stress dependent Mohr-Coulomb flow criterion. The coefficient of the normal stress dependence α was in a range of 0.04 (Lewandowski and Lowhaphandu, 2002). More recently, Wright *et al.* (2001) suggested from their uniaxial compression experiments that Vit 1 might follow a Mohr-Coulomb flow criterion with a coefficient of normal stress dependence α of 0.105.

Based on the current confinement experiments, one is able to systematically explore the influence of confining stress on flow stress at different stress states, thus the influence of hydrostatic pressure and normal stress on the flow behavior of metallic glasses. It is widely recognized that there is no strain hardening associated with the post-yielding of metallic glasses. For the typical 6 experiments performed and listed in Table 2, three or four stress states were selected from each experiment: one near the initial yielding state, another corresponds to a state near the maximum confining stress, and the other stress state(s) was (were) somewhere in between the two states. The principle stresses in the present experiments are ($\sigma_c, \sigma_c, \sigma$) where σ is the axial stress and σ_c is the radial confining stress. For instance, four stress states (in the form of ($\sigma_c, \sigma_c, \sigma$)) after the specimen yielded were used from experiment #B4. They are (434, 434, 2480), (602, 602, 2740), (1000, 1000, 3320), (1508, 1508, 4050) (units: MPa). In addition, two stress states associated with two uniaxial compression experiments were also included. A total of 23 representative stress states were utilized. The Mohr circle associated with each stress state can be easily determined: the center of each Mohr circle is the average value of the confining stress and the axial stress, whereas the radius of the circle is half of the difference between the axial stress and the confining stress. The Mohr circles corresponding to the stress states of the yielded Vit 1 specimens are plotted in Fig. 4. The normal stress and the associated shear stress at any point of each Mohr-circle can be easily determined graphically.

The average slope of the envelope of the Mohr circles (Fig. 4) from the current experimental results reveals that α=0.16 (Eq. (7)). If the Mohr-Coulomb criterion is appropriate for Vit 1, then the angle of the maximum shear plane with respect to the lading axis should be around 40 degrees. However, as mentioned earlier, the SEM examination of shear bands in deformed specimens as shown in Fig. 3 clearly indicate that all the slip (shear) planes were formed at an angle of $45 \pm 1^{\circ}$ degrees to the loading axis, if one refers to the grinding marks on the surfaces of the specimens which are initially perpendicular to the loading axis. This inconsistency suggests that a normal stress dependent flow criterion may not be appropriate to describe the flow behavior of Vit 1. In the normal stress dependent Mohr-Coulomb model (Eq. (7)), the intermediate principal stress exerts no influence on the yield behavior. Instead, one could consider a pressure dependent model by modifying the well known Tresca criterion,

$$\tau = \tau_0 + \beta p\,, \tag{8}$$

where $p = \sigma_{ii}/3$ is the hydrostatic pressure (σ_{ii} is trace of the stress tensor, σ) and β is the pressure dependency parameter. This model indicates that the critical shear stress is a function of the maximum and minimum principle stress, as well as the hydrostatic pressure. The influence of the intermediate stress is through the effect of the hydrostatic pressure. This model also implies that the maximum shear direction is always 45 degrees to the axis of the loading direction in multiaxial compression experiments with uniform lateral confinement, and the critical shear stress is dependent on the hydrostatic pressure. The experimentally obtained value of β is 0.17 for the metallic glass Vit 1, i.e., the slope of the maximum shear stress versus the hydrostatic pressure shown in Fig. 5.

5 Conclusions

The following conclusions can be drawn regarding the role of confinement on mechanical behavior of metallic glasses based on the investigation of Vit 1 subjected to multiaxial compression.

1. The metallic glass Virtreloy 1 exhibits a considerable amount of inelastic strain, more than 10 percent, if subjected to axial compression accompanied by lateral confinement. This is in contrast to its "brittle" behavior (shear failure) under uniaxial compression loading conditions. The large inelastic deformation under confinement is realized by the accumulation of multiple shear bands at a microstructural scale larger than dislocations in polycrystalline metals.
2. Detailed examination of the orientation of the shear slip on the surfaces of the recovered specimens, 45 degrees to the loading axis, suggests that the critical shear stress for flow in metallic glass is not necessarily a function of the normal stress but rather controlled by the hydrostatic pressure. This implies that a pressure dependent flow model is more appropriate than a normal stress dependent Mohr-Coulomb criterion for bulk metallic glasses, in particular for Vit 1. This observation appears to be in contrast to those of previous researches (Donovan, 1989; Bruck *et al.*, 1994; Lowhaphandu *et al.*, 1999) regarding the flow criterion of metallic glasses.

It is clear that large inelastic deformation in metallic glasses can be achieved using a mechanism (either external loading or microstructural) to arrest catastrophic shear failure and by promoting multiple shear band formation. Creating multiaxial loading condition using confining sleeves as has been demonstrated in this study can effectively enhance the macroscopic inelastic flow of Vit 1. Another way of arresting and retarding shear band propagation of monolithic Vit 1 is the introduction of a second ductile phase as reinforcement, and such a composite has been realized by Hays *et al.* (2000) by adding a small amount Nb and slightly altering the original Vit 1 composition. The mechanism associated with shear band arrest in such a composite (Pekarskaya *et al.* (2001)) appears to be different from that attained using the confining sleeve and deserves further attention.

References

Argon, A. S., Plastic deformation in metallic glasses, Acta Metall., **27**, 47-58 (1979).

Argon, A. S. and Shi, L.T., Development of visco-plastic deformation in metallic glasses, Acta Metall., **31**, 499-507 (1983).

Bowden, P. B. and Jukes, J. A., J. Mater. Sci., **7**, 52 (1972).

Bruck, H. A., Christman, T., Rosakis, A. J. and Johnson, W.L, Scripta Metall., **30**, 429 (1994).

Busch, R., Kim, Y. J. and Johnson, W. L., Thermodynamics and kinetics of the undercooled liquid and the glass-transaction of the $Zr_{41.2}Ti_{13.8}Cu_{12.5}sNi_{10}Be_{22.5}$ alloy, J. Appl. Phys., **77** (8) 4039-4043, (1995a).

Busch, R., Kim, Y. J., Johnson, W. L., Rulison, A. J., Rhim, W. K. and Isheim, D., Hemispherical total emissivity and specific-heat capacity of deeply undercooled $Zr_{41.2}Ti_{13.8}Cu_{12.5}Ni_{10.0}Be_{22.5}$ melts, Appl. Phys. Lett., **66** (23), 3111-3113 (1995b).

Chalupnik, J. D. and Ripperger, E. A., Dynamic deformation of metals under high hydrostatic pressure, Exp. Mech., **6,** 547-554 (1966).

Chen, H. S. and Turnbull, D., Formation, stability and structure of palladium-silicon based alloy glasses, Acta Metall., **17**, 1021-1031 (1969).

Cohen, M. H. and Turnbull, D., Molecular transport in liquids and glasses, J. Chem. Phys., **31** 1164-1169 (1959).

Davis, L. A. and Kavesh, S., Deformation and fracture of an amorphous metallic alloy at high pressure, J. Mater. Sci., **10**, 453-459 (1975).

de Hey, P., Sietsma, J. and van den Beukel, A., Creation of free volume in amorphous $Pd_{40}Ni_{40}P_{20}$ during high temperature deformation, Mat. Sci. Eng., **A226-228**, 336-340 (1997).

de Hey, P., Sietsma, J. and Van den Beukel, A., Structural disordering in amorphous $Pd_{40}Ni_{40}P_{20}$ induced by high temperature deformation, Acta Metall., **46** (16), 5873-5882 (1998).

Donovan, P. E., A yield criterion for $Pd_{40}Ni_{40}P_{20}$ metallic glass, Acta Metall., **37**, 445-456 (1989).

Donovan, P.E., Compressive deformation of amorphous $Pd_{40}Ni_{40}P_{20}$, Mater. Sci. Eng., **98**, 487-490 (1988).

Duine P. A., Sietsma, J. and van den Beukel, A., Defect production and annihilation near equilibrium in amorphous $Pd_{40}Ni_{40}P_{20}$ investigated from viscosity data, Acta Metall., **40**(4), 743-751 (1992).

Elliot, S. R., Physics of amorphous materials, Longman, New York (1984).

Flores, K. M., Suh, D., Howell, R., Asoka-Kumar, P., Sterne, P. A. and Dauskardt, R. H., Flow and fracture of bulk metallic glass alloys and their composites, Mater. Trans. JIM, **42** (4), 619-622 (2001).

Gilbert, C. J., Schroeder, V. and Ritchie, R. O., Mechanism for fracture and fatigue crack propagation in a bulk metallic glass, Metall. Mater. Trans. A, **30A**, 1739-1753 (1999).

Gilman, J. J., Mechanical behavior of metallic glasses, J. Applied Phys., **46**(4), 1625-1633 (1975).

Guduru, P. R., Zehnder, A. T., Rosakis, A. J. and Ravichandran, G., Dynamic full field measurements of crack tip temperatures, Eng. Fract. Mech., **68** (14), 1535-1556 (2001).

Hays, C. C., Kim, C. P. and Johnson, W. L., Microstructure controlled shear band pattern formation and enhanced plasticity of bulk metallic glasses containing in situ formed ductile phase dendrite dispersions, Phys. Rev. Lett. **84** (13), 2901-2904 (2000).

Johnson, W. L., Bulk amorphous metal – a novel engineering material, to appear in Journal of Metal (2002).

Johnson, W. L., Bulk glass-forming metallic alloys: Science and technology MRS Bull., **24** (10), 42-56 (1999).

Kim, Y. J., Busch, R., Johnson, W. L., Rulison, A. J. and Rhim, W. K., Metallic-glass formation in highly undercooled $Zr_{41.2}Ti_{13.8}Cu_{12.5}Ni_{10.0}Be_{22.5}$ during containerless electrostatic levitation processing, Appl. Phys. Lett., **65** (17), 2136-2138 (1994).

Kimura, H. and Masumoto, T., Deformation and fracture of an amorphous Pd-Cu-Si alloy in V-notch bending test - I. Model mechanics of inhomogeneous plastic flow in non-strain hardening solid, Acta. Metall., **28**, 1663-1677 (1980).

Klement, W. J., Willens, R. H. and Duwez, P., Non-crystalline structure in solidified gold-silicon alloys, Nature, **187**, 869-870 (1960).

Leamy, H.J., Chen, H. S. and Wang, T. T., Plastic flow and fracture of metallic glass, Metallurgical Transaction, **3**, 699-708 (1972).

Lewandowski, J. J. and Lowhaphandu, P., Pressure effects on flow and fracture of a amorphous metal, to appear in Philos. Mag A. (2002).

Li, J. C. M., Micromechanisms of deformation and fracture, in *Metallic Glasses*, ASM Metals Park, OH: 224-391 (1978).

Li, J. C. M., Recent studies of the mechanical properties of amorphous alloys, in *Rapidly Solidified Alloys: Processes, Structures, Properties, Applications*, Ed. Liebermann, H. H., Marcel Dekkar, Inc., New York (1983).

Li, J.C.M. and Wu, J.B.C., Pressure and normal stress effects in shear yielding, J. Mater. Sci.,**11**, 445-457 (1976).

Lowhaphandu, P., Ludrosky, L. A., Montgomery, S. L. and Lewandowski, J. J., Deformation and fracture toughness of a bulk amorphous Zr-Ti-Ni-Cu-Be alloy, Intermetallics **8**, 487-492 (2000).

Lowhaphandu, P., Montgomery, S. L. and Lewandowski, J. J., Scripta Mater., Effects of superimposed hydrostatic pressure on flow and fracture of a Zr-Ti-Ni-Cu-Be bulk amorphous alloy, Scripta Mater., **41** (1), 19-24 (1999).

Ma, Z. and Ravi-Chandar, K., Confined compression: a stable homogeneous deformation for constitutive characterization, Exp. Mech. **40** (1), 38-45 (2000).

Masuhr, A., Waniuk, T. A., Busch, R. and Johnson, W. L., Time scales for viscous flow, atomic transport, and crystallization in the liquid and supercooled liquid states of $Zr_{41.2}Ti_{13.8}Cu_{12.5}sNi_{10}Be_{22.5}$, Phys. Rev. Lett., **82** (11), 2290-2293 (1999).

Masumoto, T. and Maddin, R., Structural stability and mechanical properties of amorphous metals, Mater. Sci. Eng., **19**, 1-24 (1975).

Means, R. E. and Parcher, J. V., Physical properties of soils, Charles Merrill, Columbus, Ohio (1963).

Oguni, K., Tan, C. Y. and Ravichandran, G., Failure mode transition in unidirectional E-glass/vinylester composites under multiaxial compression, J. Compos. Mater., **34** (24), 2081-2097 (2000).

Pampillo, C. A., Review-flow and fracture in amorphous alloys, J. Mater. Sci., **10**, 1194-1227 (1975).

Pekarskaya E., Kim C. P. and Johnson W. L., In situ transmission electron microscopy studies of shear bands in a bulk metallic glass based composite, J. Mater. Res. **16** (9), 2513-2518(2001).

Peker, A. and Johnson, W. L., A highly processable metallic glass: $Zr_{41.2}Ti_{13.8}Cu_{12.5}Ni_{10.0}\,Be_{22.5}$, Appl. Phys. Lett., **63**, 2342-2344 (1993).

Ravichandran G., Critical appraisal of limiting strain rates for compression testing of ceramics in a split Hopkinson pressure bar, J. Am. Ceram. Soc., **77**(1), 263-267 (1994).

Spaepen, F., A microscopic mechanism for steady state inhomogeneous flow in metallic glasses, Acta Metall., **25**, 407-415 (1977).

Vaidyanathan, R., Dao, M., Ravichandran, G. and Suresh, S., Study of mechanical deformation in bulk metallic glass through instrumented indentation, Acta Mater. **49** (18), 3781-3789 (2001).

van Aken B., de Hey P. and Sietsma J., Structural relaxation and plastic flow in amorphous $La_{50}Al_{25}Ni_{25}$, Mat. Sci. Eng., **A278** (1-2), 247-254 (2000).

Wright, W. J., Saha, R. and Nix, W. D., Deformation mechanisms of the $Zr_{40}Ti_{14}Ni_{10}Cu_{12}Be_{24}$ bulk metallic glass, Mater. Trans. JIM, **42**(4), 642-649 (2001).

Table 1. Mechanical properties of Vitreloy 1 and C300 maraging steel

Property	Vitreloy 1	C300 maraging steel
Density (g/cm^3)	6.0	8.0
Young's modulus (GPa)	96 [a]	200 [a]
Poisson's ratio	0.36 [a]	0.3 [a]
Elastic strain limit	0.02 [b]	0.011 [c]
Yield strength (GPa)	1.90 [b]	2.26 [c]
Vickers hardness (kg/mm^2)	540 [d]	–
Plane strain fracture toughness (MPam$^{1/2}$)	~55 [d]	~88 [e]

Notes:

[a] Deduced from ultrasonic measurements; [b] Bruck *et al.*, 1994 ; [c] Determined from tensile experiment; [d] Gilbert *et al.*, 1999;. [e] Guduru *et al.*, 2001.

Table 2. Specimen dimensions and experimental parameters

Experiment #	a (mm) [a]	b (mm) [b]	b/a	$\sigma_c^{\max}$ (MPa) [c]	$p^{\max}$ (MPa) [d]	ε_0 [e]
C1	6.09	7.62	1.25	501	1,150	~0.06
A2	5.86	5.33	1.4	761	1,450	~0.09
A1	3.68	7.62	2.0	1,570	2,420	~0.10
B3	5.01	10.16	2.0	1,448	2,230	~0.03
C7	6.67	25.40	4.0	1,697	2,500	~0.03
B4	4.97	25.40	5.0	1,883	2,790	~0.06

Notes:

[a] a = diameter of the specimen; [b] b = outer diameter of the confining sleeve;

[c] $\sigma_c^{\max}$ = maximum confining stress; [d] $p^{\max}$ = maximum hydrostatic pressure;

[e] ε_0 = maximum inelastic strain.

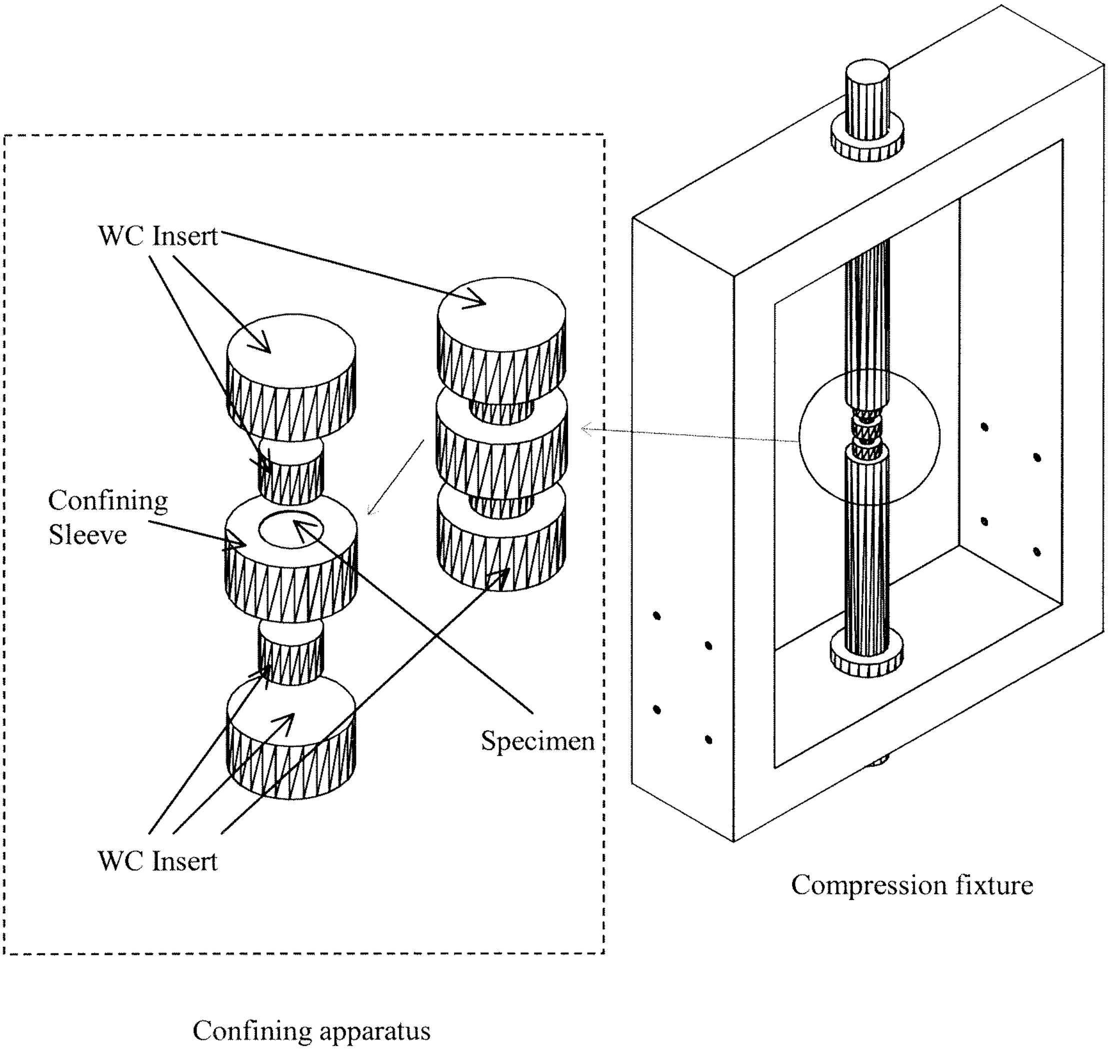

Figure 1. Quasi-static compression fixture and the confining apparatus.

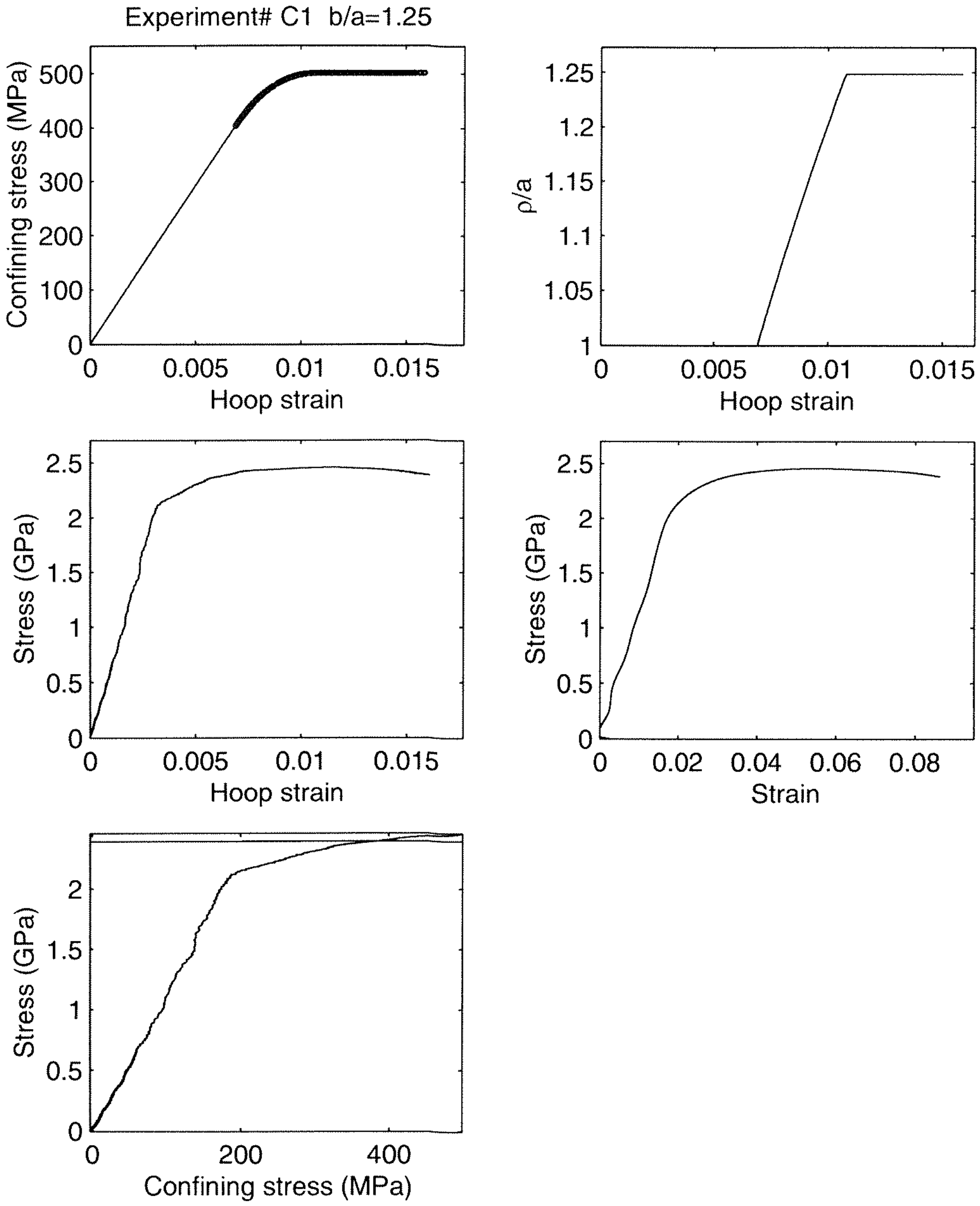

Figure 2. (a) Multiaxial compression of Vitreloy 1 using a confining sleeve with *b*/*a*=1.25.

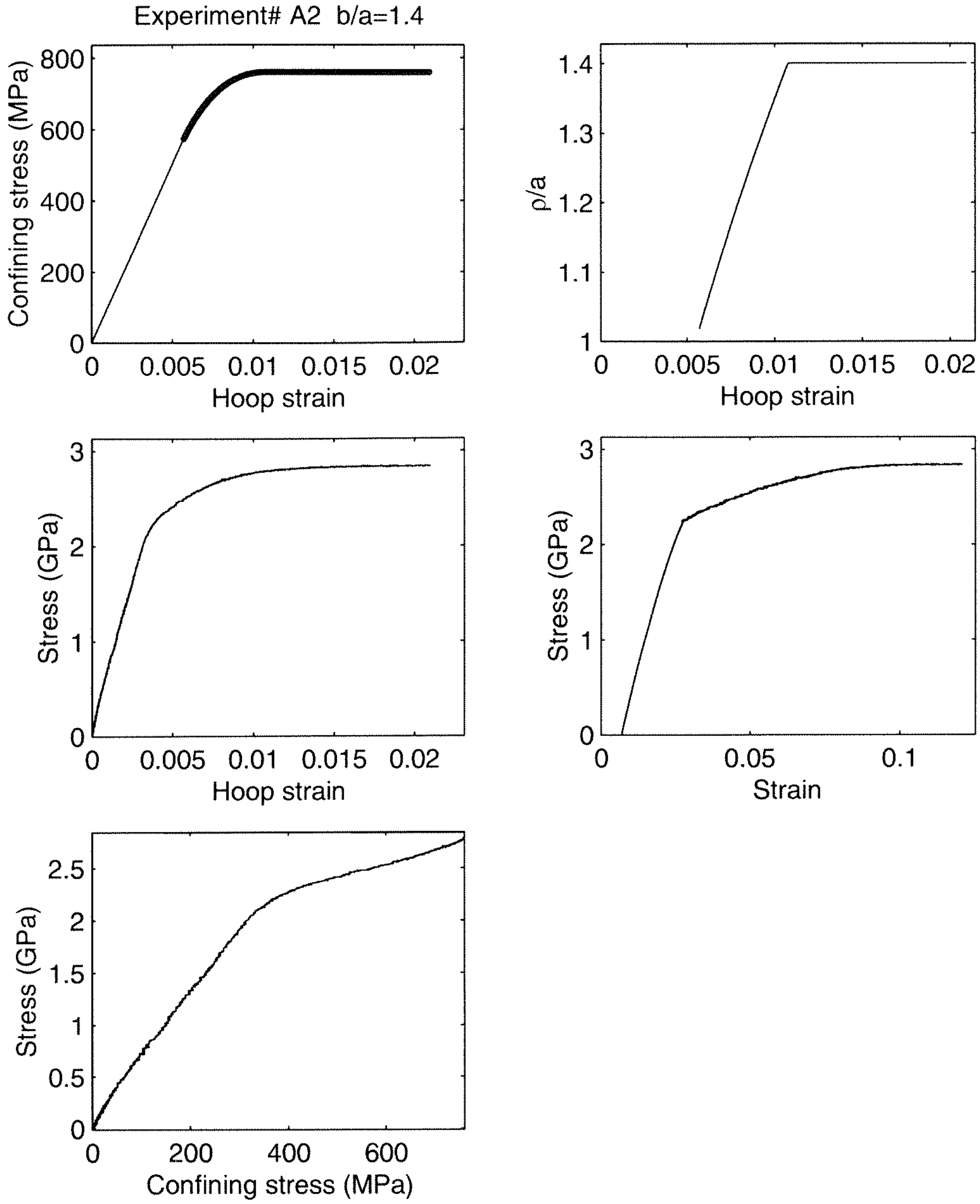

Figure 2. (b) Multiaxial compression of Vitreloy 1 using a confining sleeve with *b*/*a*=1.4.

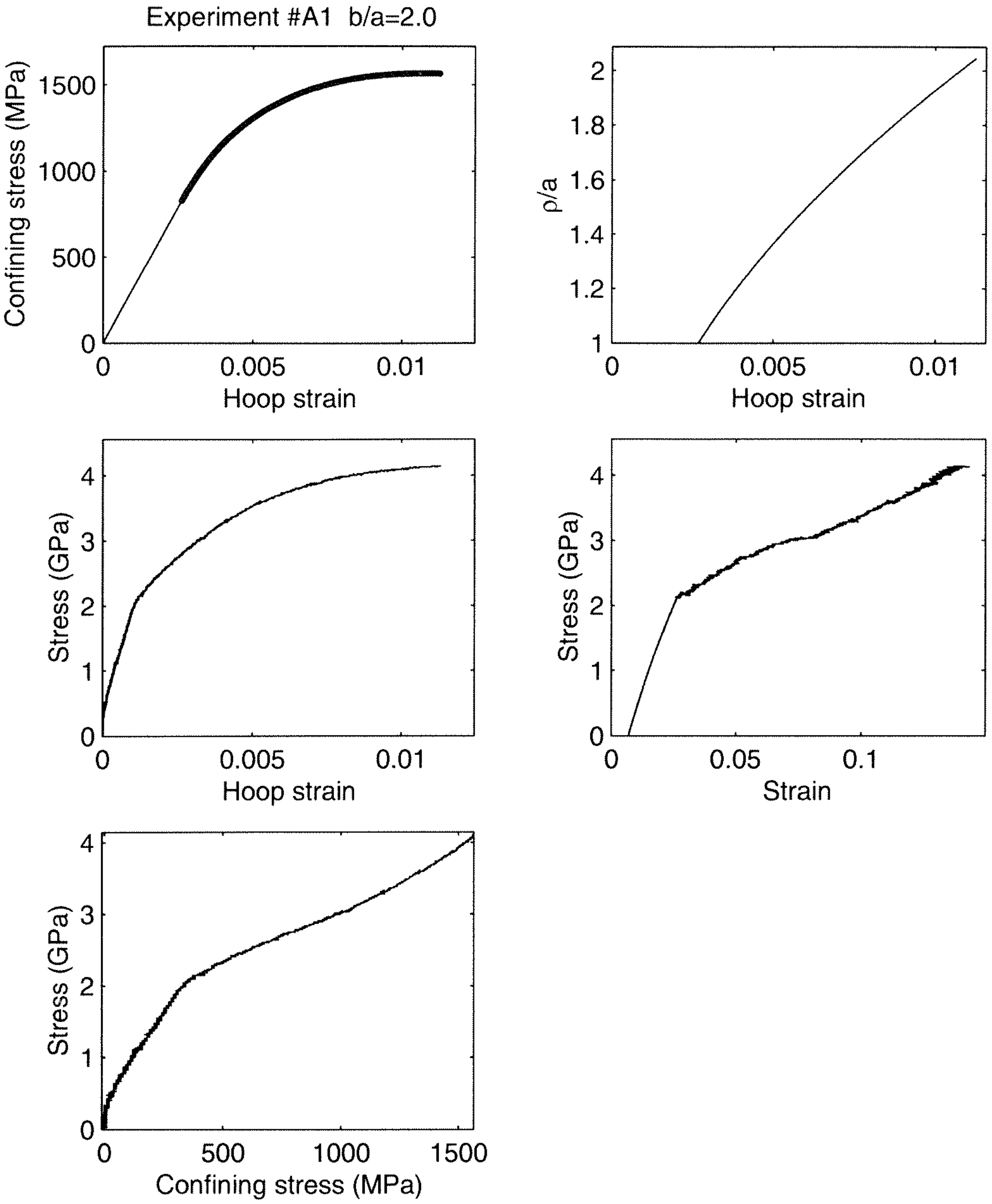

Figure 2. (c) Multiaxial compression of Vitreloy 1 using a confining sleeve with *b*/*a*=2.0.

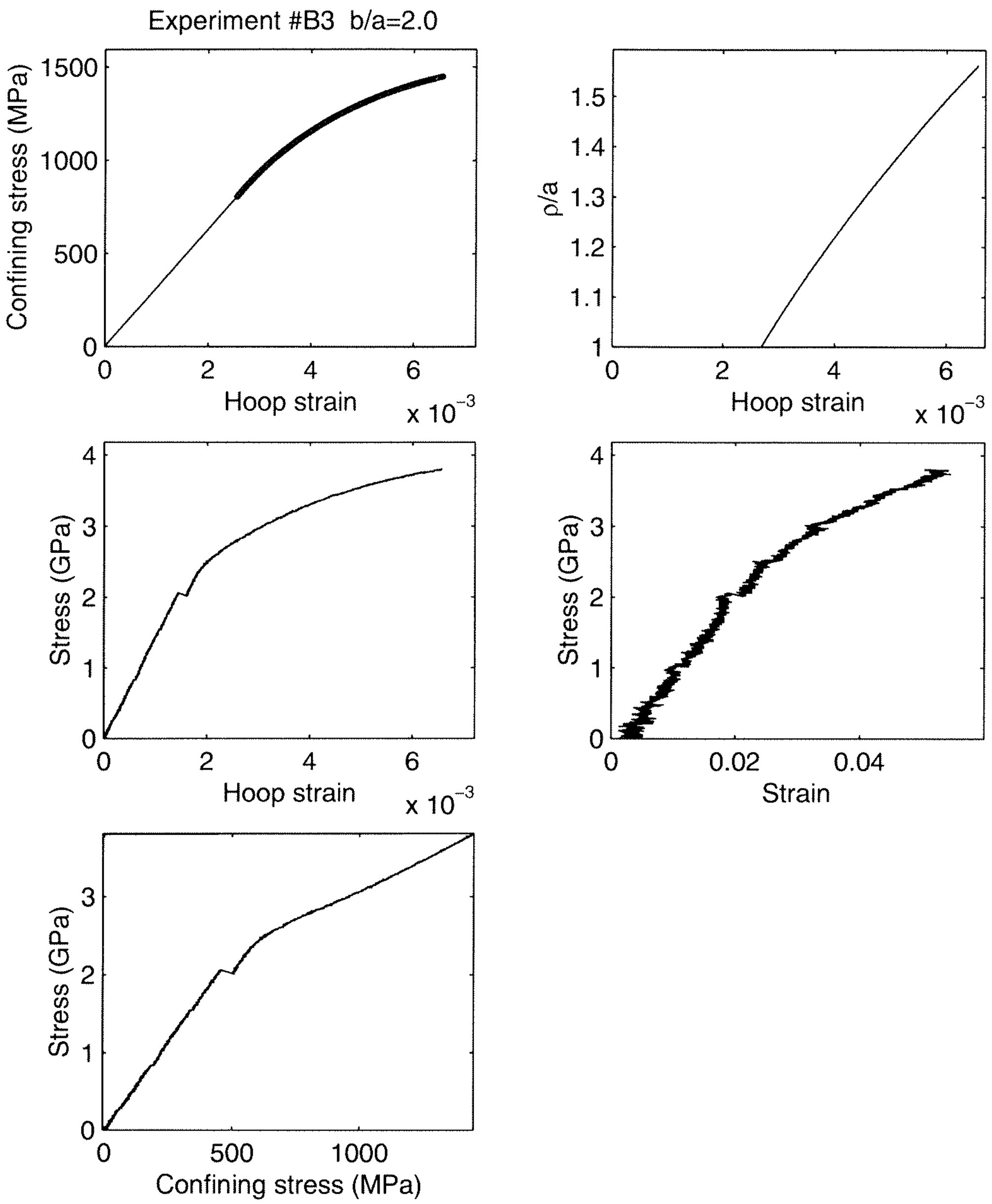

Figure 2. (d) Multiaxial compression of Vitreloy 1 using a confining sleeve with *b*/*a*=2.0.

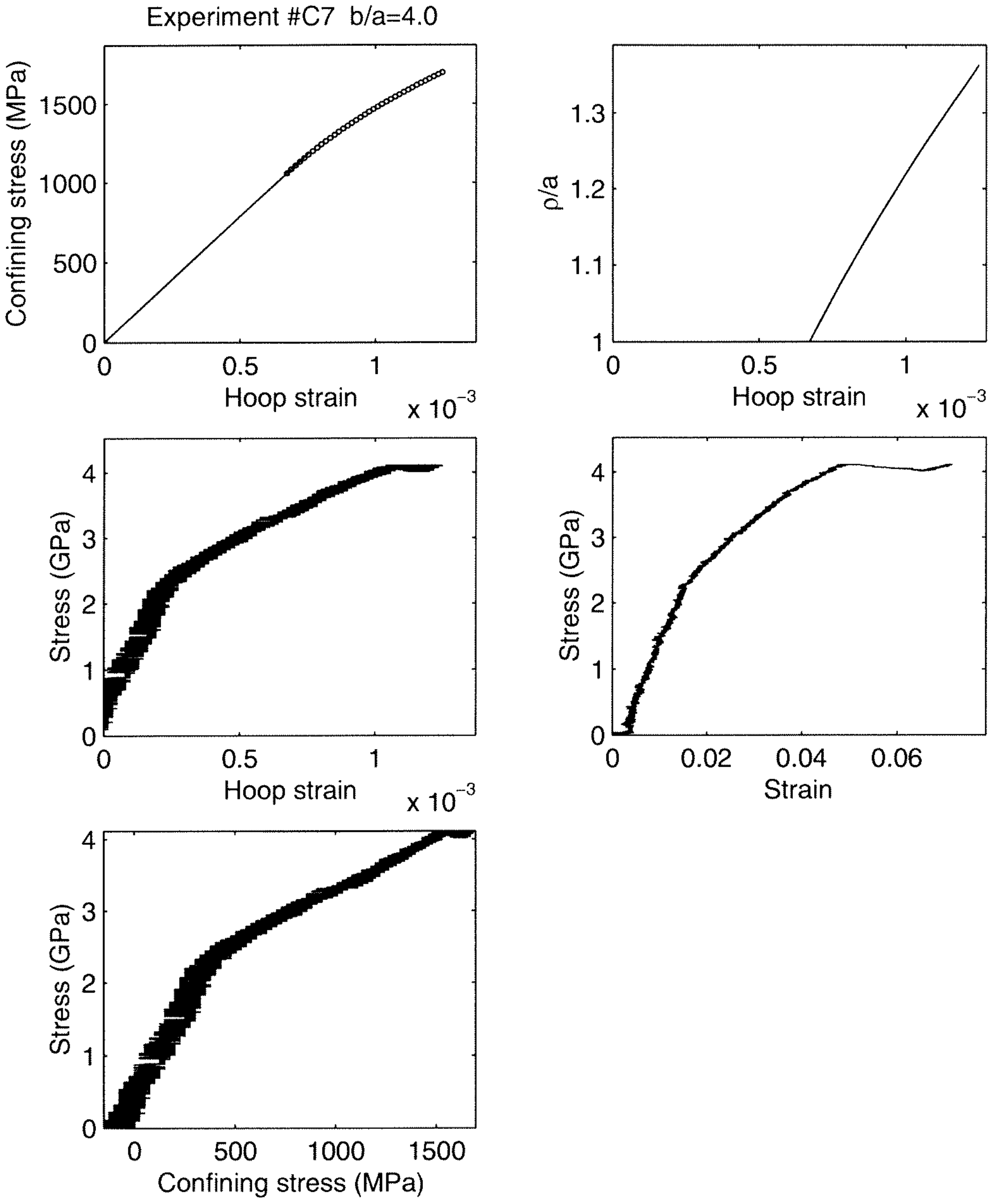

Figure 2. (e) Multiaxial compression of Vitreloy 1 using a confining sleeve with *b*/*a*=4.0.

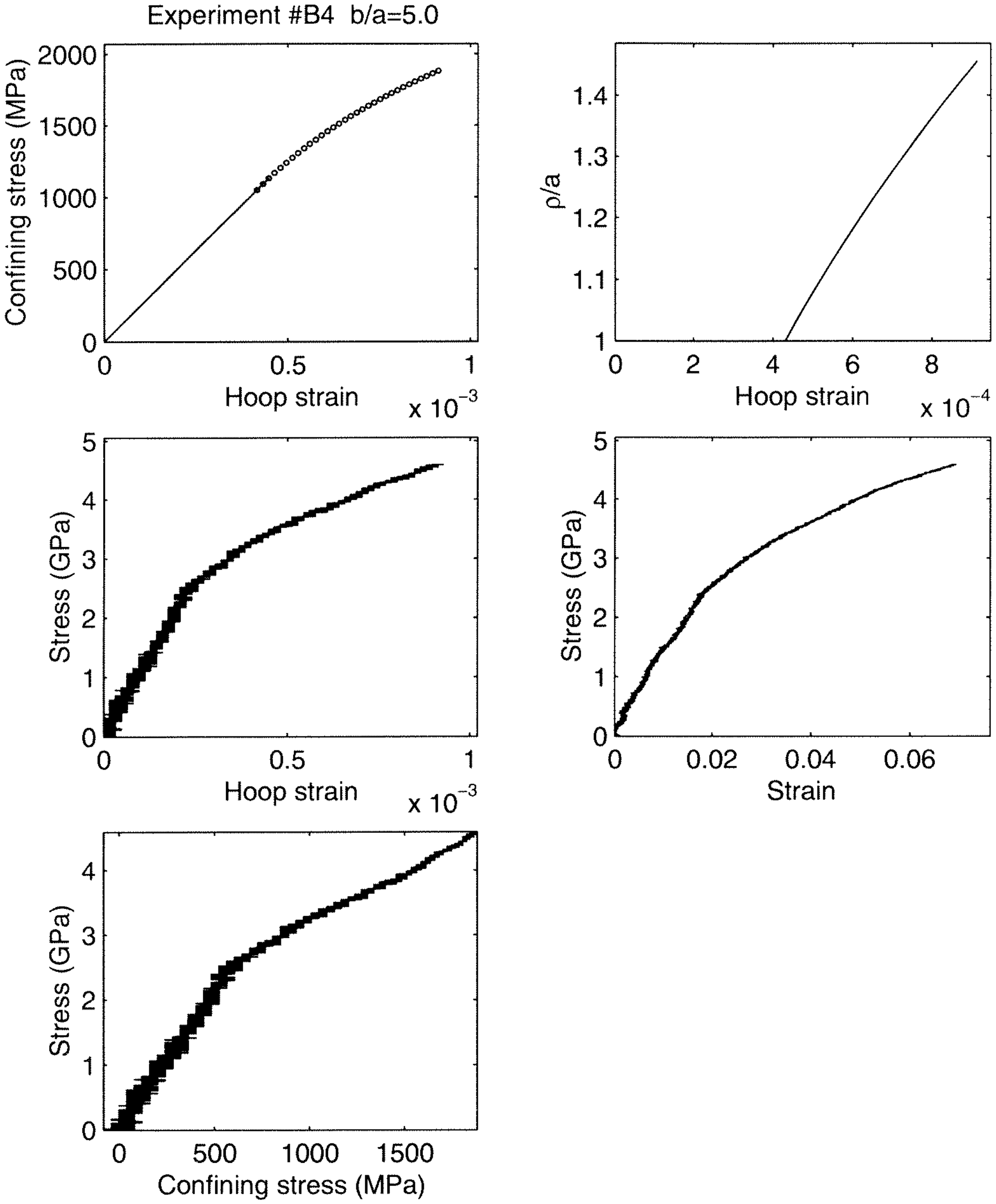

Figure 2. (f) Multiaxial compression of Vitreloy 1 using a confining sleeve with *b*/*a*=5.0.

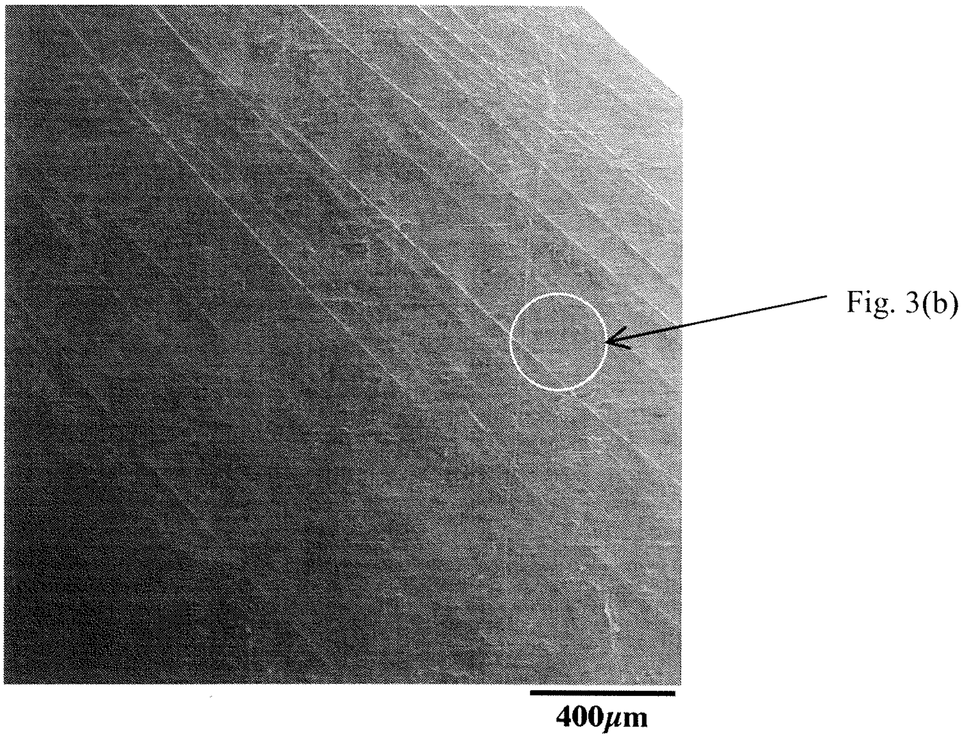

Figure 3. (a) SEM micrograph of shear bands on the surface of deformed specimen (Experiment #C1) confined by a sleeve with ratio b/a=1.25.

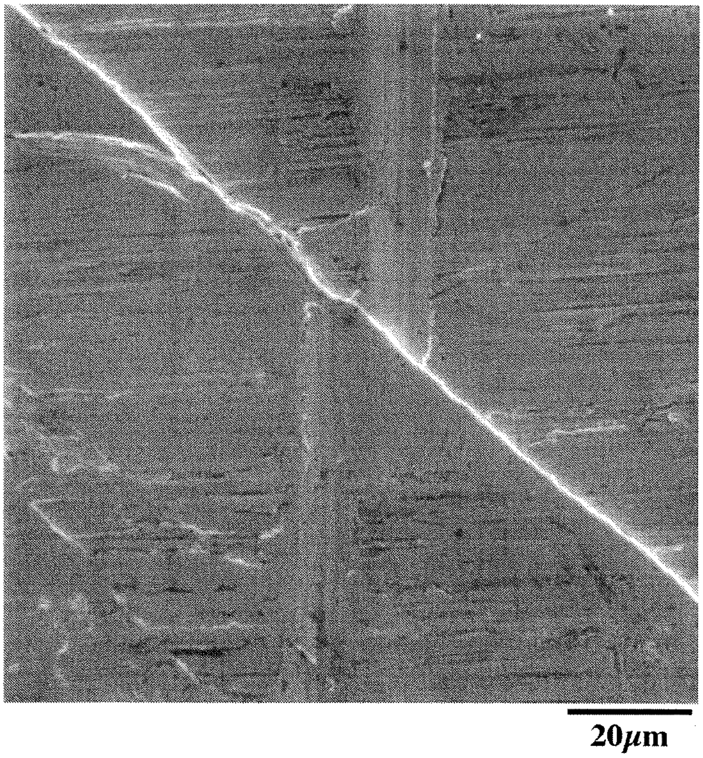

Figure 3. (b) Enlarged view of shear slips on the surface of specimen in Fig. 3(a) (Experiment #C1).

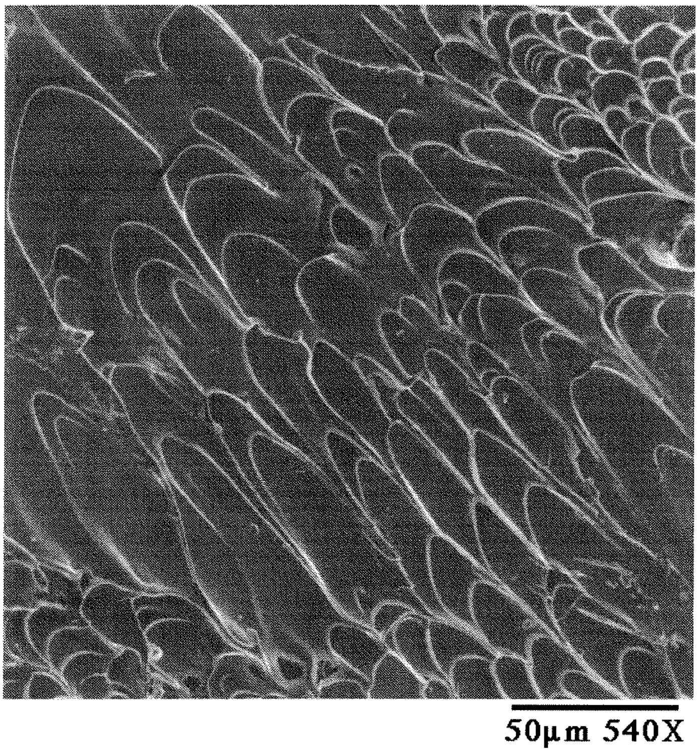

Figure 3. (c) Shear failure surface of specimen (Experiment #C1) due to failure of the confining sleeve.

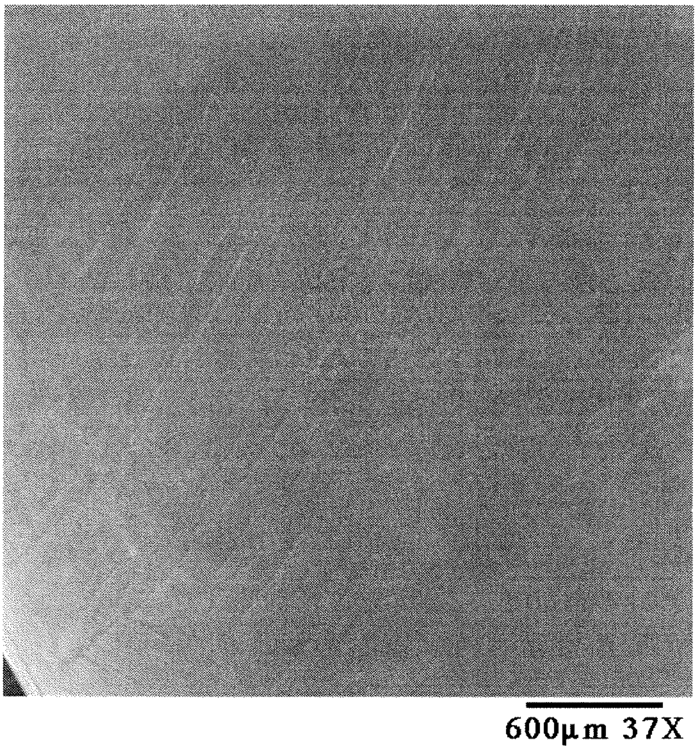

Figure 3. (d) SEM micrograph of shear bands on the surface of deformed specimen (Experiment #A2) confined by a sleeve with ratio *b*/*a*=1.4.

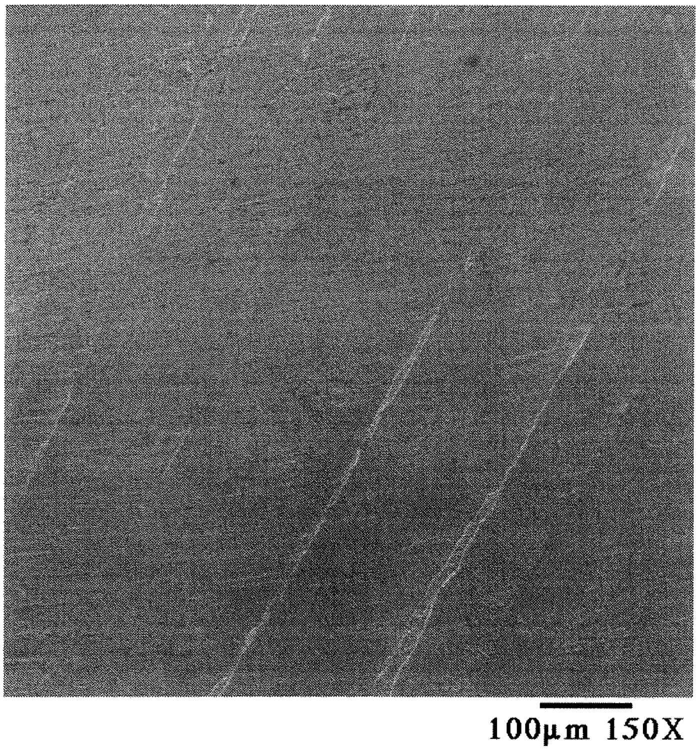

Figure 3. (e) Enlarged view of shear slips on the surface of specimen in Fig. 3(d) (Experiment #A2).

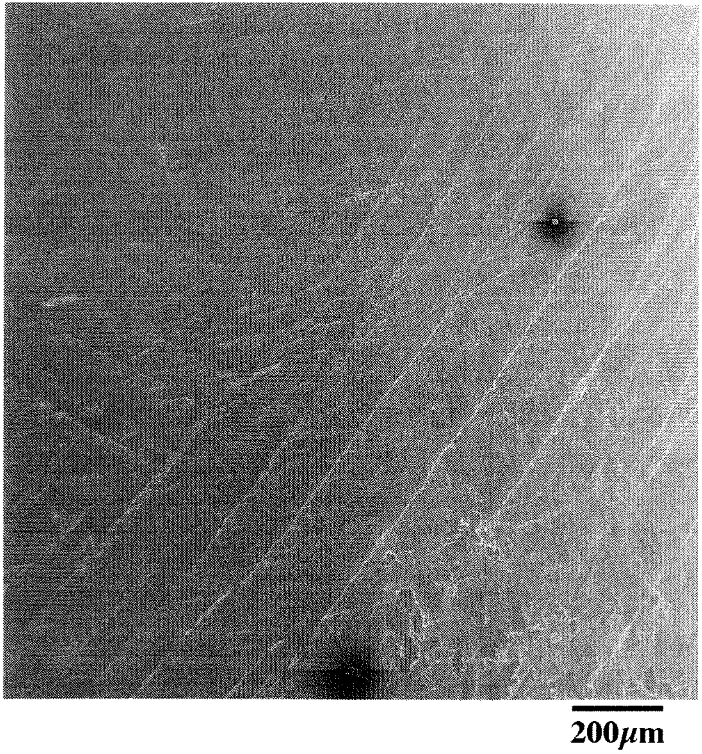

Figure 3. (f) Shear bands in multiple directions (conjugate) on the surface of a deformed specimen (Experiment #A2).

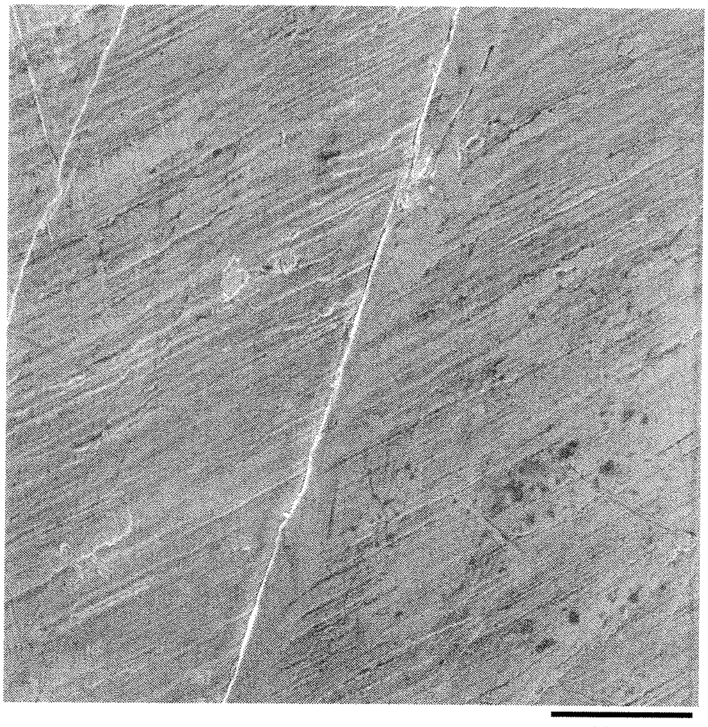

Figure 3. (g) SEM micrograph of shear bands on the surface of deformed specimen (Experiment #C7) confined by a sleeve with ratio b/a=4.0.

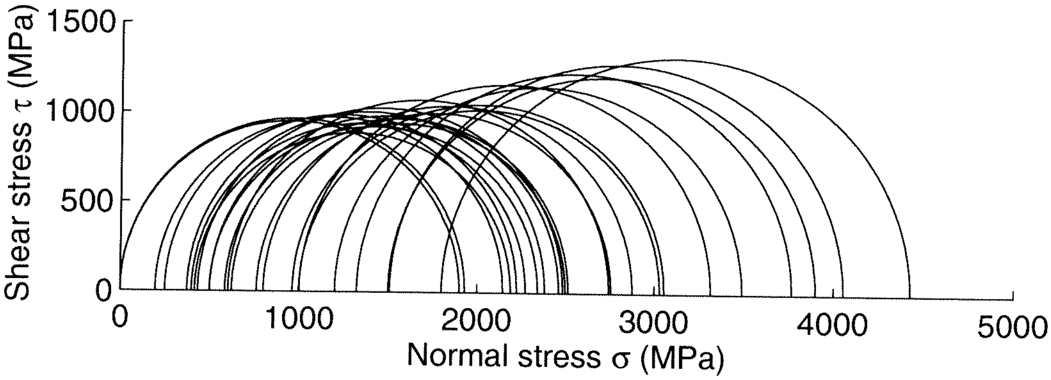

Figure 4. Mohr-Coulomb circles for Vitreloy 1 deduced from the experimental data in Fig. 2.

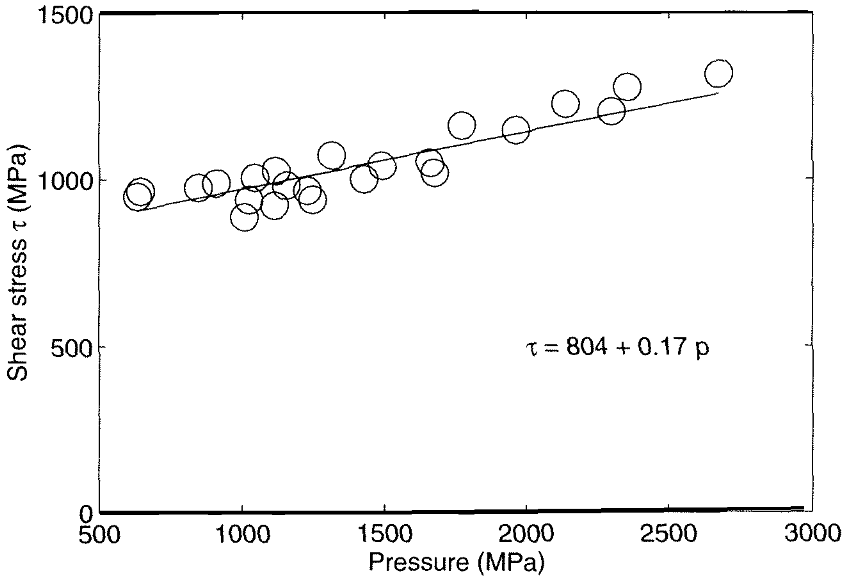

Figure 5. Plot of the maximum shear stress as a function of hydrostatic pressure for Vitreloy 1.

Chapter 5 **Shock Wave Response of Vitreloy 1 and its β-phase Composite**

Abstract

A zirconium based bulk metallic glass, $Zr_{41.2}Ti_{13.8}Cu_{12.5}Ni_{10}Be_{22.5}$ (Vit 1), and its composite, $Zr_{56.3}Ti_{13.8}Cu_{6.9}Ni_{5.6}Nb_{5.0}Be_{12.5}$ (β-Vit 1), were subjected to planar impact loading. A surprisingly low amplitude elastic precursor bulk wave, corresponding to the elastic response of the 'frozen structure' of the intact metallic glasses, was observed to precede the rate-dependent large deformation shock wave. A concave downward curvature after the initial increase of the U_s-U_p shock Hugoniots suggests that a phase-change-like transition occurred during shock compression. In addition, compression damage occurred due to the shear localization. The spalling inside Vit 1 was induced by shear localization, while in β-Vit 1, it was due to debonding of the β-phase boundary from the matrix. The spall strengths at strain rate of 2×10^6 s^{-1} were 2.35 GPa and 2.11 GPa for Vit 1 and β-Vit 1, respectively.

Keywords: Shock wave; Bulk metallic glass; Metallic glass composites

1 Introduction

Amorphous solids can be formed with all major types of bonding, covalent, ionic and metallic (Elliott, 1984). Since first being reported (Klement *et al.*, 1960), amorphous alloys, namely, metallic glasses, have been attracting the attention of many researchers. Tremendous efforts have been made continuously to develop new metallic glass materials in bulk form (Johnson, 1999), which have considerable technological promise including those which involve impact (Conner *et al.*, 1998; Choi-Yim *et al.*, 2001). Due to their noncrystalline, randomly ordered, or more strictly, kinetically constrained atomic structures resulting from the controlled solidification processes from molten state at various quenching rates, bulk metallic glasses have many unique mechanical, electrical, magnetic and corrosion properties which distinguish them from their counterparts of crystalline alloys (Inoue, 2001).

A recently developed bulk metallic glass $Zr_{41.2}Ti_{13.8}Cu_{12.5}Ni_{10}Be_{22.5}$ (Peker and Johnson, 1993) is one of the best glass formers that requires very low quenching rate (1 K/s) to suppress crystallization such that mass production of its kind in bulk form is made possible. The mechanical properties and structural performance, as well as the deformation and damage mechanisms of the metallic glass at quasi-static and dynamic loading conditions, have been studied (e.g., Bruck *et al.*, 1996; Gilbert *et al.*, 1999; Owen *et al.*, 1999; Wright *et al.*, 2001). $Zr_{41.2}Ti_{13.8}Cu_{12.5}Ni_{10}Be_{22.5}$ (commonly known as Vitreloy 1 or Vit 1) has high elastic limit (2%) and exhibits limited inelastic deformation at temperatures below its glass transition temperature (623 K), failing catastrophically by shear localization. Nevertheless, research on shock wave loading of bulk metallic glasses at higher strain rates such as 10^6 s^{-1} is still an open subject and deserves attention. Although Bach *et al.* (1991) studied parameters for the shock wave consolidation of a metallic glass powder, such as the effects of the shock wave energy and the shock wave duration, little appears to be known in the literature regarding the dynamic response and damage of metallic glasses under shock loading. The only related research was due to He *et* *al.* (1991) who investigated the crystallization of metallic glass Fe-Ni-P-B foils, but the shock response of this material was not explored because of the size of the specimens and the way in which the experiments were performed. Such crystallization event is generally not expected in bulk metallic glass $Zr_{41.2}Ti_{13.8}Cu_{12.5}Ni_{10}Be_{22.5}$ since the glass is in a strong metastable state formed by low quenching rate. Fiber-reinforced $Zr_{41.2}Ti_{13.8}Cu_{12.5}Ni_{10}Be_{22.5}$ composites have been demonstrated to have an excellent performance as armor penetrators, the loading rate of which is typically very high (Conner *et al.*, 2000). A better understanding of the impact performance of the bulk metallic glass can be achieved by performing shock loading of the metallic glass to evaluate its behavior before a comprehensive constitutive model for the composites can be proposed. In this chapter, the experimental results for the shock Hugoniot relations of $Zr_{41.2}Ti_{13.8}Cu_{12.5}Ni_{10}$ $Be_{22.5}$ and its dendritic particulate composite $Zr_{56.3}Ti_{13.8}Cu_{6.9}$ $Ni_{5.6}Nb_{5.0}Be_{12.5}$ (Kim, 2001) are presented and the associated failure mechanism are discussed.

2 Experimental

The bulk metallic glass used in this investigation was provided in the form of a 4 mm cast sheet, with a nominal composition $Zr_{41.2}Ti_{13.8}Cu_{12.5}Ni_{10}Be_{22.5}$, manufactured by Howmet Corporation, Greenwich, CT, and Amorphous Technologies, Inc., Laguna Niguel, CA, under the commercial name, Vitreloy 1 (or Vit 1) (Peker and Johnson, 1993). The β-phase composite of Vit 1 (referred to as β-Vit 1 hereafter), formed through in-situ chemical partitioning by adding Nb to bulk forming Zr-Ti-Cu-Ni-Be system, with a nominal composition of $Zr_{56.3}Ti_{13.8}Cu_{6.9}Ni_{5.6}Nb_{5.0}$ $Be_{12.5}$ (Hays *et al.*, 2000), was also used to study the effect of introducing in-situ particulate reinforcement in Vitreloy 1 on shock compression behavior. The as-received plates were carefully lapped and polished to a surface finish of 5 microns. The plate was then electrical discharge machined (EDM) into smaller circular disks with a diameter of 20.3 mm (0.8 inch). X-ray diffraction was conducted on the as-received samples. The typical presence of broad diffuse peaks and lack of discrete peaks revealed that the as-received Vitreloy 1 is amorphous.

Specimens were impacted by planar flyers of 36 mm in diameter at different velocities by a powder gun loading system in the Graduate Aeronautical Laboratories at Caltech (see Zhuang, 2002). To prevent the possible high-pressure gas leakage reported earlier (Zhuang, 2002), the gun is intended to be operated at a flyer velocity of less than 1,200 m/s. Nevertheless, high shock amplitudes can be achieved using different flyer materials, including polycarbonate (PC), 6061 aluminum alloy (Al), 304 stainless steel (SS) and tungsten (W). The release (rear) surface of the impactor (flyer) was left traction free. A 7.5 mm thick polymethylmethacrylate (PMMA) window plate was bonded to the rear surface of specimen, which supported electric pins and served as a buffer for particle velocity detection. Table 1 lists the key parameters for the experiments performed in this study. Table 2 shows the mechanical properties such as elastic wave speeds of the materials obtained using ultrasonic measurements. Table 3 provides the shock Hugoniot relations for the flyer materials which were used in estimating shock particle velocities of the Vit 1 and β-Vit 1 whenever optical signals for particle velocity measurement were not obtained. The instance of impact by the flyer on the specimen was detected using electric pins (EP) (Asay and Shahinpoor, 1993; Zhuang, 2002) that were flush mounted with the impact surface of the specimen. The arrival time of the shock wave at the rear surface of the specimen was sensed either by electric pins which were flush mounted with the rear surface of the specimen, or by a time-resolved laser velocity interferometer system, VISAR (Barker and Hollenbach, 1972; Zhuang, 2002) which provides the particle velocity history. Two sinusoidal signals having $\pi/2$ phase angle difference can be obtained using the VISAR system (Fig. 1), which makes it convenient to analyze the "sign" of the interface movement, i.e., whether the interface is accelerating or decelerating. Subsequently, the particle velocity at the interface can be obtained based on the fringe count $F(t)$ as a function of time,

$$u(t-\tau/2)=\frac{\lambda F(t)}{2\tau(1+\Delta v_0/v)}, \tag{1}$$

where τ, the delay time of the VISAR system, was set to 3.016 ns using an etalon delay leg; λ=514.5 nm is the wavelength of the Ar laser light source that was utilized in the VISAR. All the experiments were performed with a velocity fringe constant, $\lambda/2\tau$, of 85.3 m/s/fringe. The velocity correction $\Delta\nu_0/\nu$ due to the change of the refraction index of the window material was negligible. The use of manganin gage technique for stress measurement was attempted, but was not successful because of the electrical interference between the power supply and the rest of the electronic measurement system.

3 Results and discussions

3.1 Shock profiles

In this first ever attempt to investigate the response of bulk metallic glasses to shock loading, 12 experiments were performed, of which 8 valid experiments will be presented here. They are numbered #02, 05, 07, 08, 09, 10, 11 and 12 respectively (see Table 1). Figure 2 shows the particle velocity profiles at the specimen/PMMA interface for the two materials impacted by PC and Al flyers. The elastic precursor and bulk wave speeds for Vit 1 estimated based on the shock profile data (Fig. 2) are about 6-7% larger than those values obtained using ultrasonic measurements (Table 2), while for β-Vit 1 the data of the two measurements agree well with each other. However, it is surprising to observe that both the Hugoniot elastic precursors and the bulk waves have very low amplitudes, and the cause of this deserves further investigation. The shock profiles of Vit 1 also indicate that the time when the deformation shock front appeared became earlier as the shock strength was increased. It is clear for Vit 1 that the duration of the shock front (i.e., for PC and Al flyers) decreased with the increase in shock loading strength, implying a considerable rate-dependent effect under shock compression, and a similar trend of rate effect was also observed for β-Vit 1, whose shock profile by PC flyer is not shown in Fig. 2. The difference between the shock profiles for Vit 1 and β-Vit 1 impacted by Al flyers at nearly the same velocity may be attributed to the β phase crystalline dendritic particles present in the Vit 1 matrix of β-Vit 1 composite. The amorphous matrix of β-Vit 1 is much like Vit 1 with slightly different composition $Zr_{47}Ti_{12.9}Nb_{2.8}Cu_{11}Ni_{9.6}Be_{16.7}$, and the ductile particles are bcc micro-crystals with composition of $Zr_{71}Ti_{16.3}Nb_{10}Cu_{1.8}Ni_{0.9}$ (Hays *et al.*, 2000; Kim, 2001). A few small step jumps can be seen on the shock front for Vit 1 by a PC flyer, which appear to be related to the shear localization (see section 3.3) during shock compression.

3.2 Shock Hugoniots

The shock velocities are obtained using the VISAR signals and the signals from the electrical pins (EP), and the particle velocities can be deduced based on shock profiles, if available, or otherwise estimated using impedance matching method using the known Hugoniot data and impact velocity of the flyer and the measured shock velocity. The shock Hugoniots for Vit 1 and β-Vit 1 obtained in the present study are summarized in Fig. 3. The elastic and bulk wave speeds for both the initial and shocked states estimated using the VISAR velocity profiles are also indicated in Fig. 3. For particle velocities less than 200 m/s, both shock and particle velocities were deduced directly from the VISAR velocity profile data. For higher particle velocities, they were estimated using the impedance matching method, since the contrast of VISAR fringe signal was lost due to severe damage of the interface (reflecting surface) resulting from shear localization, which will be discussed later.

Unlike the shock Hugoniots of many metallic alloys whose Hugoniot can be represented using monotonically increasing parabolic relations (e.g., Marsh, 1980), Fig. 3 illustrates the complicated nature of the shock U_s-U_p Hugoniot curves for Vit 1 and β-Vit 1. The present Hugoniot curves are similar to those obtained for materials which experienced a phase change during shock compression (e.g., McQueen, 1991; Kipp and Grady, 1994). However, no evidence for structural changes induced by phase transformation have been observed in the present study. It is most likely that the large reduction of shock velocity in this region is due to the onset of catastrophic internal damage of material occurring within the shock front resulting from shear localization during shock compression. Furthermore, the increase in shock velocity with further increase in amplitude of loading is the result of competition between shock compression and damage process resulting from shear localization. For both Vit 1 and β-Vit 1, the deformation shock wave speed is much lower than the bulk wave speed suggesting the significant reduction in the shear strength at the Hugoniot state (Grady, 1994), or in the other words, some degree of damage has occurred during the process of shock compression.

3.3 Shear localization

To investigate the damage induced by shock loading, scanning electron microscopy (SEM) was employed to examine the surfaces of the recovered specimens, following the shock compression experiments. Micro slip steps and cracks formed due to shear localization were typically observed on the rear surfaces of the shocked specimens, as shown in Fig. 4. It was found that damage as indicated by the shear band or crack density on the rear surface of shocked specimens increased with the increasing amplitude of shock loading by PC, Al and SS flyers and reaches a maximum for the SS flyer. However, when the shock amplitude was increased further using tungsten (W) flyers, the damage was found to be decreasing rather than increasing. This observation of trends in damage on the rear surface of shocked specimens correlate well with the shock Hugoniot measurements shown in Fig. 3. This may be interpreted to be that the damage processes occurred under different shock loading levels are dominated by different physical mechanisms.

Under relatively weak loading, though damage does occur during shock compression, material strength plays a dominant role, and, therefore, the shock velocity increases with increasing particle velocity. When the internal damage increases to some degree, the weakening or softening of material becomes a more important factor among others. A large portion of the shock energy is converted into thermal energy in the form of temperature rise within the severely deformed shear bands or in creating new cracks, resulting in a reduction of the shock velocity. However, if the shock amplitude increases further, the rate of energy delivered into the shock front is larger than that of the energy consumed in the process of deformation and damage behind the shock front. Also, the damaged material is compressed within the shock front, resulting in a higher shock velocity.

The mechanism of shear localization induced damage during compression of Vit 1 and β-Vit 1 metallic glasses is also supported by the fact that the quality of VISAR fringe signals deteriorated only in cases where a high shock loading stress was expected. Under the loading of strong shock, upon the arrival of shock front at the rear (specimen/PMMA interface) surface of the specimen where the reflecting surface for VISAR is located, the severe non-uniform out-plane-surface deformation of the reflecting surface resulting from the internal shear localization occurs. As a result, the spatial coherence of the reflected laser light from this surface was lost and the average intensity of the reflected light without any useful velocity information of the moving surface was recorded, i.e., signals lacked contrast.

3.4 Spall

The interaction between the release waves from the free surface of flyer and the rear surface of specimen brings the shocked material into a tensile state at a location inside the specimen. If the tensile stress exceeds a critical value (spall strength), tensile damage process is initiated and eventually spall (material separation) will occur if both the amplitude and the pulse duration of the tensile wave are sufficient. The occurrence of spalling can be inferred from the velocity profile measured using the VISAR signal. The spall strength of material can be estimated using the velocity pullback during the decompression process (u in Fig. 2) (e.g., Asay and Shahinpoor, 1993). Based on the measured deformation wave speed (Fig. 3), the calculated spall strengths for Vit 1 and β-Vit 1 are 2.35 GPa and 2.11 GPa, respectively, and the estimated average strain rates corresponding to fastest rising portion of the shock front are on the order of 10^6 s^{-1}. Comparing the spall strengths with the ultimate tensile strengths at strain rate of 10^{-3} s^{-1}, which are 1.89 GPa and 1.45 GPa (Kim, 2001), respectively, the two materials are only moderately sensitive to strain rate, with β-Vit 1 exhibiting higher rate sensitivity.

The SEM micrographs of cross-sections from recovered specimens of experiments # 02 (Vit 1) and # 09 (β-Vit 1) are shown in Fig. 5. It is clearly seen that the spall damage mechanisms of the two materials are quite different. The zigzag cracks seen in the micrographs of Vit 1 (Fig. 5(a)) suggest that the spalling of Vit 1 is associated with "brittle" damage resulting from shear localization and subsequent shear failure while the sample was under tension during the decompression process. Examination under higher magnification (Fig. 5(a)) reveals that each crack was formed due to nucleation, growth and coalescence of microvoids within the shear bands. In addition, the location of the spall plane (Fig. 6) can also be detected by ultrasonic pulse-echo measurement technique, as depicted in Fig. 7. Initially, incident longitudinal (P) wave from an ultrasonic transducer (frequency, 10 MHz) was partially reflected by the spall plane and partially transmitted and reflected by the rear surface of the deformed specimen (Experiment #2). No further reflection or transmission of the pulses are sensed by the ultrasonic receiver, in contrast to the multiple pulse reflections observed for an undeformed (i.e., not subjected to shock loading) Vit 1 specimen of the same thickness.

For the composite material, β-Vit 1, the spalling is characterized to be much more ductile (Fig. 5(b)) and there are many micro voids nucleating mostly at the boundary between the β phase and the Vit 1 matrix. The spall plane was formed in the damaged area due to the growth and coalescence of such micro voids.

4 Conclusions

In this chapter, the shock responses of Vit 1 metallic glass and its composite, β-Vit 1, were investigated using planar impact technique. Through the study of shock loading on Vit 1 and its β-Vit 1 composite, the following conclusions can be drawn.

1. The shock profiles indicate a rate-dependent effect on the duration of the shock front with respect to shock loading strength. The difference between the shock profiles for Vit 1 and β-Vit 1 can be attributed to the ductile bcc crystalline flake-like phase in β-Vit 1 composite. A surprisingly low amplitude elastic precursor and bulk wave, corresponding to the elastic response of the 'frozen structure' of the intact metallic glasses, was observed to precede the rate-dependent large deformation shock wave.
2. The shock U_s-U_p Hugoniots obtained experimentally, as well as the SEM examination of recovered specimen samples, indicate a complex deformation process during shock compression. Shear localization induced damage/failure, as well as the accompanying stress relaxation characterizes the subsequent compression process. Unusual Hugoniot curves were observed for both Vit 1 and β–Vit 1: a dramatic decrease in the shock velocity as particle velocity reached around 700 m/s, which also corresponds to the maximum shear band and crack density. This may be explained by a damage mechanism which involves competition between the rate of energy delivered to the shock front and the energy consumed due to the damage process.
3. Based on the measured deformation wave speed, the calculated spall strengths for Vit 1 and β-Vit 1 are 2.35 GPa and 2.11 GPa, respectively, indicating only a mild rate sensitivity for ultimate tensile strength for the materials. The SEM micrographs reveal that the spall plane of β-Vit 1 is more ductile than Vit 1. The spalling in Vit 1 was induced by shear localization,

while in β-Vit 1 it was most likely due to debonding of the β-phase boundary from the matrix.

References

Asay, J. R. and Shahinpoor, M., High-Pressure Shock Compression of Solids, Springer-Verlag (1993).

Bach, J., Krueger, B. and Fultz, B., Shock-wave consolidation of a Ni-Cr-Si-B metallic-glass powder, Mater. Sci. Lett., **11** (10-12), 383-388 (1991).

Barker, L. M. and Hollenbach, R. E., Laser interferometer for measuring high velocities of any reflecting surfaces, J. Appl. Phys. 43, 4699 (1972).

Bruck, H. A., Rosakis, A. J. and Johnson, W. L., The dynamic compressive behavior of beryllium bearing bulk metallic glasses, J. Mat. Res., **11** (2), 503-511 (1996).

Choi-Yim, H., Conner, R. D., Szuecs, F. and Johnson, W. L., Quasistatic and dynamic deformation of tungsten reinforced $Zr_{57}Al_{10}Cu_{15.4}Ni_{12.6}$ bulk metallic glass matrix composites, Scripta Mater., **45**, 1039-1045 (2001).

Conner, R. D., Dandliker, R. B., Scruggs, V. and Johnson, W. L., Dynamic deformation behavior of tungsten-fiber/metallic-glass matrix composites, Int. J. Impact. Eng. **24** (5) 435-444 (2000).

Elliott, S. R., Physics of amorphous materials, Longman Group (1984).

Gilbert, C. J., Schroeder, V. and Ritchie, R. O., Mechanisms for fracture and fatigue-crack propagation in a bulk metallic glass, Metall. Mater. Trans., **A30** (7), 1739-1753 (1999).

Grady, D. E., Shock-wave strength properties of boron-carbide and silicon-carbide, J. Phys. IV, **4**(C8), 385-391 (1994).

Hays, C. C., Kim, C. P. and Johnson, W. L., Microstructure controlled shear band pattern formation and enhanced plasticity of bulk metallic glasses containing in situ formed ductile phase dendrite dispersions, Phys. Rev. Lett. **84** (13), 2901-2904 (2000).

He, H. L., Xu Y.F., Jin, X. G..and Wang, W. K., , Crystallization of metallic-glass Fe-Ni-P-B under shock loading, J. Mater. Sci. Lett., **10** (23), 1389-1391 (1991).

Inoue, A., Bulk Amorphous Alloys, in Amorphous and nanocrystalline materials: preparation, properties and applications, ed. by Inoue, A. and Hashimoto, K., Springer (2001).

Johnson, W. L., Bulk glass-forming metallic alloys: Science and technology, MRS Bull., **24** (10) 42-56 (1999).

Kipp, M. E. and Grady, D. E., Shock phase-transformation and release properties of aluminum nitride, J. Phys. IV, **4**(C8), 249-256 (1994).

Klement, W., Willens, R. H. and Duwez, P., Non-crystalline structure in solidified gold-silicon alloys, Nature, **187**, 869-870 (1960).

Marsh, S. P., LASL shock Hugoniot data, University of California Press, California (1980).

McQueen, R. G., in High-pressure equations of state: theory and applications, Proc. Int. School of Physics, Course CXIII, ed. by Eliezer, S. and Ricci, R. A., North-Holland, 101 (1991).

Owen, D. M., Rosakis, A. J. and Johnson, W. L., Dynamic failure mechanisms in beryllium-bearing bulk metallic glass., Mat. Res. Soc. Symp. Proc., Vol **554**, 419-430 (1999).

Peker, A. and Johnson, W. L., A highly processable metallic glass: $Zr_{41.2}Ti_{13.8}Cu_{12.5}Ni_{10.0}Be_{22.5}$, Appl. Phys. Lett., **63**, 2342-2344 (1993).

Zhuang, S., Shock Wave Propagation in Periodically Layered Composites, Ph.D. Thesis, California Institute of Technology (2002).

Table 1. Experimental parameters for the shock wave loading experiments

Experiment #	Flyer Material*	Flyer Thickness (mm)	Flyer Velocity (km/s)	Specimen Material	Specimen Thickness (mm)	Diagnostic System(s)$^+$
#05	PC	2.87	0.969	Vit 1	3.71	VISAR
#08	PC	2.87	0.976	β-Vit 1	3.32	VISAR
#02	Al	1.53	0.544	Vit 1	3.72	VISAR
#09	Al	1.53	0.586	β-Vit 1	3.36	VISAR
#12	SS	1.47	0.857	Vit 1	3.61	EP,VISAR
#10	SS	1.45	0.840	β-Vit 1	3.38	EP
#07	W	1.79	1.218	Vit 1	7.38	EP,VISAR
#11	W	1.78	1.182	β-Vit 1	6.71	EP

PC= Polycarbonate, Al= 6061 aluminum alloy, SS=304 stainless steel, W=Tungsten
+VISAR=Velocity Interferometer System for Any Refelctor, EP=Electric Pins

Table 2. Mechanical properties of Vit 1 and β-Vit 1 obtained using ultrasonic measurements

Material	ρ (g/cm^3)	C_l (km/s)	C_s (km/s)	C_k (km/s)	E (GPa)	G (GPa)	K (GPa)	ν
Vit 1	6.00	5.185	2.464	4.335	98.6	36.4	113.	0.354
β-Vit 1	6.21	4.795	2.167	4.090	80.0	29.2	104	0.372
PC	1.20	2.130	0.918	1.848	2.79	1.01	4.08	0.386
Al	2.69	6.231	3.191	5.025	72.4	27.4	67.9	0.322
SS	7.89	5.935	3.161	4.680	205.	78.8	173.	0.302
W	17.7	5.266	2.862	4.100	374.	145.	298.	0.290
PM*	1.18	2.744	1.401	2.216	6.14	2.32	5.81	0.324

*PM=Polymethylmethacrylate(PMMA)

Table 3. Hugoniot parameters of the materials used for the flyers (data from Marsh, 1980)

Material	C_0	C_1
PC	2.93	0.98
AL	5.35	1.34
SS	4.58	1.49
W	2.86	2.08

Note: Shock Hugoniot relation in the form of $U_S = C_0 + C_1 U_P$ is assumed.

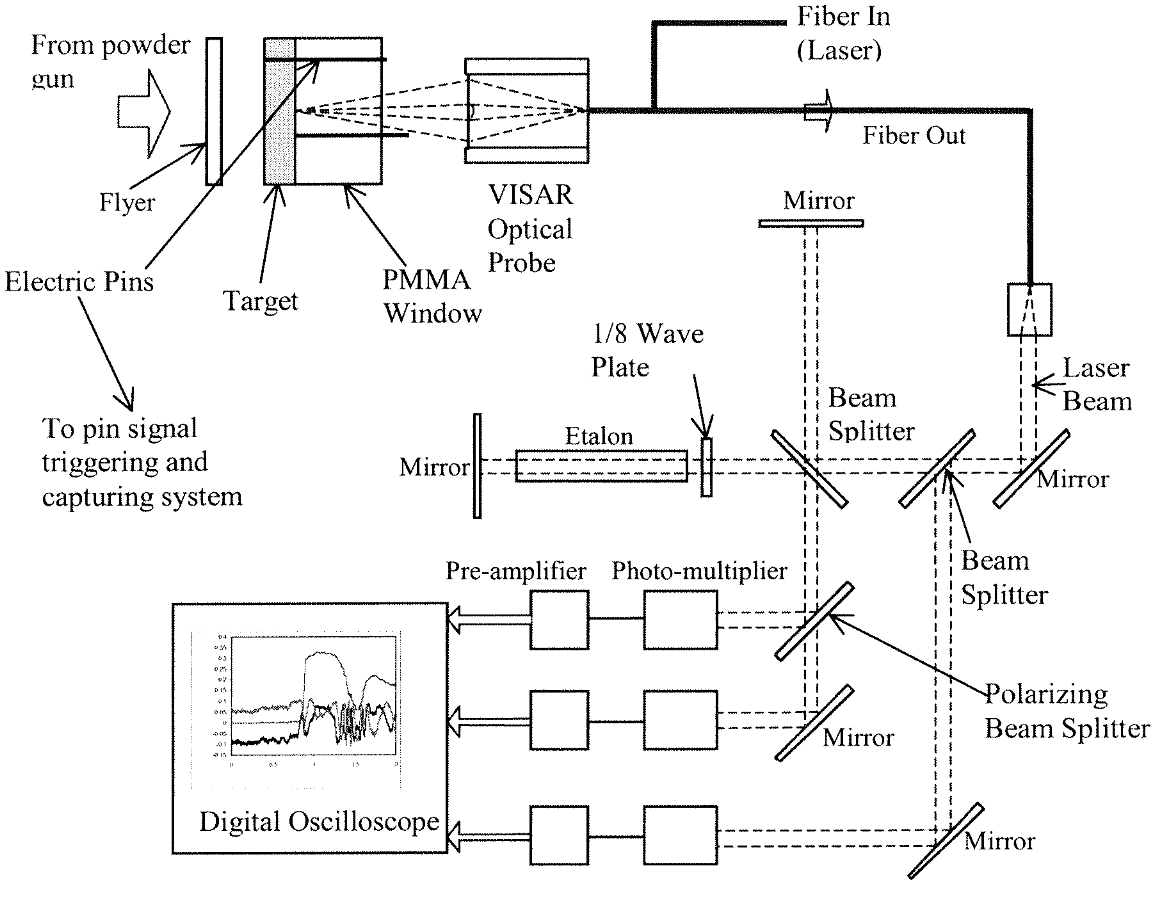

Figure 1. Schematic of the shock wave experimental setup including the VISAR diagnostic system used to measure particle velocity (adapted from Zhuang, 2002).

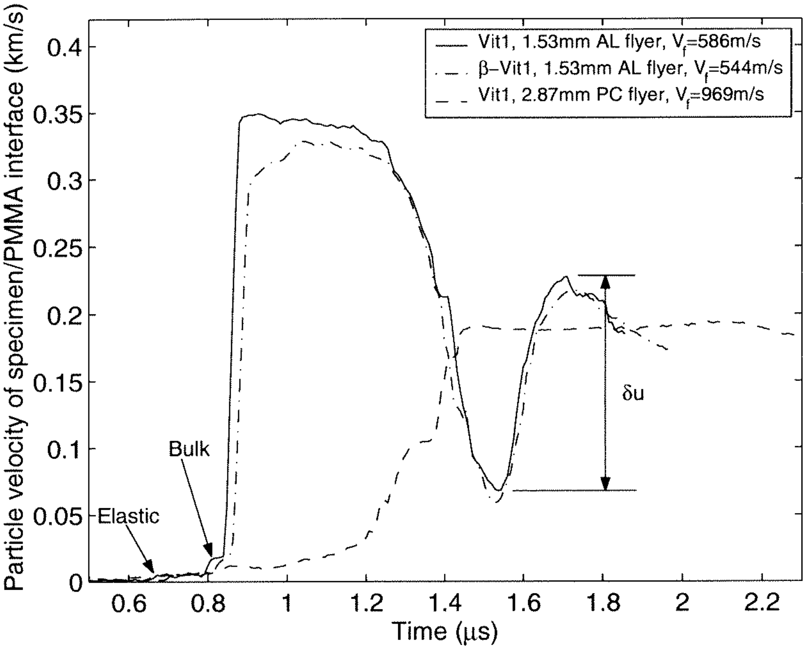

Figure 2. Particle velocity profiles at the specimen/PMMA window interface obtained using VISAR for Vit 1 and β-Vit 1 specimens impacted by different flyers at various velocities.

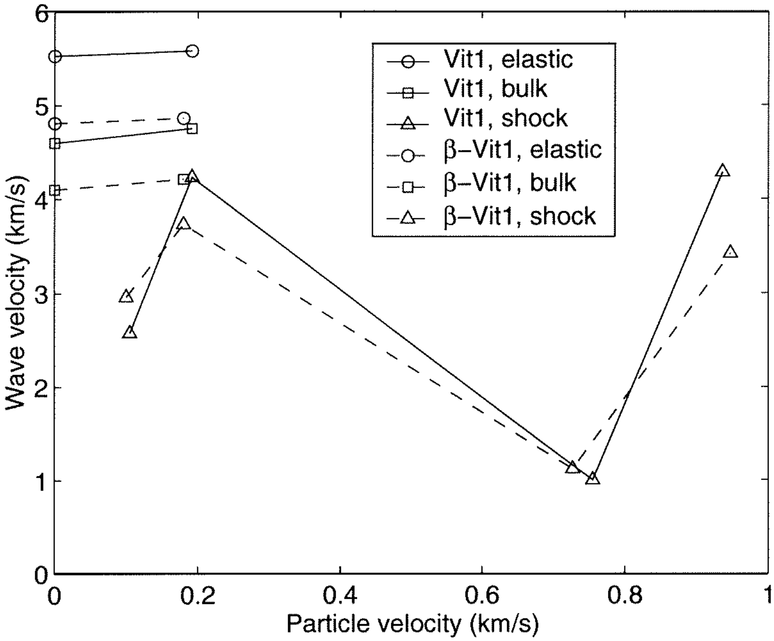

Figure 3. Shock Hugoniot curves for Vit 1 metallic glass and β-Vit 1 metallic glass composite.

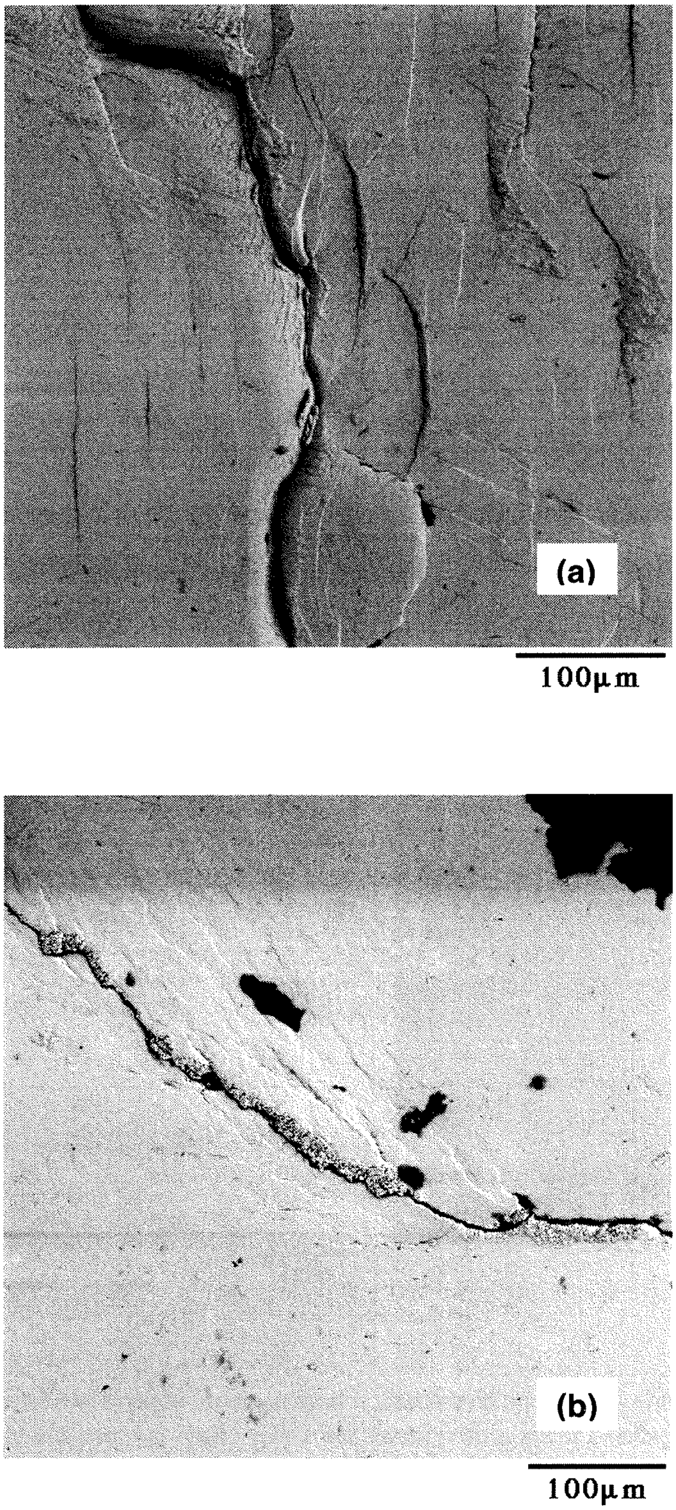

Figure 4. Typical micrographs of shear bands/cracks observed on the rear surface of recovered specimens after shock loading: (a) Vit 1 (Experiment #07); (b) β-Vit 1 (Experiment #11).

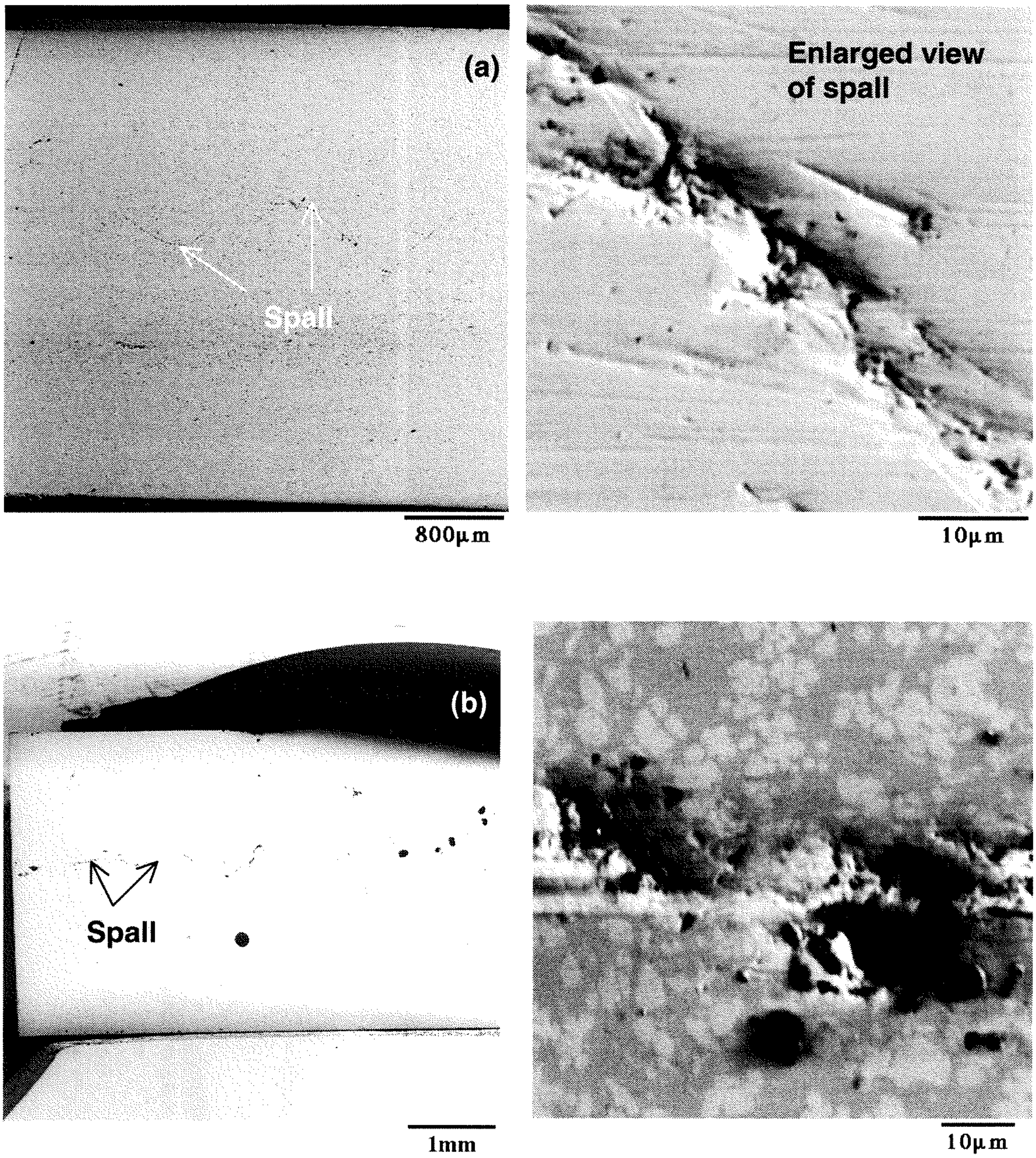

Figure 5. Microgrpahs of typical cross-section in recovered specimens showing the damage area around the spall plane: (a) micro voids nucleated within shear bands in Vit 1 (Experiment #02); (b) microvoids nucleated at the phase boundaries of the β phase (bright spots) in β-Vit 1 (Experiment #09).

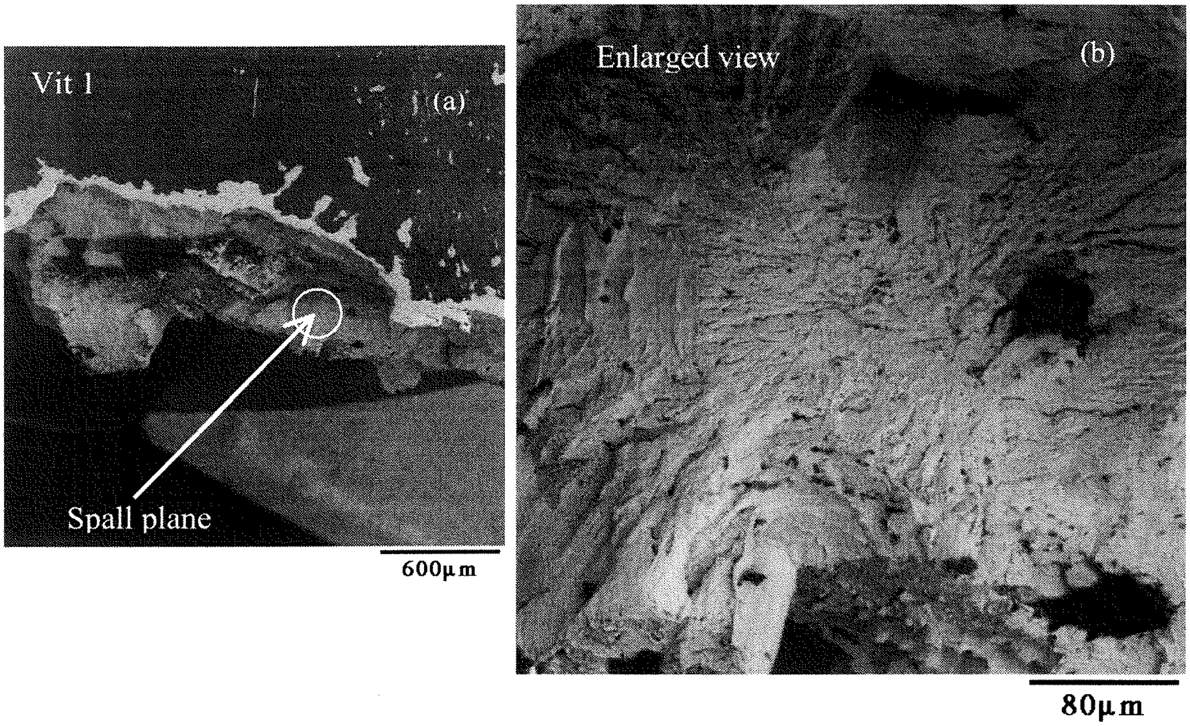

Figure 6. Micrographs of spall plane in shocked Vit 1 (Experiment #02): (a) general view; (b) an enlarged view of the spall plane at the location pointed by the arrow in (a).

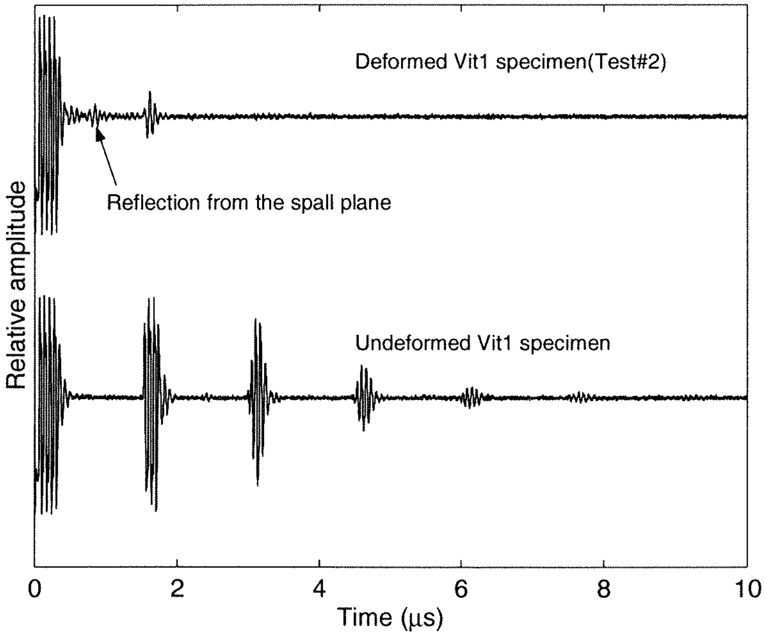

Figure 7. Typical ultrasonic signals obtained on Vit 1 specimens: "deformed specimen" refers to the recovered specimen (Experiment #2) which has been shock loaded; "undeformed specimen" refers to specimen prior to shock loading.